STUDY OF ZERO-GRAVITY POSITIVE

EXPULSION TECHNIQUES

CONTRACT NAS7-149

INTERIM REPORT NO. 8230-933007

APRIL 1964

JUN 1   Rec'd

FOREWORD

Presented in this interim report are the results of work accomplished by the Bell Aerosystems Company during the period 16 March 1963 through 15 January 1964. This work was authorized as a continuation of Contract NAS7-149 for the National Aeronautics and Space Administration, under the administration of NASA's Western Operations Office.

The final report for the initial phase of this contract was published by the Bell Aerosystems Company under the title "Study of Zero-Gravity Positive Expulsion Techniques" (Reference 1). The initial contract period extended from 16 April 1962 through 15 February 1963.

Mr. Frank E. Compitello of NASA Headquarters, Washington, D. C., was the Project Manager and Mr. Richard N. Porter of the Jet Propulsion Laboratory was the Technical Manager of the program.

Principal contributors to this report at Bell Aerosystems are:

I. DePuy - Structural Investigation
V. Daniels - Dynamics Investigation
A. Lytle - Dynamics Investigation
R. Herrmann - Bellows Design
W. Walters - Permeability
W. Clarke - Permeability

APPROVED:

Kurt Berman
Assistant Chief Engineer
Design and Development/Rockets

R. F. Goerke
Program Manager

Report No. 8230-933007

SUMMARY

_~730?_

    This report summarizes the work conducted by the Bell Aerosystems Company during the 10-month continuation effort under the basic NAS7-149 program. The presentation of report material is similar in sequence to the final report on the original program (Reference 1) in that the effort is subdivided into major tasks, each reported as a separate section. The major tasks considered for this follow-on effort are:

    Section 2 - Structural Investigation of Metallic Bellows

    Section 3 - Dynamics Investigation of Metallic Bellows

    Section 4 - Permeation Technology

    Section 5 - Optimum Envelope Investigation

    Section 2 of the report discusses the modifications incorporated into the structural analysis which was started during the basic program. Also presented are results from a preliminary study of the effects of variation in geometric parameters.

    The dynamics analyses in Section 3 include a comparison of the bellows accordion mode and the general case of a longitudinal homogeneous bar fixed at both ends. A mathematical model for the liquid modes was also developed. This porous bar concept demonstrated good agreement with test data. Results of an experimental test program to determine the dynamic characteristics of double-ply bellows are included.

    The permeation work in Section 4 is a continuation of the investigations initiated during the original program on detectors. As a result of this work, the thermistor-type detector was selected as the most practical. Both the design and the application of this detector are discussed. A new permeation chamber, using a corrugated diaphragm in place of a bellows, is discussed and the results of development testing with this apparatus are presented.

    In Section 5, on bellows assemblies, a series of graphs is presented for use in selecting the lightest weight bellows assembly.

    A more-detailed synopsis of each major task on this program is presented at the beginning of Sections 2, 3, 4, and 5.

    Section 6 contains a list of references used throughout this report.

iv

CONTENTS

CONTENTS (CONT)

ILLUSTRATIONS

ILLUSTRATIONS (CONT)

TABLES

SECTION 1

INTRODUCTION

During the follow-on effort of the NAS7-149 contract, work was continued at Bell Aerosystems Company on the major tasks started during the basic program (Reference 1):

(1) Structural Investigation of Metallic Bellows

(2) Dynamics Investigation of Metallic Bellows

(3) Permeation Technology

The structural analysis computer program was modified to improve its accuracy and versatility. Using the modified program, a study was conducted to determine the effects of variations in design parameters on the stress-deflection relationships.

A detailed investigation of the liquid modes of vibration was conducted and a theoretical model was formulated to predict frequencies. The merits of double-ply bellows in a dynamic environment were evaluated and an analysis of test results is included in the discussion.

A new permeation chamber was designed and fabricated. This unit uses a corrugated diaphragm to allow for volumetric expansion, rather than the formed bellows assembly used in the original chamber design. The design and operation of this new apparatus are discussed and data are presented from representative tests. Thermistor-type thermal conductivity detectors were investigated for applicability to the Bell-designed permeation test apparatus. The stability of the thermistor over extended periods of time and the repeatibility limits of detection are evaluated. Data from these tests are included in Appendix I.

Finally, a preliminary design method is presented for the evaluation of bellows assemblies with respect to liquid volumes, weights, and envelopes.

SECTION 2

STRUCTURAL INVESTIGATION OF METALLIC BELLOWS

A. SYNOPSIS

An IBM program for computing nonlinear, elastic stresses and deflections in a welded bellows was developed during the original contract period (Reference 1). This program solves the nonlinear differential equations for axisymmetrically-loaded thin shells of revolution (Reference 2). Employing the novel computational method of Archer (Reference 3), the complete stress and deflection distribution in a particular bellows can be computed within a few seconds for each load or pressure increment. The program, as presented in Reference 1 is limited to computations in the elastic range for welded bellows having leaves of constant thickness and uniform temperature distribution. The bellows must remain a surface of revolution throughout its loading range. The loading must not vary circumferentially. Six bellows leaves, which must have equal developed lengths in the radial direction, are considered joined together. No stress concentration effect is included at the leaf junctures and the local weld bead thickness is neglected.

During the follow-on contract period, the computer program was modified to account for the stiffening effects of the leaf juncture weld bead. The program also was modified so that the mathematical model could be pressurized, internally or externally, while confined to a given total axial deflection. Using the modified computer program, studies were made of the effects on spring rate-and allowable elastic deflection caused by variations of leaf shape, bellows diameter, span, pitch, and leaf thickness.

A subprogram was written to detect the occurrence of local buckling where the buckled shell deviates from a surface of revolution. These asymmetric buckling loads must be detected because, at this point, the basic computer program ceases to be applicable. The subprogram, which is not yet operational, is limited to shallow shells of revolution. Although not yet written into a subprogram, the theoretical work was completed to remove the shallow shell restrictions of the present subprogram.

Although the structural computer program is specifically applicable only to welded bellows, the method of computation is applicable to a large family of symmetric shell problems including formed bellows, Belleville springs, and corrugated circular diaphragms.

B. PROGRAM MODIFICATIONS

The nonlinear, elastic stress computer program for welded bellows, which appears as Appendix III of Reference 1, does not take into account the local stiffening effect of the weld bead at the leaf junctures. During the initial effort, it was determined that to include weld bead effects would require changes to the unique matrix inversion routine of the program. Assuming that, for expulsion applications, a bellows would be of a large diameter where the weld bead stiffness would be small, the effect was neglected.

At the beginning of the follow-on work, the question of weld bead stiffness effects was re-examined. One bellows manufacturer confirmed that the weld bead size is important in computations of small diameter bellows. It became apparent that, wherever practical, a general computer program of this type should be usable for a variety of applications. By including the effect of the weld bead stiffness, the program becomes usable to compute stresses and deflections in small bellows for instrument or seal applications. Since the importance of the weld bead stiffness can only be assumed, its inclusion increases the confidence in the accuracy of subsequent calculations. In consultation with Dr. Robert Archer of Case Institute of Technology, modifications were made to the leaf boundary expressions in the computer program to include the effects of the weld bead stiffness. It was found that these expressions may be used in such a way that the rapid tri-diagonal inversion routine of the original program is preserved. The weld bead was assumed to be a compact ring with the leaf mid-planes attached to it at a common point. The small eccentricity thus neglected could have been included, but a more complex set of boundary expressions are required to account for changes in ring loading and rotational stiffness as the ring rotates under load. The weld bead ring cross-section was assumed to be a half-ellipse with its semi-axis normal to the bellows centerline. The boundary expressions at the weld bead, however, are independent of ring cross-section properties. This assumption is geometrically convenient and also closely approximates the shape of weld beads from typical bellows assemblies. A free-body diagram of a typical outer-radius leaf juncture is shown in Figure 1. The radial deflection, u_r, and the cross-section rotation, β_r, of the ring are:
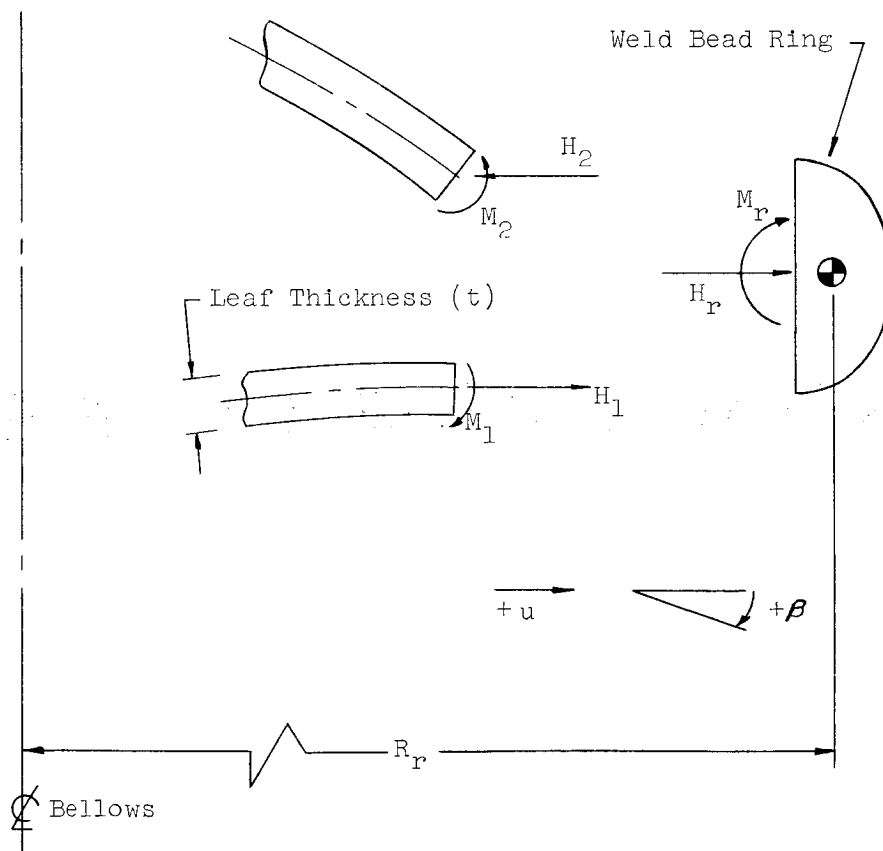
Figure 1. Free-Body Diagram of Typical Leaf Juncture

$$u_r = \frac{H_r R_r^2}{E A_r} \quad ; \qquad \beta_r = \frac{M_r R_r^2}{E I_r}$$

where R_r is the radius of the ring cross-section centroid, A_r is the ring cross-section area, I_r is the moment of inertial of the ring cross-section with respect to an axis normal to the bellows centerline, and E is the modulus of elasticity; u_1, β_1, M_1 and u_2, β_2, M_2 are the radial deflection, clockwise rotation, and meridional moments at the upper and lower leaf end-points, respectively. From Reference 2, the stress function, ψ, is defined as HR. To maintain continuity at the juncture, $u_1 = u_2 = u_r$; $\beta_1 = \beta_2 = \beta_r$; $M_r = M_2 - M_1$; $\psi_2 = \psi_1 + \psi_r$. Since ψ and β are the two unknowns of the basic differential equations of the shell from Reference 2, where the expressions for u_1, u_2, M_1, M_2 may be obtained, the required boundary conditions are defined. Since the differential equations are nonlinear with loads always acting on the deformed shell, the value of I_r depends upon β_r. By using the last iteration value of β_r in the calculation of I_r, the nonlinear term is handled in the same manner as the nonlinear terms in the shell equations. Iteration continues until the previous values of ψ and β agree with the computed values at every solution point within a specified error.

Several other modifications of the computer program were considered, however, the program was restricted to shells of constant thickness. The changes to take into account a variable shell thickness were evaluated, but one difficulty was encountered which caused postponement of this change. The additional subscripted variables required for the program exceeded the available memory storage of the IBM 7090 computer at Bell Aerosystems. This difficulty could be overcome by temporary storage of some items on tape. However, the run time for a typical problem would increase, even when computing constant-thickness problems. Therefore, it is advisable to write a separate program to compute problems of variable shell thickness. Since considerable study must first be conducted on constant-thickness bellows, this new program has not been written. Writing and checking out such a program, although not difficult, will be so time-consuming that this task will be accomplished only when a specific need is indicated.

It is well-known that various modes of elastic instability may occur in welded bellows. An analytical method of stresses and deflection determination should include means of accounting for and studying this phenomenon. The nonlinear shell equations of Reference 2 used in IBM computer program 1753 have been shown by Dr. Archer, Reference 3, to be applicable to the calculation of axisymmetric buckling. The method used in program 1753, however, does not permit calculation in the post-buckling range. The load deflection curve is found by successive stepping of load, solving the differential equations, and computing the deflections. Modification of the program, as suggested by Dr. Archer, so that loads are found as a result of successive deflection steps permits post-buckling calculations. These modifications were made to the single-leaf version of the computer program, under another contract, to compute snap action of a Belleville spring. Some success was achieved with this program, but difficulties have been encountered obtaining convergence in some cases. When this difficulty has been resolved, the process will be included in the 1753 program. Because this process requires more computer time than the present method, a choice of methods will be introduced into the program to obtain optimum speed. The condition of asymmetric buckling which may also occur in a bellows is a special problem discussed later in this report.

Some interest was expressed in adding to the program a capability for thermal stress distribution. Thermal stresses in expulsion bellows would probably arise only when using hot gases as a pressurizing medium. Temperature gradients on the bellows under such an exposure would surely not be axisymmetric in nature. Because the 1753 program is limited to axisymmetric shells of revolution with axisymmetric loading, the applicability of a thermal stress modification would be severely limited. This change could be made if the specific need arises within the resulting limitations.

The program of Reference 1 includes the nonlinear effects of local pressure. However, when pressure is introduced, the bellows is either compressed or extended from pressure forces on the bellows end plate. To evaluate the relative pressure-carrying capacity of various leaf designs, changes were incorporated which confined the bellows to a given axial motion while under pressure. Such a condition corresponds to the condition of expulsion bellows extension with the bellows end plate in contact with the tank. Extension or compression to a given axial motion by a force, other than pressure on the end plate, with subsequent pressure introduction, is another condition included in this modification. In addition to the extension of the program to accommodate several expulsion bellows design conditions, the study of stresses in bellows seals was also made possible by this modification.

Although the next logical step was to perform checks of the modifications and additions to the program, no suitable check problem was available in the literature. The requirements for an experimental test bellows to provide a suitable check of the program preclude the use of a production specimen. In addition to the requirements outlined in Reference 1, strain gages must be installed in the mid-span region to check computed stresses on the leaf before final welding. Because of the time consumed modifying and checking out the computer program, no special test model was purchased. The need for a closely controlled experimental check of results from the computer program is obvious. The program now contains sufficient sophistication to justify the purchase of a test bellows which is to be given a high priority in any continuing effort.

C.   PARAMETRIC STUDY

Since an optimum bellows design cannot be obtained because of the mathematical complexity of the problem, the desired goal must be approached by parametric study.

The first steps toward parametric study of the effects of geometric changes were made before incorporation of the weld bead stiffness modification. There seemed to be some disagreement as to the value of the "cone angle" used by some bellows manufacturers in ripple leaf designs. Each of the four basic shapes studied had a different cone angle, yet each shape was given a different pitch so that all designs would have exactly the same weight. The four designs are shown in Figure 2. As a result of this first parametric investigation, it was obvious that no single geometric parameter can be changed without also changing at least one other parameter. The change of spring rate with combined "cone angle" and pitch is shown in Figure 3. Note the nonlinear effect of spring rate reduction with increasing thrust load which is extending the bellows. Since a large number of trials with different pairs of parameter changes is required to isolate the "cone angle" effect, it was decided to reduce the complexity of parametric study by dealing with simple shapes. Thus, the parametric study reported here indicates some of the general effects of variations in bellows diameter, leaf shape, initial pitch, span, and leaf thickness.

After incorporating the weld bead stiffness into the program, further parametric study computations were begun. During the last week of the contract period, while computing

6   Report No. 8230-933007
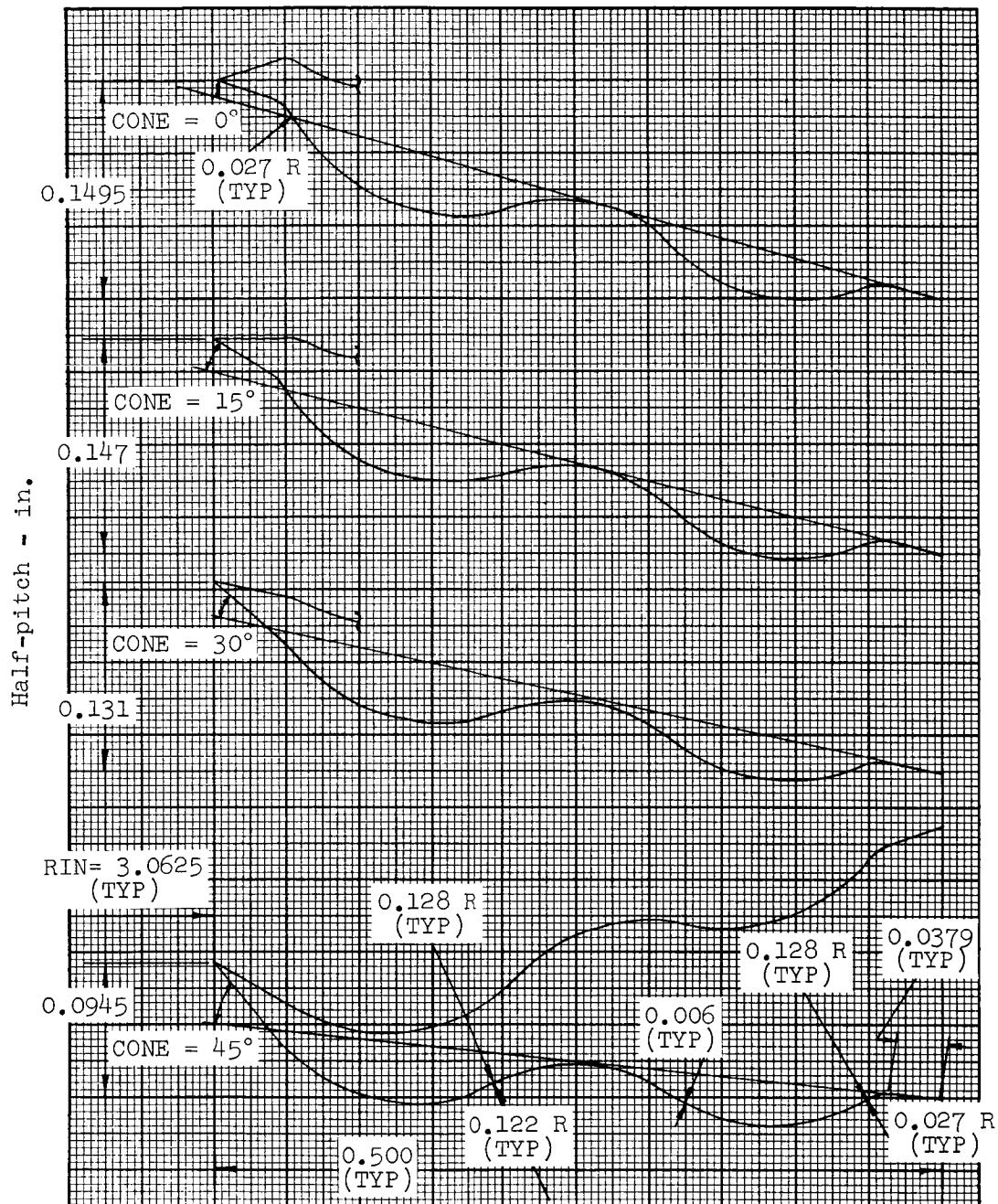
Figure 2. Variation of Pitch with Cone Angle on Four Leaf Shapes
of Equal Weight and Span

stresses on a small bellows seal under another contract, an error was found in the program
weld bead stiffness modifications. Some local pressure effects on the small seal problem
pointed out an obvious discrepancy in the results which did not appear in any of the 40 para-
metric study cases. While the loss involved in recomputing the 40 cases is regrettable, the
monetary loss is much less than would be expected for even linear computation using more
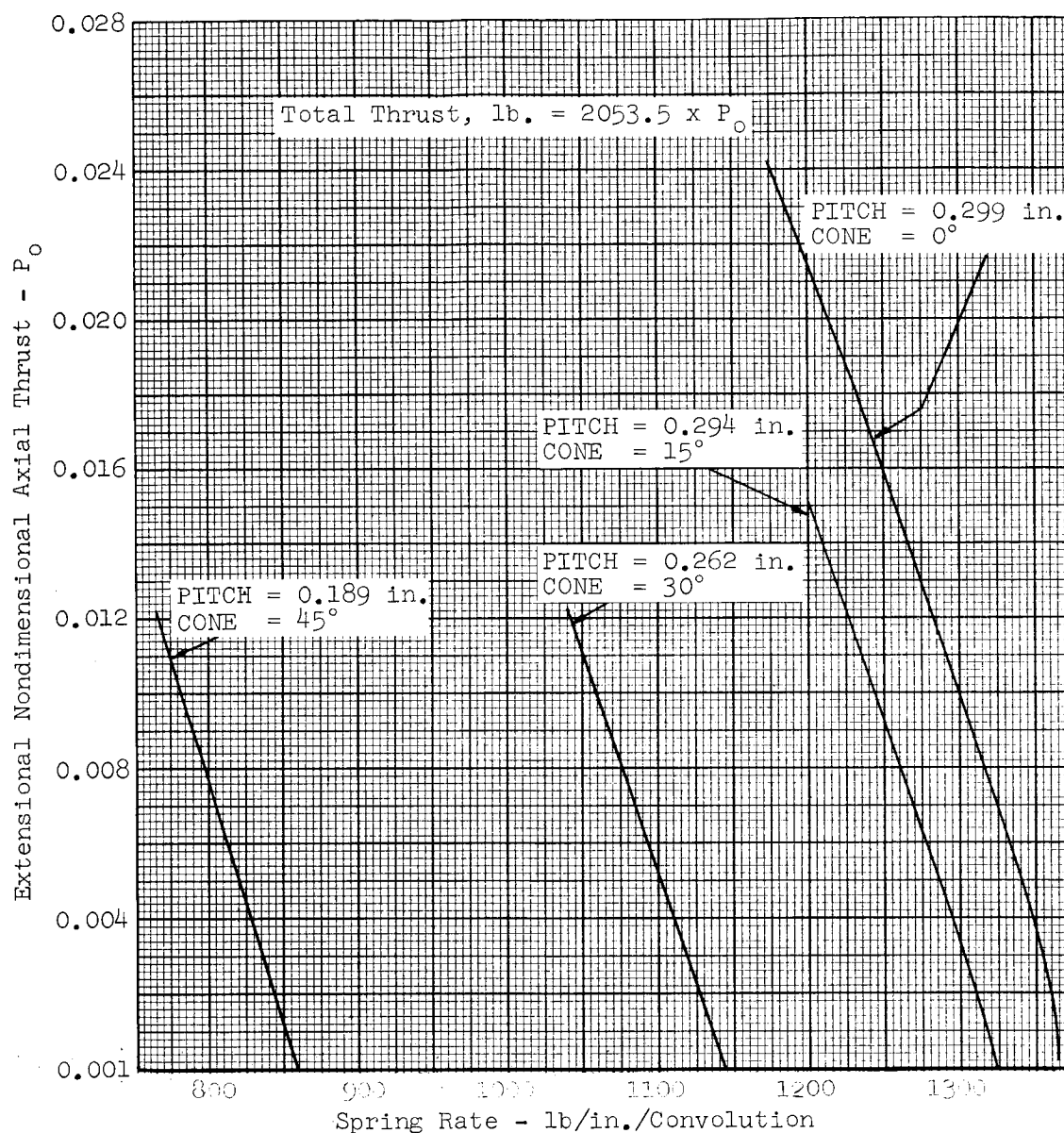
Figure 3. Spring Rate vs Compression Thrust of Four Leaf Shapes
Shown in Figure 2

conventional programs. The average computation cost of one study problem is $6.00. Even when this cost is doubled by the necessity of correcting errors, the result is only a small fraction of the cost of hardware trials for product improvement.

An interesting result of the subsequent small seal problem calculations, after program correction, is that agreement was obtained with actual seal spring rates within less than 5%. Although the seal bellows geometry was obtained from enlarged photographs of sectioned samples which show some variation from leaf to leaf, the agreement of spring rate at least indicates that the new nonlinear computer program is accurate enough for parametric study.

One case was computed, not as a part of the parametric study, but to show the effect of the weld bead stiffness addition compared with results from the program as reported in

Reference 1. The geometry used was that of the Test Case 1 calculated by Hetenyi and Timms in Reference 4. As shown in Reference 1, this case was used to show effects of leaf boundary conditions.

The effect of the introduction of weld bead stiffness is shown in Table 1. The weld bead size used in this case represents the relationship to leaf thickness taken from an enlarged photograph of a typical weld bead from a bellows manufacturer's catalog. The weld bead is

TABLE 1

COMPARISON OF STRESS RATIOS

	Without Weld Bead		With Weld Bead	
Radius Location	Stress Ratio At Low Load	Stress Ratio At 30,000 psi Max. Stress	Stress Ratio at Low Load	Stress Ratio At 30,000 psi Max. Stress
2.012	-30.21	-30.06	-30.42	-30.25
2.089	+11.18	+11.08	+12.27	+12.22
2.171	+13.14	+11.11	+14.45	+12.48
2.258	-14.23	-19.29	-13.14	-18.15
2.349	-56.72	-64.73	-55.91	-63.89
2.445	-100.72	-109.85	-100.20	-109.32
2.543	-132.79	-139.74	-132.50	-139.46
2.644	-141.94	-143.14	-141.82	-143.07
2.747	-123.42	-117.02	-123.41	-117.05
2.851	-80.39	-67.57	-80.41	-67.65
2.957	-23.08	-7.59	-23.09	-7.64
3.062	+34.89	+48.47	+34.95	+48.49
3.167	+80.99	+89.37	+81.08	+89.45
3.277	+107.24	+109.45	+107.40	+109.63
3.374	+111.79	+108.93	+112.13	+109.32
3.474	+98.34	+92.69	+98.88	+93.18
3.572	+74.31	+67.99	+75.03	+68.70
3.666	+48.54	+43.04	+49.44	+43.94
3.756	+29.84	+25.80	+30.78	+26.74
3.842	+26.02	+23.33	+26.63	+23.95
3.923	+40.64	+38.67	+40.36	+38.41

Comparison of ratios of total stress on the convex side of the third leaf to total axial thrust load for the geometry of Case 1 of Reference 2. Loading is acting to compress a bellows of six leaves. Signs are reversed to compare with graphs of References 1 and 2.

3t thick and 4t in the radial direction with these dimensions added to the extremities of the original test case. This procedure of measuring the inside and outside bellows radii from the weld-leaf juncture is used throughout the parametric study to isolate weld bead ring stiffness effects. There is obviously a much smaller effect due to the small inside and outside radius change than the effect of shortening the shell span when placing the weld bead within the original radii.

The results of Table 1 indicate that the weld bead stiffness could properly have been neglected in computing this specific case. The case in point, however, has a much greater thickness (0.023 inch) than is usually encountered either in expulsion bellows or small bellows seals. In such a case, the leaf stiffness provides the most important boundary condition to its neighbor, having a radial stiffness greater than the weld bead ring. The weld bead rotational restraint has a slight effect simply because the joints of such a stiff bellows tend to experience only slight rotational distortion under load.

Zero weld bead dimensions may be introduced in the new program to eliminate the weld bead effect. This was done for a 6-inch diameter bellows with a single, 0.006-inch thick, arc-shaped leaf of 0.500-inch span and 0.176-inch initial pitch. Compared with the results of the same bellows design, with a weld bead 3t thick and 1.2t wide, stresses and deflections differ by only about 0.1%. Although the two cases examined show negligible effect of inclusion of weld bead stiffness, the general importance of such inclusion is still unknown. The question of whether the weld bead stiffness inclusion in the program was, in fact, justified is academic. Since, in the foregoing comparisons, the weld bead ring was attached at the existing inner and outer leaf boundaries, the comparisons show only the effects of weld bead stiffness. The indirect effect of reduction of leaf span caused by weld bead introduction within existing boundaries, although not studied here, may be expected to show considerable change in stress and spring rate. Additional work is required to produce design specification information regarding weld bead shape.

In all the parametric study, stresses and deflections are computed only in the third and fourth of the programs six leaves. All six leaves, of course, are involved in the differential equation solution of the bellows. The two end boundary convolutions are a special problem and, therefore, are omitted from the stress calculations to conserve computer time. The maximum number of solution points allowed by the program, 101 per leaf, are used in the computation of each study case to assure maximum accuracy. The weld bead size used in the parametric study is smaller than used for the case shown in Table 1. The smaller dimensions, 3t thick and 1.2t wide, represent more closely the current bellows welding practice as specified on bellows being purchased by Bell Aerosystems Company.

The effects of bellows size on spring rate for three different basic leaf shapes is shown in Figures 4 and 5. Figure 4 shows the initial spring rate at small axial deflection which is essentially linear from zero load to this value. Figure 5 shows the spring rate at the maximum allowable stress which was taken at 30,000 psi to represent the yield stress of a typical 300 series stainless steel. Comparison of Figures 4 and 5 shows the degree of geometric nonlinearity at the larger deflections. The actual developed length of the three shapes, other than the cone, are exactly the same; thus, at any given diameter, the weights are also identical. The fact that the spring rates decrease in some cases and increase in others, with the nonlinear effects also fluctuating, indicates the complexity of the problem of large elastic deflections of bellows.
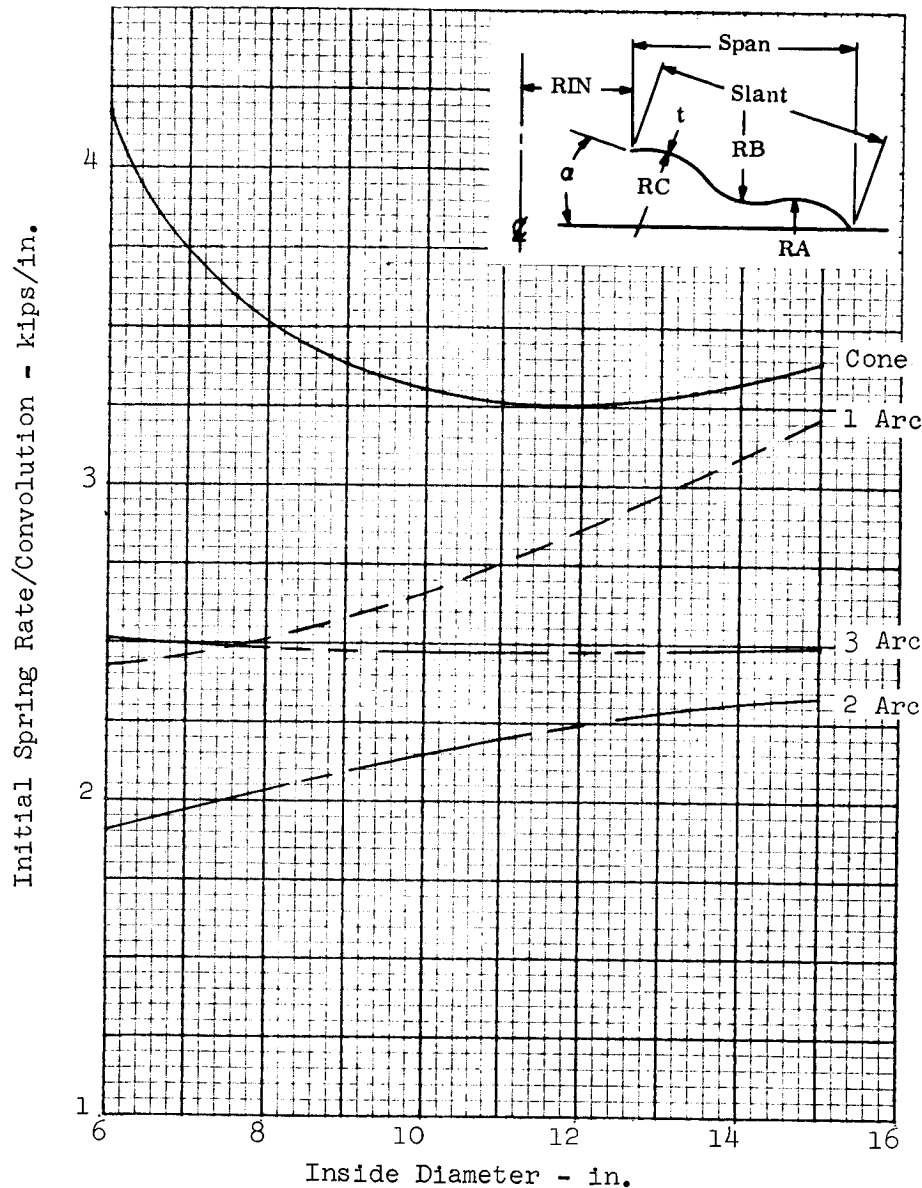
Figure 4. Initial Spring Rate vs Inside Diameter

One important criterion for expulsion bellows is the amount of elastic deformation that can occur before reaching the elastic limit stress. Figure 6 shows the effects on this parameter of bellows size and leaf shape at a given initial pitch. This figure shows the actual maximum deflection one convolution can absorb without exceeding the 30,000 psi stress anywhere in the convolution.

If the bellows leaf shape were to be selected on the basis of a maximum deflection criterion alone, a different shape would be used in each of three ranges of diameter. Naturally, the bellows leaf shape selection must depend upon other criteria, such as stability

t = 0.006 in., a = 30°, span = 0.50 in., max. stress = 30 ksi,
RA + RB + RC = slant, RA = RB = RC
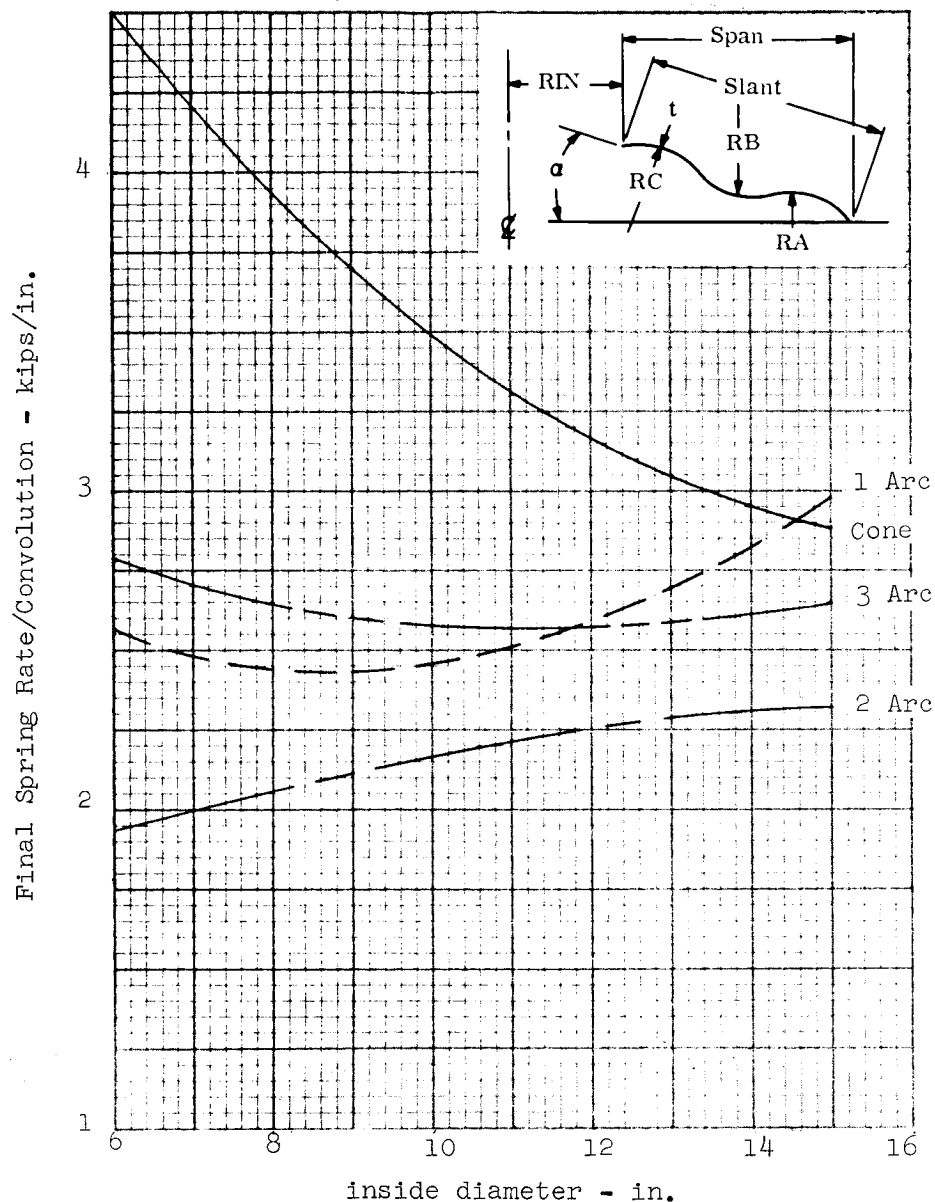
Figure 5. Final Spring Rate vs Inside Diameter

and pressure-carrying ability. However, since the maximum deflection criterion would select different shapes as a function of diameter, it is reasonable to assume that the other criteria would show a similar result. No pressure loading is considered in these parametric studies because pressure is expected to have a more-complex effect. It was decided that use of an axial extension thrust for preliminary parametric study would produce sufficient general trend information without unnecessary complication. Continuation of these parametric studies will certainly require consideration of relative pressure-carrying capability.

12

t = 0.006 in., a = 30°, span = 0.50 in., max. stress = 30 ksi
RA + RB + RC = slant, RA = RB = RC
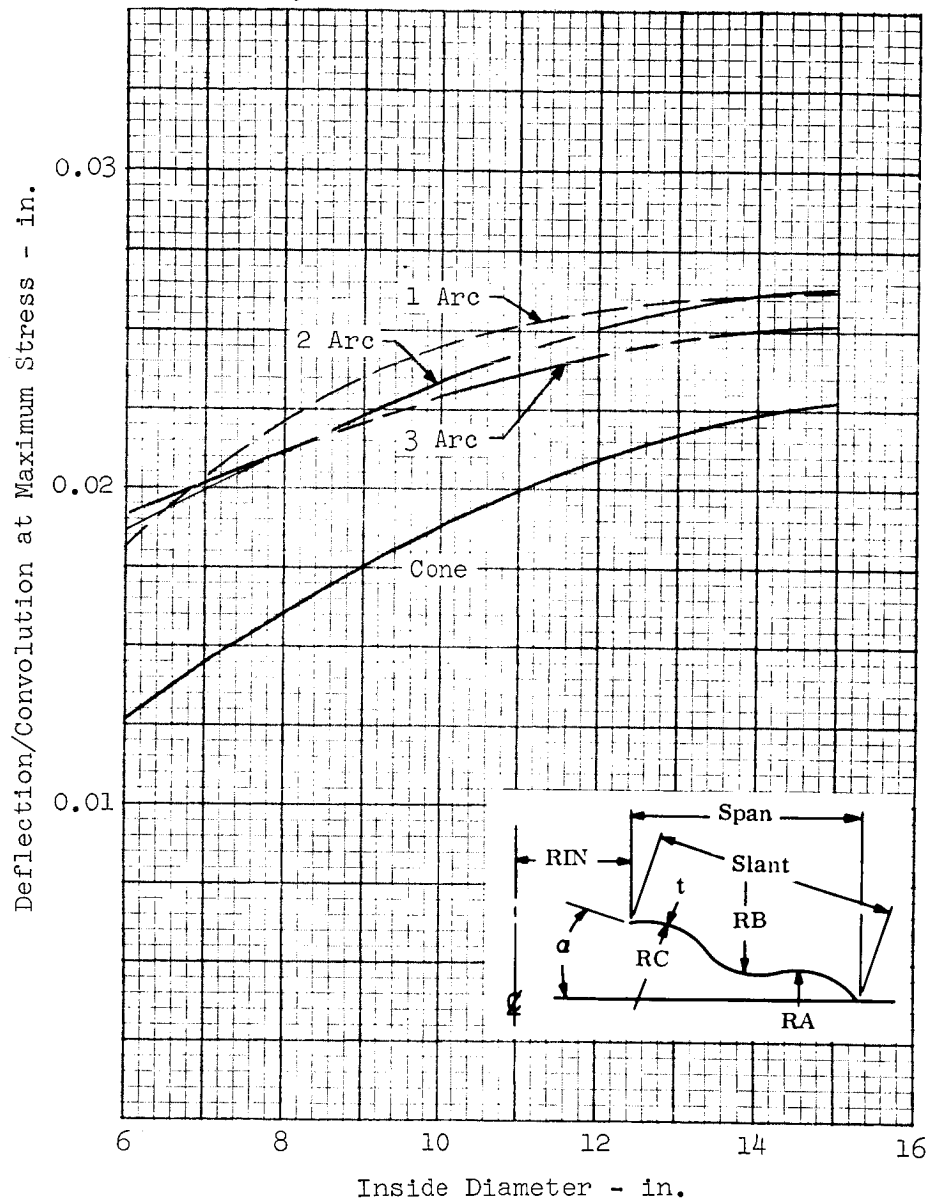
Figure 6. Deflection at Maximum Stress vs Inside Diameter

When the first cases using different leaf shapes were studied, it was noted that total convolution deflection consisted of nearly equal deflection in both leaves except in the two- and three-arc shapes. This phenomenon is shown as a function of bellows diameter in Figure 7.

Although this phenomenon is only of academic interest, it adds to our understanding of the effects of leaf shape. The boundary moments apparently tend to reduce the radius of curvature of the third leaf and increase it in the fourth leaf. Perhaps the inequality of deflection is most extreme in the two-arc shape because the curvature is exactly reversed on opposite sides of the mid-span.

Report No. 8230-933007
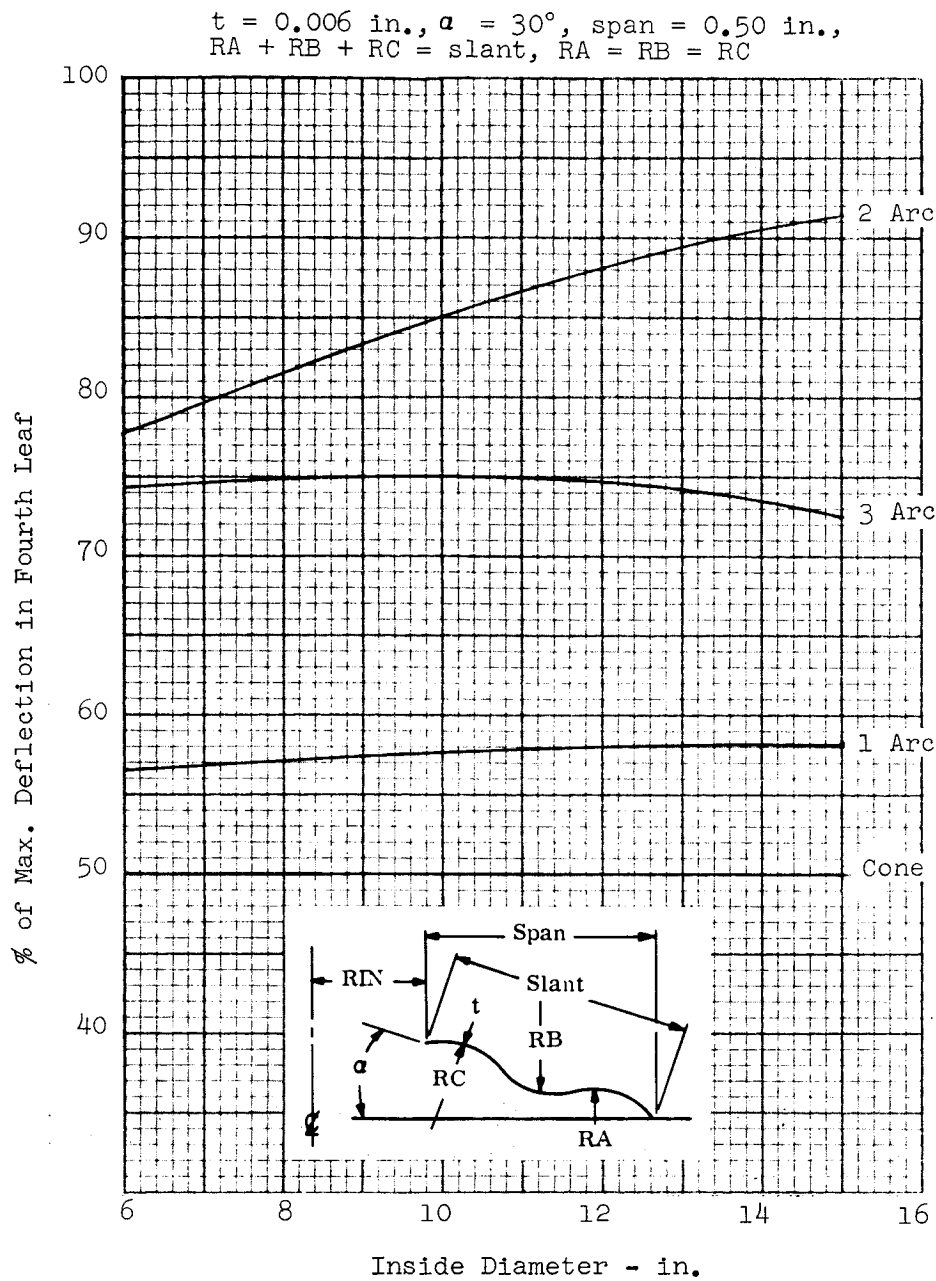
Figure 7. Percentage of Total Deflection in Fourth Leaf vs Inside Diameter

The effect of bellows pitch at the start of axial loading when in a state of zero stress was examined because of the coupled effect with "cone angle" observed previously. The effect of pitch on initial spring rate for the four basic shapes is shown in Figure 8. Comparison with the effects of pitch on the spring rate at maximum stress, Figure 9, shows varying degrees of nonlinearity. As in the study of diameter effect, the largest deflection at maximum stress does not necessarily coincide with the highest degree of nonlinearity of spring rate as shown in Figure 10.

14

Figure 8. Initial Spring Rate vs Pitch, 9-inch Diameter

As might be expected, the stress distribution from inside to outside diameter varies considerably for different shapes of leaf and different initial pitch. The largest stresses always seem to occur in the radial direction although the circumferential stresses are by no means negligible. Some typical stress distributions are shown for various shapes and pitch angles in Figures 11 through 16. For comparison, the third leaf stresses have been used for the most part. The location of the maximum stress in the convolution varies from case to case. Because of variations in bending moment directions, the maximum stress location may be on the outside or inside bellows surface. Because of the marked difference in leaf deflec-

Figure 9. Final Spring Rate vs Pitch, 9-inch Diameter

tions of the two-arc shape, noted earlier, the stress distribution of both leaves has been plotted in Figures 12 through 14. The comparative magnitude of radial-to-circumferential stress is shown by Figures 13 and 14. Figure 13 shows that the maximum stress in a bellows need not occur at the weld bead although the stress at the inside weld bead is nearly 30,000 psi. The previously mentioned curvature reverse at the mid-span seems to be demonstrated by the coincidence of stresses at that point in Figure 13. A composite effect of shape on stress distribution is shown for a given pitch and bellows size in Figure 16.

t = 0.006 in., RIN = 4.5 in., span = 0.50 in.,
max. stress = 30 ksi, RA + RB + RC = slant, RA = RB = RC
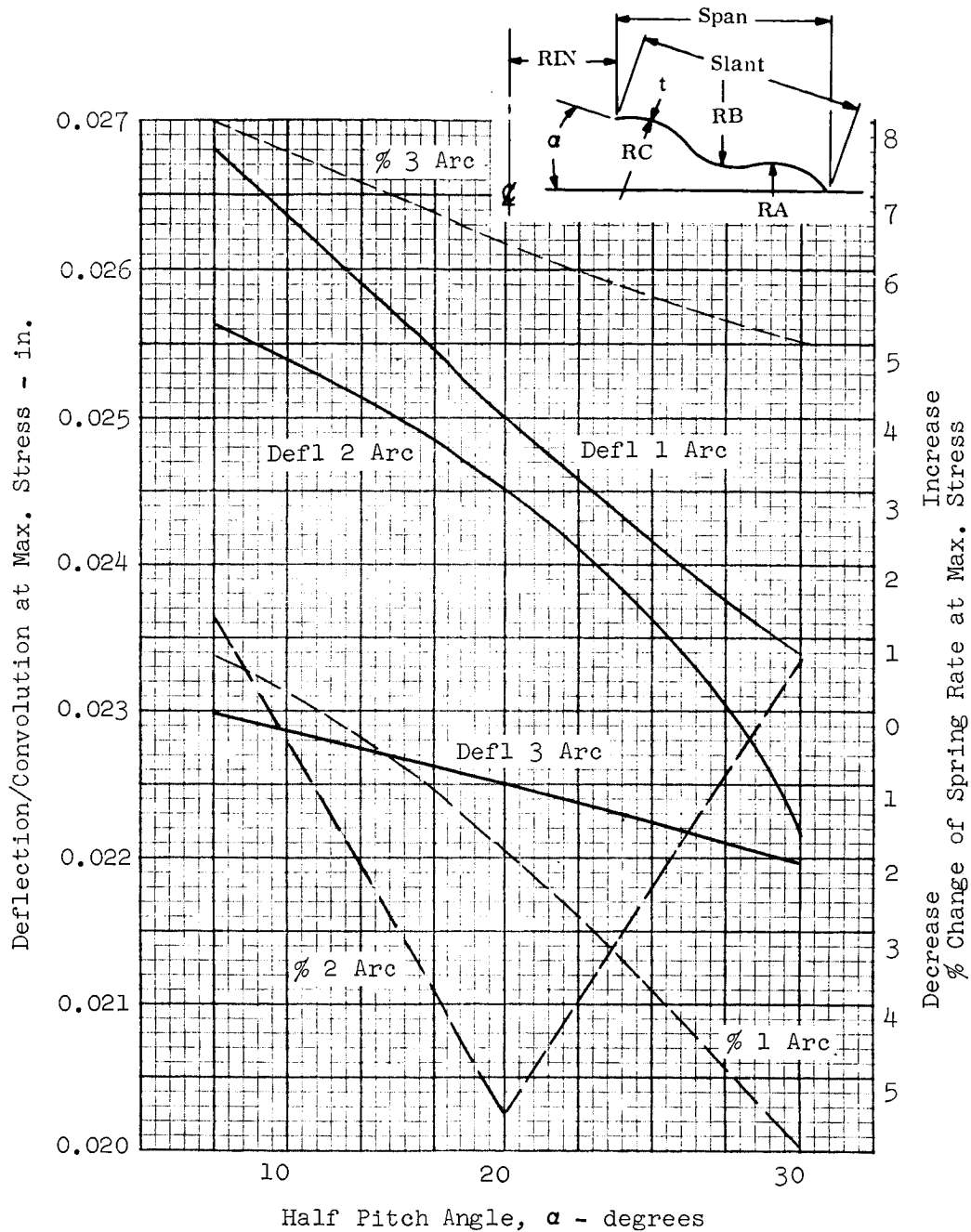
Figure 10. Maximum Deflection and Spring Rate Change vs Pitch, 9-inch Diameter

t = 0.006 in. (inside surface third leaf), RA = slant
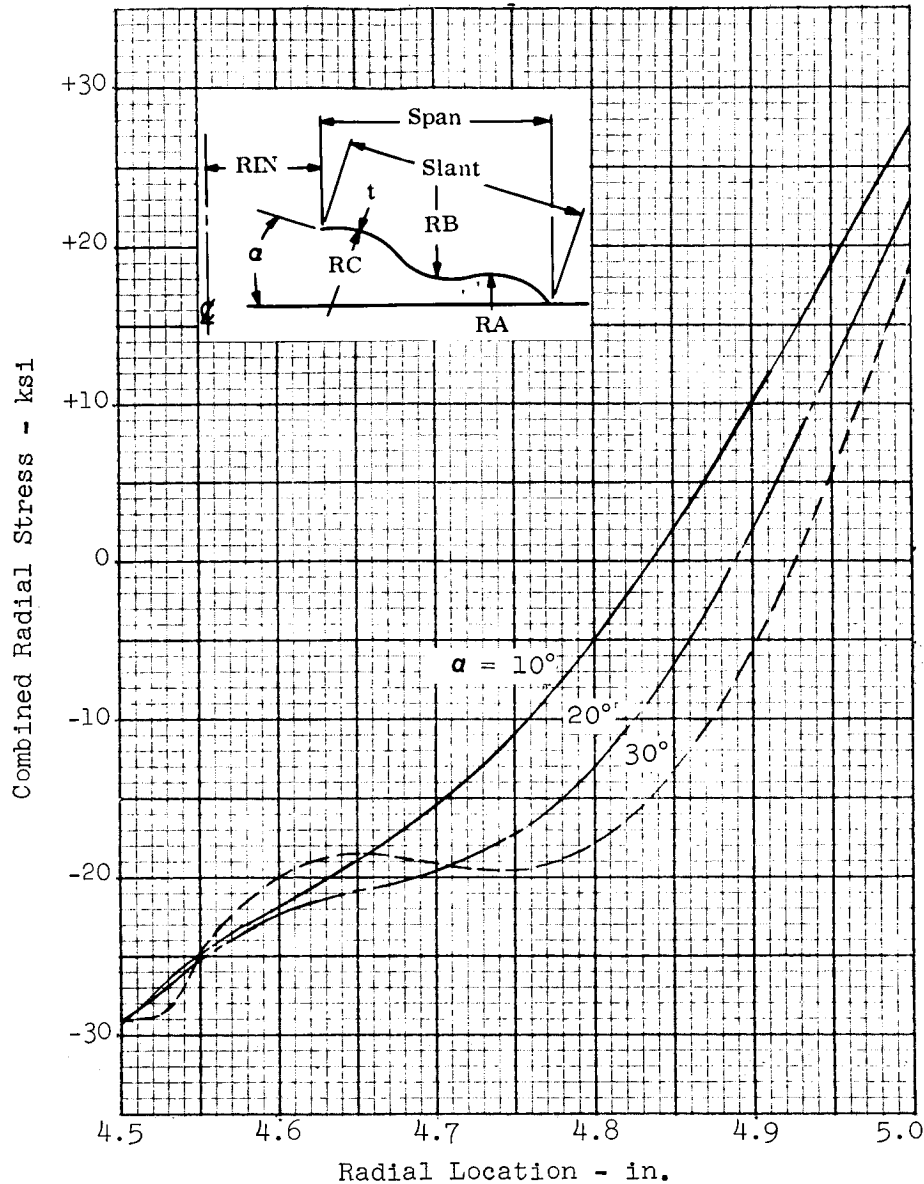
Figure 11. Radial Stress Distribution vs Pitch, 1 Arc Shape

Another important parameter in bellows design is span. The effect of variation of span, for a given diameter and pitch, on spring rates is shown in Figures 17 and 18. The span effect on maximum elastic deflection at 30,000 psi stress for the same diameter and pitch is shown in Figure 19. As might be expected from the previous observations, the effect of span variation is different for each basic leaf shape. Comparison of maximum deflection per unit developed length, shown in Figure 20, provides an essentially constant weight comparison.

The last parametric variable considered in this study was thickness. Thickness variation effect on spring rates, for a 9-inch inside diameter with a 0.5-inch span at an initial

18   Report No. 8230-933007
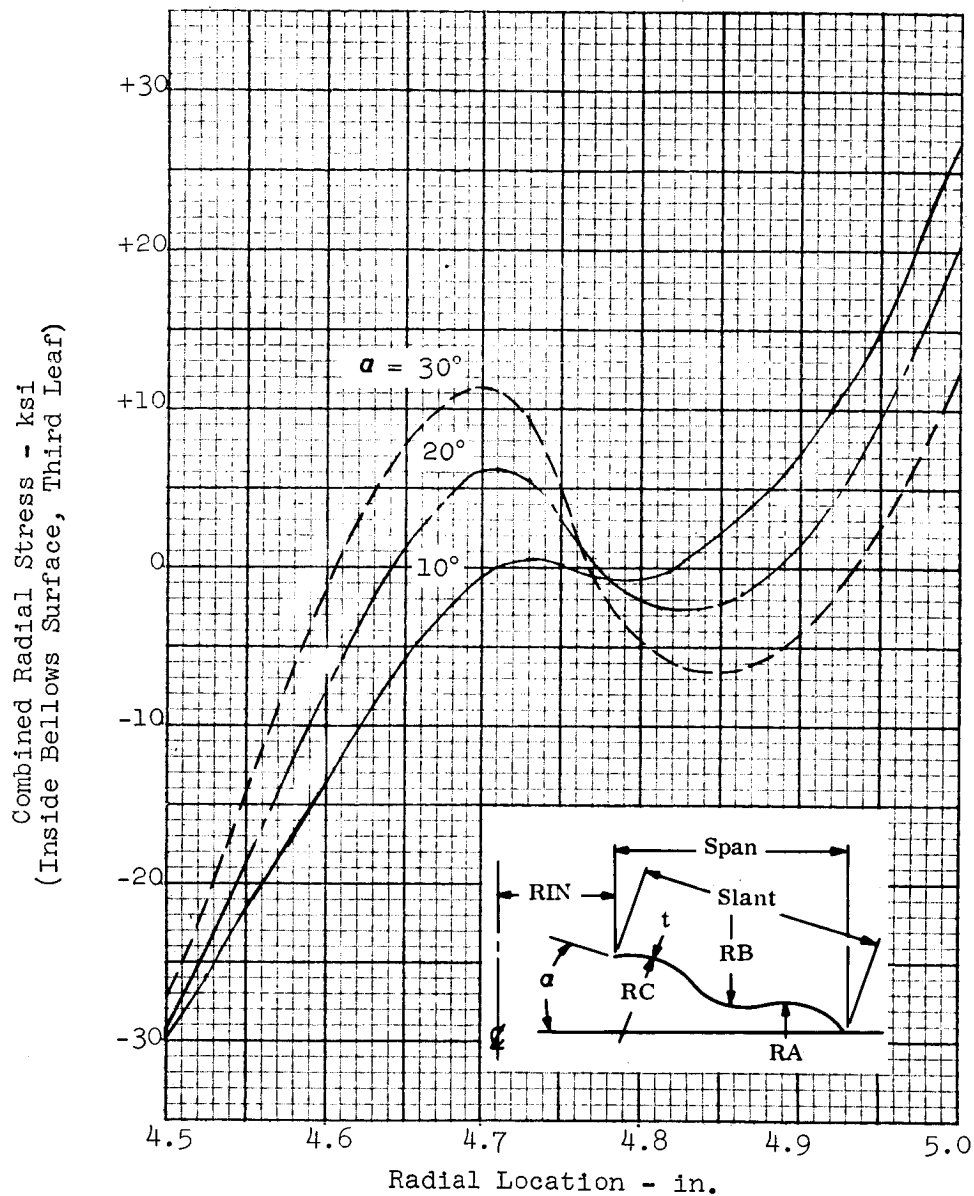
Figure 12. Radial Stress Distribution vs Pitch, 2 Arc Shape

pitch half angle of 10°, is shown in Figures 21 and 22. The thickness effect on maximum elastic deflection at 30,000 psi stress for the same bellows size and pitch is shown in Figure 23. Again, the parameter effects differ for each basic leaf shape. Thickness variation effects on spring rate and maximum elastic deflections for a different size bellows with the same pitch are shown in Figures 24, 25, and 26. The thickness variation effect on both spring rate and maximum elastic deflection may be compared with the same effects on a circular flat plate under small deflections. The flat annular plate spring rate will vary as the cube of the thickness, while its maximum deflection will vary as the inverse of the first power of thickness. If the thickness variation effect on initial spring rate of a bellows were expressed as
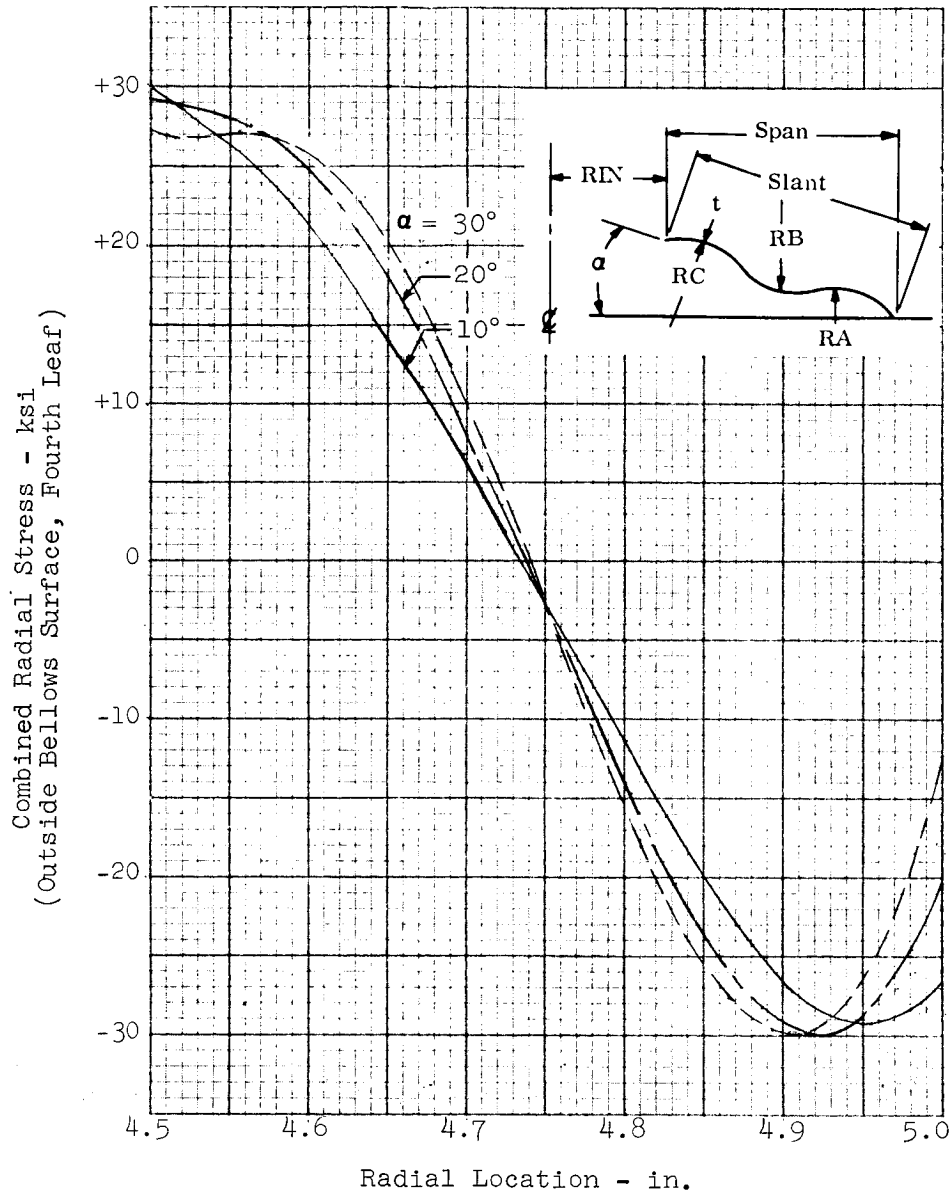
Figure 13. Radial Stress Distribution vs Pitch, 2 Arc Shape

a power of thickness, the exponent required would vary from 2.33 to 2.88, depending upon the thickness range, diameter, and leaf shape. Maximum allowable deflections, expressed as the inverse power of thickness, similarly show exponent variations from 0.715 to 1.09. It is apparent, therefore, that a different formula is required for each specific problem.

Some limited cross-plots are available as a result of the number of parameter variations. For example, the effect of pitch variation at a different diameter than used in Figures 7, 8, and 9 is shown for a single arc in Figure 27.
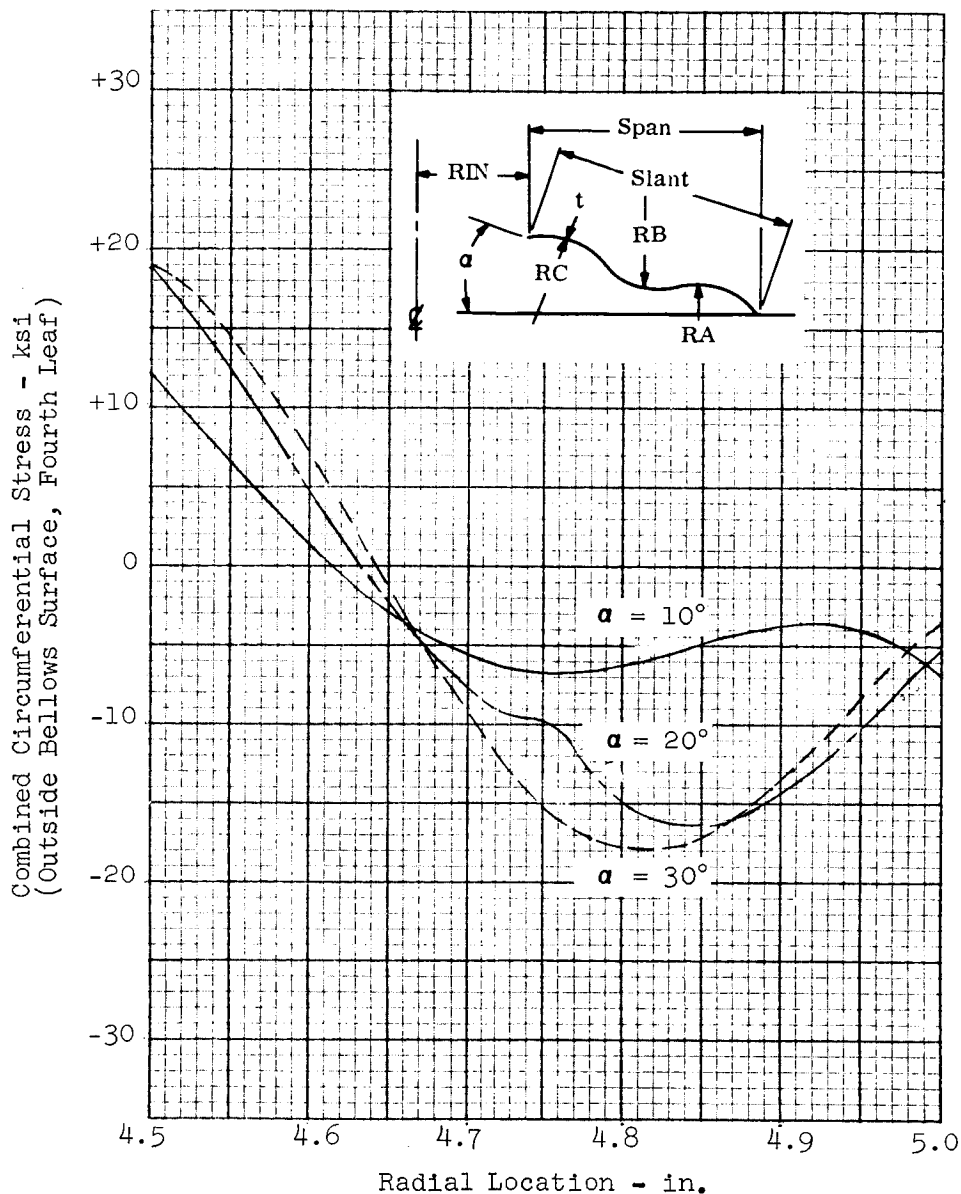
Figure 14. Circumferential Stress Distribution vs Pitch, 2 Arc Shape

No attempt was made to study the effects of changing the radius of curvature within the general shape family. One such case was obtained by accident because of a computer input error. Thus, a comparison exists for two 15-inch diameter bellows with 0.5-inch spans, equal 0.006-inch thickness, and 30° half pitch angle, but with two-arc shapes whose radii of curvature differ by a factor of two. The larger the radius of curvature, the closer the shape approaches a pure cone. Comparison of the results, in fact, shows that the initial spring rate and the maximum deflection for the larger radii case fall between those same values for the smaller radii and the cone. The larger radii of curvature, however, causes an even greater

t = 0.006 (inside surface third leaf),
RA + RB + RC = slant, RA = RB = RC
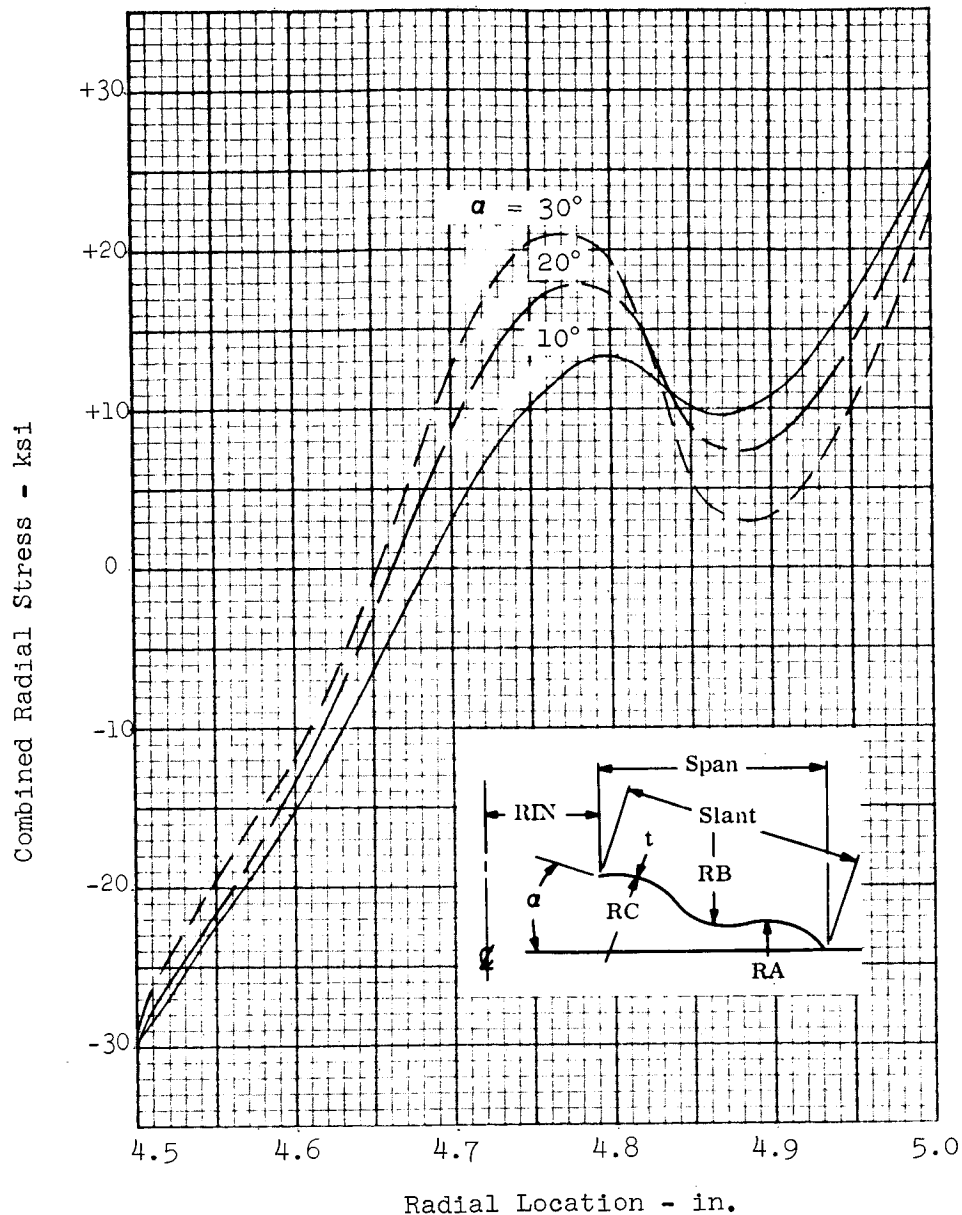
Figure 15. Radial Stress Distribution vs Pitch, 3 Arc Shape

share of the convolutions deflection to be carried by the fourth leaf than the smaller radius of curvature case. If one isolated comparison is a valid indication, the next studies ought to include the effects of reduced radii of curvature in obtaining larger allowable elastic deflections.

$\alpha = 30°$ (inside surface third leaf)
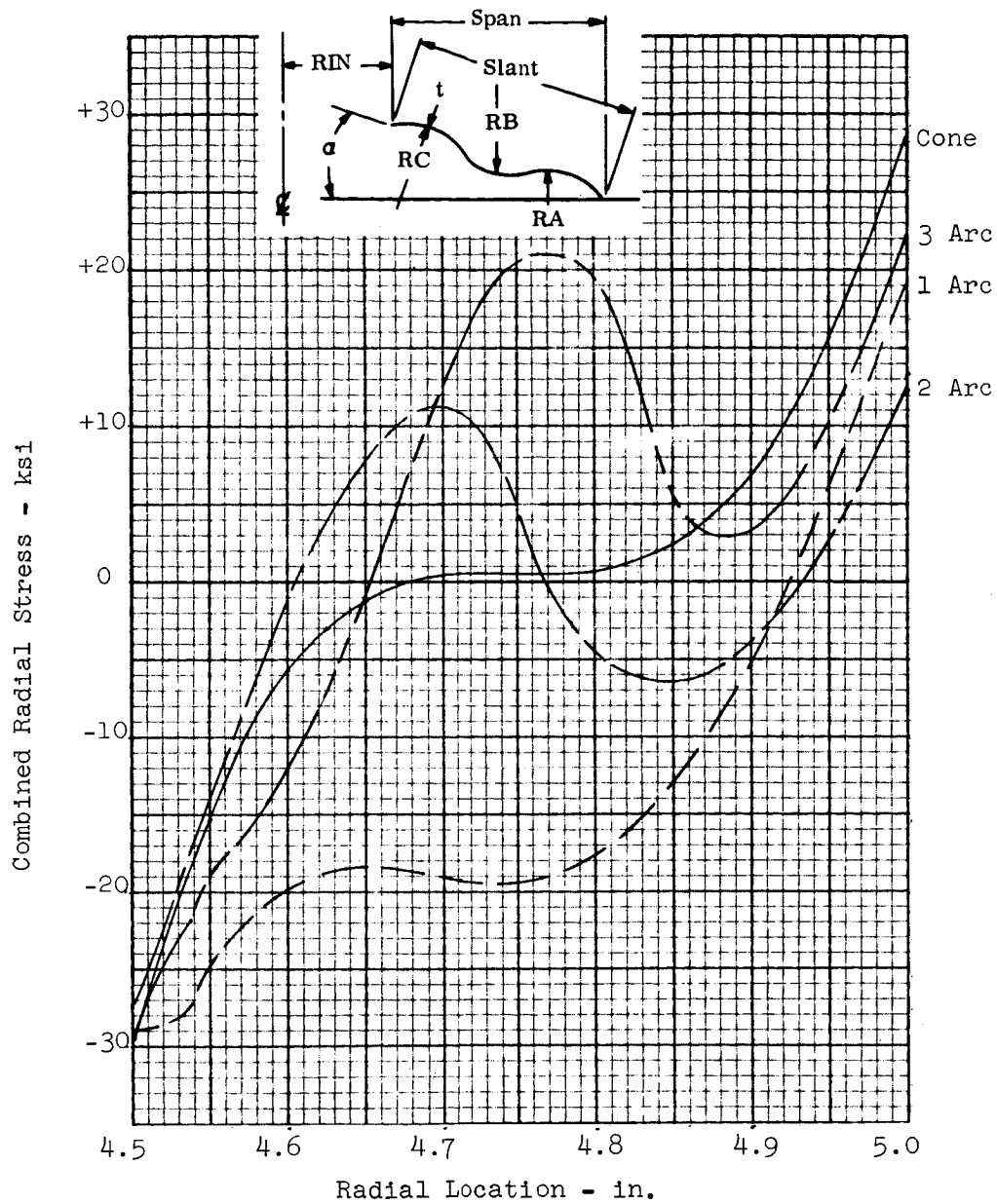
Figure 16. Radial Stress Distribution vs Shape

t = 0.006 in., RIN = 4.5 in., RIN = 4.5 in., α = 30°
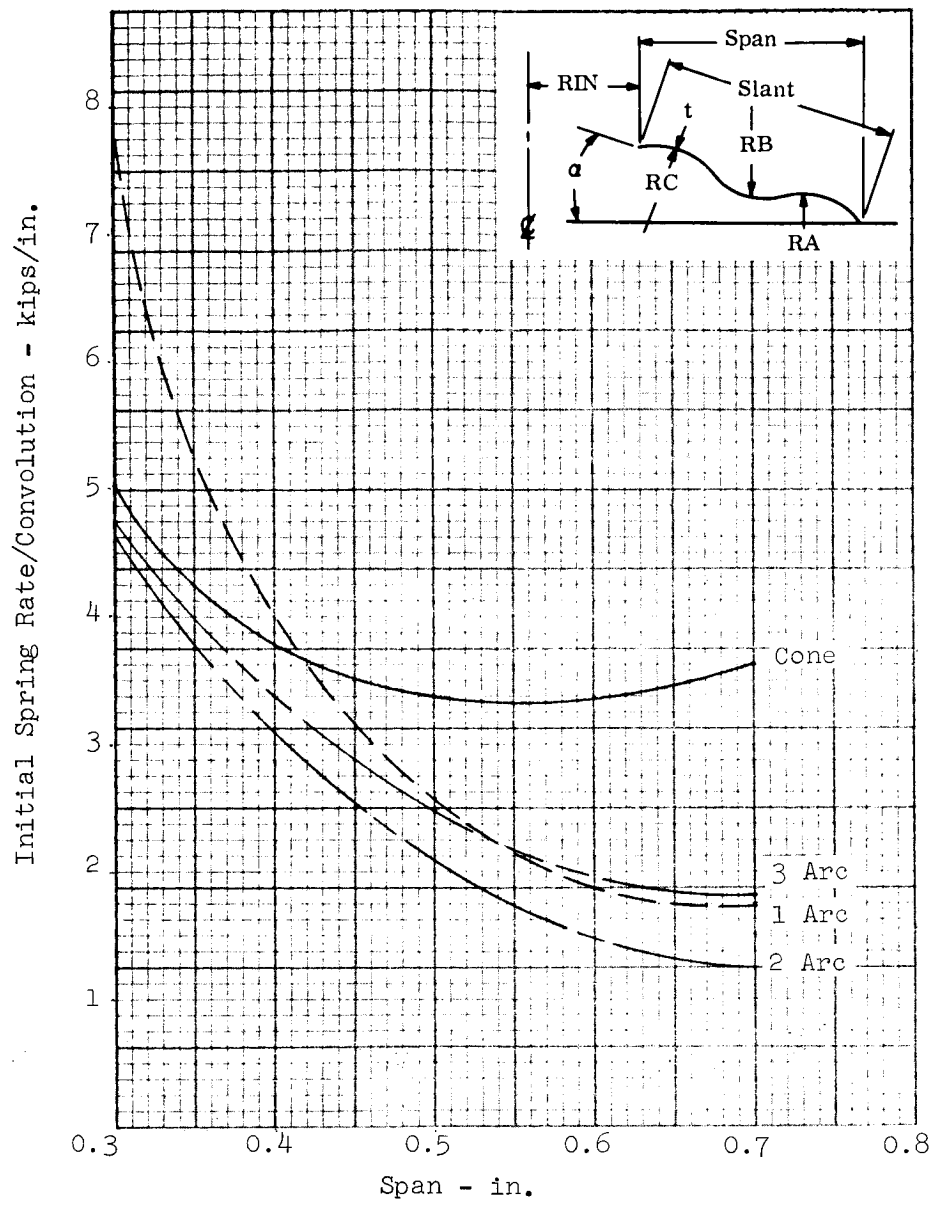
Figure 17. Initial Spring Rate vs Span

t = 0.006 in., RIN = 4.5 in., α = 30°, max. stress = 30 ksi,
RA + RB + RC = slant, RA = RB = RC
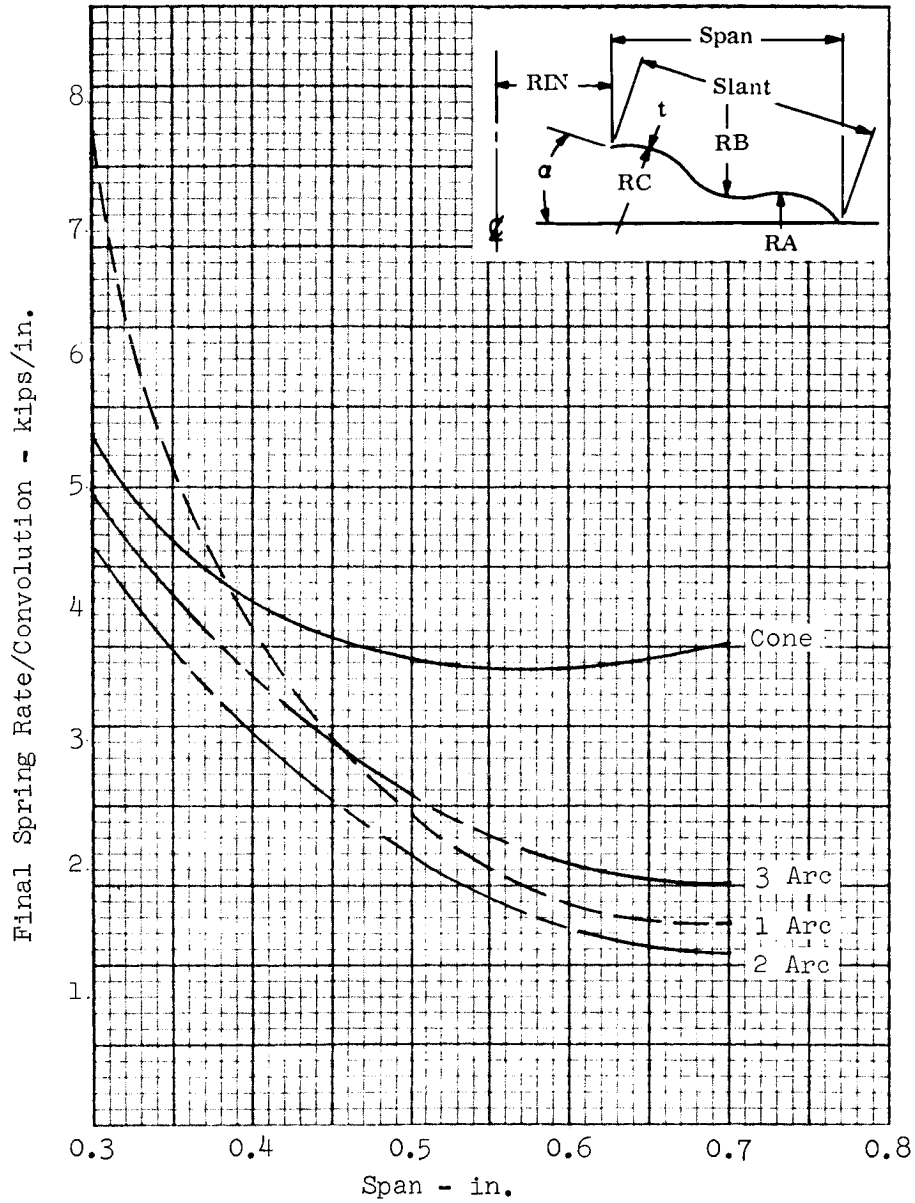
Figure 18. Final Spring Rate vs Span

t = 0.006 in., RIN = 4.5 in., a = 30°, max. stress = 30 ksi,
RA + RB + RC = slant, RA = RB = RC
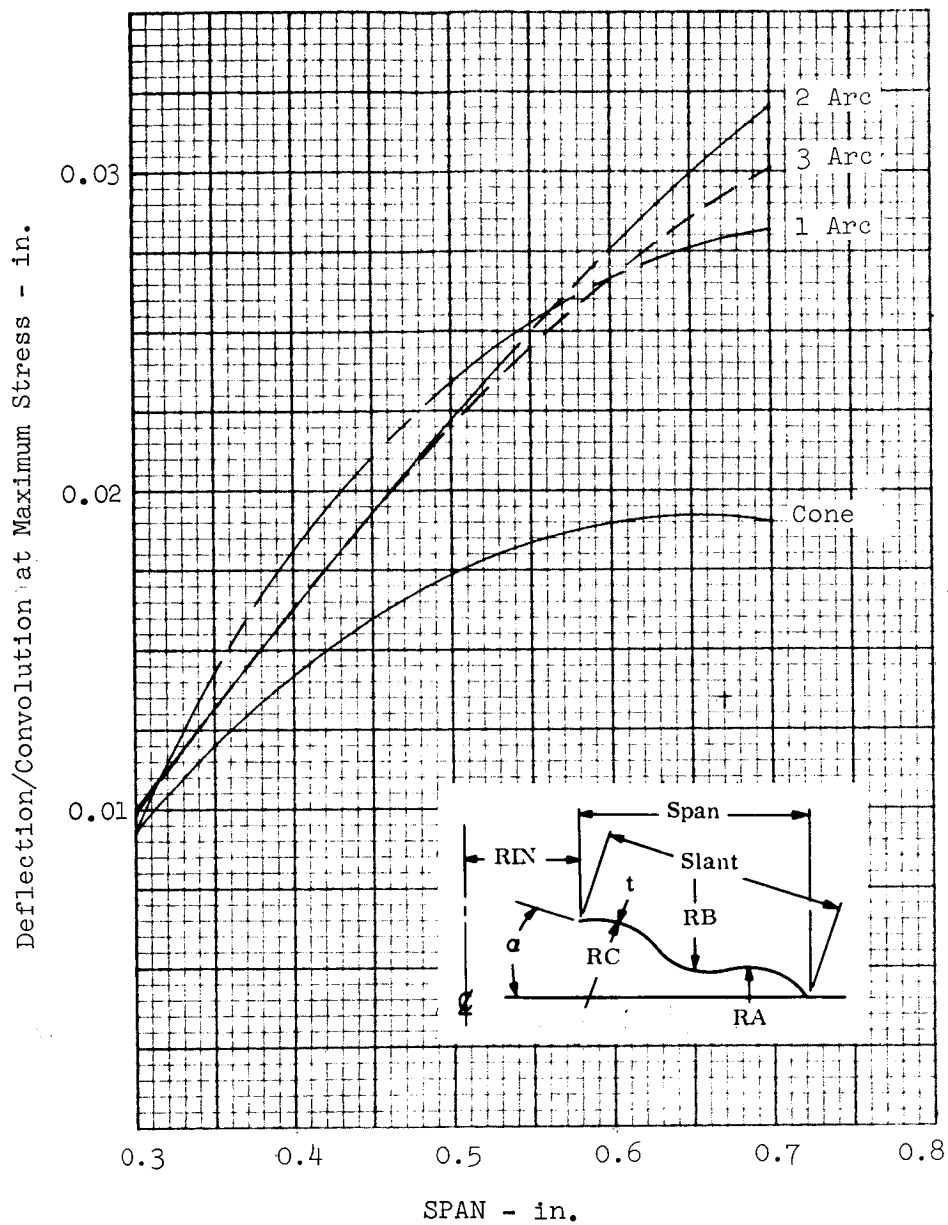
Figure 19. Deflection at Maximum Stress vs Span

t = 0.006 in., RIN = 4.5 in., α = 30°, max. stress = 30 ksi,
RA + RB + RC = slant, RA = RB = RC
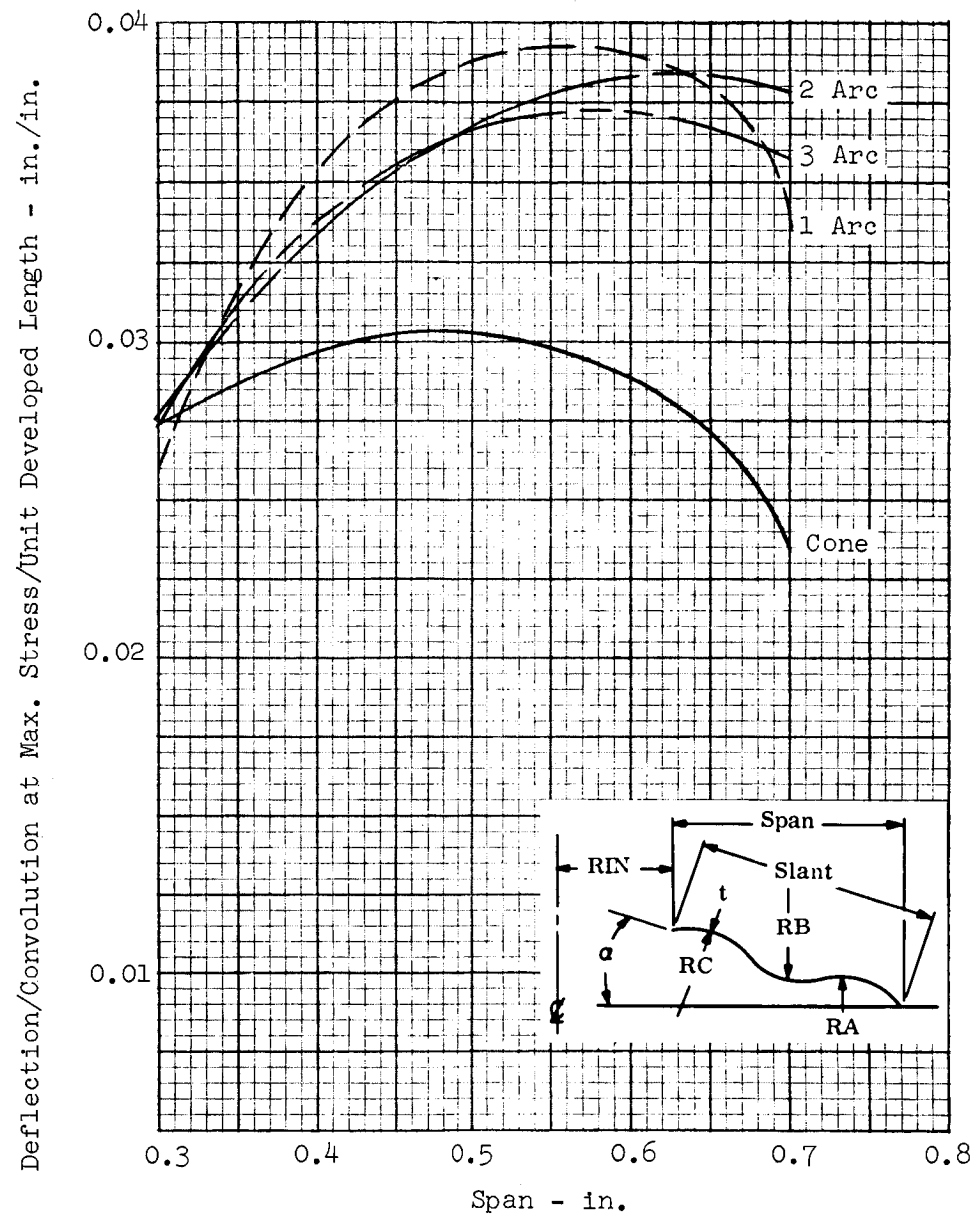
Figure 20. Constant Weight Deflection/Convolution at Maximum Stress
vs Span

RIN = 4.5 in., α = 10°, span = 0.50 in.,
RA + RB + RC = slant, RA = RB = RC
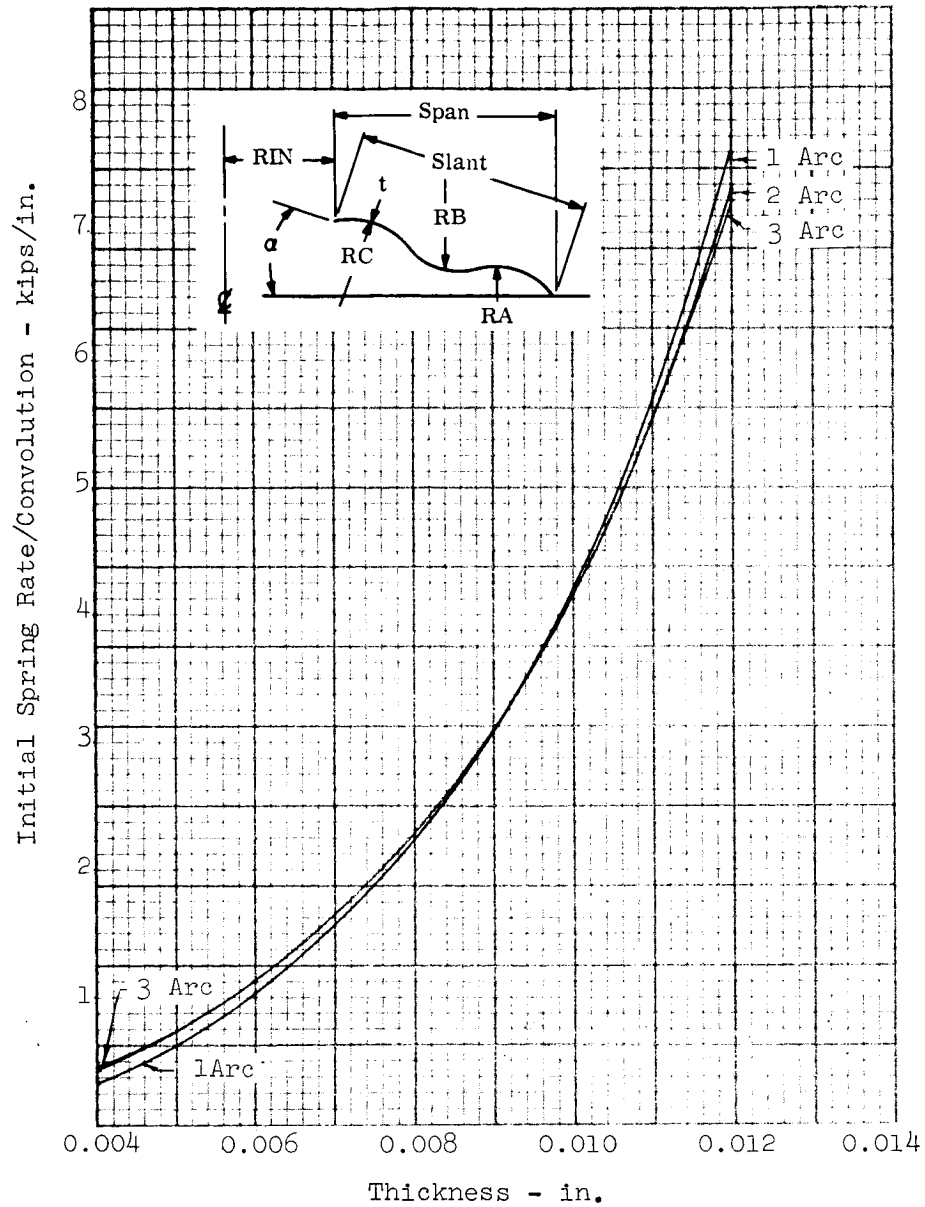
Figure 21. Initial Spring Rate vs Thickness, 9-inch Diameter

RIN = 4.5 in., α = 10°, span = 0.50 in., max. stress = 30 ksi,
RA + RB + RC = slant, RA = RB = RC
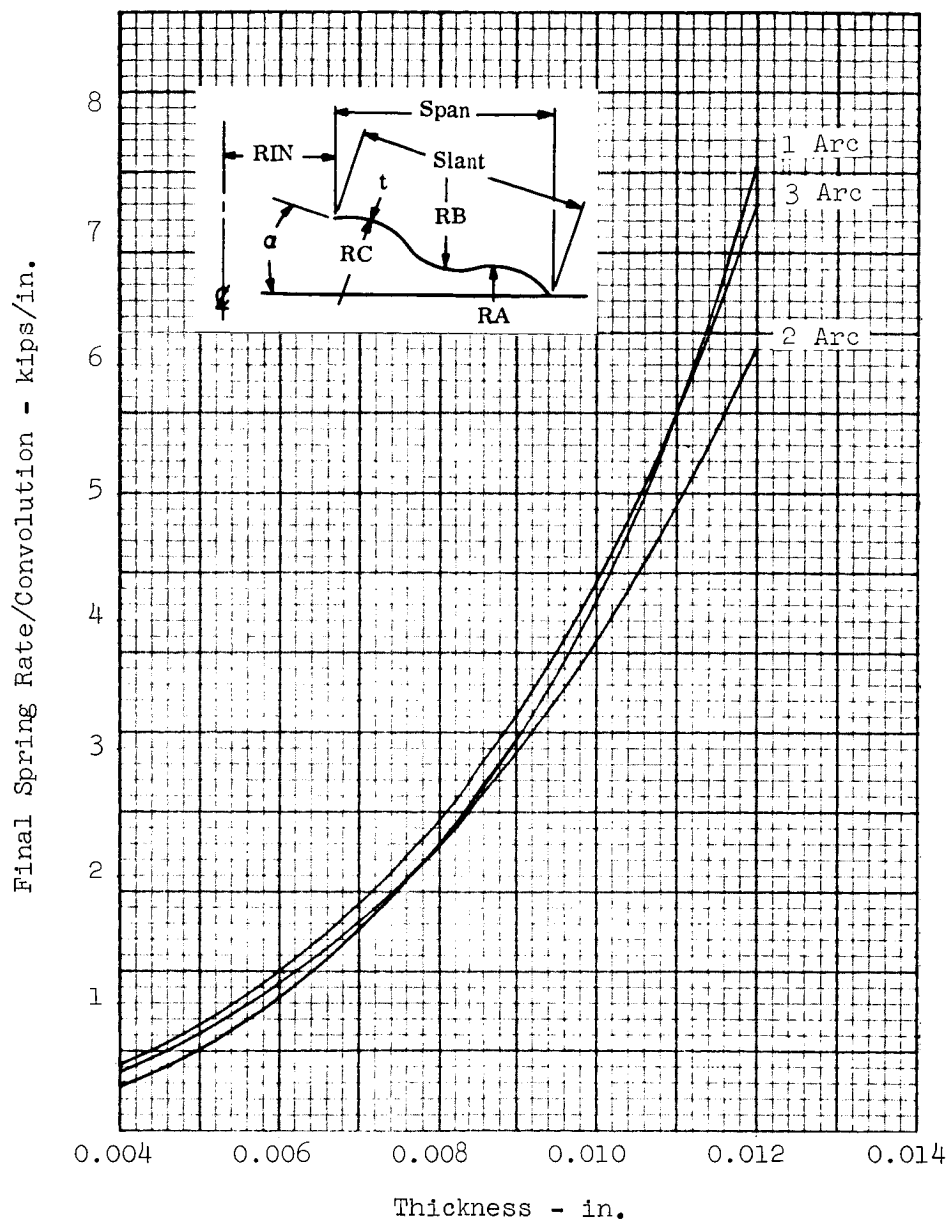
Figure 22. Final Spring Rate vs Thickness, 9-inch Diameter

RIN = 4.5 in., α = 10°, span = 0.50 in., max. stress = 30 ksi
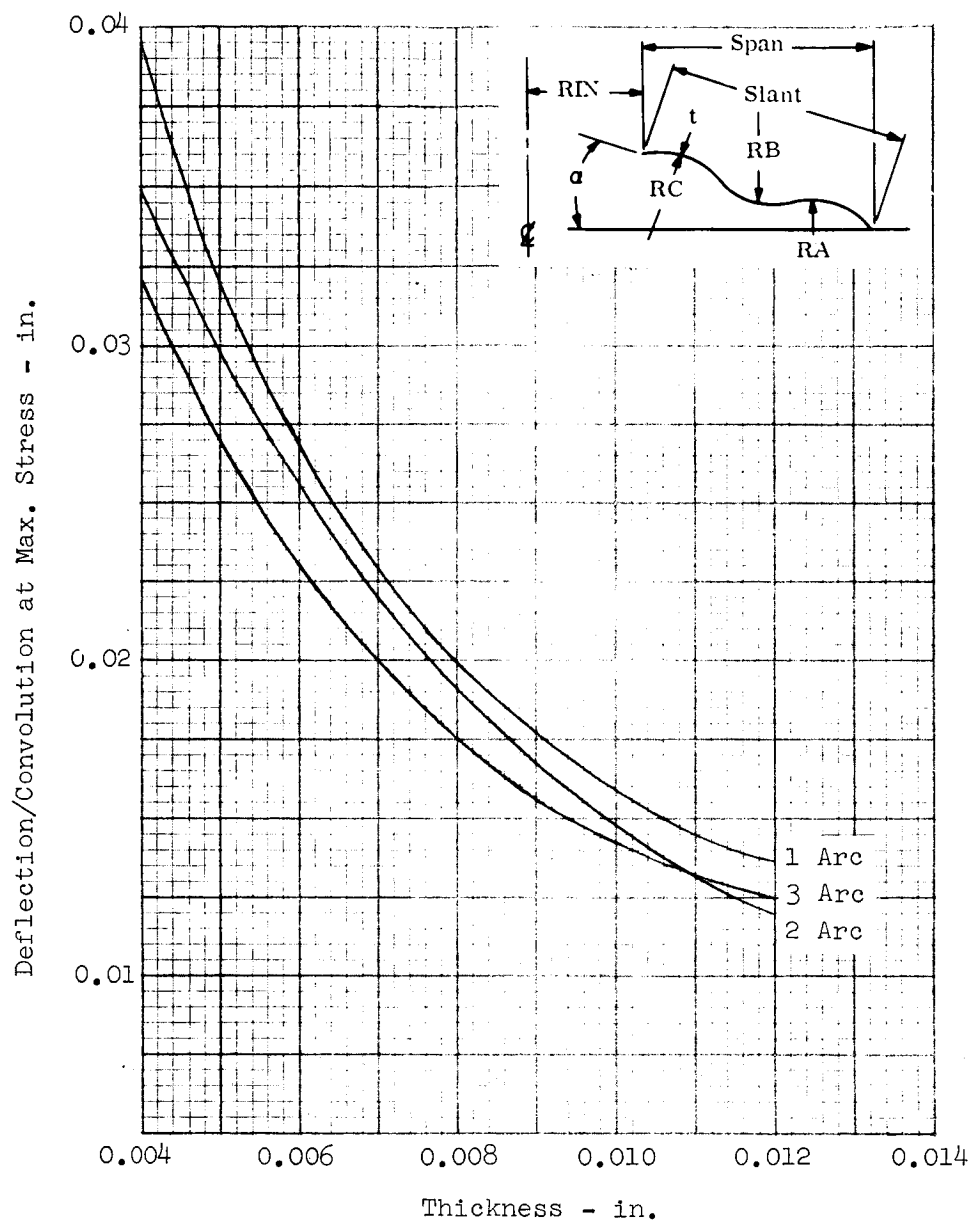
Figure 23. Deflection at Maximum Stress vs Thickness, 9-inch Diameter

RIN = 3.0 in., α = 10°, span = 0.50 in.,
RA + RB + RC = slant, RA = RB = RC
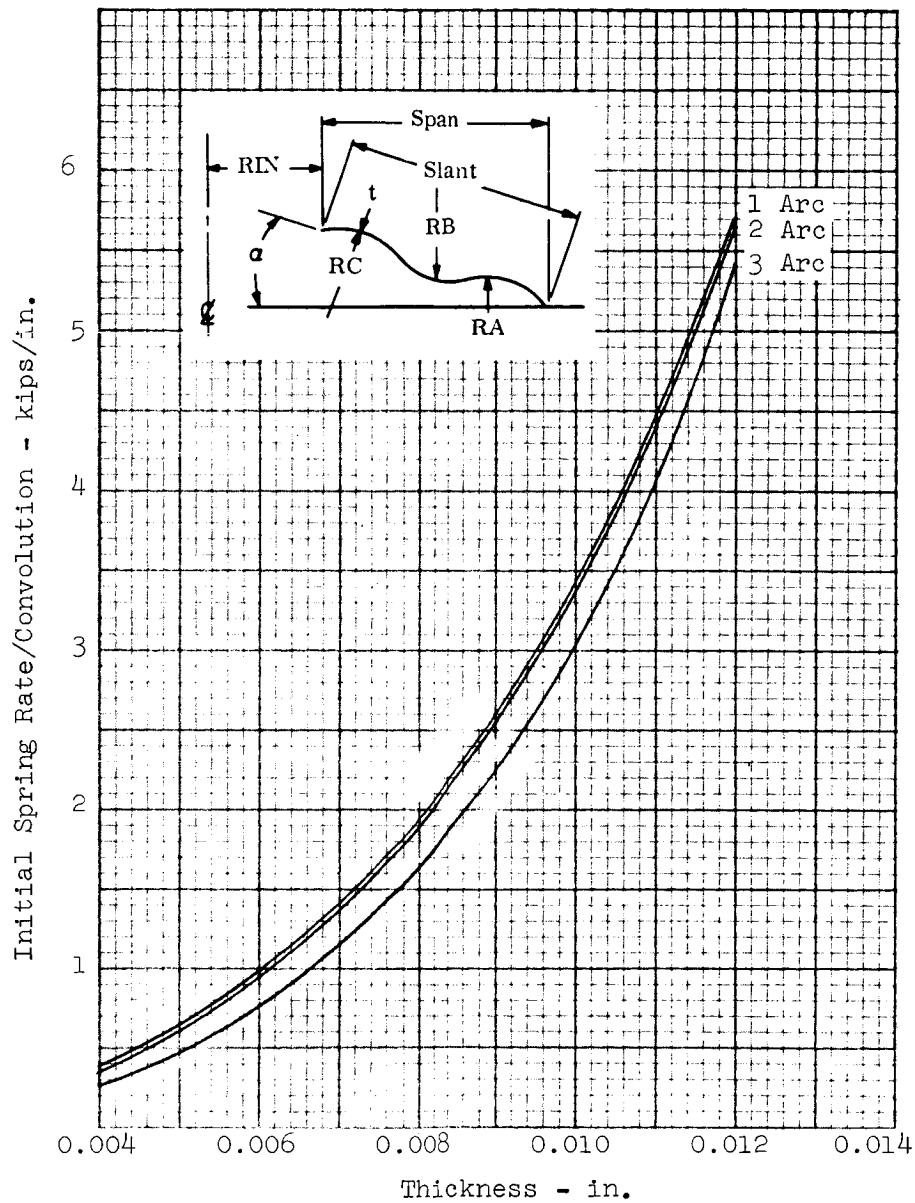
Figure 24. Initial Spring Rate vs Thickness, 6-inch Diameter

RIN = 3.0 in., α = 10°, span = 0.50 in., max. stress - 30 ksi,
RA + RB + RC = slant, RA = RB = RC
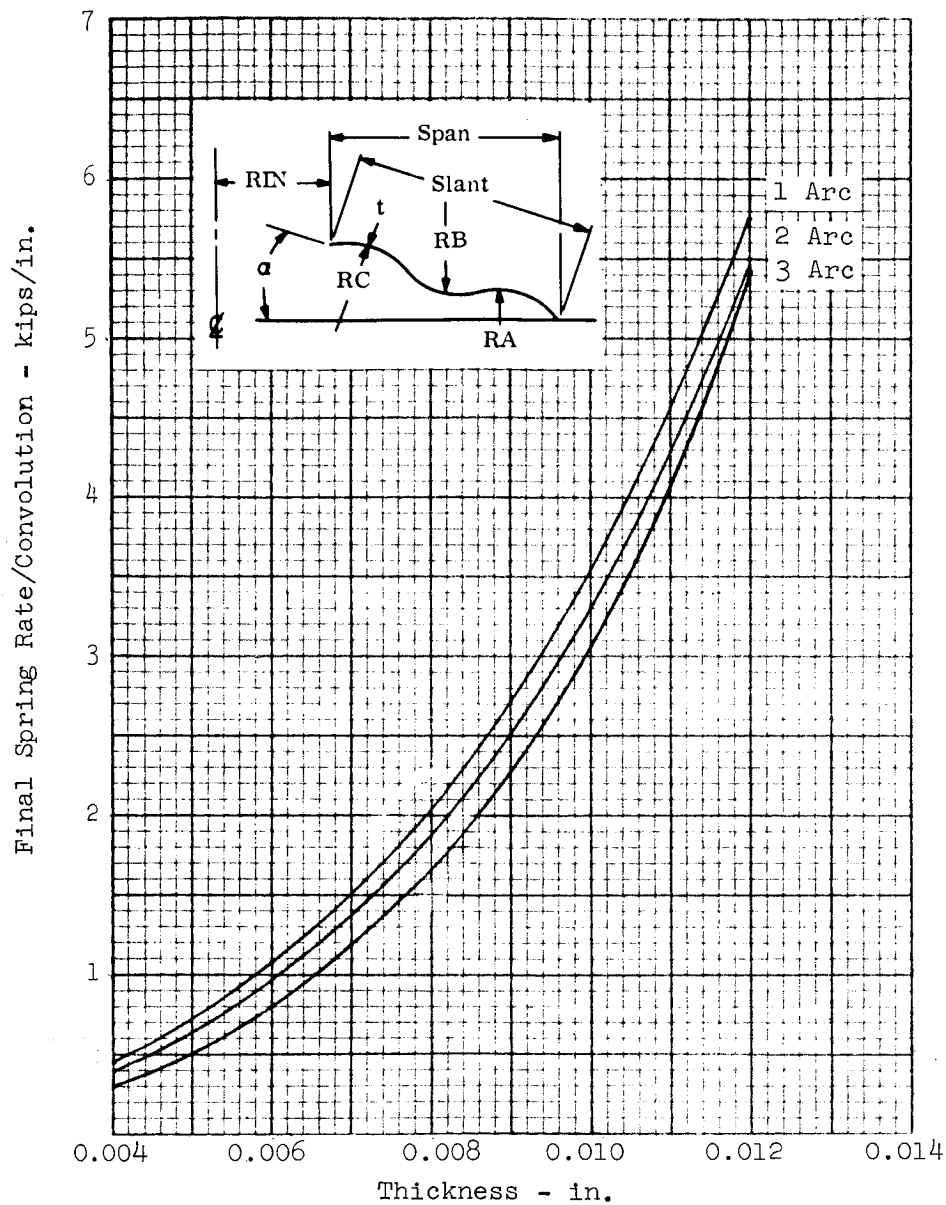
Figure 25. Final Spring Rate vs Thickness, 6-inch Diameter

RIN = 3.0 in., a = 10°, span = 0.5 in., max. stress = 30 ksi,
RA + RB + RC = slant, RA = RB = RC
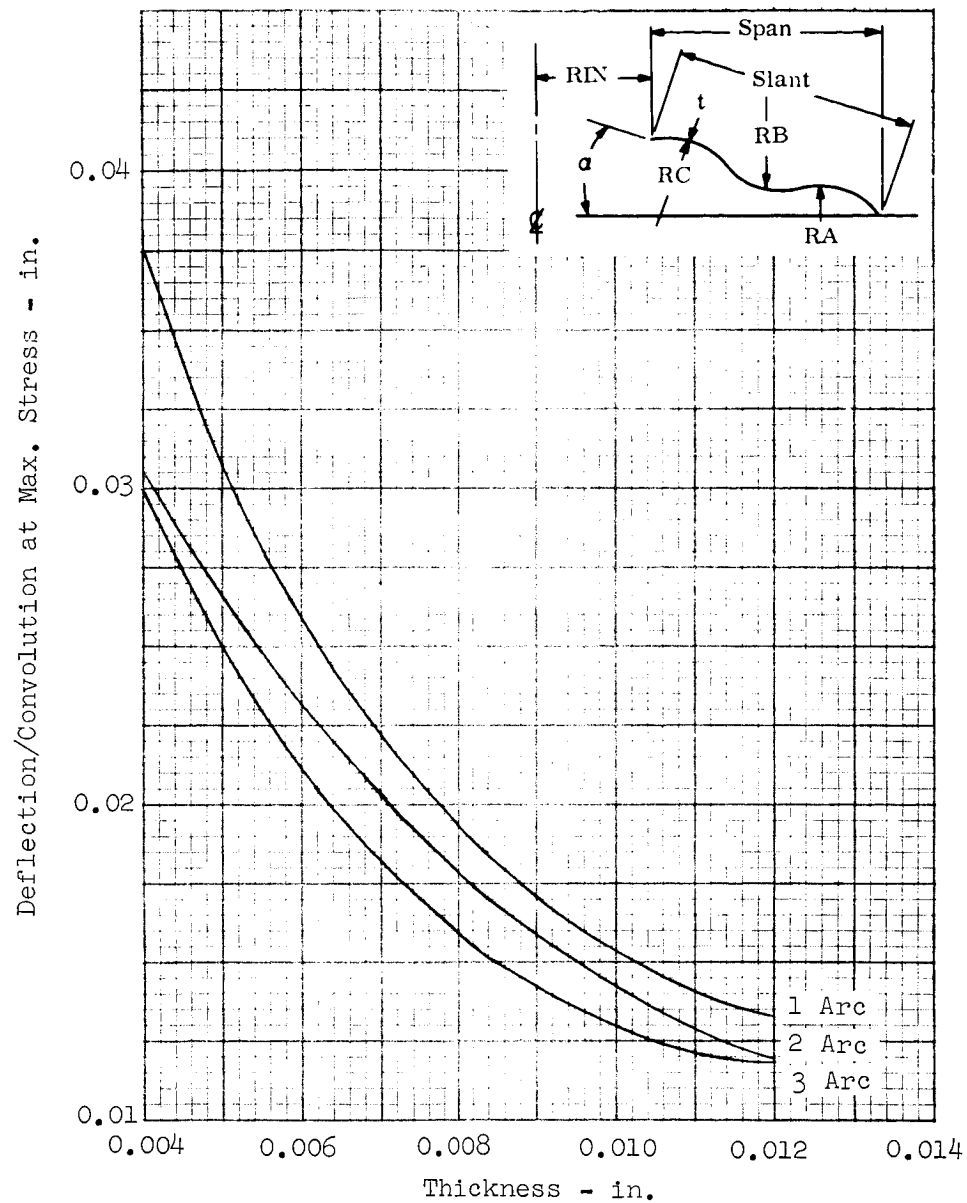
Figure 26. Deflection at Maximum Stress vs Thickness, 6-inch Diameter

t = 0.006 in., RIN = 3.0 in., span = 0.50 in., RA = slant
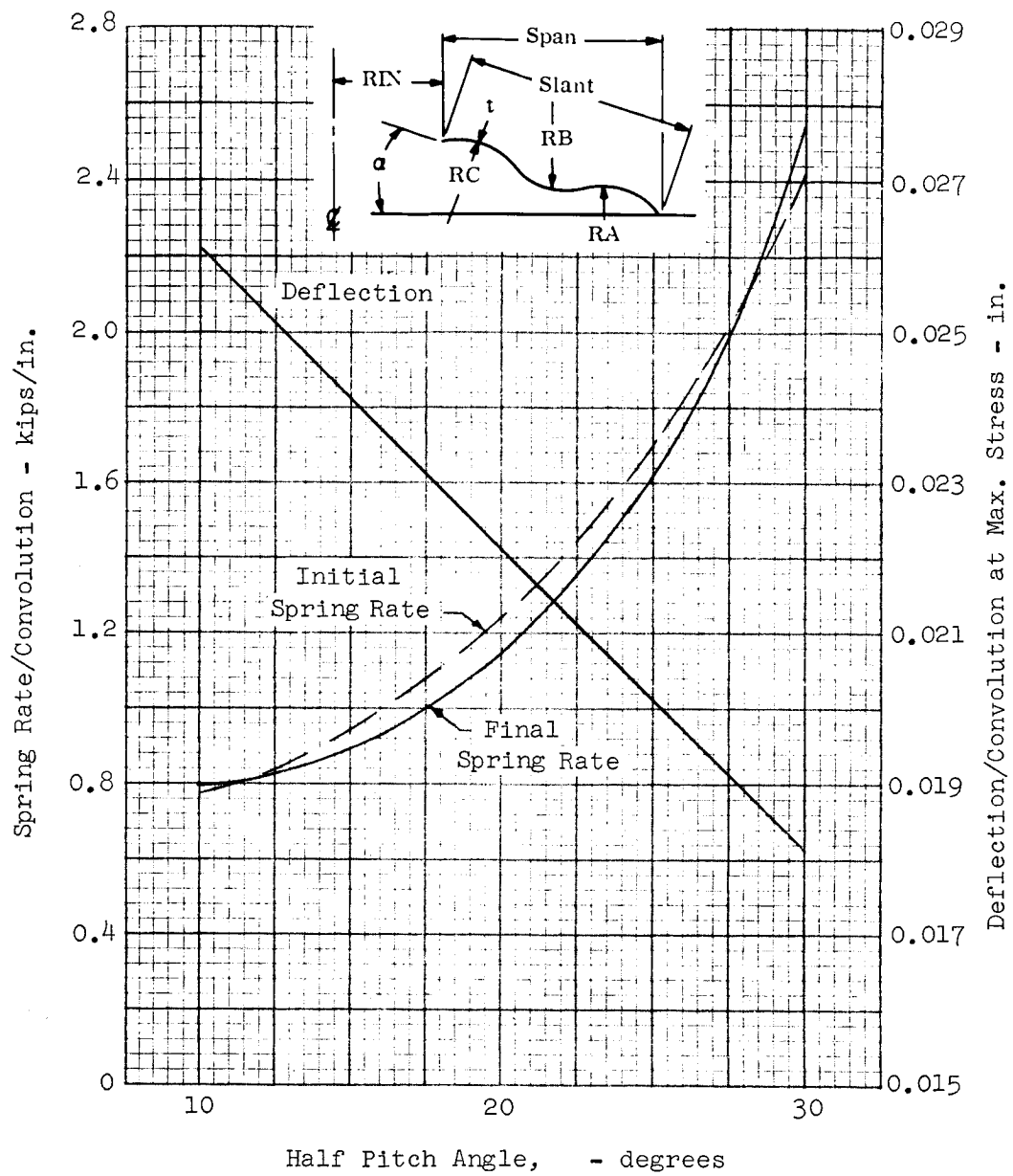
Figure 27. Spring Rate and Deflection vs Pitch, 6-inch Diameter

D. PARAMETRIC STUDY CONCLUSIONS

The strong influence of the various individual geometric parameters and their apparent complex coupling effects on the stress-deflection relationships of welded bellows has been demonstrated. The folly of using approximate formulas, such as bending of flat plates, to calculate these relationships is clearly indicated.

On the basis of a small number of samples, it appears that variations in weld bead size or shape have a negligible effect for bellows with inside diameters of 6 inches or greater. The diameter at which the weld bead properties become significant has not yet been determined.

E. ASYMMETRIC INSTABILITY

Thin shells of revolution, such as occur in typical welded expulsion bellows designs, are subject to elastic instability when loaded in compression or exposed to collapsing pressures. In Reference 5, Weinitschke demonstrates that a shell may buckle in an asymmetric mode at a load below that required for a symmetric mode. The asymmetric deflections are described as having the form $W = W(r) \cos n\theta$ which is essentially a description of circumferential waves of various shapes. While the work of Weinitschke was for spherical shallow shells, the basic principle should be applicable to the welded bellows. Welded bellows leaf designs, however, frequently exceed the limits of the shallow shell assumption. It was decided, therefore, to proceed first with work on bellows with shallow shell shapes so that the work of Weinitschke could be used as a special check case. Acting as consultant to Bell Aerosystems Company, Dr. R. Archer subsequently prepared a report showing the mathematical development and outlining the computer program required. The primary deformed state of the shell at any given loading is computed using IBM program 1753. The deformed shell is then introduced into the asymmetric stability equations. For any stage of the loading process, the stability (both symmetric ($n = 0$) and nonsymmetric ($n \geq 1$)) can be checked by transferring to the stability subprogram and computing $DSTAB_n$ for a selected value of n. The loss of stability corresponding to a given circumferential mode ($\cos n\theta$) will be signaled by a change in sign of the corresponding $DSTAB_n$; $DSTAB_n$ is the accumulative multiplication of the determinant at each shell solution point obtained in the inversion of the matrix from the finite difference form of the stability equations. A solution of the stability equation has been passed in the loading process when the $DSTAB_n$ determinant changes sign from its value at the previous load. Since it is desired merely to detect the lowest unstable loading, only the stability determinant, $DSTAB_n$, need be computed and saved rather than the stability equation solution. This procedure results in a reduction of computer time and required memory storage.

The shallow shell stability subroutine was then written because changes could easily be made later to remove the shallow shell restrictions. The subroutine was written into the single-leaf program so that the results of Weinitschke for shallow spherical shells could be used as a check. The first check runs of the subprogram clearly indicated the presence of programming errors. During the debugging process, the results of Huang were published in Reference 6 which disagreed with the numerical results of Weinitschke. At this time, Dr. R. Archer also stopped work on the development of the deep shell stability equations until the disagreement could be resolved. Toward the end of the contract period a letter was received from Dr. R. Archer stating that he had obtained some independent results indicating that Huang's results are reliable. The deep shell asymmetric stability analysis report was received a short time later.

The computer subprogram required for the deep shell asymmetric stability analysis is so different from the shallow shell stability subroutine that a completely new subprogram must be written. With insufficient time remaining, the writing of the new subprogram had to be left until a later date.

Some additional time was spent on checking out the shallow shell subroutine. Some errors were found, but subsequent check runs did not check out with the results of Huang. While the shallow shell subprogram has not been made operational during this contract period, continued effort in this area is recommended. A successful operating shallow shell stability subprogram will be of considerable value in checking shallow shell cases computed with a new deep shell stability subprogram.

SECTION 3

DYNAMICS INVESTIGATION OF METALLIC BELLOWS

A. SYNOPSIS

The dynamic investigation was conducted to establish the vibrational modes of welded bellows when subjected to external dynamic environments.

During the report period from April 1962 to January 1963, both longitudinal (accordion) and lateral modes were predicted for bellows with uniform leaf geometries by substituting bellows effective spring rates and masses into elastic homogeneous bar formulas. For non-uniform leaf geometries a general matrix of influence coefficients was developed for digital computations. Good experimental agreement was obtained in both elastic and inelastic strain regions. The effect of external and internal pressure on these modes was also established. Attenuation of large bellows motions was achieved by installing ring baffles inside the bellows at strategic locations. In order to obtain the inelastic spring rate of a bellows, an experimental method was developed. Other vibrational modes such as local leaf resonance, bellows head resonances, ring bending resonances, etc., were found to be of little practical interest.

During experimental test, a longitudinal (liquid) mode was found. Liquid pressure oscillations of considerable severity occurred at low frequencies at very low input sinusoidal g levels. Considerable head translation, head rocking, and lateral bellows motion accompanies the pressure oscillations. Jelled liquid studies were also conducted to define liquid motion at resonance.

During this interim report period a mathematical model and the simple frequency formula in Table 3 was developed for the liquid mode. The calculated lowest natural frequency agreed reasonably well with vibration tests on seven bellows ranging in size from 4 inches to 10 inches in diameter and 8 inches to 44 inches in length. This model will require further adjustments to predict the magnitude of the pressure distribution caused by convolution pumping, liquid inertia body forces, external gas density and other causes. Tests on different size bellows have shown that the most effective means of attenuating potentially damaging liquid pressure oscillations is to apply external gas pressure. The internal liquid dynamic pressure decreases as a function of increasing external gas pressure. Dissolved gas in the propellant and gas entrainment devices also affect these pressure oscillations.

Multi-ply bellows were found to be more resonant than single-ply bellows. A dependable damping treatment using viscoelastic materials between two ply leaves was suggested.

B. PURPOSE AND OBJECTIVES

The dynamics investigation was directed primarily toward a detailed analytical and experimental investigation of the modes which were previously discussed in Reference 1 and

were called longitudinal liquid displacement modes. The objective was to establish a theoretical model that would predict the frequency and the internal pressure distribution at these vibratory modes as functions of applicable bellows parameters. These modes are especially significant with leaf materials in the geometric nonlinearity region, since low-cycle, high-stress bellows failure may occur when dynamic stresses, due to leaf motion and liquid pressure fluctuations, are superimposed on the steady-state stresses. The development of various devices to attenuate these dynamic stresses was a further objective of this investigation.

The model covering the liquid mode analysis presented here was decided upon after investigation of several other potential causes, such as leaf contour distortion, lateral shear beam action, local cavitation in the bellows leaves, liquid cylinder sonic wavelength, and radial pressure-wave generation in the leaves. Dr. Nelson Isada, University of the State of New York at Buffalo, was consulted to provide certain mathematical concepts.

The dynamics analysis of metallic bellows was extended to consider the merits of a double-ply leaf construction. The vibration testing provided additional experimental data for the liquid mode, accordion mode, and lateral mode analyses.

C. NOMENCLATURE

$A, A_N, B, C, C_1, C_2, D$ - Constants

a - Inside radius of bellows (in.)

A - Area (in.^{2})

A_i - Inside area of bellows (in.^{2})

A_L - Planform area of convolution (in.^{2})

B $- \dfrac{a}{4}\left(\dfrac{d_o^2}{d_i^2} - 1\right)$ Constant for each bellows (in.)

d_o - Outside diameter of bellows (in.)

d_i - Inside diameter of bellows (in.)

E - Effective modulus of elasticity of bellows (lb/in.^{2})

F - Force on bellows (lb)

F_e - Other forces on bellows (lb)

F_r - Body force per unit volume in longitudinal direction (in./sec^2)

F_z - Body force per unit volume in radial direction (in./sec^2)

$f(ka)$ - Function of bellows length and inside diameter

g - Gravitational constant (in./sec^2) = 386

I_o — Modified Bessel Function of the first kind zero order

I_1 — Modified Bessel Function of the first kind first order

K — Spring force (lb)

K_A — Spring rate (lb/in.)

K_o — Modified Bessel Function of the second kind

k — $\dfrac{n\pi}{L}$; n = 1, 3, 5, $\cdots$ (1/in.)

L — Length of bellows (in.)

M — Mass (lb sec^2/in.)

n — Interger and mode number

p_o — External pressure

p_i — Internal pressure

p_a — Internal pressure at liquid column boundary, r = a

P — Pressure (lb/in.^{2})

Q — Transmissibility, output displacement/input displacement, nondimensional

Q_e — Volume of fluid expelled from convolution per unit length (in.^{2})

$q(t)$ — Function of t

r — Radius (in.)

$r(x)$ — Function of x

Δr — Change in radius (in.)

S — Stress (lb/in.^{2})

S_a — Stress in uniform porous bar (lb/in.^{2})

$T(t)$ — Function of t

t — Time (sec)

u — Axial fluid velocity (in./sec)

V — Volume (in.^{3})

ΔV — Change in volume (in.^{3})

v   - Radial fluid velocity (in./sec)

w   - Weight per unit length

W_i - Weight of liquid inside of bellows, lb

W_m - Weight of convolutions, lb

W_t - Weight of liquid trapped in convolutions, lb

X(x)   - Function of x

x   - Coordinate along bellows longitudinal axis

y   - Coordinate along bellows radius

α (Alpha) - Angle (radians)

α_n - Wave number

β (Beta)   - $\dfrac{\omega}{\gamma} \left(\dfrac{\text{radians}}{\text{in.}} \right)$

γ (Gamma) $\sqrt{\dfrac{Kg}{W}}$ (in./sec)

ϵ (Epsilon) - Displacement (in.)

      ϵ_a - Unit radial displacement of liquid column at r = a (in.)

      ϵ_r - Unit radial displacement of liquid column at r (in.)

      ϵ_x - Unit strain in bellows along longitudinal axis (in./in.)

      θ - (Theta) - Angle (radians)

      λ - (Lambda) - Convolution displacement (in.)

      λ_o - Input displacement (in.)

$\dfrac{\Delta\lambda}{\Delta x}, \dfrac{\partial\lambda}{\partial x}$ - Effective bellows strain, elongation per unit length (in./in.)

μ (MU) - Viscosity (lb sec/in.^{2})

ν (NU) - $\dfrac{\mu}{\rho}$ Kinematic viscosity (in.^{2}/sec)

π - (PI) - 3.14 Constant (radians)

ρ (RHO) - Effective mass density of bellows (lb sec^2/in.^{4})

τ (TAU) - $\dfrac{M}{\dfrac{W_L}{g}} = \dfrac{\text{end mass}}{\text{bar mass}}$

                                                                    Report No. 8230-933007

ω (OMEGA) - Frequency (1/sec)

ω_L - Liquid mode natural frequency (radians/sec)

ω_a - Accordion Mode Natural Frequency (radians/sec)

ω_f - Natural frequency of elastic bar (radians/sec)

Single dot above symbol indicates FIRST DERIVATIVE with respect to time (LINEAR VELOCITY, ANGULAR VELOCITY)

Double dot above symbol indicates SECOND DERIVATIVE with respect to time (LINEAR ACCELERATION, ANGULAR ACCELERATION)

Single prime above symbol indicates FIRST DERIVATIVE with respect to displacement (SLOPE)

Double prime above symbol indicates SECOND DERIVATIVE with respect to displacement (CURVATURE)

D.   MATHEMATICAL ANALYSIS

The dynamics of elastic containers containing a fluid has been given extensive attention by several authors (References 7 and 8). Mode shapes and natural frequencies have been found to be complex and any mathematical theory describing this phenomenon will most certainly depart from the elementary and conventional frequency and mode shape equations. In the following analysis, several theories are developed in an attempt to obtain a mathematical model that can be used to study and evaluate the dynamic properties of bellows containing an incompressible fluid. This work is, to a large extent, a continuation and extension of work previously accomplished (Reference 1).

In Reference 1, it was found that the accordion modes and natural frequencies of bellows could be predicted with reasonable accuracy by assuming that the bellows is a homogeneous elastic bar clamped or fixed at both ends. This assumption is reasonable for a bellows closed at both ends and containing an incompressible fluid. Fixing the ends does not prevent relative motion of the convolutions with the ends. However, no convolution motion occurred at even interger multiples of the fundamental accordion mode frequency. In addition, the experimental data pointed out the need for modification of the basic analytical model because, at certain frequencies, the fixed-fixed end restraint assumption was violated with substantial bellows head motion.

In this development, the assumption that bellows dynamics may be investigated by application of elastic, porous bar concept is applied and extended.

The mathematical model developed gives reasonable approximations to the liquid mode frequencies observed in laboratory testing. The analysis presented is divided into three major subdivisions (1) accordion mode, (2) liquid mode, and (3) pressure distribution.

1.   Accordion Mode Analysis

The following theory is based upon the assumption that the bellows in a mathematical sense may be treated as a homogeneous elastic bar. Motion of the bellows

base and head are the same since the head is essentially being moved back and forth by action of the internal incompressible fluid. This liquid usually has a bulk modulus equal to approximately 300,000 pounds per square inch as compared to the bellows effective modulus of elasticity of approximately 30 pounds per square inch (not 30,000,000).

a. Vibration Input at Each End

The solution of the wave equation:

$$\frac{\partial^2 \lambda}{\partial t^2} = \gamma^2 \frac{\partial^2 \lambda}{\partial x^2} \tag{1}$$

can, therefore, be expressed as a product solution of the form:

$$\lambda = X(x) \, T(t) \tag{2}$$

where:

X(x) function of x only

T(t) function of time only

Substituting Equation (2) into (1) yields:

$$X \ddot{T} = \gamma^2 X'' T, \text{ or}$$

$$\gamma^2 \frac{X''}{X} = \frac{\ddot{T}}{T} = - \omega_f^2 = \text{constant}$$

Hence:

$$X'' + \frac{\omega_f^2}{\gamma^2} X = 0$$

$$\ddot{T} + \omega_f^2 T = 0$$

Where solutions respectively are:

$$X(x) = A \cos \frac{\omega_f}{\gamma} x + B \sin \frac{\omega_f}{\gamma} x \tag{3}$$

$$T(t) = C \cos \omega_f t + D \sin \omega_f t \tag{4}$$

Therefore:

$$\lambda(x_1 t) = (A \cos \frac{\omega_f}{\gamma} x + B \sin \frac{\omega_f}{\gamma} x)(C \cos \omega_f t + D \sin \omega_f t) \tag{5}$$

For the problem shown in Figure 28, the motions at the boundary are:

$$x = 0 \qquad \lambda = \lambda_o \cos \omega_f t \tag{6}$$
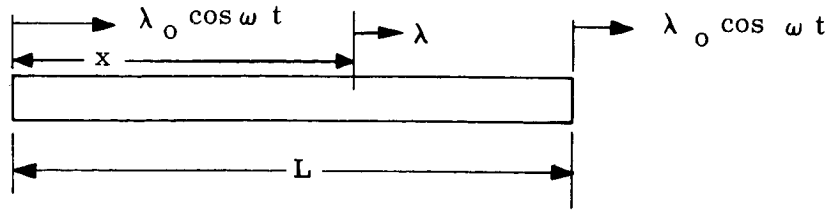
Figure 28. Elastic Bar Vibrated at Both Ends (Bellows Accordion Modes)

$$x = L \qquad \lambda = \lambda_0 \cos \omega_f t \tag{7}$$

Substituting 6 into 5 yields:

$$\lambda_0 \cos \omega_f t = (A + 0)(C \cos \omega_f t + D \sin \omega_f t)$$

$$A C = \lambda_0 \tag{8}$$

$$D = 0 \tag{9}$$

Substituting Equations (7), (8), and (9) into Equation (5) yields:

$$\lambda_0 \cos \omega_f t = (A \cos \frac{\omega_f}{\gamma} L + B \sin \frac{\omega_f}{\gamma} L)(C \cos \omega_f t), \text{ or,}$$

$$A C \cos \frac{\omega_f}{\gamma} L + B C \sin \frac{\omega_f}{\gamma} L = \lambda_0, \text{ and,}$$

$$B C = \lambda_0 \frac{1 - \cos \frac{\omega_f}{\gamma} L}{\sin \frac{\omega_f}{\gamma} L}$$

Hence, the steady-state solution is:

$$\lambda(x,t) = (\lambda_0 \cos \frac{\omega_f}{\gamma} x + \lambda_0 \frac{1 - \cos \frac{\omega_f}{\gamma} L}{\sin \frac{\omega_f}{\gamma} L} \sin \frac{\omega_f}{\gamma} x) \cos \omega_f t$$

$$\lambda(x,t) = \left\{ \lambda_0 \left[1 + \left(\frac{1 - \cos \frac{\omega_f}{\gamma} L}{\sin \frac{\omega_f}{\gamma} L} \right)^2 \right]^{1/2} \cos \left(\frac{\omega_f}{\gamma} x - \alpha_1 \right) \right\} \cos \omega_f t \tag{10}$$

where:

$$\alpha_1 = \frac{\omega_f L}{2 \gamma}$$

$$\lambda(x,t) = \left[\lambda_0 \ Q \right] \cos \omega_f t \tag{11}$$

where:

$$Q \text{ (transmissibility)} = \sqrt{2} \sqrt{\dfrac{1-\cos \dfrac{\omega_f}{\gamma} L}{\sin^2 \dfrac{\omega_f}{\gamma} L}} \quad \cos\left(\dfrac{\omega_f}{\gamma} x - a_1\right) \qquad (12)$$

The expression for transmissibility Q, output/input = λ / λ_o is given in Equation (12). The behavior of the second term under the bracket in Equation 12 will now be evaluated.

Investigate $f(\theta) = \dfrac{1-\cos \theta}{\sin^2 \theta}$, where $\theta = \dfrac{\omega_f}{\gamma} L$. Suppose:

$$\theta = 0 \; ; \lim_{\theta \to 0} \frac{1-\cos \theta}{\sin^2 \theta} = 1/2 \text{ (No amplification)}$$

$$= \frac{\pi}{6} \quad f(\theta) = 0.536$$

$$= \frac{\pi}{4} \qquad\qquad = 0.586$$

$$= \frac{\pi}{3} \qquad\qquad = 0.667$$

$$= \frac{\pi}{2} \qquad\qquad = 1.000$$

$$= \pi \qquad\qquad = \infty \quad \text{(Resonance at odd integer 1)}$$

$$= \frac{3\pi}{2} \qquad\qquad = 1.000$$

$$= 2\pi \qquad\qquad = 1/2 \text{ (No amplification at even harmonics)}$$

$$= 3\pi \qquad\qquad = \infty \text{ (Resonance at odd interger 3)}$$

The proof that the:

$$\lim_{\theta \to 0} \frac{1-\cos \theta}{\sin^2 \theta} = 1/2$$

is found by differentiating and applying L'hospital's rule:

$$f'(\theta) = \frac{\sin \theta}{2 \sin \theta \cos \theta} = \frac{1}{2 \cos \theta}$$

$$\lim_{\theta \to 0} f'(\theta) = \lim_{\theta \to 0} \frac{1}{2 \cos \theta} = 1/2$$

Thus, when the inputs are identical sinusoidal displacements applied at ends of the bellows, i.e., the base and head, no amplification occurrs for the even harmonics. It is, however, conceivable that other types of excitation such as acoustics can excite the even harmonics.

44

b. Steady-State Response of Bellows with No Mass at the End and Subjected to Sinusoidal Motion Input at the Base

Response developed here is used in liquid mode pressure distribution section later. Figure 29 represents this problem.
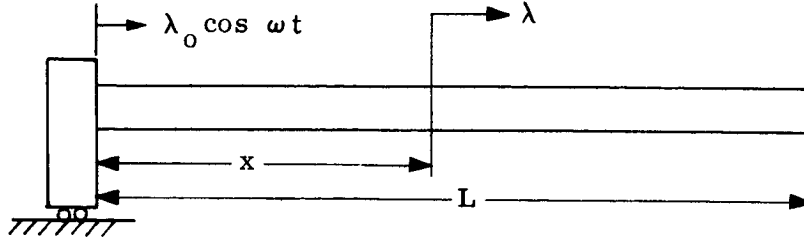
Figure 29. Bellows Fixed at One End, Free at the Other End
(Liquid Mode Model)

The steady-state solution computed in Section 3.D.1.a. was found to be:

$$\lambda(x,t) = (A \cos \frac{\omega_f}{\gamma} x + B \sin \frac{\omega_f}{\gamma} x)(C \cos \omega_f t + D \sin \omega_f t) \qquad (5)$$

$$\frac{\partial \lambda}{\partial x} = (-A \frac{\omega_f}{\gamma} \sin \frac{\omega_f}{\gamma} x + B \frac{\omega_f}{\gamma} \cos \frac{\omega_f}{\gamma} x)(C \cos \omega_f t + D \sin \omega_f t \qquad (13)$$

$$x = 0; \quad \lambda(0,t) = \lambda_0 \cos \omega_f t \qquad (14)$$

Substituting Equations (14) into (5):

$$\lambda_0 \cos \omega_f t = (A+0)(C \cos \omega_f t + D \sin \omega_f t)$$

Hence, equating coefficients of like terms:

$$\lambda_0 = A C \qquad (15)$$

$$0 = A D, \text{ or,} \qquad (16)$$

$$\lambda_0 = A C$$

$$D = 0$$

Therefore:

$$\frac{\partial \lambda}{\partial x} = (-A \frac{\omega_f}{\gamma} \sin \frac{\omega_f}{\gamma} x + B \frac{\omega_f}{\gamma} \cos \frac{\omega_f}{\gamma} x)(C \cos \omega_f t) \qquad (17)$$

At $x = L, \frac{\partial \lambda}{\partial x} = 0$, (force at end is zero) $\qquad (18)$

Substituting Equation (18) into (17) yields:

$$0 = (-AC \frac{\omega_f}{\gamma} \sin \frac{\omega_f}{\gamma} L + B C \frac{\omega_f}{\gamma} \cos \frac{\omega_f}{\gamma} L) \cos \omega_f t$$

$$0 = (- \lambda_o \frac{\omega_f}{\gamma} \sin \frac{\omega_f}{\gamma} L + B C \frac{\omega_f}{\gamma} \cos \frac{\omega_f}{\gamma} L)$$

$$B C = \lambda_o \tan \frac{\omega_f}{\gamma} L \tag{19}$$

Substituting (19) and (15) into (17):

$$\lambda(x,t) = (\lambda_o \cos \frac{\omega_f}{\gamma} x + \lambda_o \tan \frac{\omega_f}{\gamma} L \sin \frac{\omega_f}{\gamma} x) \cos \omega_f t$$

$$= (\cos \frac{\omega_f}{\gamma} x + \tan \frac{\omega_f}{\gamma} L \sin \frac{\omega_f}{\gamma} x) \lambda_o \cos \omega_f t$$

$$= \left[(1 + \tan^2 \frac{\omega_f}{\gamma} L)^{1/2} \cos (\frac{\omega_f}{\gamma} x - \alpha) \right] \lambda_o \cos \omega_f t \text{ (using}$$
trigonometric functions)

$$= \left[\sec \frac{\omega_f}{\gamma} L \cos (\frac{\omega_f}{\gamma} x - \alpha) \right] \lambda_o \cos \omega_f t \tag{20}$$

where:

$$\alpha = \tan^{-1} \frac{\tan \frac{\omega_f}{\gamma} L}{1} = \frac{\omega_f}{\gamma} L$$

At:

$$x = L$$

$$\lambda(L,t) = (\cos \frac{\omega_f}{\gamma} L + \tan \frac{\omega_f}{\gamma} L \sin \frac{\omega_f}{\gamma} L) \lambda_o \cos \omega_f t \tag{21}$$

$$= (\cos^2 \frac{\omega_f}{\lambda} L + \sin^2 \frac{\omega_f}{\gamma} L) \frac{1}{\cos \frac{\omega_f}{\gamma} L} \lambda_o \cos \omega_f t$$

$$= \frac{1}{\cos \frac{\omega_f}{\gamma} L} \lambda_o \cos \omega_f t$$

$$= \lambda_o \sec \frac{\omega_f}{\gamma} L \cos \omega_f t \qquad n = 2n_o + 1$$

When:

$$\frac{\omega_f}{\gamma} L = \frac{\pi}{2}, \frac{3\pi}{2}, \frac{5\pi}{2} \cdots \frac{2n_o + 1}{2} \pi, n_o = 0, 1, 2, 3 \cdots \tag{22}$$

then resonance exists because $\sec \frac{\omega_f}{\gamma} L \to \infty$. Note that resonance also occurs at odd multiples in this case (when n = 1, 3, 5, etc) but at frequencies different than the accordion mode case in Section 3.D.1.a.

2. Liquid Mode Analysis

A study and literature survey of the problem of liquid vibration in a closed flexible pipe has resulted in the formulation of a theory that gives results reasonably close to observed test results. Solutions for the thin-wall circular pipe are available (Reference 8). The present configuration is unique in that the surface confining the liquid is not a thin-wall cylindrical one; hence the curved plate extensional theory used by other investigators (References 8 and 20) is not directly applicable. Figures 30 and 31 serve to illustrate this point.
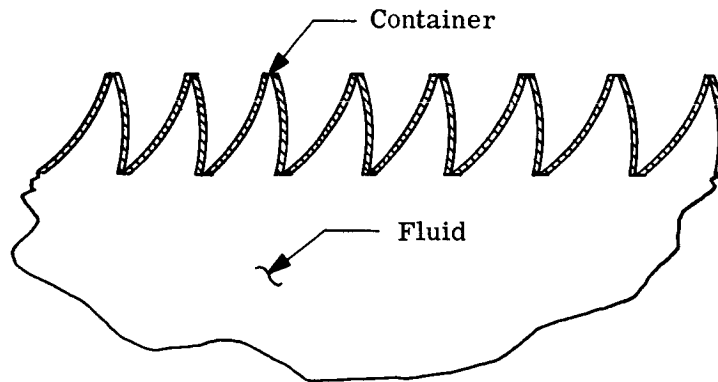
Figure 30. Schematic of Typical Bellows Geometry
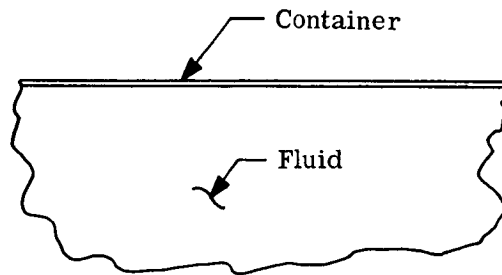
Figure 31. Schematic of Typical Thin-Wall Cylinder

The divergence of the bellows boundary from the thin cylindrical boundary is reflected in different allowable mode shapes and the system natural frequencies. The equivalence of the two systems in effective diameter variation due to breathing may indeed be established. The effective fluid column radius in the bellows is a function of the relative convolution element displacement along the longitudinal axis while in the thin wall cylinder the radial extension governs this phenomenon. This discussion simply reveals the importance of obtaining proper boundary conditions for the present analysis.

A mathematical model will be presented for use in predicting the frequency of the fundamental liquid mode and its higher harmonics which were previously discovered by tests (Reference 1). The internal column pressure and velocity streamlines will be discussed.

A similar situation exists in hyper- and ultra-high-frequency waveguides (Reference 18). Here, communication engineers are confronted by cavity resonance that is somewhat synonomous to the fluid resonance condition. The bellows displacement gives rise to a radial flow that is related to seepage or diffusion problem (Reference 13). Vortex theory is also similar in nature to this problem (Reference 11).

These analogies and similarities are not too surprising since the partial differential equations describing the motion in each case are similar in form.

Since the relative convolution motion is reflected as a change in diameter, the fluid column tends to acquire the shape shown in Figure 32. Note that, along the bellows length, the convolution density is periodic. This condition exists in uniform homogeneous bars, as well as springs under vibration; hence, it can be expected to exist in bellows. Figure 32 reveals further that, in the region where the leaves are extending, more fluid may be entrained. This results in an increase in the mean effective fluid column diameter; however, in the region where the leaves are contracting, the converse is true. This type of column breathing is discussed by Lord Rayleigh in Reference 13. Since the convolutions are vibrating in this mode, the local pressure is functionally related to the mode shape. When this relationship is established, the streamlines throughout the column volume may be readily determined. The importance of these streamlines should not be minimized because their existence and location may well serve to give insight into control of the mode shape and indeed the suppression, if not the complete elimination or shifting of the natural frequency. A possible streamline mapping is shown in Figure 32.
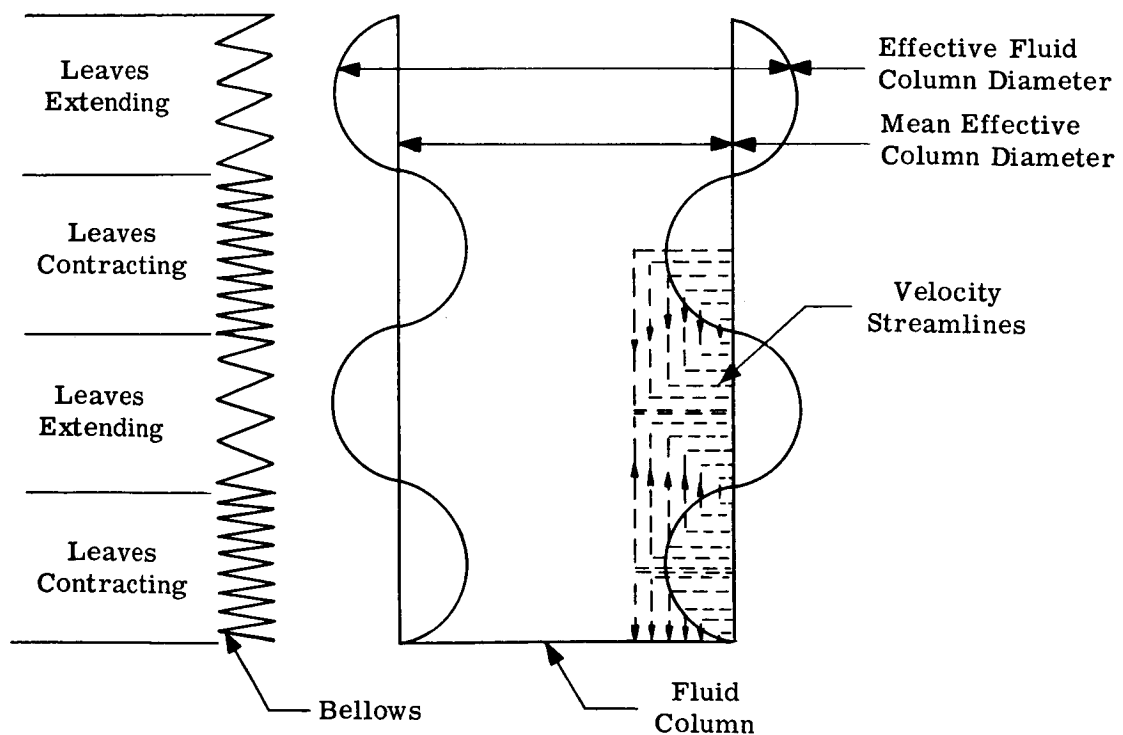
Figure 32. Bellows Mode Shape and Streamlines

The results of an experimental investigation to determine critical frequencies were reported previously along with appropriate equations for prediction of accordion and lateral frequencies (Reference 1). This report presents the formulation of a mathematical model that is employed to predict the liquid mode frequency along the longitudinal axis of the bellows.

a. Formulation of Problem

The bellows coordinate system is shown in Figure 33.
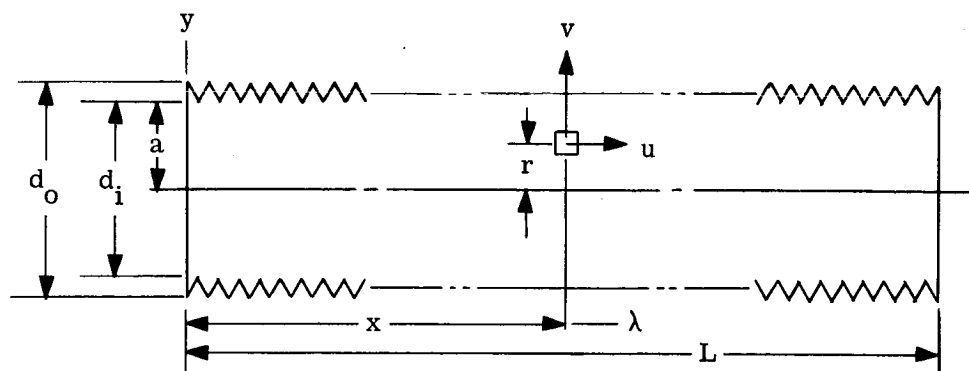
Figure 33. Bellows Coordinate System

It is assumed that the fluid motion inside the bellows is described by the Navier-Stokes equation and the appropriate continuity equation. For this analysis, the equation is modified for incompressible flow. In the basic Navier-Stokes equation, terms describing viscosity and nonlinear effects are present. The effect of these nonlinear terms becomes more pronounced for large flow rates. Since high flow rates are not present in this application and anticipated flow rates will be oscillatory with near-zero mean, the nonlinear effects tend to be cancelled. In this analysis, the viscosity and nonlinear terms are assumed equal to zero.

The accordion or bellows motion is equivalent to the corresponding motion of a homogeneous, elastic bar. While the convolutions themselves appear to violate seriously this assumption, tests reported previously substantiate this assumption. Armed with the forementioned assumptions, the task now resolves into the determination of effective coupling between the convolutions and the fluid column. This coupling produces the resonant frequencies of the liquid column which must be determined.

Equations of State

With reference to the coordinate system presented in Figure 33, the Navier-Stokes equations governing the fluid motion assuming circular symmetry may be approximated as:

$$\frac{\partial u}{\partial t} + u\frac{\partial u}{\partial x} + v\frac{\partial u}{\partial r} = -\frac{1}{\rho}\frac{\partial p}{\partial x} + \nu\left(\frac{\partial^2 u}{\partial x^2} + \frac{\partial^2 u}{\partial r^2} + \frac{1}{r}\frac{\partial u}{\partial r}\right) + F_z \quad (23)$$

$$\frac{\partial v}{\partial t} + u\frac{\partial v}{\partial x} + v\frac{\partial v}{\partial r} = -\frac{1}{\rho}\frac{\partial p}{\partial r} + \nu\left(\frac{\partial^2 v}{\partial x^2} + \frac{\partial^2 v}{\partial r^2} + \frac{1}{r}\frac{\partial v}{\partial r} - \frac{v}{r^2}\right) + F_r \quad (24)$$

The continuity equation is approximated as:

$$\frac{1}{r} \frac{\partial(rv)}{\partial r} + \frac{\partial u}{\partial x} = 0 \qquad (25)$$

The bellows motion is approximated by the wave equation which determines the motion of an elastic bar, Reference 20. (The equivalent porosity effect assumed earlier is neglected in the derivation of this equation.)

$$\frac{\partial^2 \lambda}{\partial t^2} = \frac{E}{\rho} \frac{\partial^2 \lambda}{\partial x^2} \qquad (1)$$

Equations (1), (23), (24) and (25) are the equations of state which will yield a general solution. Subsequently, the complete solution will be obtained by applying appropriate boundary conditions. For the present study, the parameter of primary interest is the natural frequency; hence, the complete solution will not be acquired at this time.

b.   Boundary Conditions

The fluid boundary in the radial direction is assumed to be the inside diameter of the bellows, r = a. There is, of course, relative motion between the bellows and the fluid column giving rise to a shear effect. For the present, this shear effect will be neglected.
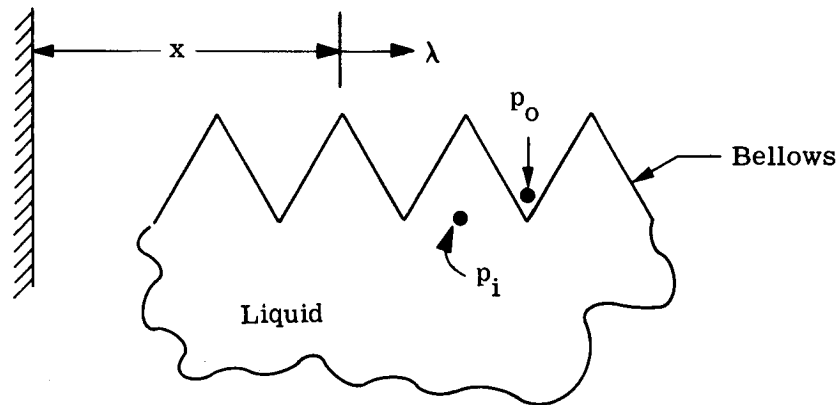
Figure 34. Convolution Displacement Geometry

The parameter λ denotes the displacement of a convolution element located at a distance x in Figure 34. However, since the convolution displacements are assumed to be governed by the wave equation, the entrapped fluid volume is proportional to $\Delta \lambda$, the change in λ referenced to any given position along the longitudinal axis. This phenomenon gives rise to the $\Delta \lambda$ term, shown in Figure 35, which reveals that a convolution is subjected to a displacement and a corresponding strain, $\Delta \lambda / \Delta x$.

Using Figure 35 and the homogeneous elastic bar analogy, it is concluded that to a first approximation the unit strain in the convolutions is given by:

$$\epsilon_x = \frac{\partial \lambda}{\partial x} \qquad (26)$$
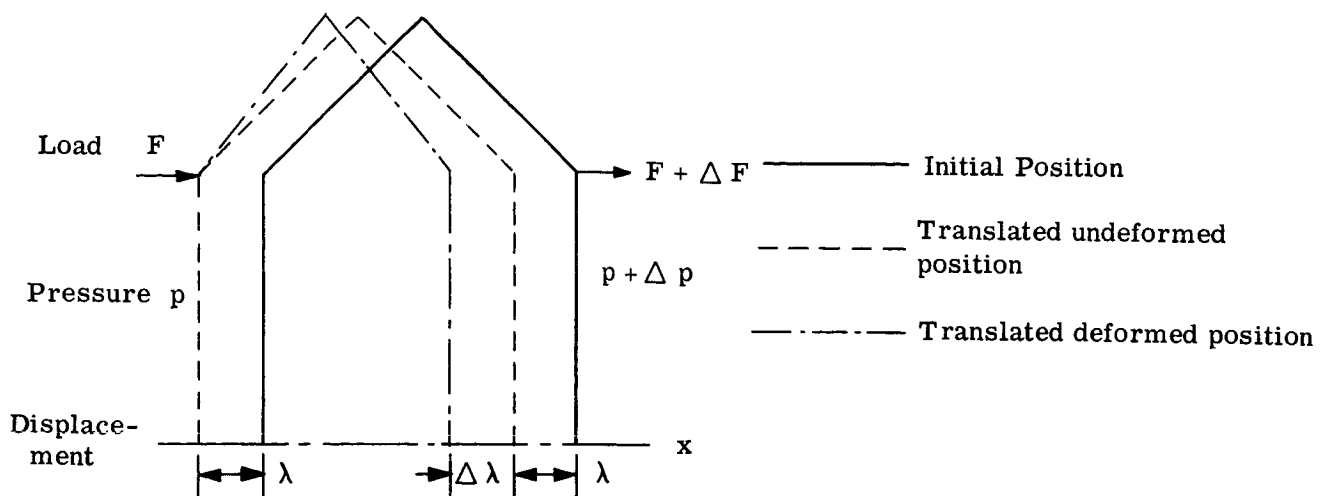
Figure 35. Geometry of Differential Displacement

Since fluid is ejected from each convolution and Equation (26) implies that in the limit, mathematically, generated strains are continuous, the convolutions should ideally be represented by a continuous media capable of absorbing and ejecting fluid. A porous media or sponge satisfies this criteria. Hence, the bellows convolutions in a mathematical sense lends to a porous elastic bar. See Figure 36.
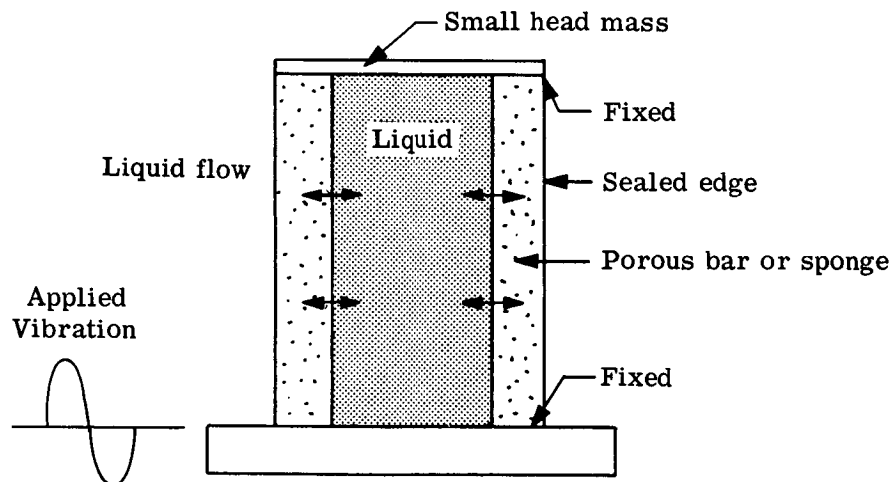
Figure 36. Porous Bar Concept of Liquid Mode

The volume of fluid per unit length expelled from a convolution is approximated as:

$$Q_e = \frac{A_L}{2} \frac{\partial \lambda}{\partial x} \tag{27}$$

where A_L is the projected planform area of a convolution.

The factor 1/2 being necessary since fluid is on one side of the element only. See Figure 37.
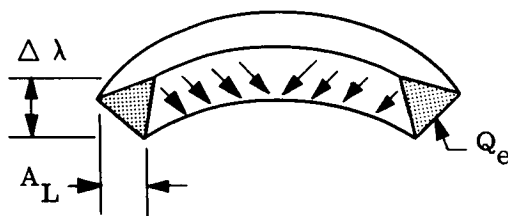
Figure 37. Liquid Ejected from a Bellows Due to a Change in Pitch of the Convolutions

Another approach will now be given. A typical single convolution of any shape is postulated. The volume is computed with the free inside edge at a nominal operating position. The inside edges are compressed and the corresponding change in volume computed. From this procedure, a term $\partial Q_e/\partial \lambda$ is obtained. Equation 27 can now be written as:

$$Q_e = \frac{\partial Q_e}{\partial \lambda} \frac{\partial \lambda}{\partial x} \qquad (27a)$$

The approximation given by Equation (27a) should be superior to that given by Equation (27), and, certainly, any nonlinearities will be detected. The average value of $\frac{\partial Q_e}{\partial \lambda}$ over a prescribed range of λ will probably be different for each initial bellows length when a permanent set is acquired due to stretching the bellows beyond its elastic limit. Equation (27a) will be given further attention; however, for the present analysis, Equation (27) will be used.

The original method takes into account the equivalent porosity of the elastic bar. Although this effect is omitted in the derivation of the conventional wave equation, it cannot be neglected here. Theoretically, it can be concluded that the radial displacement of the fluid column is proportional to the equivalent porosity of the elastic bar.

The flow in and out of the bellows described by Equation (27) implies that the mean effective column diameter is disturbed. An approximation to this functional relationship will now be determined under the assumption that all fluid flowing into the convolution serves to increase the mean effective column diameter.

Assume a cylinder of unit length and radius r:
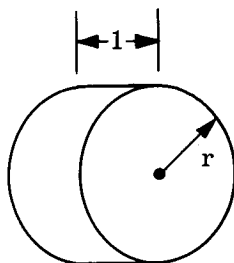
The cross-sectional area of the cylinder is given as:

$$A = \pi r^2$$

The differential change in area is related to the differential change in radius as obtained by taking the differential of both sides of the equation, or:

$$dA = 2 \pi r \, dr = \frac{2 \pi r^2}{r} \, dr = \frac{2}{r} A \, dr \tag{28}$$

The corresponding change in volume per unit length is approximated as:

$$dV = \frac{2}{r} A \, \epsilon_r \cdot 1 \qquad \text{where } \epsilon_r = dr \tag{29}$$

Since Equation (27) gives the flow from the bellows, and Equation (29) gives the increase in effective diameter, for continuity, $Q_e \equiv \Delta V$, for $r = a$. Hence, with $\epsilon_a = \epsilon_r \cdot 1 \mid_{r=a}$, the following will result:

$$\epsilon_a = \frac{a}{4} \frac{A_L}{A_i} \frac{\partial \lambda}{\partial x} \tag{30}$$

Since:

$$\frac{A_L}{A_i} = \left(\frac{d_o^2}{d_i^2} - 1 \right)$$

Then:

$$\epsilon_a = B \frac{\partial \lambda}{\partial x} \tag{31}$$

Where:

$$B = \frac{a}{4} \left(\frac{d_o^2}{d_i^2} - 1 \right)$$

Equation (31) reveals that, for any cross-section, the longitudinal strain of the bellows $\partial \lambda / \partial x$ is equivalent to radial displacement of the local effective column diameter ϵ_a. This implies that the liquid column is in a state of extensional diameter breathing. Several investigators have treated different classes of extensional breathing modes (References 7 and 8). However, direct analogy between these investigations and the present conditions could not be made.

Not only must the motion be continuous at the boundary $r = a$, but also the pressure must be consistent at the boundary. This implies that the pressure rise due to bellows strain must equal the pressure in the fluid column at $r = a$.

Since the bellows is equivalent to a uniform porous bar, the force acting on an element of a bar is:

$$E = \frac{\text{Stress}}{\text{Strain}} = \frac{F/A_L}{\dfrac{\partial \lambda}{\partial x}} \qquad\qquad F = A_L E \frac{\partial \lambda}{\partial x} + F_e \tag{32}$$

Where F_e represents the effects of forces other than the elastic contribution. Recalling Equation (27), one-half the planform area must be used because liquid is stored in the inside

of the bellows only. Hence, to maintain similarity between the elastic homogeneous bar and the bellows, the equivalent E must be multiplied by a factor of 2. The corresponding stress in the bar becomes:

$$S_a(x,t) = \frac{F}{A_L} = 2E \frac{\partial \lambda}{\partial x} + \frac{F_e}{A_L} \tag{33}$$

The assumption is now made that the stress in the bar at a given point is equivalent to the local pressure at that point. This assumption is not unreasonable because the modulus E is the effective modulus of the bar (bellows), not the modulus of the bar material. Given the bellows spring rate, the effective modulus can be readily computed. Ideal pressure recovery has been assumed. Actually, the first term on the right-hand side of Equation (33) should be multiplied by a recovery factor. For the present analysis, this factor is assumed to be unity. Assuming:

$$S_a(x,t) = p_a(x,t) \tag{34}$$

Then:
$$p_a(x,t) = 2E \frac{\partial \lambda}{\partial x} + \frac{F_e}{A_L}$$

Equation (34) gives the pressure rise at the boundary due to the bellows convolution motion $\lambda(x,t)$.

c. Solution of Equations

The solution will now be derived subject to the following assumption:

(1) The fluid is assumed to be nonviscous, $\nu = 0$.
(2) All nonlinearities and second-order terms are negligible.
(3) Shear and pressure effects are negligible, $F_e = 0$, Equation (32)

These assumptions are somewhat stringent. However, for frequency determination only, condition (3) has the most effect upon the resulting error. Under these conditions, the system of Equations (23), (24), (25), (1), (31) and (34) becomes:

$$\frac{\partial u}{\partial t} = -\frac{1}{\rho} \frac{\partial p}{\partial x} \quad \text{nonviscous flow equation} \tag{35}$$

$$\frac{\partial v}{\partial t} = -\frac{1}{\rho} \frac{\partial p}{\partial r} \quad \text{nonviscous flow equation} \tag{36}$$

$$\frac{\partial v}{\partial r} + \frac{\partial u}{\partial x} + \frac{v}{r} = 0 \quad \text{continuity equation} \tag{37}$$

$$\frac{\partial^2 \lambda}{\partial t^2} = \frac{E}{\rho} \frac{\partial^2 \lambda}{\partial x^2} \quad \text{wave equation} \tag{1}$$

$$\epsilon_a = B \frac{\partial \lambda}{\partial x} \quad \text{radial displacement of column} \tag{31}$$

$$p_a(x,t) = 2E \frac{\partial \lambda}{\partial x} \quad \text{pressure at liquid column boundary} \tag{38}$$

Differentiating Equations (35) and (36) with respect to x and r, respectively, Equation (37) with respect to t, and combining yields:

$$\frac{\partial^2 p}{\partial r^2} + \frac{1}{r} \frac{\partial p}{\partial r} + \frac{\partial^2 p}{\partial x^2} = 0 \qquad (39)$$

Equation (39) is identified as a second-order equation of the pressure. To solve it, assume:

$$p(x,r) = P(r) \sin \frac{n\pi}{L} x \qquad (40)$$

where P(r) is a function of r alone.

Using Equation (40) in (39) yields:

$$\frac{d^2 p}{dr^2} + \frac{1}{r} \frac{dp}{dr} + k^2 P = 0 \qquad (41)$$

Where: $\quad k^2 = -\dfrac{n^2 \pi^2}{L^2} \qquad (42)$

This equation is identified as a modified Bessel equation. The general solution to Equation (41) is found to be:

$$P(r) = A \, I_0(kr) + B \, K_0(kr)$$

Where $I_0(k_r)$ = modified Bessel function of the first kind.

$\quad K_0(k_r)$ = modified Bessel function of the second kind.

This analysis demands that P be finite, when r = 0. It is concluded that, B = 0.

With this restriction, Equation (40) becomes:

$$p(x,r) = A \, I_0(kr) \sin \frac{n\pi}{L} x \qquad (43)$$

Where again: $\quad k = \dfrac{n\pi}{L}$

To compute the radial acceleration of the fluid at the boundary, Equation (36) is evaluated at r = a. Thus:

$$\left. \frac{\partial v}{\partial t} \right|_{r=a} = -\frac{1}{\rho} \left. \frac{\partial p}{\partial r} \right|_{r=a} = \dot{v}(a) \qquad (44)$$

Using Equation (43) in (44) yields:

$$p_a = -\rho \frac{I_0(ka)}{k I_1(ka)} \dot{v}(a) \qquad (45)$$

Where: $\quad \dfrac{d}{dr} I_0(kr) = k I_1(kr)$

Since $\dot{v}(a)$ is directed along the y axis, it is concluded that $\dot{v}(a) = \ddot{\epsilon}_a$, and Equation (45) becomes:

$$p_a = -\rho \; \frac{I_o(ka)}{k \, I_1(ka)} \; \ddot{\epsilon}_a \tag{46}$$

The general solution of Equation (1) is found to be:

$$\lambda = c_1 \, e^{-i\omega t} e^{-i\alpha_n x} \tag{47}$$

Where:

$$\alpha_n = \frac{\omega}{\left(\dfrac{E}{\rho}\right)^{1/2}} = \text{a wave number}$$

Using Equation (47) in Equation (31) yields:

$$\epsilon_a = -B \, i \, \alpha_n \, \lambda \tag{48}$$

From which:

$$\ddot{\epsilon}_a = B \, i \, \alpha_n \, \ddot{\lambda} \tag{49}$$

and Equation (45) becomes:

$$p_a = \rho \; \frac{I_o(ka)}{k I_i(ka)} \; B \, i \, \alpha_n \, \ddot{\lambda} \tag{50}$$

Using Equations (31) and (48) in Equation (38) yields:

$$p_a = -2E \, i \, \alpha_n \, \lambda \tag{51}$$

Since the pressure must be continuous, the pressure produced by pulsation of the column, Equation (50), must equal the pressure produced by the strain in the convolution, given by Equation (51). Equating these two equations yields:

$$\ddot{\lambda} = -2 \, \frac{E}{\rho} \; \frac{k}{B \dfrac{I_o(ka)}{I_1(ka)}} \; \lambda \tag{52}$$

Substituting for B, Equation (52) is written as:

$$\ddot{\lambda} = -\frac{E}{\rho} \, k^2 \; \frac{8}{\left(\dfrac{d_o^2}{d_i^2} - 1\right) ka \dfrac{I_o(ka)}{I_1(ka)}} \; \lambda \tag{53}$$

$$\ddot{\lambda} = -\omega_a^2 \; \frac{4}{\dfrac{1}{2}\left(\dfrac{d_o^2}{d_i^2} - 1\right) ka \dfrac{I_o(ka)}{I_i(ka)}} \; \lambda \tag{54}$$

56

Where: $\frac{E}{\rho} k^2 = \omega_a^2$ (ω_a = accordion mode frequency).

Defining ω_L as the liquid mode frequency, Equation (54) is written as:

$$\ddot{\lambda} + \omega_L^2 \ell = 0$$

Where:

$$\omega_L = \omega_a \sqrt{\frac{4}{\frac{1}{2}\left(\frac{d_o^2}{d_i^2} - 1\right) ka \frac{I_o(ka)}{I_i(ka)}}} \tag{55}$$

For convenience, Equation (55) is written in the following form:

$$f(ka) = \left[\frac{1}{2}\left(\frac{d_o^2}{d_i^2} - 1\right)\right]^{1/2} \frac{\omega_L}{\omega_a} \tag{56}$$

Where:

$$f(ka) = \left[\frac{4}{ka \frac{I_o(ka)}{I_i(ka)}}\right]^{1/2}$$

Using Reference 16, the numerical values of f(ka) vs ka are plotted in Figures 38 and 39. Solutions of Equation (55) yield liquid mode frequencies in closed form. From this equation, the following conclusions are made:

(1) There are as many liquid frequencies as there are accordion frequencies.

(2) The liquid mode frequencies are functions of bellows inside and outside diameter in the form of a size factor given by $\left[\frac{1}{2}\left(\frac{d_o^2}{d_i^2}-1\right)\right]^{1/2}$

(3) The liquid mode frequencies appear to be independent of end restraints.

The third conclusion appears to be most revealing because it implies that the frequency is the same for both an open end and a closed end bellows.

It is interesting to determine how well the derived formula predicts the magnitude of the critical liquid mode frequency. Figure 40 shows a comparison of the computed and experimentally determined frequencies for several bellows. The comparison is fair. This seems to imply that the term F_e in Equation (32) is of secondary importance, as far as natural frequencies are concerned as was originally assumed.

Experimental tests revealed that, for the 4-, 5-, and 6-inch diameter bellows, liquid frequencies higher than the first mode failed to appear. According to the theory, these modes should be present. This indicates the theory is not sufficient and that the porosity effect should be incorporated in the wave equation. Although this approach was taken, it is not sufficiently advanced to report.
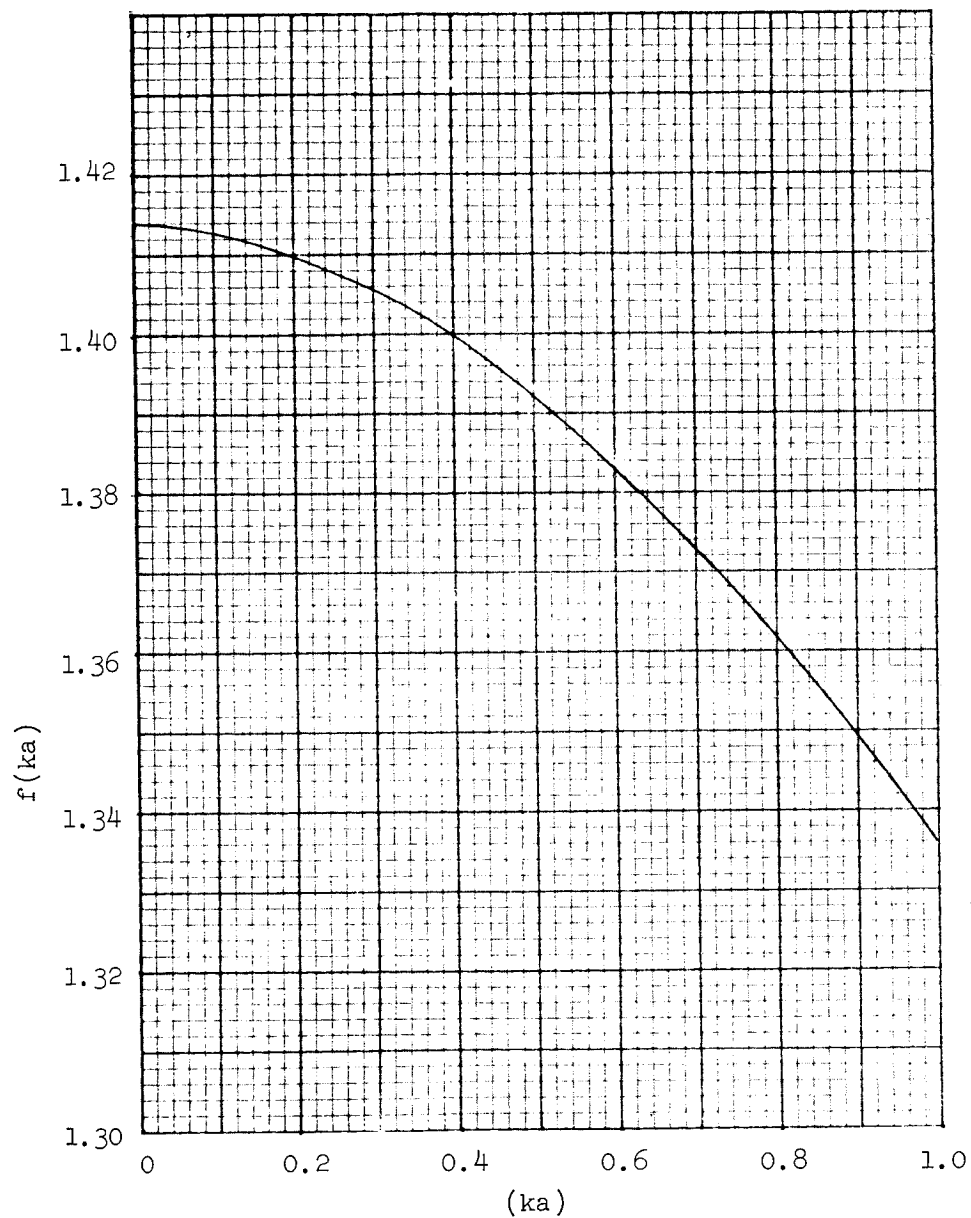
Figure 38. Nondimensional Plots of Liquid Mode Frequencies Functions,
f (ka) vs (ka)
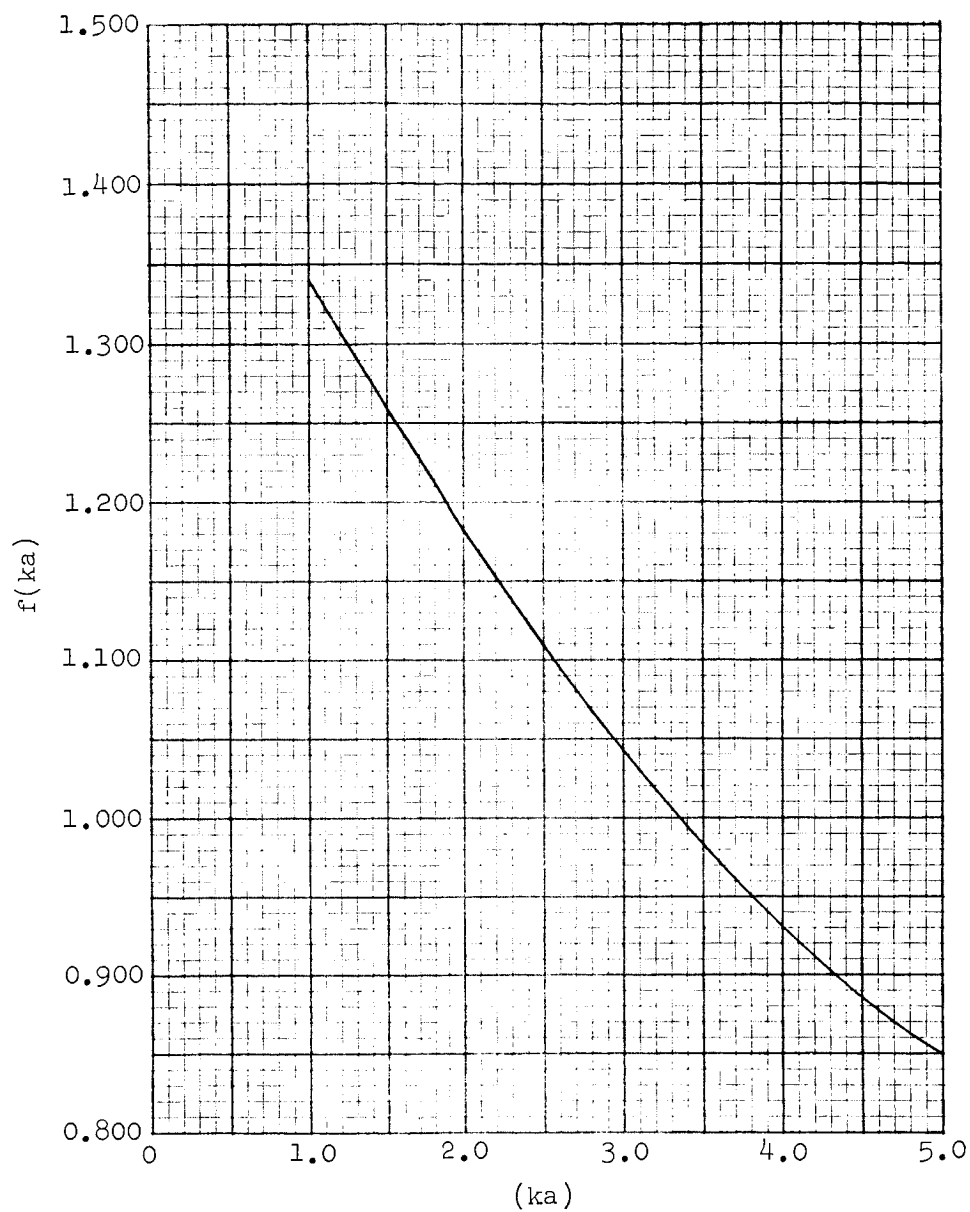
Figure 39. Nondimensional Plots of Liquid Mode Frequencies Functions,
f (ka) vs (ka)

⊙ = Calculated

△ = Test

Bellows vibration lengths noted are in inches
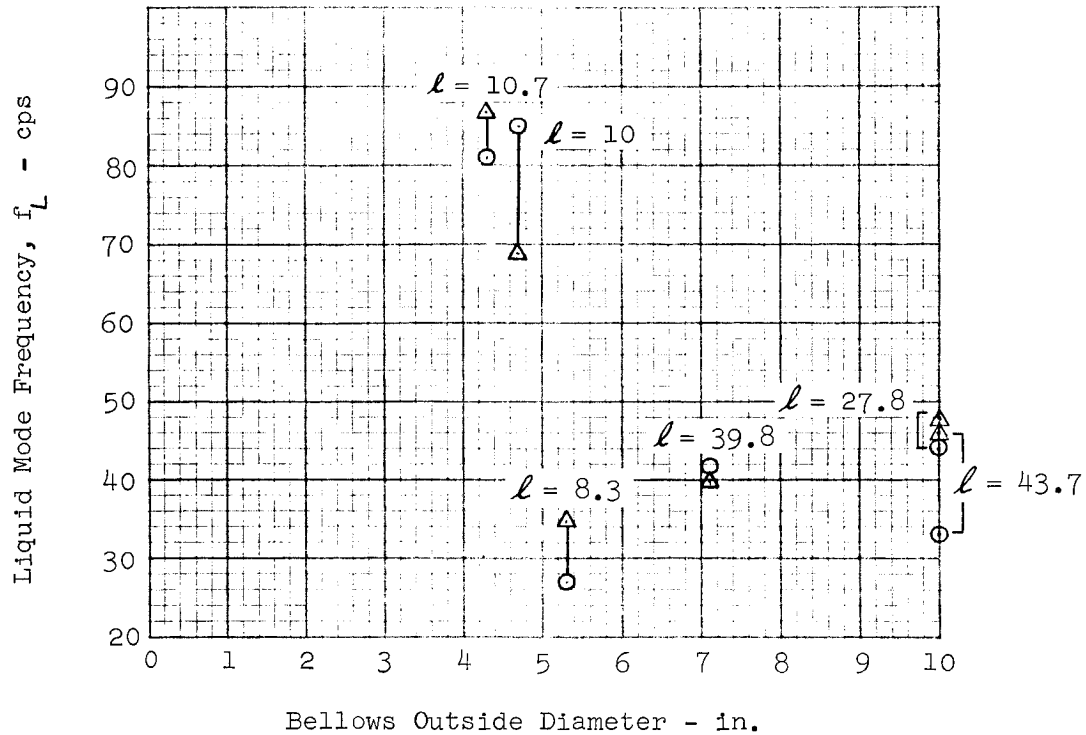
Figure 40. Fundamental Liquid Mode Natural Frequency (Calculated vs Test for Various Bellows Sizes)

3. Pressure Distribution

The liquid mode frequency theory developed in the previous section yields solutions that agree reasonably well with theory. Vibration of the bellows convolutions produces pressure pulses and a corresponding pressure distribution inside the contained liquid. Since the source of excitation is the convolution motion, the equivalent pressure distribution in the convolution should be obtained. The term equivalent pressure distribution is used here because the bellows is assumed to be a homogeneous bar. The terms equivalent elasticity and equivalent strain or stress were established previously; hence, the equivalent pressure and equivalent stress are synonomous. Here again, the bellows geometry appears in violent opposition to the homogeneous bar assumption. However, since the calculated frequencies are reasonably close to test results, it would be interesting to compute pressure distribution on the same basis.

The equivalent pressure inside the convolutions, which serves as a boundary condition for the calculation of distribution inside the column, will be obtained. Neglecting secondary effects, the equivalent stress or equivalent pressure is given by:

$$p_a (x, t) = 2 E \frac{\partial \lambda}{\partial x} \tag{38}$$

It is now assumed that the bellows excitation is applied to the convolutions alone. That is, the liquid column enclosed by the bellows is not distributed by the input vibration. Thus, the pressure variation will be only due to the relative motion of the convolutions, the body force of the column having little effect.

For an elastic bar fixed at one end and free at the other end, the convolution motion is found to be:

$$\lambda(x, t) = \lambda_0 \frac{\cos \frac{\omega_f}{\gamma}(x-L)}{\cos \frac{\omega_f}{\gamma} L} \cos \omega_f t \tag{20}$$

From which:

$$\frac{\partial \lambda}{\partial x} = \lambda_0 \frac{\omega_f}{\gamma} \frac{\sin \frac{\omega_f}{\gamma}(x-L)}{\cos \frac{\omega_f}{\gamma} L} \cos \omega_f t \tag{57}$$

Using Equation (38) the pressure distribution is:

$$p(x, t) = 2 E \lambda_0 \frac{\omega_f}{\gamma} \frac{\sin \frac{\omega_f}{\gamma} L\left(\frac{x}{L} - 1\right)}{\cos \frac{\omega_f}{\gamma} L} \cos \omega_f t \tag{58}$$

From Equation (22) resonance occurs when:

$$\frac{\omega_f}{\gamma} L = \frac{n\pi}{2}; \quad N = 1, 3, 5 \ldots N \text{ odd}$$

Equation (58) gives the equivalent pressure distribution for frequencies other than the accordion mode natural frequency at which the pressure theoretically becomes infinite. Actually, the observed pressure will be finite because of damping and other physical conditions neglected in the theoretical development. A damping term will probably be necessary in the wave equation to obtain more-realistic data at a near resonance. Pressure magnitude and distribution in the region of the liquid mode frequency is of paramount importance. The mechanics of this condition are not well-understood.

As shown previously, the pressure at the liquid column boundary for free vibrations is approximated as:

$$p(x, a, t) = -\rho \frac{I_0(k a)}{k I_1(k a)} \ddot{\epsilon} \tag{59}$$

If sinusoidal radial pressure variation is assumed then:

$$\epsilon = \epsilon_a \cos \omega t, \text{ and,} \tag{60}$$

$$\ddot{\epsilon} = -\epsilon_a \omega^2 \cos \omega t \tag{61}$$

Since:

$$\epsilon_a = B \frac{\partial \lambda}{\partial x} \tag{31}$$

Then:

$$\ddot{\epsilon} = -B \omega^2 \cos \omega t \frac{\partial \lambda}{\partial x} \tag{62}$$

and, finally:

$$p(x, a, t) = \rho a B \omega^2 \frac{I_0 (ka)}{ka I_1 (ka)} \cos \omega t \frac{\partial \lambda}{\partial x} \tag{63}$$

The $\partial \lambda / \partial x$ term must be obtained from formulas yielding the exact mode shape of the convolution motion. Since pressure distribution at resonance is of primary interest, a damping term must be employed in further investigations to obtain more-exact values of displacement at resonance.

E.   TEST VERIFICATION OF LIQUID MODE ANALYSIS

1.   Rigid Pipe Tests

Vibration tests were conducted on a rigid pipe to obtain baseline pressure data, to observe a liquid surface under high-frequency vibration above 50 cps, and to check out the special right-angle, hand-held dynamic pressure probe and the charge amplifier shown in Figure 41. The pipe was of commercial grade, 0.5-inch thick, 5 inches in diameter, and 10 inches long. The pipe was filled to a depth of 9.2 inches during vibration.

The following discussion of the dynamic pressure-measuring system used throughout this report is given to clarify the test data. (See also Reference 1.)

a.   Description of Dynamic Pressure Measuring System

Dynamic pressure transducers and associated charge amplifiers manufactured by the Kistler Instrument Company were utilized for evaluation of dynamic pressure phenomena. Dynamic pressure is defined as the high-frequency true variation of pressure with time about a constant or slowly varying static pressure level. (See Figure 42.) Although static pressure levels are also sensed by the pickup, these are electronically compensated such that only dynamic data are monitored.

The Model 601A transducer used has a natural frequency of 140,000 cps, and a pressure range of 0.1 to 3000 psia. This transducer, used with the Model 568 charge amplifier, was capable of frequency responses between 2 and 28,000 cps. Signal errors, due to mechanical vibration of the pickup, are negligible and can be neglected.

The transducer is so constructed that, as pressure is applied to the diaphragm, the quartz crystal within the pickup is stressed, generating a charge proportional to the pressure. The charge amplifier sensing this charge creates an output voltage that can be moni-

62

Report No. 8230-933007
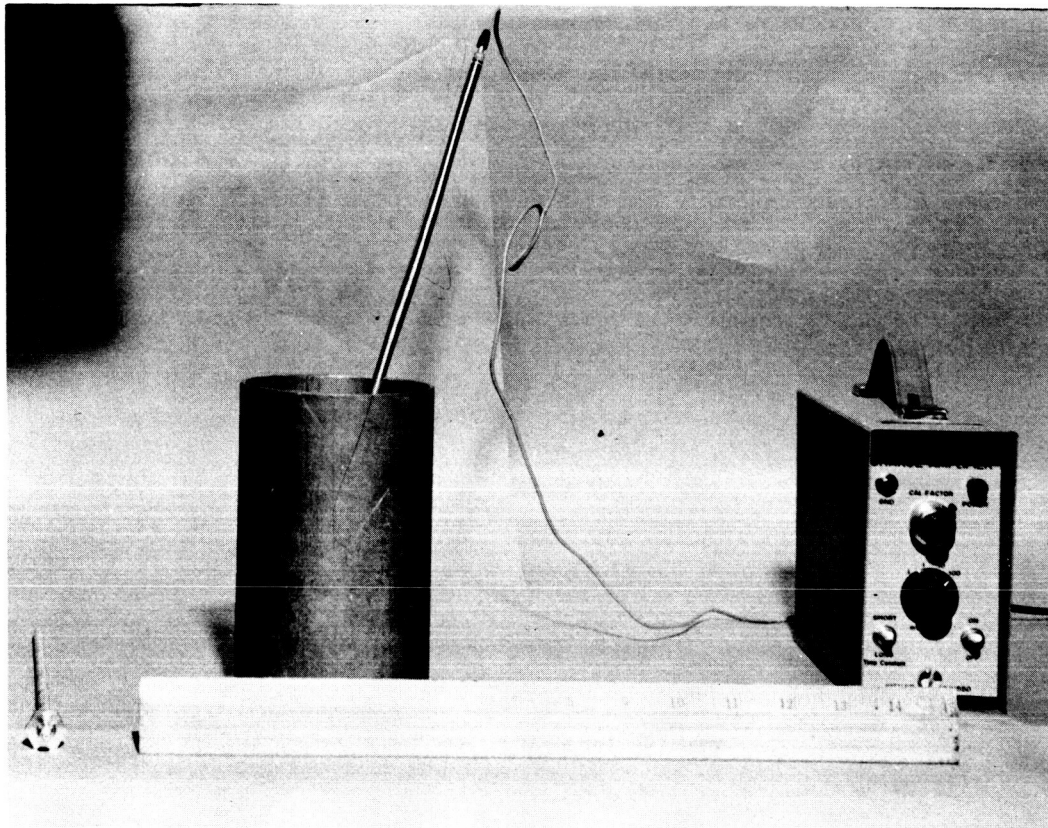
Figure 41. Dynamic Pressure Probes and Rigid Pipe
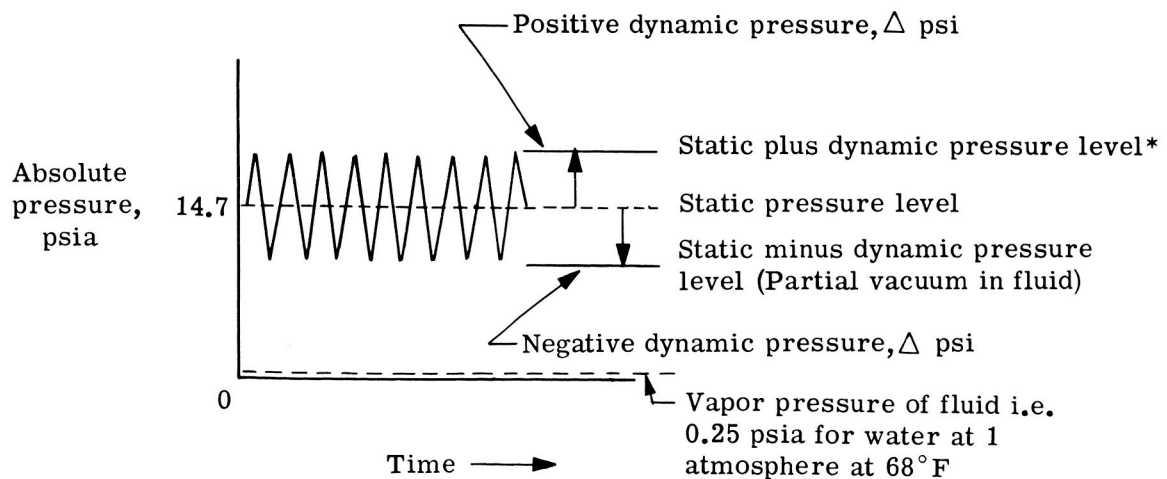
Figure 42. Definition of Dynamic Pressure

tored on an oscilloscope or vacuum tube voltmeter, or recorded on magnetic tape for subsequent reduction or plotted on a X-Y recorder at the test site for immediate analysis. Since the charge amplifier input circuitry contains resistors and capacitors directly connected to the transducer, the charge on the transducer crystal will discharge at a rate determined by the RC time constant of this circuitry. If a calibration or test measurement is being made, the two-position selector switch on the face of the amplifier is set for either a long time-constant (approximately 1000 sec) or for a short time-constant (approximately 1 sec).

The transducer is calibrated by applying a static calibration pressure to the transducer diaphragm, with the selector switch in the long time-constant position. The charge amplifier output is monitored on an oscilloscope. If the system is operating properly, the amplifier output will not decay for an appreciable time and the magnitude of the resultant oscilloscope trace deflection can be accurately measured. After venting the calibration pressure, and without altering the amplifier gain, a 60-cps calibrate voltage, measured on a vacuum tube voltmeter is applied to the calibration signal jack at the back of the amplifier. This voltage is adjusted so that the amplifier output results in a peak-to-peak oscilloscope trace deflection equal in magnitude to the deflection corresponding to the calibration pressure. This calibrate voltage, measured in millivolts RMS, represents the transducer output signal with the transducer subjected to a dynamic pressure of peak-to-peak value equal to the calibration pressure level. The transducer sensitivity in $\frac{MV\text{-}RMS}{psi\ peak\text{-}to\text{-}peak}$ is determined by $\frac{V}{P}$ where V equals calibrate voltage in MV-RMS and P equals static calibrate pressure in psi. By dividing this sensitivity by a factor of two, an output sensitivity in $\frac{MV\text{-}RMS}{+\ psi}$ is derived.

After calibration, the selector switch is set at the short time-constant position preparing the system for dynamic pressure measurements. For test measurements, a transducer/charge amplifier/recorder system calibration is effected by inserting a known calibrate voltage at the calibrate signal jack of the charge amplifier and measuring the corresponding recorder indication. Since the transducer sensitivity is known, the calibrate voltage represents an equivalent transducer pressure to stimulus. A calibration of recorder output in terms of transducer pressure input is thereby established. In this short time-constant position, static charges on the transducer crystal are dissipated within a few seconds and dynamic pressures, in the 2 to 28,000 cps range, can be effectively measured, with static pressures producing no effect on the output signal.

Test results plotted on Figure 43 show that dynamic pressure varies linearly with depth. Note that, as the base falls away from the liquid, a partial vacuum is indicated. The magnitude of this pressure variation at 2g input, 9-inch depth, was 0.64 psi; this can be calculated by $p = h \rho g$, where p = 9 in. x 0.0362 lb/cu in. of water x 2g = 0.64 psi. Varying the g-level, the frequency of excitation between 50 to 500 cps, or measuring at partial depths, did not change the predictable results; i.e., a linear relationship still existed within the instrument calibration accuracies.

2. Nonrigid Pipe Tests

The 5-inch diameter single-ply test bellows simulating a nonrigid pipe was vibrated as shown in Figure 44. The upper plate was removed to facilitate probing inside the bellows. A liquid mode was obvious at 123 cps because at first, liquid spray occurred, then the free surface erupted similar to a drinking-water fountain. The pressure variations within a bellows are rather dramatic, especially when one inserts his hand into the vibrating liquid.

Report No. 8230-933007

O Nonrigid Pipe (bellows with head grounded)
△ Rigid Pipe
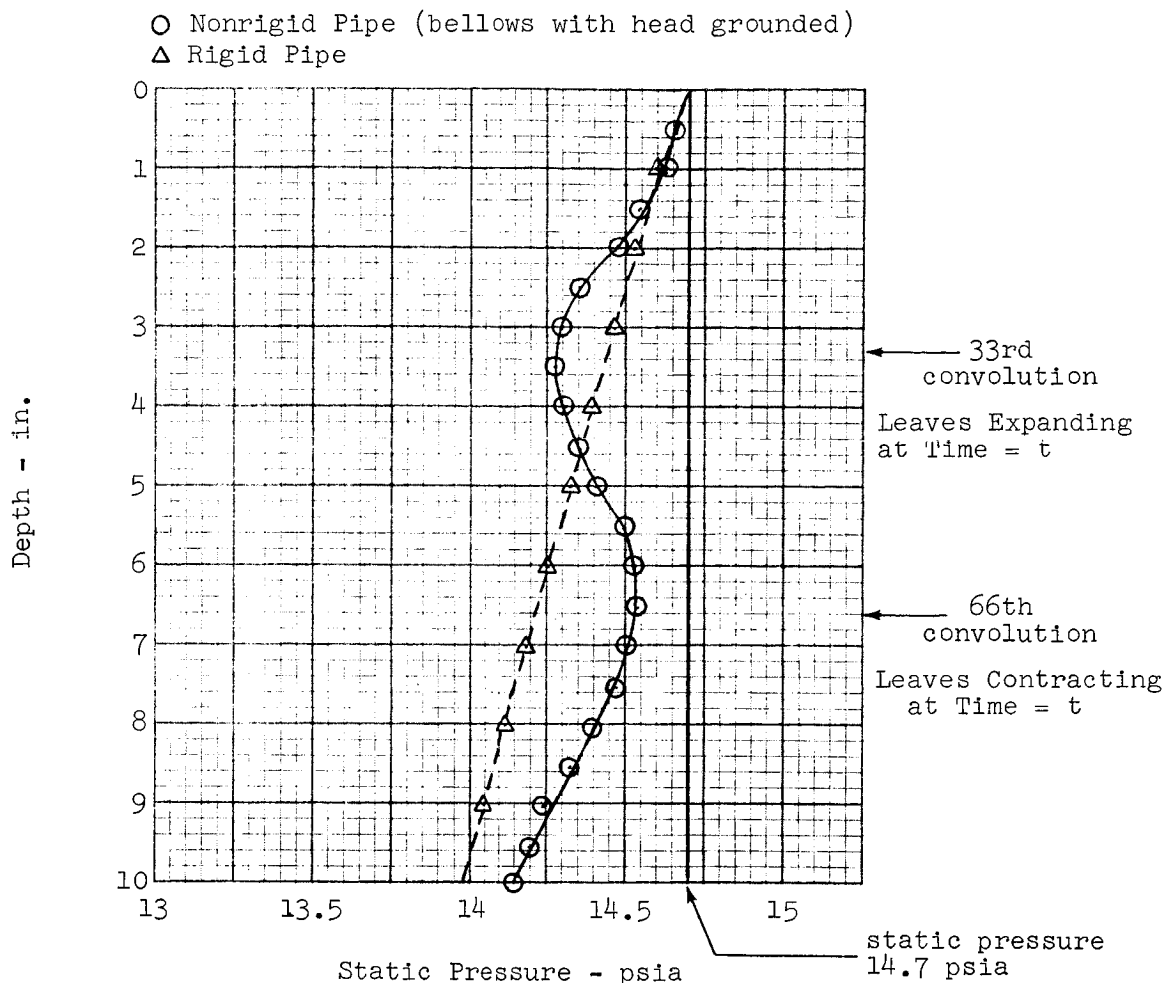
Figure 43. Comparison of Dynamic Pressure vs Depth for Rigid and
Nonrigid Pipes at 120 cps
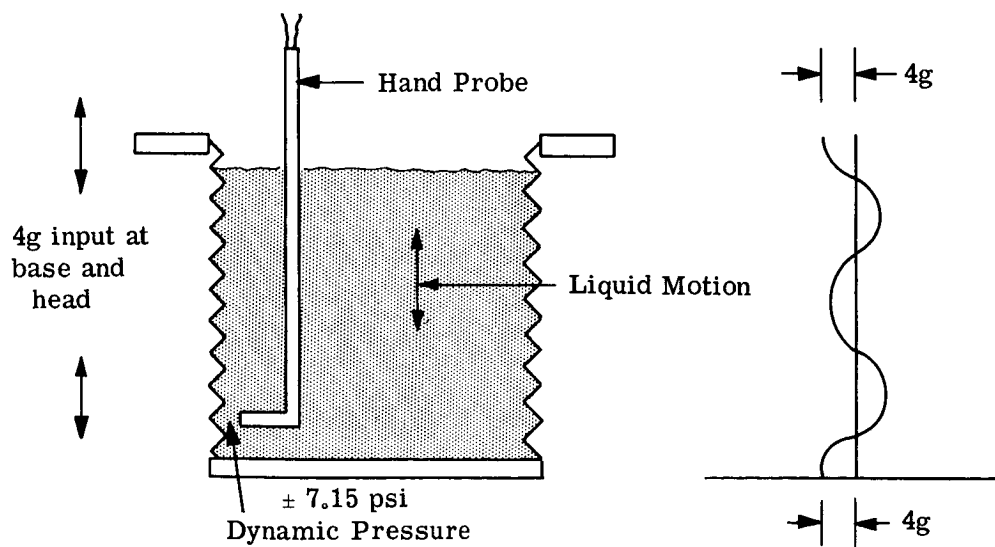
Figure 44. Lowest Liquid Mode Resonance at 120 cps with Head Free

Qualitatively, one might compare this prickley, tingly feeling to the sensation of touching an open electric circuit. Replacing the lost water and lowering the frequency to 120 cps, the bellows depth was probed to determine the pressure fluctuations at 4g input levels. A value of ±7.15 psi was read at the bellows head, which is 10 inches in depth from the free surface. Notice that the water, bellows base, bellows head, and convolutions are vibrating as illustrated in Figure 44.

Next, the head was mechanically grounded to the vibrator frame such that only the bellows convolutions were driven by the input base as shown in Figures 45 and 46.
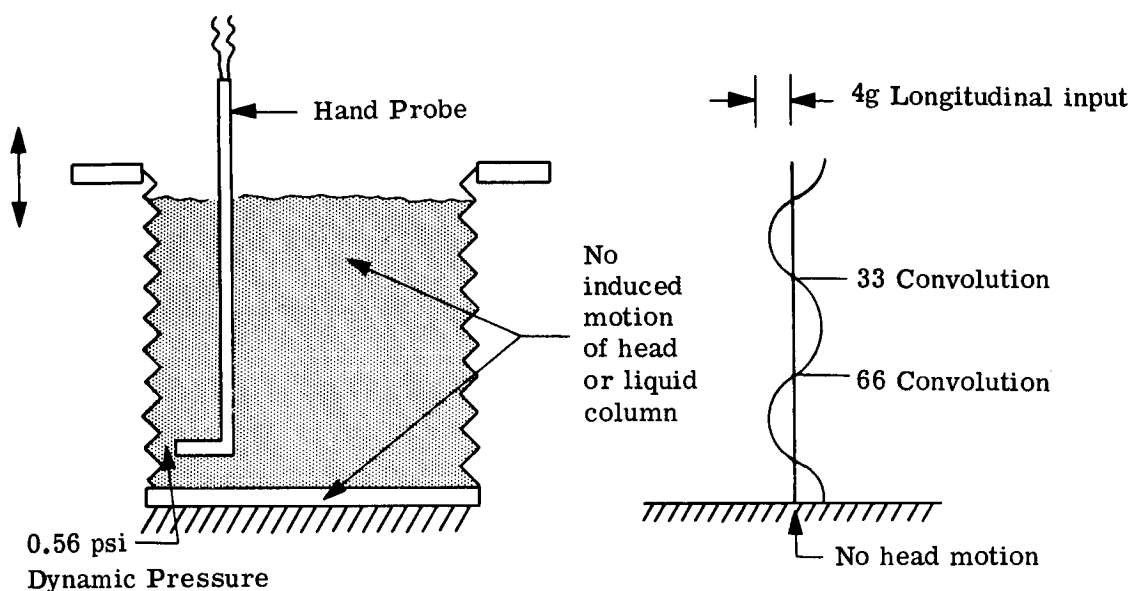
Figure 45. Lowest Liquid Mode Resonance at 82 cps with Head Grounded

This experiment showed that, although no body force is present since the liquid column is not being vibrated, an oscillatory pressure of ±0.56 was measured at the grounded head. This is most likely caused by a change in pitch that squeezes the convolutions together. In Figure 43, notice at the 33rd convolution that the leaves are expanding and the static pressure is less than at the 66th convolution where the convolutions are contracting, neither follows a straight line or linear distribution of pressure from the free surface at the bellows base. Probing across the head diameter also showed ±0.1 psi difference from convolutions to center when the head was grounded, as compared to no change when the head was free to vibrate. A further point to note is that 0.56 psi due to pumping, plus 1.45 psi due to body forces does not equal the 7.15 psi. Some, and perhaps all the difference may be due to the lateral bellows movement which rocks the convolutions, thereby pumping additional liquid out from the convolutions.

Next, the single-ply bellows was vibrated with the upper plate attached to the bellows base thereby closing up the bellows (Figure 61). The liquid mode at 67 cps was found to be rather nonlinear, i.e., the pressure varied with time, with a fixed vibrator setting of 2g. To overcome this difficulty the vibrator was set at 61 cps, which is below the unstable range of 63 to 70 cps. Probe measurements from bellows base to head ranged from 3.5 to

Report No. 8230-933007

Figure 46. Method of Grounding Head to Detect Convolution Liquid Pumping

0.44 psi. The pressure in the center of the liquid column was the same as the pressure 0.10 inch from the liquid column/convolution inner weld bead tips.

<div align="center">CAUTION</div>

> Even with careful bleeding, the liquid mode
> frequency will be slightly different from test
> to test. This accounted for the liquid mode
> frequency at 67 instead of 69 cps as shown in
> Figure 64.

3. Liquid Mode Comparisons on Various Bellows Sizes

Concurrent with this NASA study, vibration tests were conducted with bellows used in the Gemini target system. This includes a 6-inch diameter elastic range bellows and a 10-inch diameter oxidizer and fuel plastic range bellows. A summary of these bellows data and test theory calculations is presented in Table 2. A sample liquid mode calculation is given in the following for the 5-inch-diameter single-ply bellows. Accordion and lateral modes were calculated using methods developed in Reference 1. Bellows formulas for these major response modes are summarized in Table 3.

TABLE 2

BELLOWS DESCRIPTION AND TEST RESULTS

Description	4-inch	5-inch Single-ply	5-inch Double-ply	6-inch	7-inch	10-inch Oxidizer	10-inch Fuel
Outside Diameter, in.	4.3	4.750	4.745	5.255	7.125	9.89	9.89
Inside Diameter, in.	3.644	4.086	4.080	3.750	6.125	8.89	8.89
Span, in.	0.328	0.332	0.332	0.752	0.50	0.50	0.50
Leaf Thickness, in.	0.004	0.006	0.012	0.007	0.006	0.006	0.006
Number of Convolutions	100	100	100	65	135	95	149
Material, Stainless Steel	410	347	347	AM350	321	347	347
Material test range	Elastic	Elastic	Elastic	Elastic	Plastic	Plastic	Plastic
Total effective spring rate during vibration, lb/in.	10.8	18.4	41.4	8.4	15	22.0	14.05
Spring rate/convolution during vibration, lb/in.	1080	1840	4140	546	2025	2090	2090
Test liquid in bellows	Water	Water	Water	Water	Water	Methylene Chloride	Water
Test gas outside bellows	Air	Air	Air	Air	Air	Nitrogen	Nitrogen
Bellows weight, lb	1.00	1.81	3.55	2.85	5.18	5.46	8.35
Head Weight, lb	1.47	0.76	0.69	2.74	2.4	1.36	1.36
Trapped liquid weight, lb	0.82	0.83	0.83	1.51	7.6	10.42	11.7
Compressed length, in.	-	2.5	5.0	1.95	3.75	2.51	3.94
Free length after compression, in.	8.75	5.57	8.4	8.14	19.12	11.4	17.97
Extended length, in.	12	12	12	10	40.5	31.34	44.7
Vibration length, in.	10.7	10	10	8.3	39.8	27.8	43.7
Vibration pitch, in.	0.107	0.10	0.10	0.13	0.295	0.293	0.293

Type Mode	Identification	4-inch Calc.	4-inch Test	5-inch Single-ply Calc.	5-inch Single-ply Test	5-inch Double-ply Calc.	5-inch Double-ply Test	6-inch Calc.	6-inch Test	7-inch Calc.	7-inch Test	10-inch Oxidizer Calc.	10-inch Oxidizer Test	10-inch Fuel Calc.	10-inch Fuel Test
Accordion	Fundamental	23.90	23.75	25.9	26	30.2	31.5	13.6	16.0	10.30	11.0	11.6	*	8.20	8.3
	3rd Harmonic	71.70	71.00	77.7	81	90.6	100.0	40.9	56.0	30.70	34.0	34.7	*	24.60	25.7
	5th Harmonic	119.50	117.50	130.0	133	151.0	167.0	68.0	**	50.60	56.0	57.8	*	41.00	41.8
	7th Harmonic	167.00	178.00	181.0	184	211.0	235.0	95.2	**	72.10	**	80.9	*	57.40	58.5
	9th Harmonic	*	*	233.0	232	272.0	300.0	*	*	*	*	*	*	*	*
Liquid	Fundamental	80.50	87.00	85.3	69	99.2	76.0	26.9	34.0	41.30	39.5	44.8	*	33.40	46.0
	3rd Harmonic	241.50	**	256.0	**	298.0	**	80.7	**	117.80	119.0	134.1	110.0	100.20	129.0
	5th Harmonic	402.50	**	427.0	**	496.0	**	135.0	**	182.20	191.0	224.0	**	167.00	208.0
Lateral	Fundamental	12.25	16.20	17.0	20	21.2	24.0	11.5	17.0	0.62	**	4.6	*	1.70	*
	3rd Harmonic	67.40	61.00	93.5	72	116.5	93.0	63.2	**	3.41	**	25.3	*	9.35	*

Notes: * - Not obtained
        ** - Not present
        All calculations and test frequencies are in cps

TABLE 3

SUMMARY OF BELLOWS FORMULAS

Bellows Modes	Frequency - cps
Longitudinal accordion	$f_a = \dfrac{n}{2} \sqrt{\dfrac{K_A \, g}{W_t + W_m}}$
Longitudinal liquid	$f_L = f_a \, f(ka) \sqrt{\dfrac{1}{\dfrac{1}{2}\left(\dfrac{d_o^2}{d_i^2} - 1\right)}}$ where $f(ka) = \sqrt{\dfrac{4}{ka\left[\dfrac{I_o(ka)}{I_i(ka)}\right]}}$
Lateral	$f_\ell = \dfrac{A_N}{2\pi} \sqrt{\dfrac{K_A \, r^2 \, g}{2L^2 (W_t + W_m + W_i)}}$

a	=	inside radius of liquid column, assumed as $\dfrac{d_i}{2}$
A_n	=	numerical constant 22.0, 121, 298.2 ...
d_i	=	inside diameter of bellows, in.
d_o	=	outside diameter of bellows, in.
$I_o(\ )$	=	modified Bessel function of the first kind zero order
$I_i(\ )$	=	modified Bessel function of the first kind first order
g	=	386
f(ka)	=	function of bellows length and inside diameter
k	=	$\dfrac{n\pi}{L}$
K_A	=	longitudinal total effective spring rate of all convolutions, lb/in.
L	=	length of bellows, in.
n	=	mode number and numerical constant of 1, 3, 5 . . .
r	=	effective radius of bellows, assumed as $d_o/2$
W_i	=	weight of liquid inside of bellows, lb
W_m	=	weight of convolutions, lb
W_t	=	weight of liquid trapped in convolutions, lb

Note:
Approximate f(ka) values are plotted in Figures 38 and 39. Exact values are compiled using a Bessel function table.

Report No. 8230-933007

Where: $a = \dfrac{d_i}{2} = 2.043$

$k = \dfrac{n\pi}{L} = \dfrac{(1)(3.14)}{10} = 0.314$

$ak = 0.642$

f (ka) is obtained from Figure 38 as 0.614 or from Table II, page 699 of Reference 16.

$f_a = 25.9$ cps, calculated

$f_L = (25.9)(0.614)\dfrac{1}{\sqrt{\dfrac{1}{2}\left[\dfrac{(4.75)^2}{(4.086)^2} - 1\right]}}$

$f_L = 85.3$ cps liquid mode frequency at vibration length of 10 inches shows fair agreement with a test value of 69 cps.

F. METHODS USED TO ATTENUATE THE LIQUID MODES

1. Bell Model 8250 (Agena/Gemini) Development Program

Vibration tests were conducted at Bell Aerosystems on a Model 8250 fuel bellows (10-inch diameter) to study the effects of external pressures and reduced pitches. This bellows was filled with water to an extension of 0.30 inch pitch (43.7 inches long) and enclosed in a pressurized metal tank. The volume of the liquid in the bellows was approximately 2700 in.^{3}. The volume occupied by the pressurizing nitrogen gas was approximately 450 in.^{3}. Sinusoidal and random vibration, along with shock inputs, were applied in both longitudinal and lateral directions. The longitudinal axis of the tank was maintained parallel to gravity in all tests except the lateral shock tests.

Figure 47 shows the response of a dynamic pressure pickup mounted inside the bellows at the base during longitudinal vibration tests. Both the fundamental liquid mode at 46 cps and its 3rd harmonic at 129 cps are reduced in magnitude and frequency when 200 psig is applied outside the bellows. Replacing the water with isopropanol resulted in the plots shown on Figure 48, which also clearly show attenuation with pressure. Head acceleration plots, not presented here, corroborated the dynamic pressure data. Piston type head motion is possible because there will be a sinusoidal or spike-shaped pressure force acting in the liquid mode. In constrast only small dynamic pressure forces are acting in the accordion mode and incompressible liquid effect prevents any relative head to base motion.

The data presented in the upper curve of Figure 49, taken with zero external pressure on the bellows, shows that the fundamental liquid mode increases from 46 to 65.5 cps with a pitch decrease from 0.30 to 0.10 inch. However the fundamental accordion mode decreased from 8.35 to 6.5 cps for the same pitch decrease.
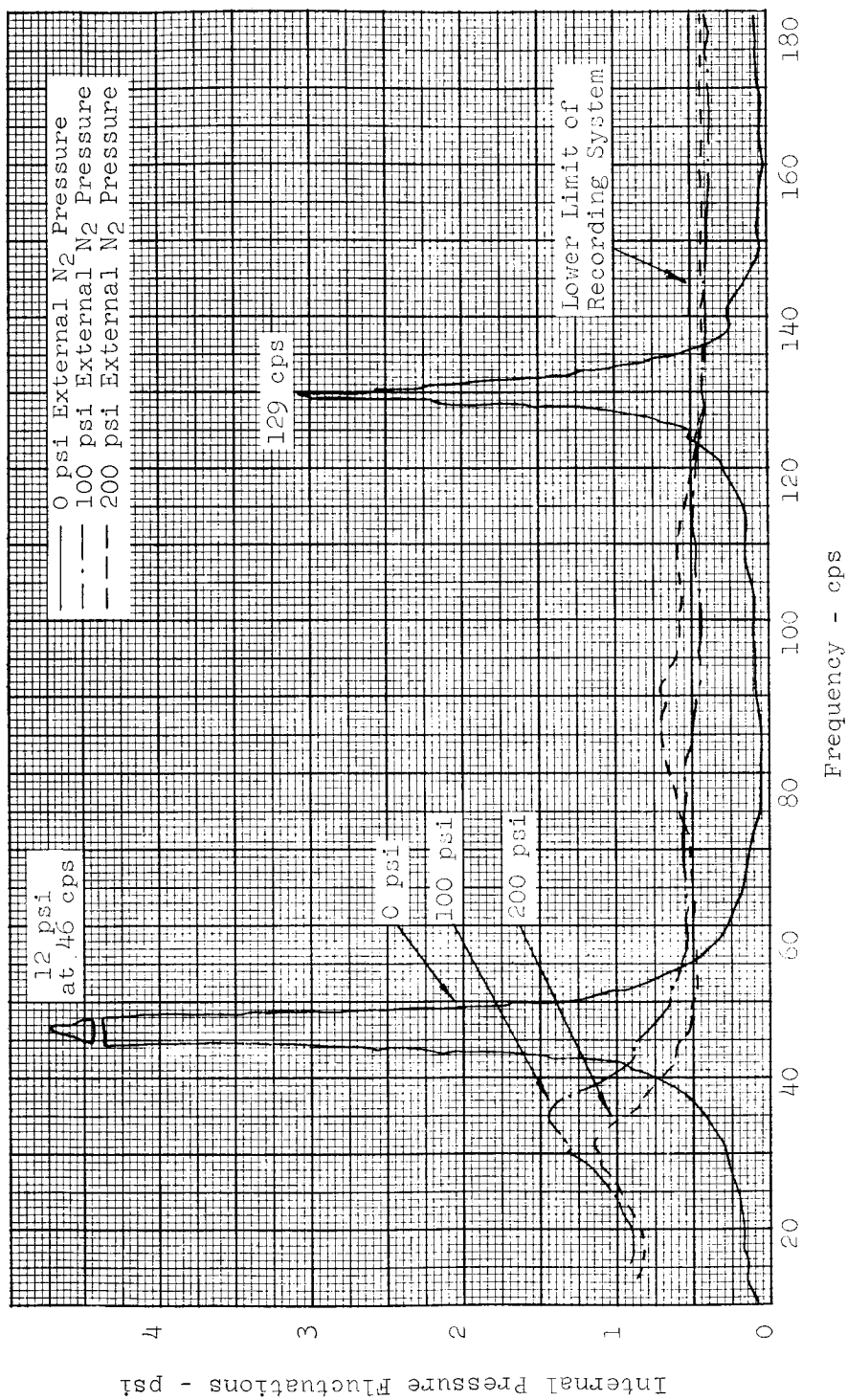
Figure 47. Water Dynamic Pressure Fluctuations at Base of 10-inch Diameter
Bellows During Vibration Scans of 0.5g
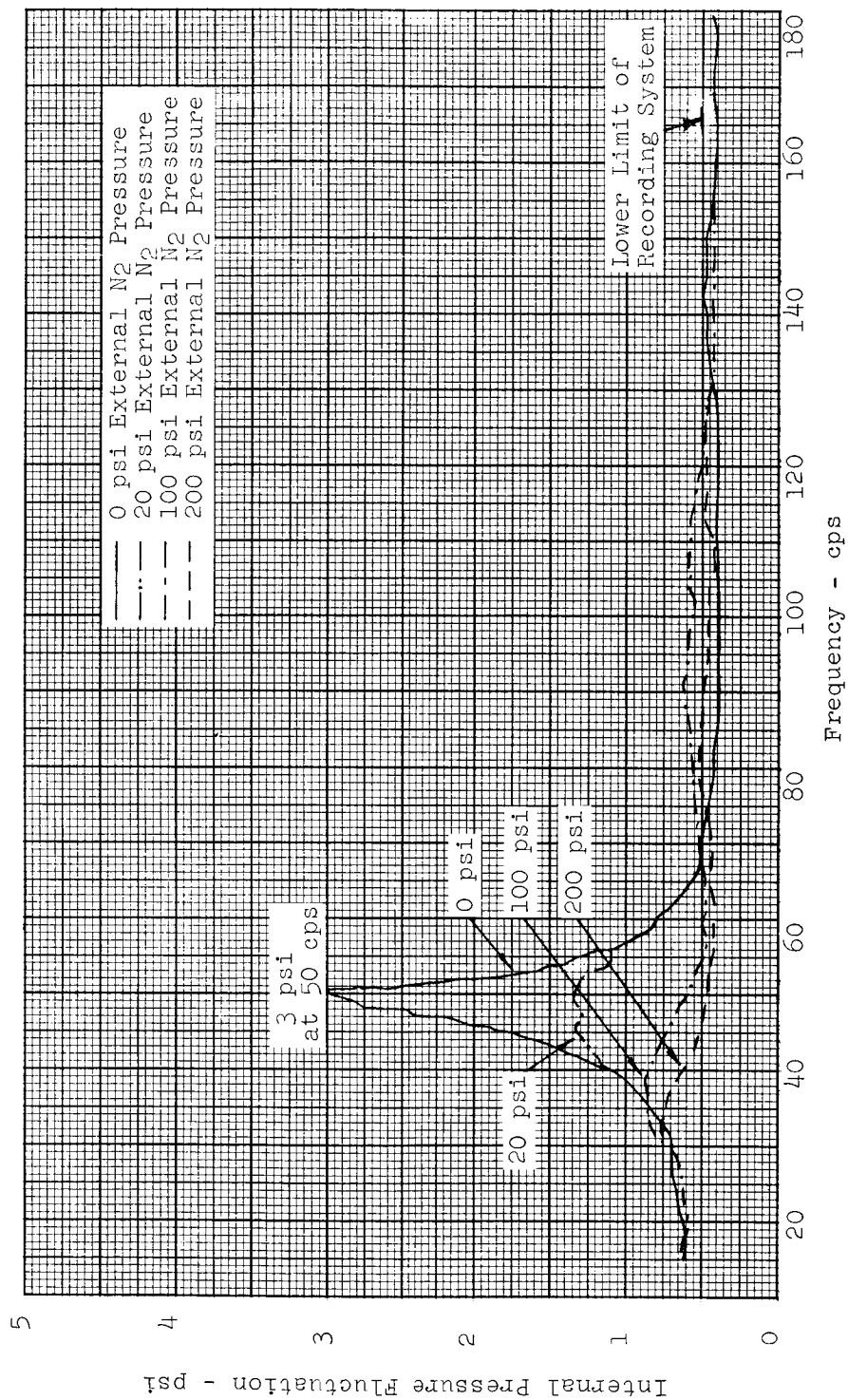
Figure 48. Isopropanol Dynamic Pressure Fluctuations at Base of 10-inch Diameter Bellows During Vibration Scans of 0.5g
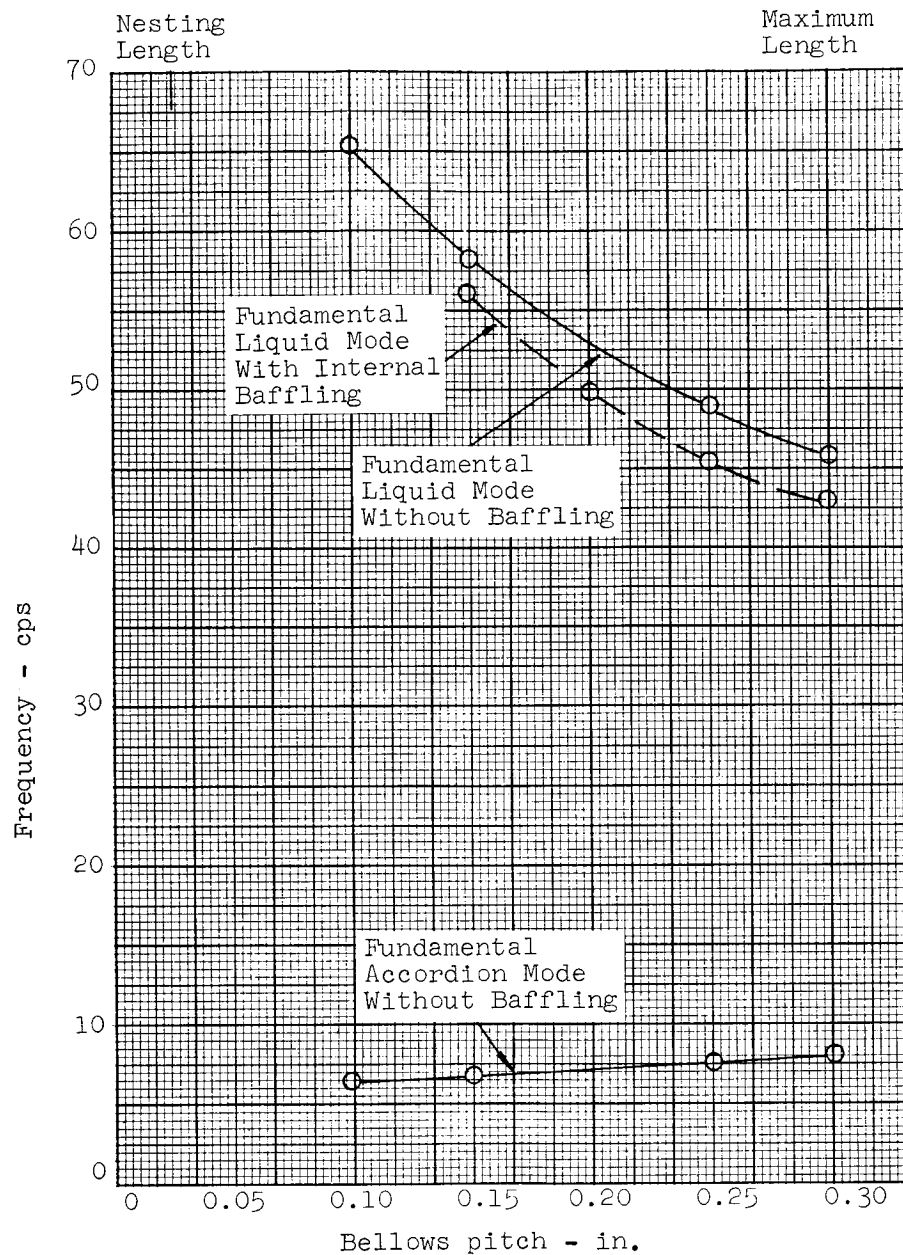
Figure 49. Reduced Pitch Effect on Liquid and Accordion Modes of 10-inch Diameter Bellows

Figures 50 and 51 show the revised descriptions of bellows convolution motion in the accordion and liquid modes respectively. These replace the description given in Reference 1. The lateral convolution tip motion noted on Figure 51 for the liquid mode case can be compared with "snaking" of the bellows in the static case, i.e., an internal pressure buildup and decay. Figure 52 illustrates that the longitudinal liquid mode can also be excited (but with less severity) with lateral vibration inputs. This figure also describes how much attenuation was obtained when a gas entrainment device (balloon) was placed inside the bellows.
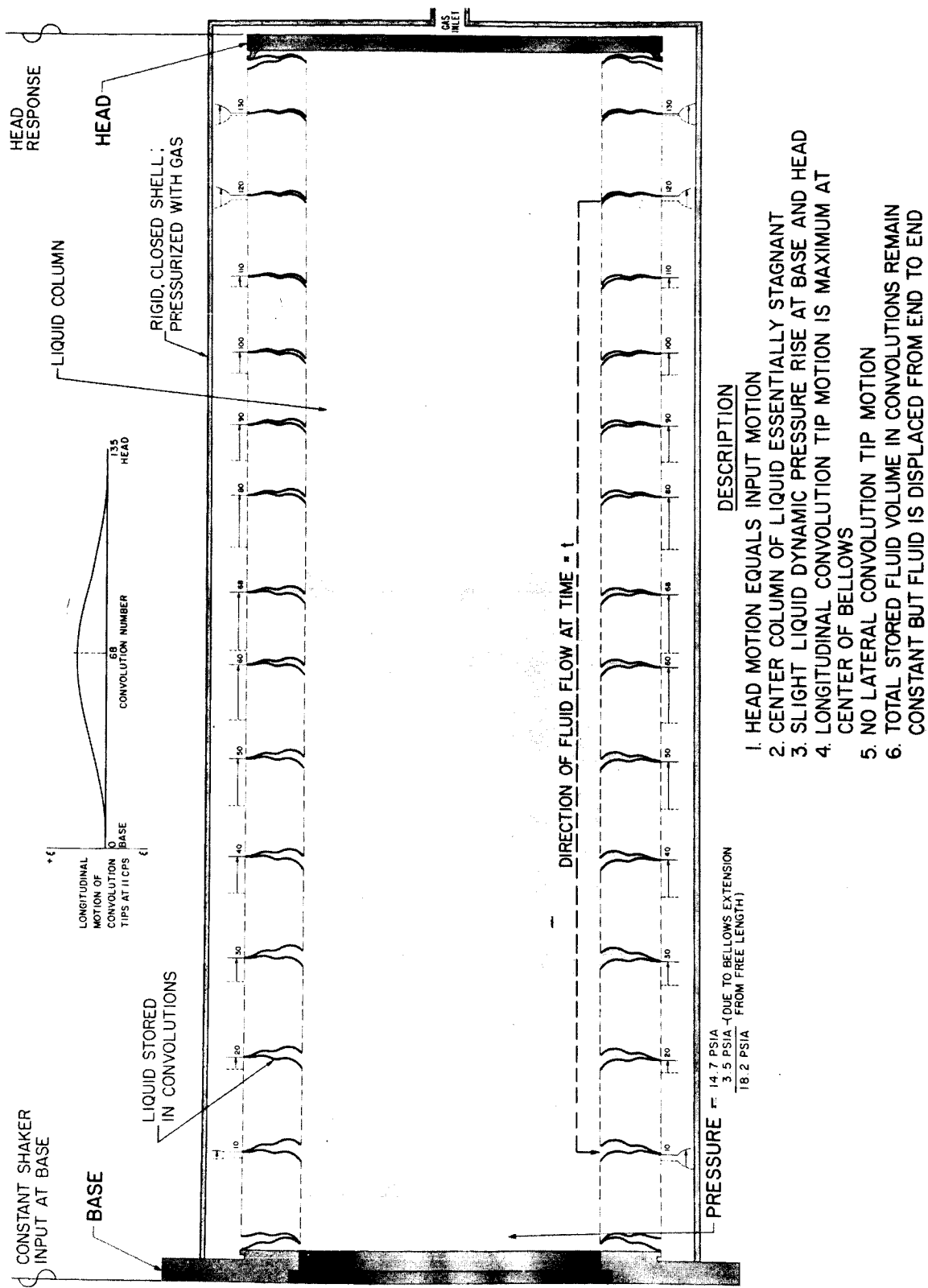
Figure 50. Bellows Fundamental Accordion Mode at 11 cps

DESCRIPTION

1. HEAD MOTION EQUALS INPUT MOTION
2. CENTER COLUMN OF LIQUID ESSENTIALLY STAGNANT
3. SLIGHT LIQUID DYNAMIC PRESSURE RISE AT BASE AND HEAD
4. LONGITUDINAL CONVOLUTION TIP MOTION IS MAXIMUM AT CENTER OF BELLOWS
5. NO LATERAL CONVOLUTION TIP MOTION
6. TOTAL STORED FLUID VOLUME IN CONVOLUTIONS REMAIN CONSTANT BUT FLUID IS DISPLACED FROM END TO END
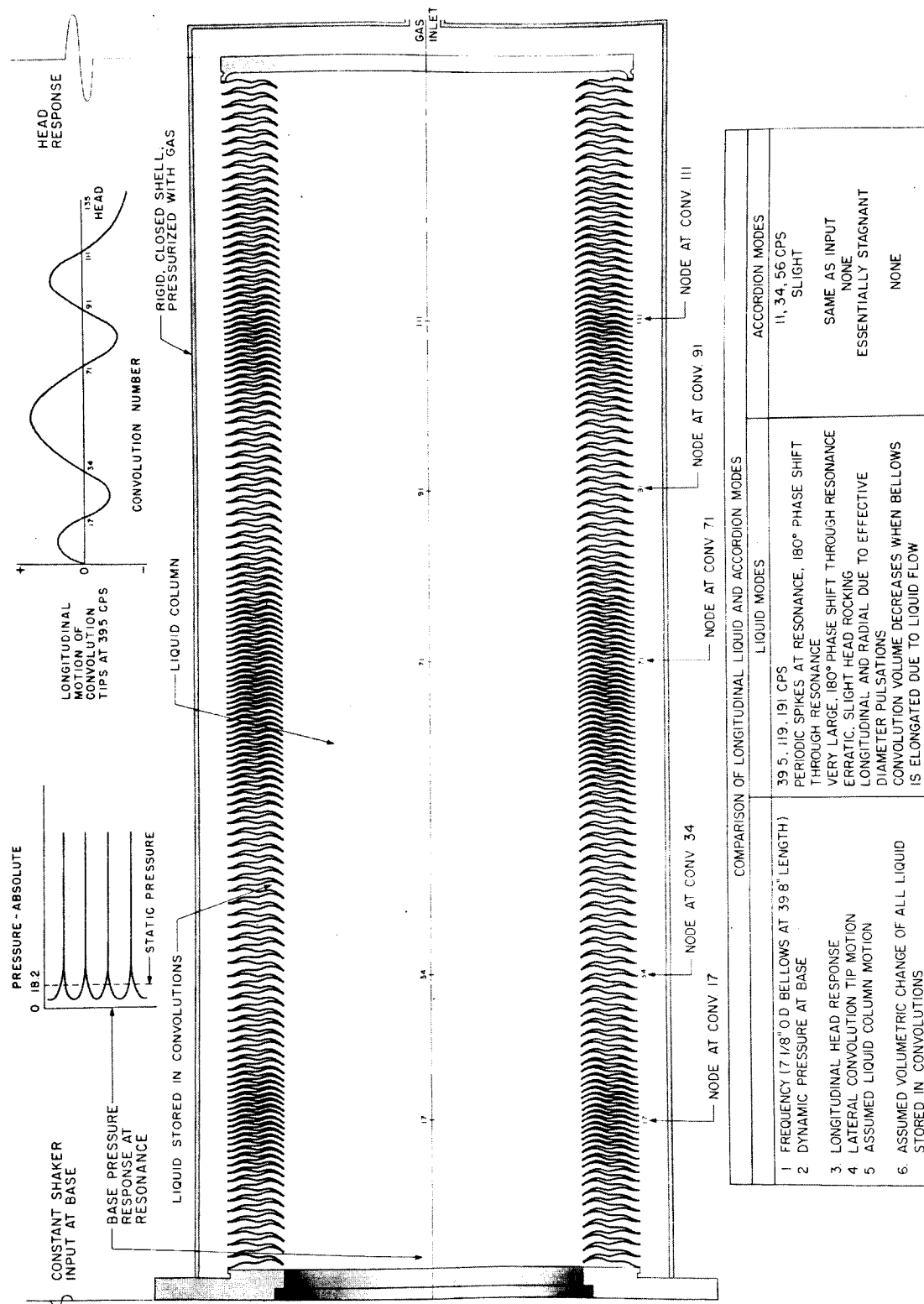
Figure 51. Bellows Fundamental Liquid Mode at 39.5 cps
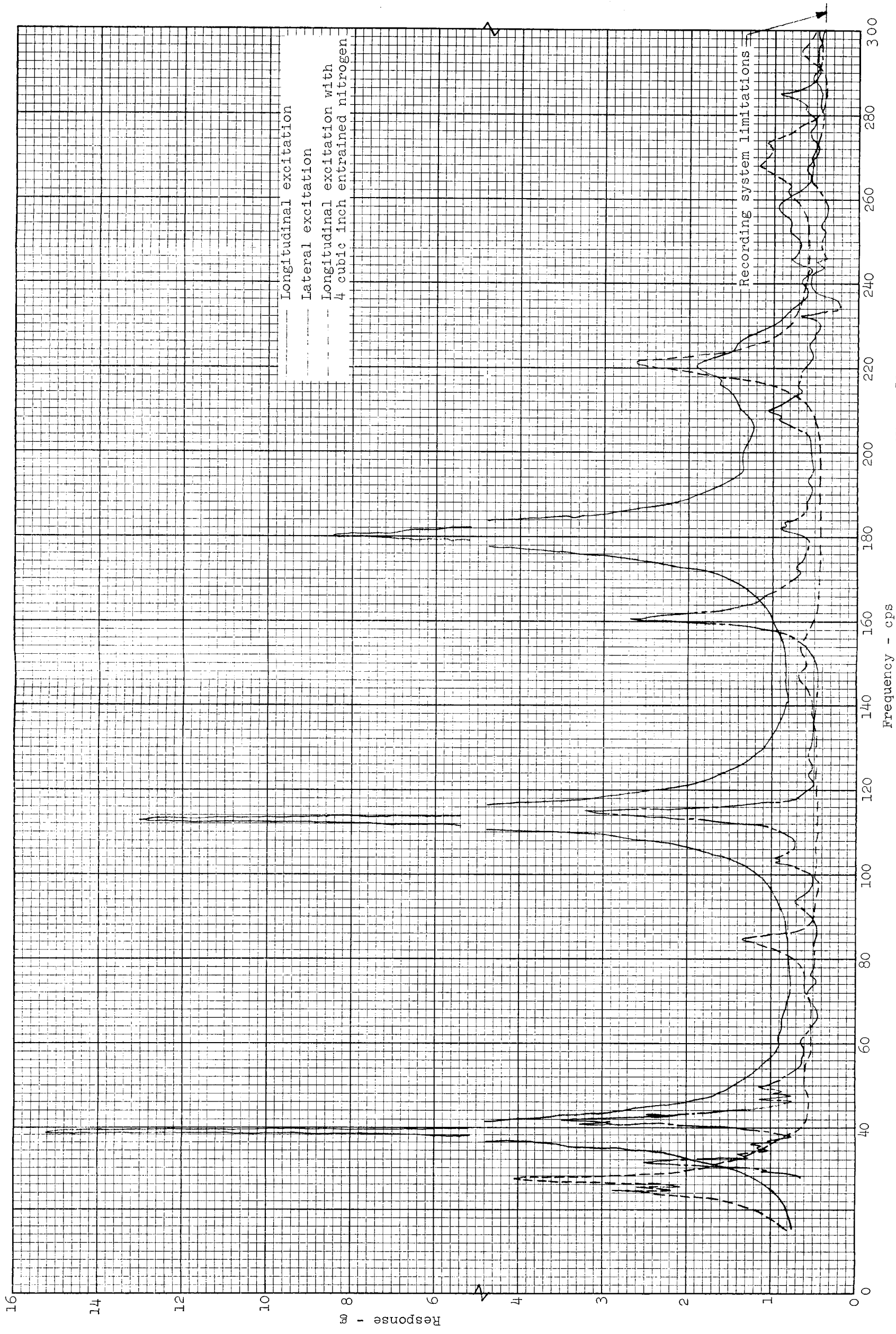
Figure 52. Longitudinal Head Acceleration Response at 1/2 g Base Input, 7-inch Diameter Bellows

77

Four other changes affect the liquid mode:

(1) An air entrainment device inside the bellows attenuates the dynamic pressure in much the same manner as external pressure.

(2) Reducing the external pressure (may be due to dissolved gases in propellant).

(3) A poor liquid bleed reduced the fundamental liquid mode frequency as much as 7 cps.

(4) Internal baffling reduced the liquid mode frequency 3 cps (see Figure 49).

During shock tests in the longitudinal direction, an internal dynamic pressure rise of 50 psi was recorded (with 200 psi applied outside the bellows) when a 40g, 8 millisecond, half sine wave input was applied. During longitudinal random vibration with an applied 0.07g²/cps input, a time-averaged dynamic pressure response of 0.21 psi²/cps with a peak value of 20 psi was recorded.

These vibration and shock tests were conducted with the bellows mounted within a thick boilerplate shell shown in Figure 53a. Additional tests were performed in a prototype shell as shown in Figure 53b.
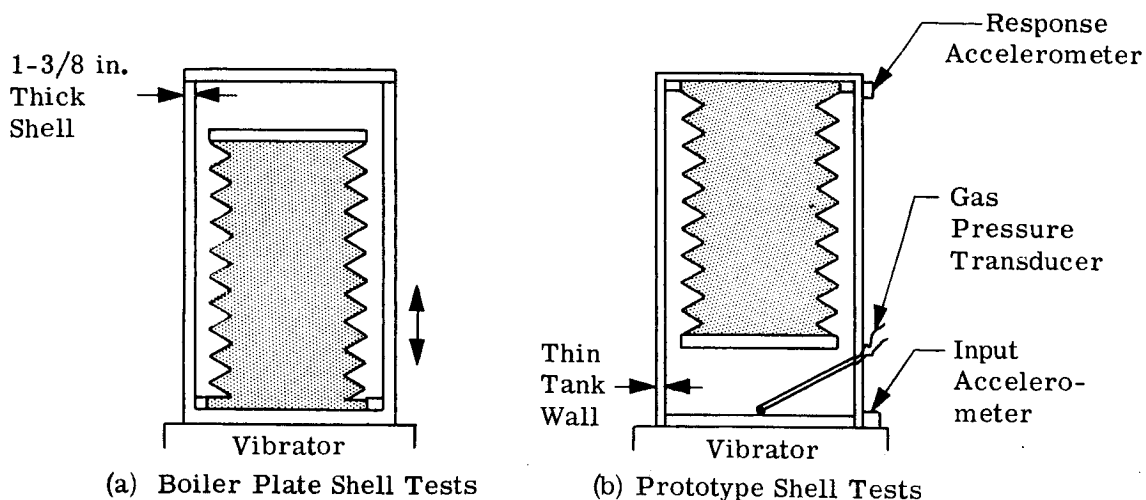
Figure 53. Comparison of Bellows Tank Test Setups

Data from these tests show that method (a) is preferred because the bellows base directly receives only the input vibration; in method (b), considerable shell amplification increases the amount of vibration affecting the bellows. It was also noticed that gas pressure oscillations occurred during vibration at the same frequency of liquid pressure and shell acceleration oscillations.

2. Bell Model 8247 (Agena/Gemini) Development Program

Vibration tests were also conducted at Bell Aerosystems on a 6-inch diameter bellows to determine its basic response and to study further its internal pressure distribution, see Figure 54. This latter investigation with various gases and liquids outside the bellows was made to provide data that would help explain why gas pressure attenuated liquid pressure and head motion in previous bellows tests.
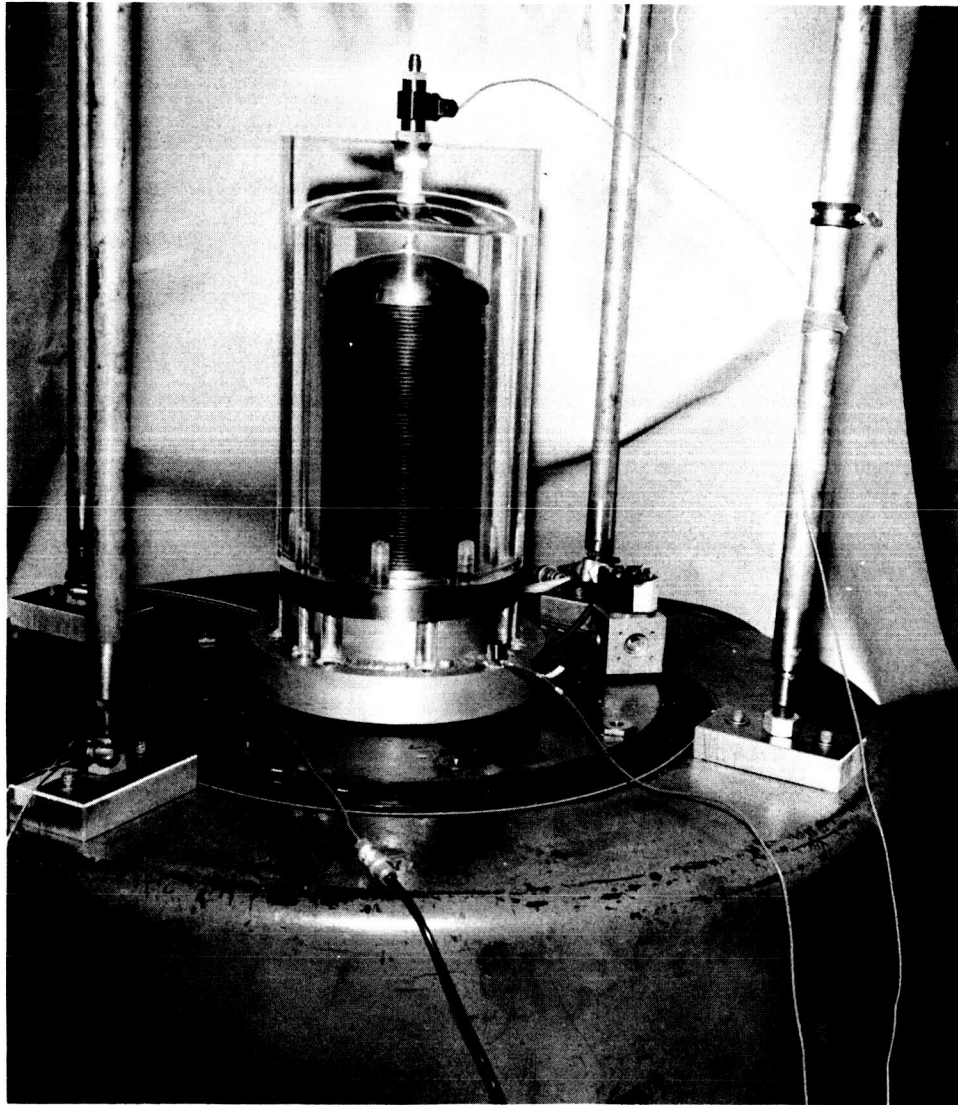
Figure 54. 6-inch Bellows in Upright Position

The fundamental liquid mode occurred at 34 cps when the bellows was upright as shown in Figure 54. Inverting the bellows, to determine any gravity influence as shown in Figure 55, caused the liquid mode to occur at 29 cps, with no change in the accordion mode frequency. At both frequencies, high-pressure spikes occurred at the base of the bellows similar to that shown in Figure 56. Notice that the static pressure is well above 0.25 psia (the vapor pressure cavitation value) of water. Below resonance or at resonance low g-input levels will produce a sinusoidal dynamic pressure response.
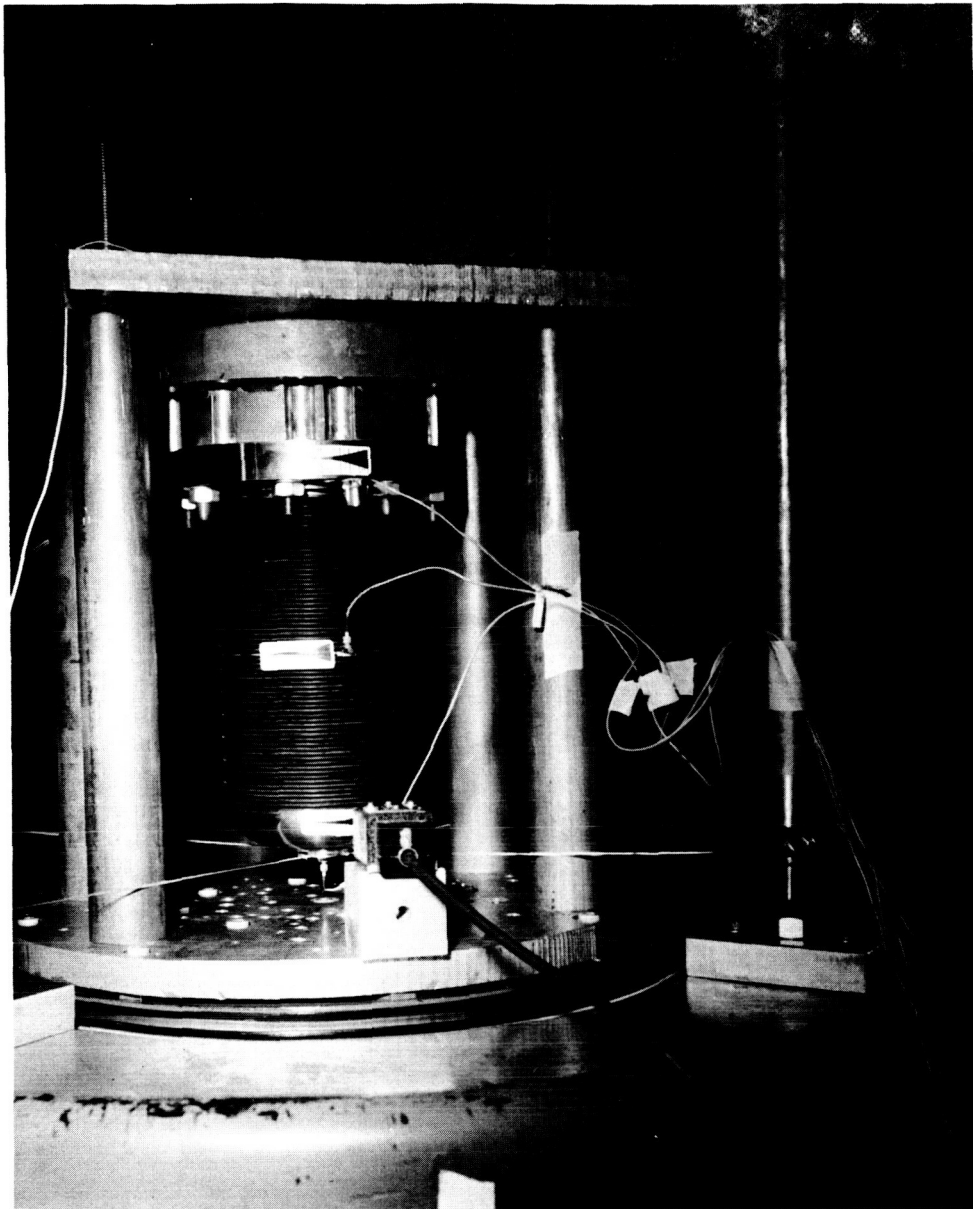
Figure 55. 6-inch Bellows in Inverted Position

       Water placed outside the bellows in the upright position almost completely dampened any internal liquid pressure fluctuations. Various gases were also placed outside the bellows and liquid dynamic pressures changed appreciably. Head response, which also reflects the magnitude of static pressure rise at liquid modes, decreased as follows at 0.5 g inputs: 32 to 1 with no plexiglass shell, 20 to 1 with metal shell in place, 12 to 1 with 40 psi nitrogen gas pressure, and 9 to 1 with 2.5 psia nitrogen pressure. The near vacuum drawn outside the bellows, expanded the dissolved air in the water and displaced the bellows head upward 0.20 inch. This dissolved gas would attenuate motion in much the same manner as the gas entrainment device.
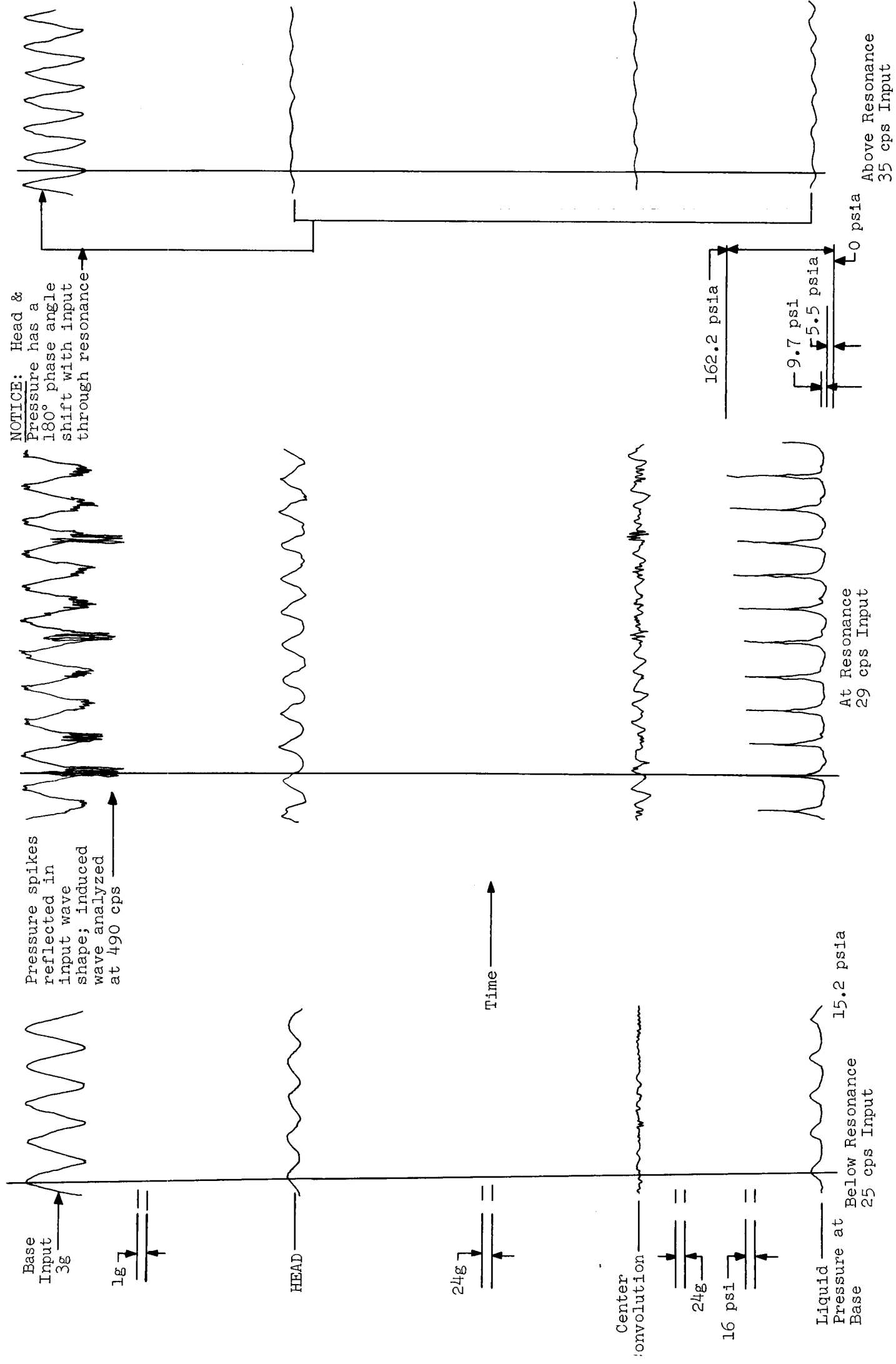
Figure 56. Liquid Mode Resonance of 6-inch Diameter Inverted Bellows

Various gas properties such as viscosity, bulk modulus, and density were compared with the test data. It appeared that only gas densities would fit the data at ambient and 40 psig conditions. Figure 57 shows a definite trend toward liquid mode attentuation with increased gas density.
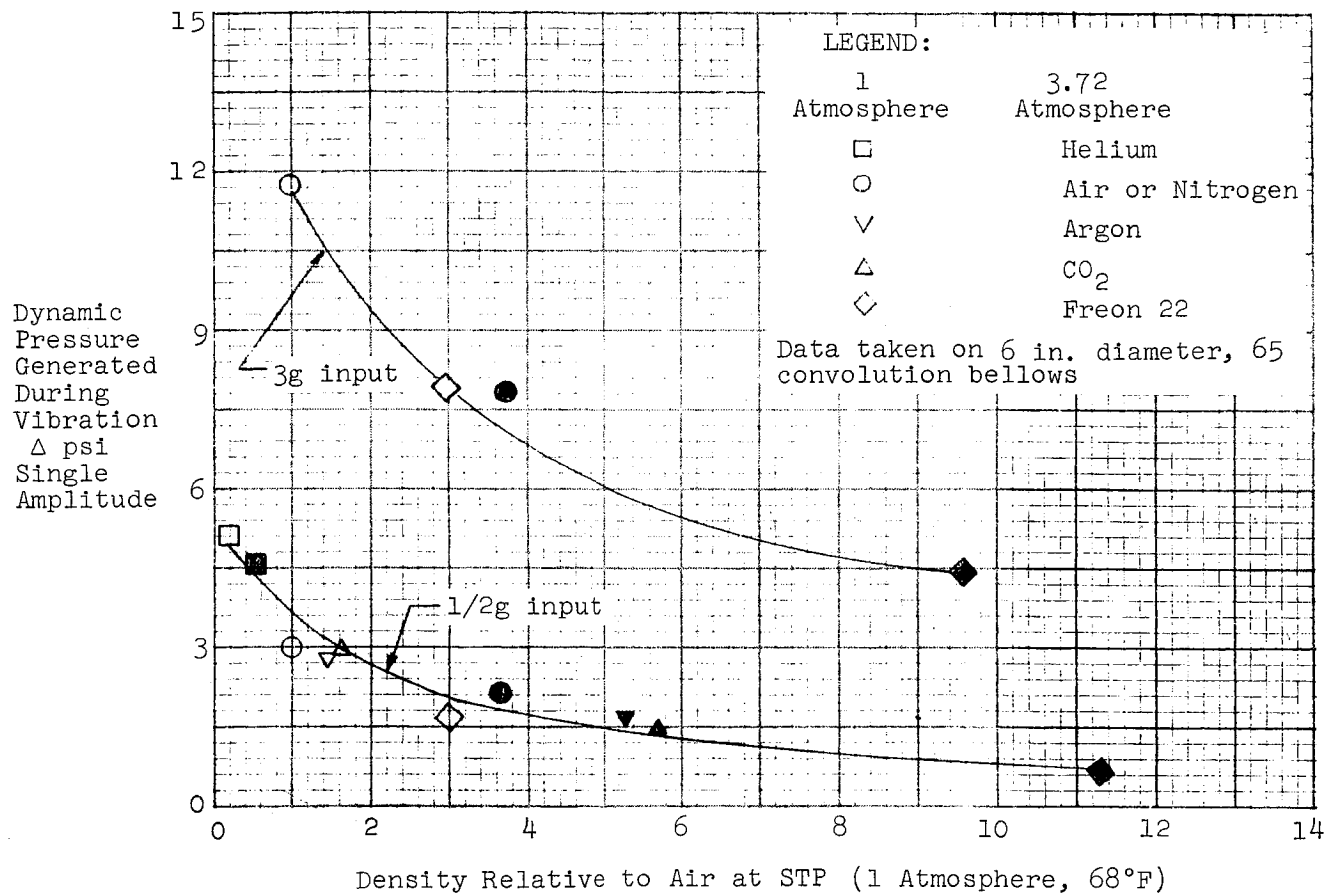
Figure 57. Suppression of Liquid Mode with Various External Gases

One possible explanation may be that a moving flat plate encounters forces proportional to:

$$F = \frac{1}{2} \rho \, v^2 s \, C_D$$

where:

ρ = gas density

s = projected area of plate

C_D = coefficient

v = velocity of plate
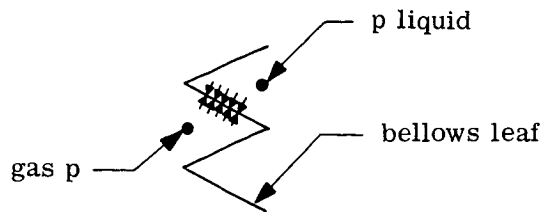
Increasing the gas density will decrease the liquid pressure by decreasing the leaf deflection or strain which was assumed proportional to the pressure generated in the liquid mode analysis.

The other possible explanation is that the equations of motions used in the liquid mode analysis should be applicable to the outside fluid by changing the value of the density, and with the stress in the convolutions being partitioned between the inside and outside fluids, hence the inside pressure is less.

G.   MULTI-PLY LEAF INVESTIGATION

Sinusoidal vibration tests were conducted at a constant g-level to compare the dynamic response of single-ply and double-ply bellows construction. In Figure 58 notice that the weld bead joins two leaf metal thicknesses in a single-ply bellows and four thicknesses in a double-ply bellows.
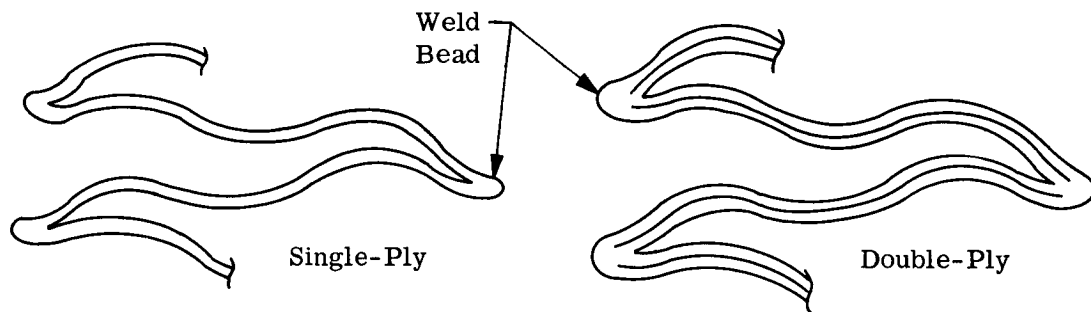
Figure 58. Comparison of Single-Ply and Double-Ply Bellows Construction

A photograph of the 5-inch diameter test bellows in the "as received" condition is presented in Figure 59; the physical properties are described in Table 2. Identical forming dies and the same material batch were used to make both bellows alike prior to welding.

Resonant frequencies and associated motion amplification or attenuation data were obtained to identify the principal bellows modes. These are the longitudinal accordion modes, the longitudinal liquid modes, and the lateral bending modes. These bellows were also used to study further the internal liquid behavior in conjunction with the liquid mode analysis described elsewhere in this report.

1.   Test Setup and Results

Initially, an experimental spring rate was obtained as shown in Figure 60 for each bellows at the length at which vibration was to be applied. These force-deflection

Double Ply Bellows   Single Ply Bellows
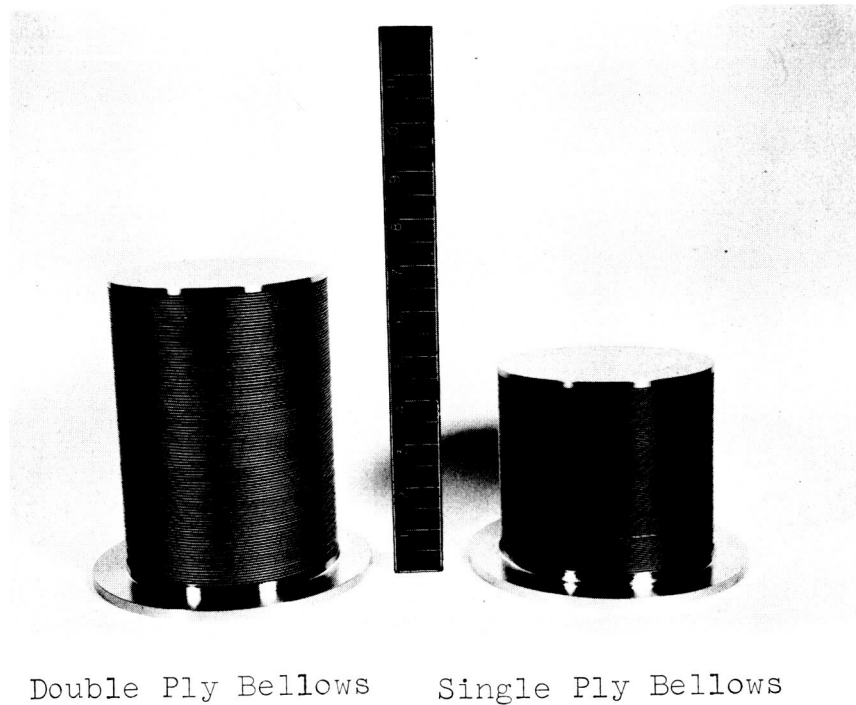
Figure 59. Double-Ply and Single-Ply Test Bellows in "As Received"
Condition

curves were obtained by reading decreasing internal pressures and converting this pressure
to extension force using the cross sectional area at the bellows mean diameter.

For vibration testing, Figure 61 shows a typical setup for the longitudinal direc-
tion. The summary of the test data presented in Table 4 was taken from the vibration
response data shown in Figures 62 through 65.

2. Discussion of Test Results

The spring rate of the double-ply bellows was 225% of the single-ply bellows;
two springs directly in parallel would yield a spring rate of 200%.

The amplification factor output/input for the double-ply bellows was greater in
the accordion, liquid and lateral fundamental modes. This was not expected since some
frictional damping should have existed between the plies. Since bellows failure is pro-
portional to convolution pitch change and internal pressure fluctuations, this points out a
slight disadvantage of going to a multi-ply construction with the same leaf thicknesses.

No unexpected phenomenon other than damping decrease was seen on the double-
ply bellows. Agreement of all three major bellows resonant modes was obtained using
accordion and lateral formulas developed in Reference 1 and in the liquid mode section of
this report. This test-theory agreement shown in the lower portion of Table 4 provides
confidence in the theoretical lateral and liquid mode analysis, especially with considerably
higher spring rates.

84
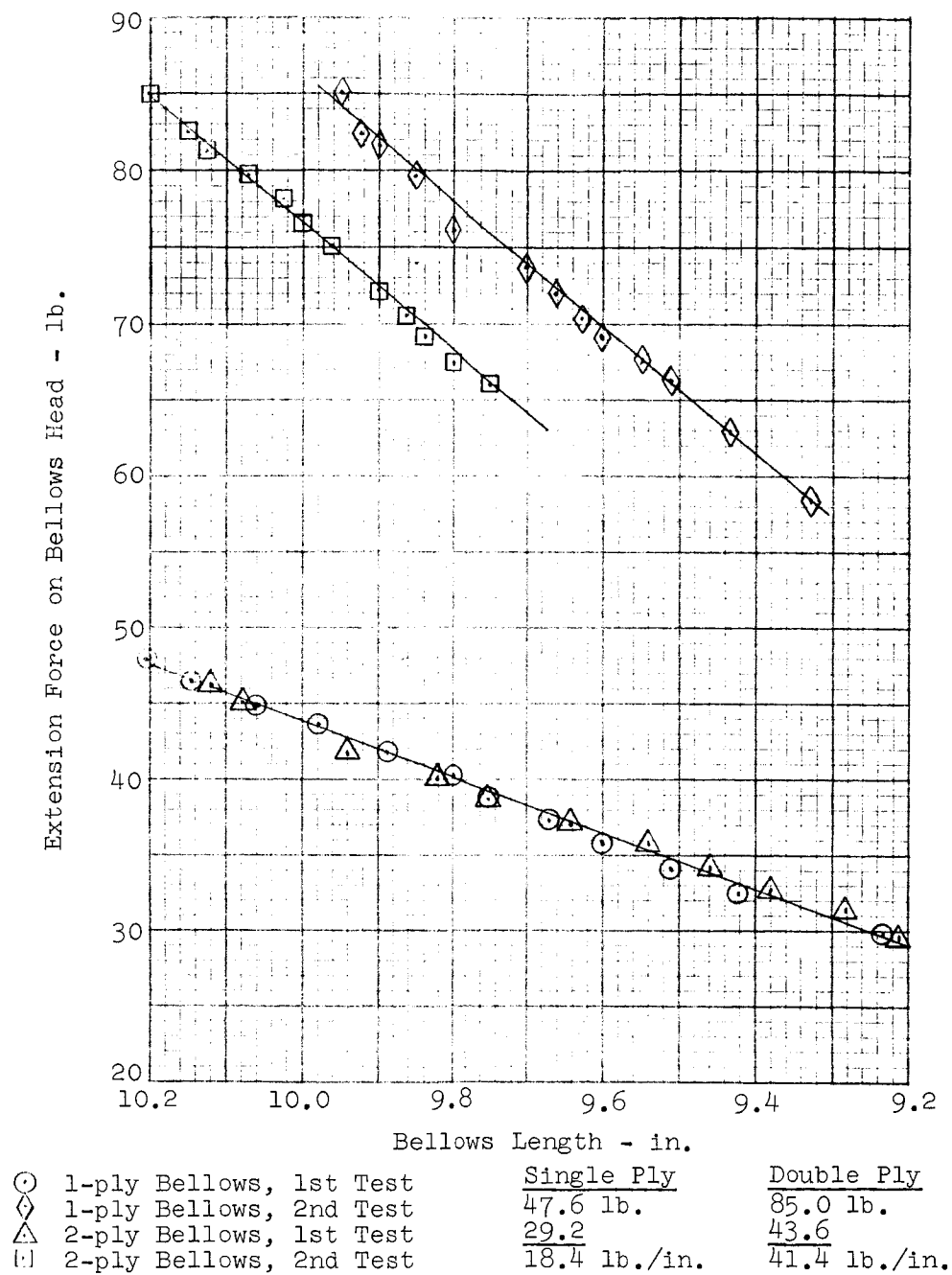
Figure 60. Determination of Spring Rates for Single-Ply and Double-Ply
Bellows
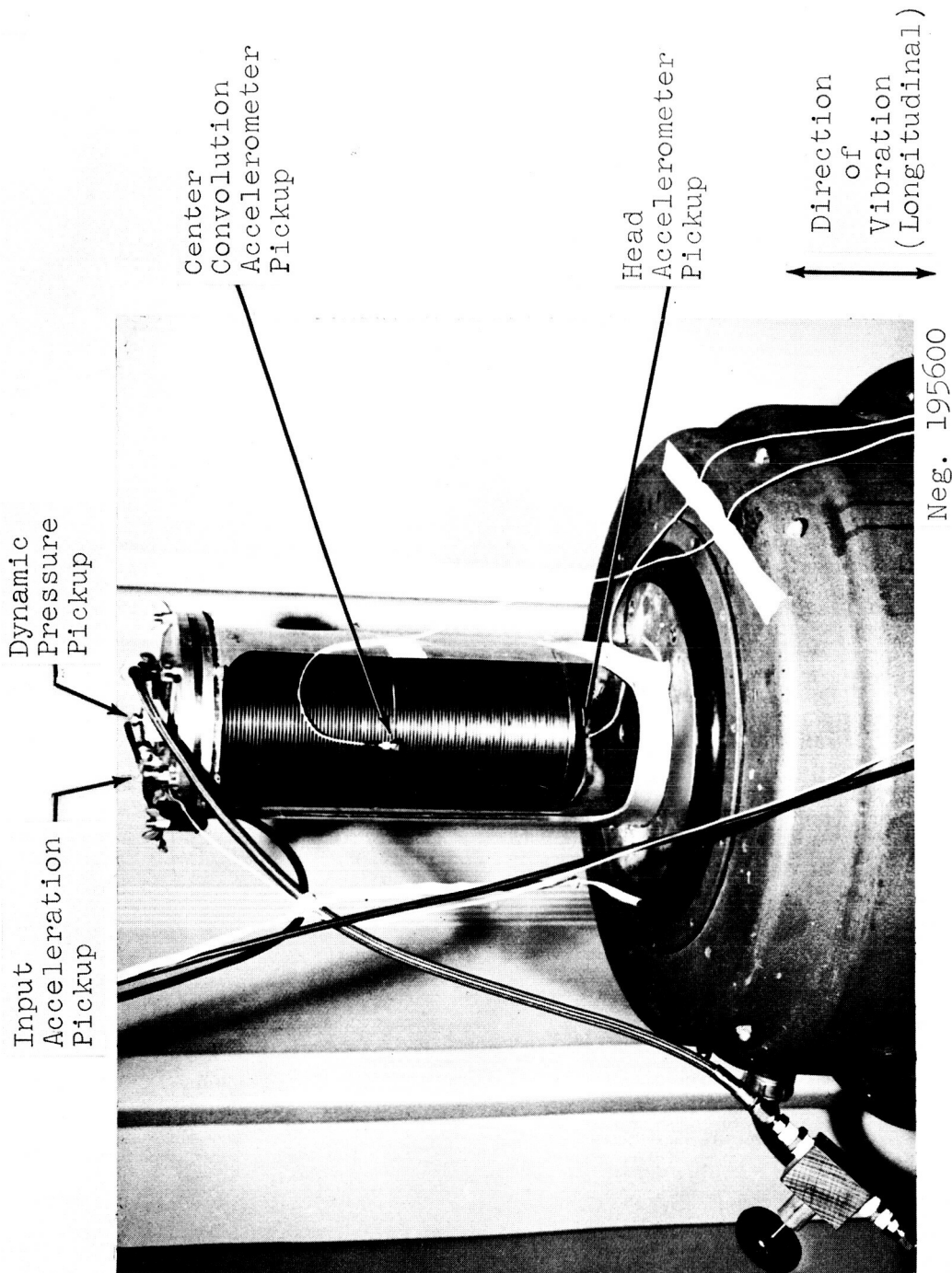
Figure 61. Vibration Setup for 5-inch Diameter Bellows

Center
Convolution
Accelerometer
Pickup

Head
Accelerometer
Pickup

Direction
of
Vibration
(Longitudinal)

Dynamic
Pressure
Pickup

Input
Acceleration
Pickup

Neg. 195600

TABLE 4

VIBRATION RESPONSE OF SINGLE-PLY AND DOUBLE-PLY BELLOWS WITH
CONSTANT 2g SINUSOIDAL INPUT AT BASE OF BELLOWS

	Single-Ply Bellows 18.4 lb/in.			Double-Ply Bellows 41.4 lb/in.		
Accordion Mode	Mode No.	cps	g	Mode No.	cps	g
Center convolution response - (frequency and acceleration)	1	26	28.6	1	31.5	41.6
	3	81	6.8	3	100	4.4
	5	133	8.6	5	167	5.4
	7	184	6.2	7	235	8.4
	9	232	2.2	9	300	13.0
Liquid Mode	Mode No.	cps	g	Mode No.	cps	g
Head response- (frequency and acceleration)	1	69	25	1	76	36
Base dynamic pressure -	Mode	cps	psi	Mode	cps	psi
(Frequency and pressure)	1	69	7.3	1	76	14.4
Lateral Mode	Mode No.	cps	g	Mode No.	cps	g
Center convolution response -	1	20	8.4	1	24	30.4
(Frequency and acceleration)	3	72	11.4	3	93	5.6

3. Discussion of Multi-Ply Bellows Damping Devices

    Sales literature indicates that one major advantage of multi-ply bellows leaf
construction is to provide greater resistance to static and dynamic internal or external
pressure forces without a substantial increase in bellows axial stiffness that would normally
result from a thicker leaf. To be effective, the adjacent multi-ply leaves should be in contact
with each other. One bellows manufacturer using the TIG welding process, provides vents in
the outer ply to release any trapped gases prior to a heat treatment process. The double-ply
bellows used in the tests previously described had neither heat treatment nor vents.

    From a dynamics standpoint, interest in multi-ply construction primarily has
been in their potential to dissipate vibratory energy as heat by some form of leaf interface
treatment, (as suggested in Figure 66) without risking contamination of propellant or gas
side of the bellows.
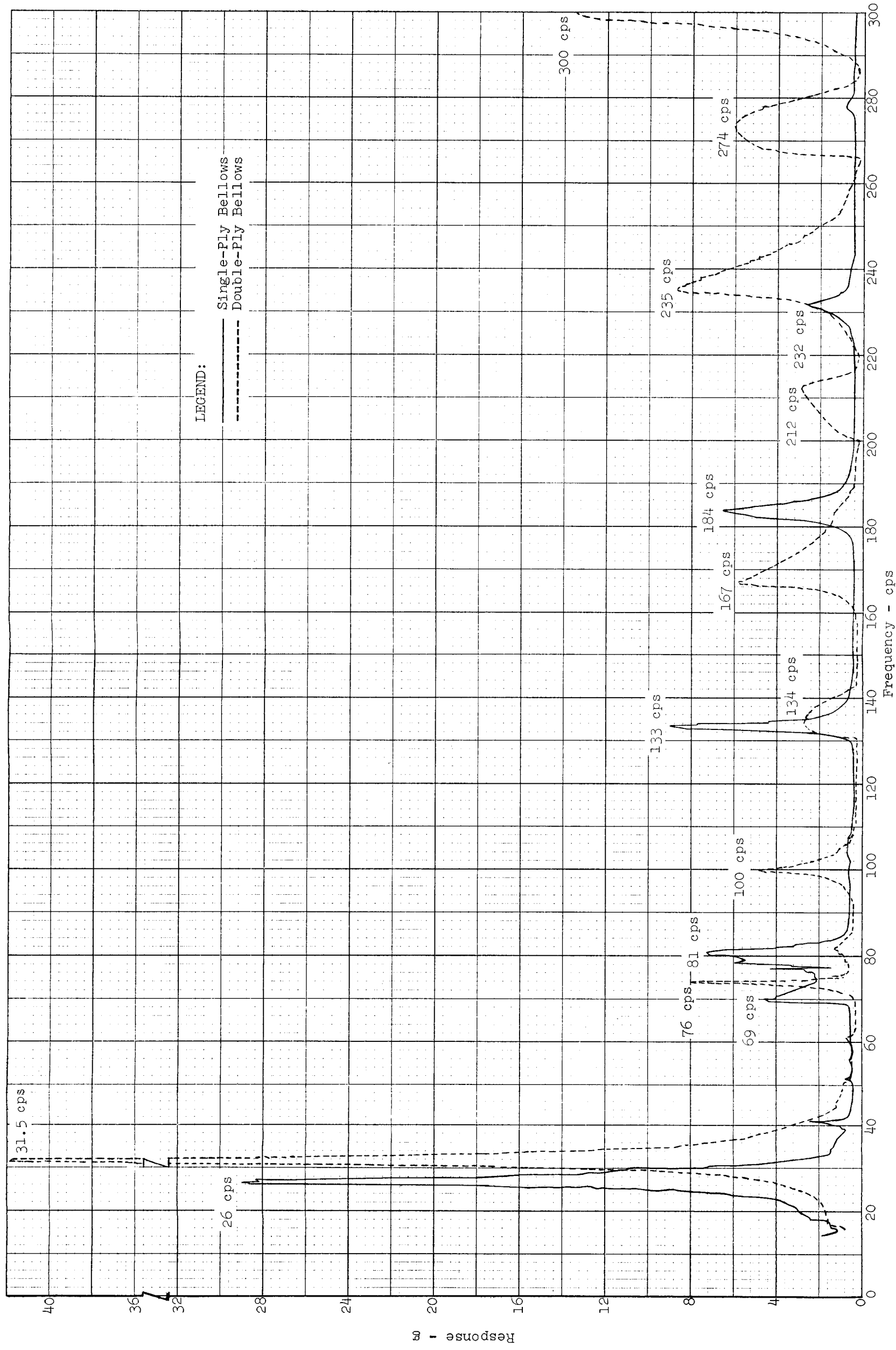
Figure 62. Longitudinal Center Convolution Response with 2g Base Input
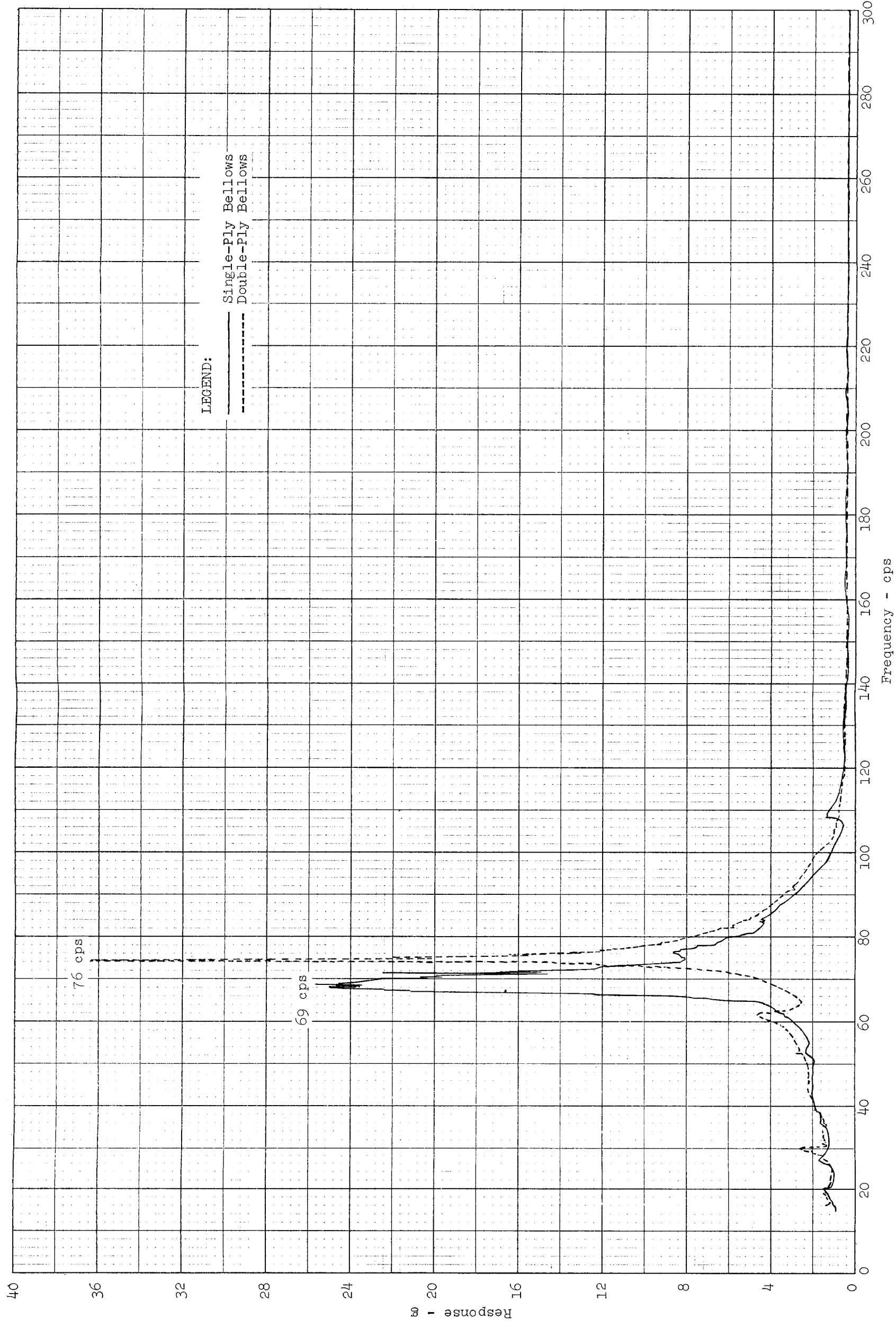
Figure 63. Longitudinal Head Acceleration Response with 2g Base Input
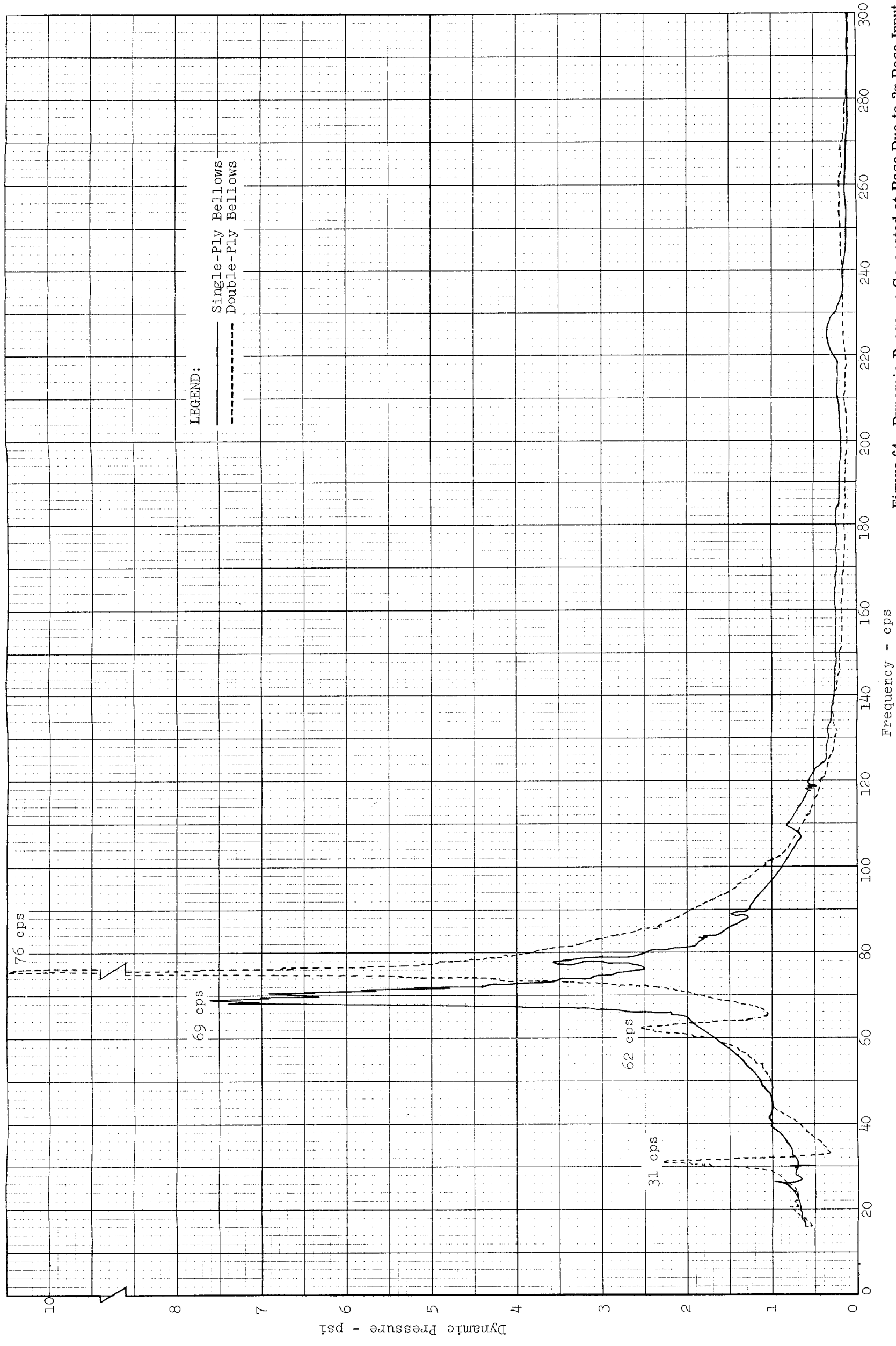
Figure 64. Dynamic Pressure Generated at Base Due to 2g Base Input

Report No. 8230-933007

90
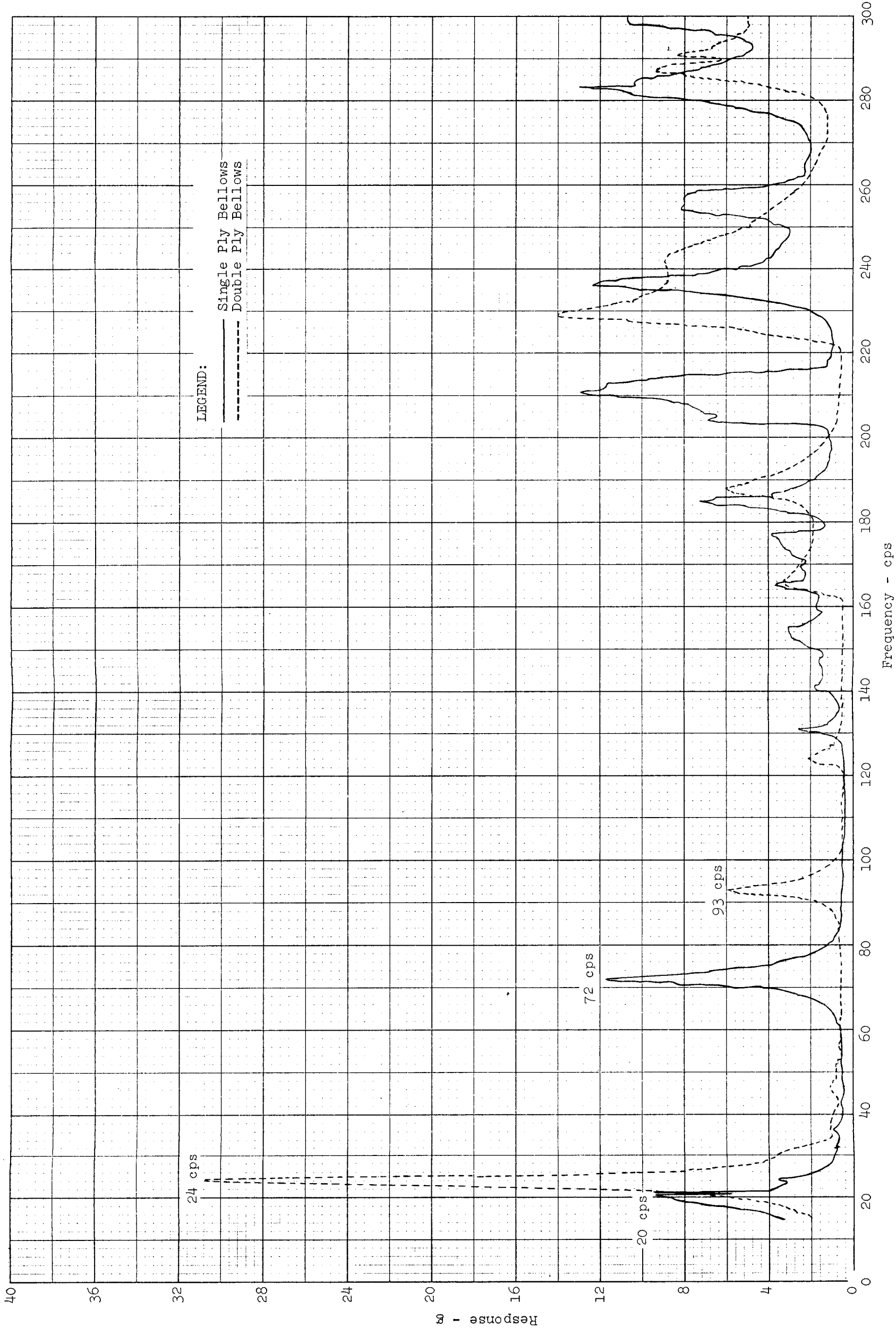
Figure 65. Lateral Center Convolution Response with 2g Base Input

t_o = 0.002 in. thick outer ply

Shear distortion of visco-elastic materials such as adhesives, pressure-sensitive tape, or bonded elastomers placed prior to or after welding of plys. For damping $t_o > t_i > t_o$

Liquid Side

Gas side

t_i = 0.006 in. thick inner ply. Type of SST may be different than 0.002 in. ply
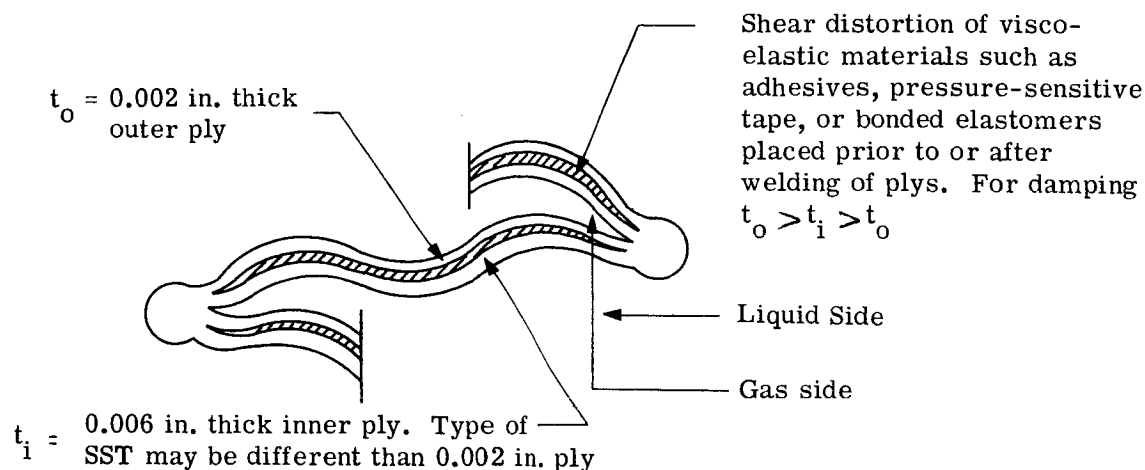
Figure 66. Damping of Two-Ply Bellows by Various Interface Treatments

This energy may result from sinusoidal vibration, random vibration, shock, acoustic noise, or hydraulic shock environments in which the bellows must operate thereby adding dynamic stresses; see items (3), (4), (5), and (6) in the following list.

Causes of leaf distortion and leaf stresses:

(1) Leaf extension from free length (elastic range) to lift-off length (plastic range).

(2) Static pressure inside bellows, ΔP across bellows.

(3) Change in pitch due to vibratory longitudinal motion of leaves - usually a maximum at longitudinal modes.

(4) Increase in pitch of all convolutions due to longitudinal head motion caused by the internal liquid pressure force on the head.

(5) Dynamic pressure forces due to item (3).

(6) Dynamic pressure forces during vibration due to inertia of fluid - usually a maximum at bellows attachment and appears to be independent of bellows attitude.

Items (1), (2), and (3) are significant in accordion and lateral modes; all items apply to liquid modes.

The test data show that equal thickness double-ply construction with nearly equal strains in each leaf and little relative motion at their interface resulted in substantial vibration amplifications. If nonequal leaf thicknesses are used, relative motion may be predictable for structural Computer Program 1753 with considerable program modification.

Coulomb friction damping may be used if interface pressure can be accurately controlled during fabrication. In most engineering applications, this mechanism is not reliable over the long run; thus, some type of viscous damping would be desirable. Considerable research and development has been, and is still being, conducted on viscoelastic damping of mechanical structures (see Reference 22). This reference discusses surface

damping treatments such as pressure sensitive tape and mastic deadeners. However, many of these can be eliminated because the operating characteristics of the bellows must not be compromised with damping treatments. Distortion of an interface adhesive in shear in Figure 66 shows promise, but no test data were obtained to substantiate this device because tests of this nature were considered prohibitive in this study from a cost standpoint. Leaf strains should be carefully analyzed using Program 1753 before undertaking a full-scale development test program to minimize leaf strains by viscoelastic damping devices.

To illustrate how much distortion is possible, Program 1753 was used to obtain a comparison of leaf deflections of two thickness convolutions. These convolutions, selected at random, had the same shape as shown in Figure 67 but the thicknesses were in a ratio of
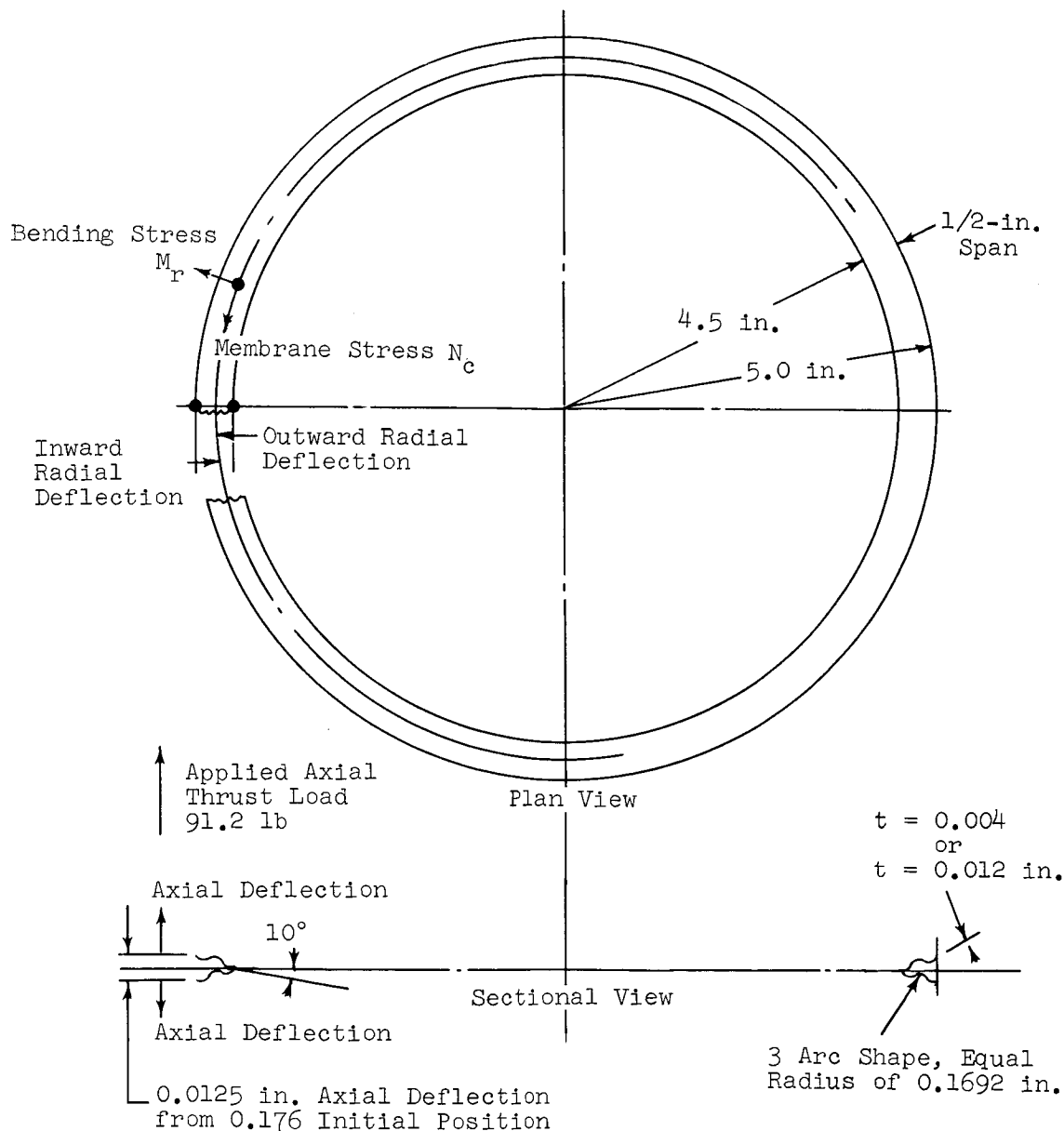
Figure 67. Bellows Convolution, 3rd and 4th Leaves

three to one. As shown in Figures 68 and 69, there was a maximum radial difference in deflection of 0.0023 inch and an axial deflection difference of 0.0008 inch as shown in Figure 70 for the third and fourth leaf. Whether or not this distortion is enough to supply sufficient viscous damping remains to be seen.
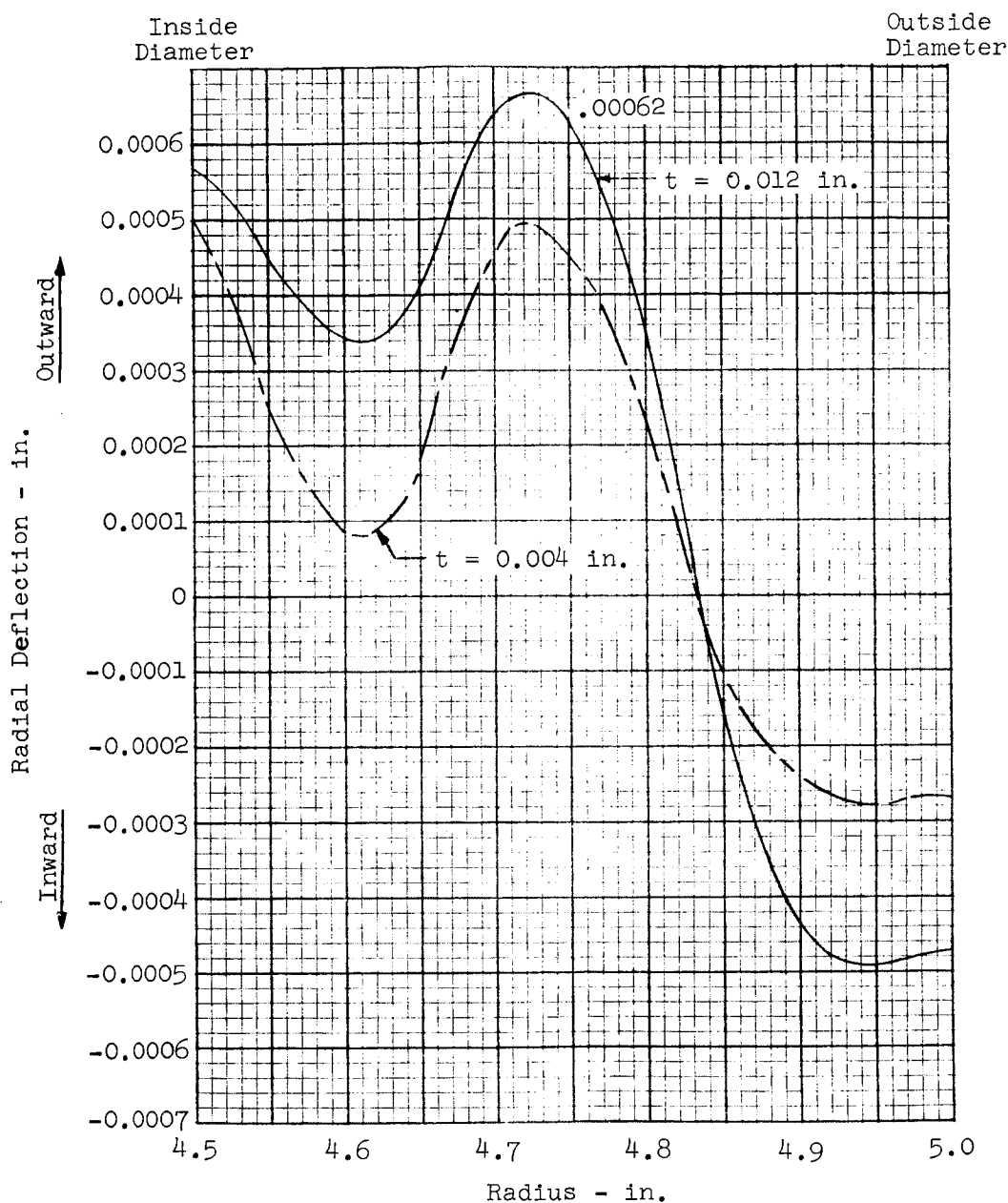
Figure 68. Radial Deflection, 3rd Leaf
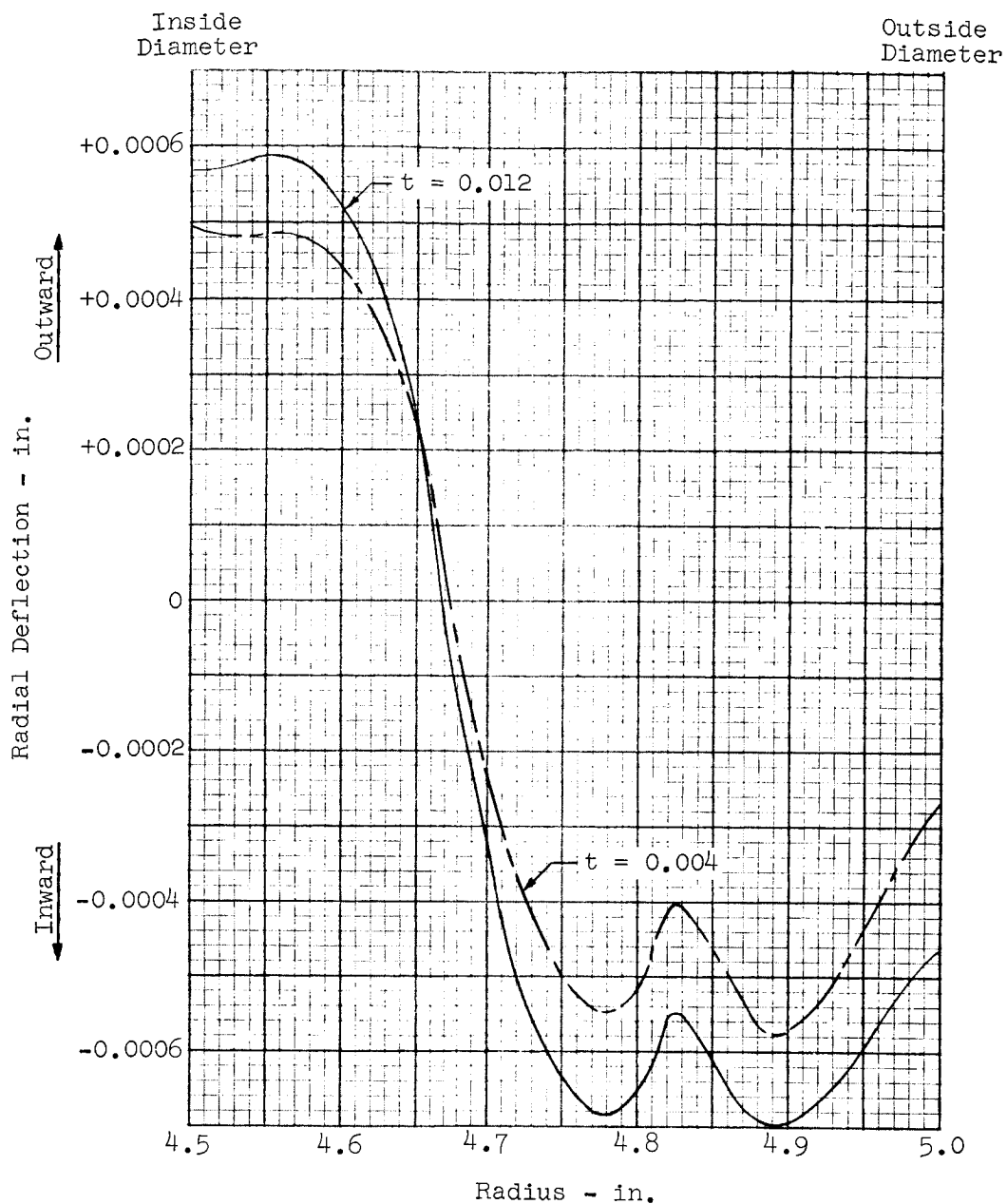
Figure 69. Radial Deflection, 4th Leaf

The radial and axial deflections of the third and fourth leaf will be typical of all the other bellows leaves except for the end leaves. Note that the elastomer is expected to distort as follows:

(1) Radially - shear strain differences

(2) Circumferentially - bending strain differences because of different strained diameters radii

(3) Axially - compressions and tensions due to axial motion differences on both leaves.
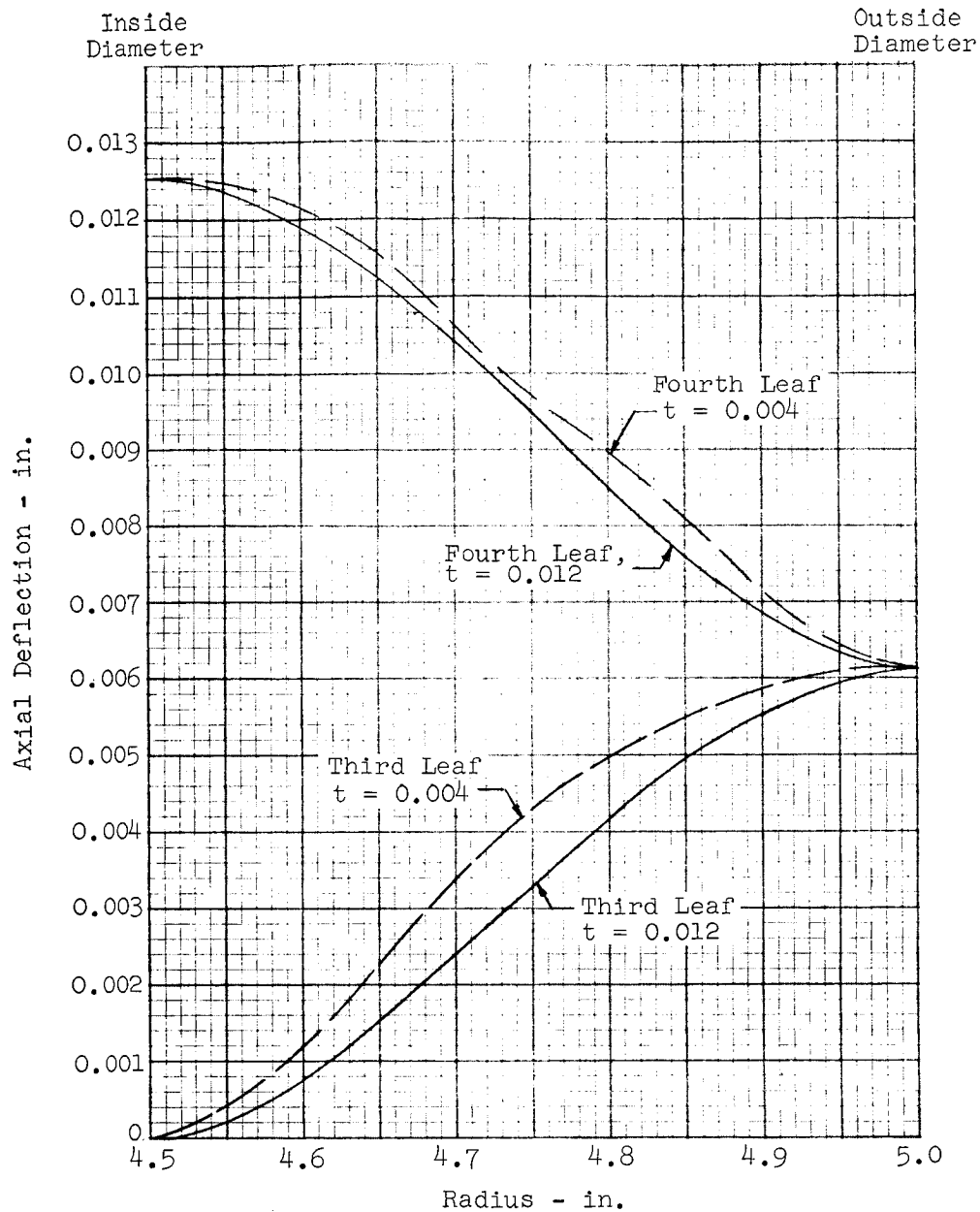
Figure 70. Axial Deflection

Optimum elastomer thicknesses, mechanical properties, viscous damping capacity to reduce strains, fabrication problems, as well as leaf geometries in the single-ply leaf replacement application still remains to be established.

H. CONCLUSIONS

Although the dynamics computer program, established in earlier work (see Reference 1), formed the basis for calculation of the bellows longitudinal accordion modes and lateral modes, it was decided to look deeper into how a bellows accordion mode compares with the general case of longitudinal homogeneous bar response. The two cases considered were a bar subjected to sinusoidal motion at both ends and a bar subjected to motion at one end, with the other end free.

These analyses formed the analytical building blocks to develop the liquid mode formulas that substitute a porous bar in place of the homogeneous bar. The basic homogeneous bar analysis also showed that the lack of even-number harmonic response in the accordion, liquid, and lateral modes was because these modes become self-damping cases with motion applied at either or both ends of a bellows. However, these even harmonics would be excited if motion could be applied somehow at the center of a bellows, perhaps the acoustic noise case.

The liquid mode phenonoma (see Reference 1) was investigated by establishing a porous bar mathematical model, where bellows convolutions are acting as a sponge or porous bar in the liquid mode as compared with an elastic homogeneous bar for the accordion modes. This model assumed that longitudinal motion of a bellows strains the leaves because of a convolution change in pitch. Leaf strain times the effective modulus of elasticity equals equivalent leaf stress. Convolution elastic displacements well defined by the wave equation for the accordion mode, will closely obey the same elastic laws in the liquid mode.

A reduction in convolution pitch squeezes liquid out, thus imparting a radial inner displacement and a radial inner acceleration to the entrapped liquid. The radial displacement of the liquid column can be expressed in terms of equivalent convolution strain. The radial acceleration of the liquid column can then be put in terms of convolution acceleration. This squeezing out of entrapped liquid also tends to decrease the effective liquid column diameter. Conversely, an increase in the effective liquid column occurs when the convolutions are expanding.

To have a radial inner displacement, an increased liquid pressure will occur at the liquid column boundary. This liquid boundary pressure, which is now equivalent to the complex leaf stress or strain, can be expressed in terms of radial displacement of the fluid, radial acceleration of the fluid, leaf displacement, leaf acceleration, leaf strain, and convolution change in pitch. To equate liquid pressure to liquid acceleration, the Navier-Stokes equations and continuity equations must be used. In the liquid mode analysis for frequency determinations these equations were simplified by neglecting nonlinear, viscosity, and body force terms. What remains are equations for radial and longitudinal flows which express the relationships between liquid acceleration, density and pressures as functions of time. In solving these differential equations the ratio of two Bessel functions occurred.

Effective coupling is established because the liquid pressure and liquid acceleration expressions in the Navier-Stokes equations at the boundary are the same liquid pressure and liquid accelerations due to fluid ejection from the leaves. When liquid ejection from each convolution occurs in the right time sequence, liquid mode resonance occurs.

The simple frequency formula developed multiplied the accordion mode frequency by a factor which need only include the bellows length and diameter. The bellows spring rate and mass terms are contained in the accordion mode frequency equations. Fair agreement with test frequencies on seven different bellows configurations was obtained. However, the model

needs further refinement to predict internal and external pressure distributions, liquid stream lines, convolution mode shape and higher harmonic frequency limitations.

Laboratory vibration tests with rigid pipes and fixed head bellows provided some quantitative data on body force pressures and convolution pumping pressures. Test results from other bellows programs included herein showed the effects of positive and negative external gage pressures on the liquid mode. Test results showed that the internal liquid dynamic pressure decreases as a function of increasing external gas density. Dissolved gas in the liquid and internal gas entrainment devices will also affect pressure oscillations. Because of the severity of the liquid mode pressure oscillations, some type of suppression device should be considered to preclude bellows failure in services. External pressure appears to be the easiest way to accomplish this.

Tests results from one double-ply bellows test indicated that multi-ply bellows are more resonant than single-ply. No control of the friction forces between the leaves was maintained during manufacturing; from a dynamics standpoint it was recommended that dependable damping could be obtained by using a viscoelastic material between the leaves.

SECTION 4

PERMEATION TECHNOLOGY

A.   SYNOPSIS

The initial phase of this contract (Reference 1) ended with a choice of three detectors to be used in conjunction with a permeation chamber for conducting permeation tests. In this report on the follow-on effort, the thermistor-type detector, chosen from the three as the most practical, is discussed with respect to design, application, and problems to be solved.

A new permeation chamber was designed and fabricated, using a corrugated diaphragm instead of a bellows. The bellows allows for volumetric changes of the liquid so that a zero differential pressure can be maintained across the test specimen. Satisfactory tests were conducted to prove the integrity of this design.

Also discussed, under Conclusions, are several areas requiring further investigation.

B.   GENERAL

Reference 1 describes in detail the work accomplished under the initial contract and concludes that three detection systems warranted further investigation as a detector for a general-purpose permeation apparatus: (1) the Karmen voltage-breakdown detector, (2) the thermistor-type thermal conductivity detector, and (3) the cross-section detector.

During the first quarter of the follow-on program, these three detectors were further investigated and it was concluded that efforts should be directed toward work on the thermistor type. This decision was based upon the large amount of existing knowledge on thermistors and thermistor-type thermal conductivity cells; there is limited knowledge available on the other two. Moreover, the thermistor will detect a wide range of concentrations. The voltage breakdown detector will not function properly at higher concentrations (10% of saturation or higher). Although the cross-section detector is designed to function over a wide range of concentrations, the device is new and little functional information is available. Furthermore, the cross-section detector contains a radioactive source that requires an AEC license.

After selection of the thermistor-type detector for use with the permeation apparatus, the following work outline was prepared.

Detector Evaluation and Calibration

The thermistor-type thermal conductivity detector was to be investigated for its applicability to the Bell-designed permeation test apparatus. As part of the evaluation of the thermistor, tests were to be conducted to determine:

(1)   The stability of the thermistor (including accessory components) over a period not to exceed 2 weeks.

(2) The effects of pressure and temperature on thermal conductivity of known mixtures of propellants and gases.

(3) The repeatability of detection using known concentrations of propellant vapors in nitrogen or helium.

(4) The operating temperature limits; in particular, operation of the thermistor at cryogenic temperatures.

To conduct permeation tests, it would be necessary to calibrate the detector with propellants to be tested. Calibration curves were to be determined for N_2O_4, UDMH, He, N_2, and O_2, including the minimum detectable concentration.

Permeation Tests at Room Temperatures

Two tests were planned with an oxidizer (N_2O_4) and two tests with a fuel (UDMH) to verify the design and operation of the integrated detector and permeation chamber.

Permeation Tests at Cryogenic Temperatures

It was planned to conduct one test using liquid nitrogen (LN_2) with LN_2 as the coolant. Helium was to be the pressurizing gas. This would be a feasibility test to prove the validity of the Bell design and further verify the operation of the detector.

To conduct the cryogenic tests, the test apparatus would be submerged in a pool of LN_2, contained in a stainless Dewar, and cooled to LN_2 temperature; LN_2 would then be admitted to the apparatus and the system pressurized with helium.

Permeation Tests Under Temperature-Cycling Conditions

This was believed to be an environmental condition that could, in theory, at least, cause a much greater loss of propellant due to permeation than isothermal tests have indicated.

It was planned to conduct a test using a small ASTM-type chamber; the chamber would hold N_2O_4 on one side of a Teflon membrane and pressurizing gas on the other side. It was to be thermally cycled over a range of about 20° to 100°F. At the conclusion of the test, the gas would be analyzed to determine if the propellant content was greater than in a similar chamber held at constant temperature.

To satisfy these requirements, the work was divided into two major areas:

(1) Design of the permeation chamber.

(2) Design of the thermistor detector.

These subjects are discussed in the following paragraphs.

C. DESIGN OF PERMEATION CHAMBER

The permeation chamber designed during the initial NAS7-149 contract and the test conducted with the apparatus are described in Reference 1; Figure 71 is a sketch of the
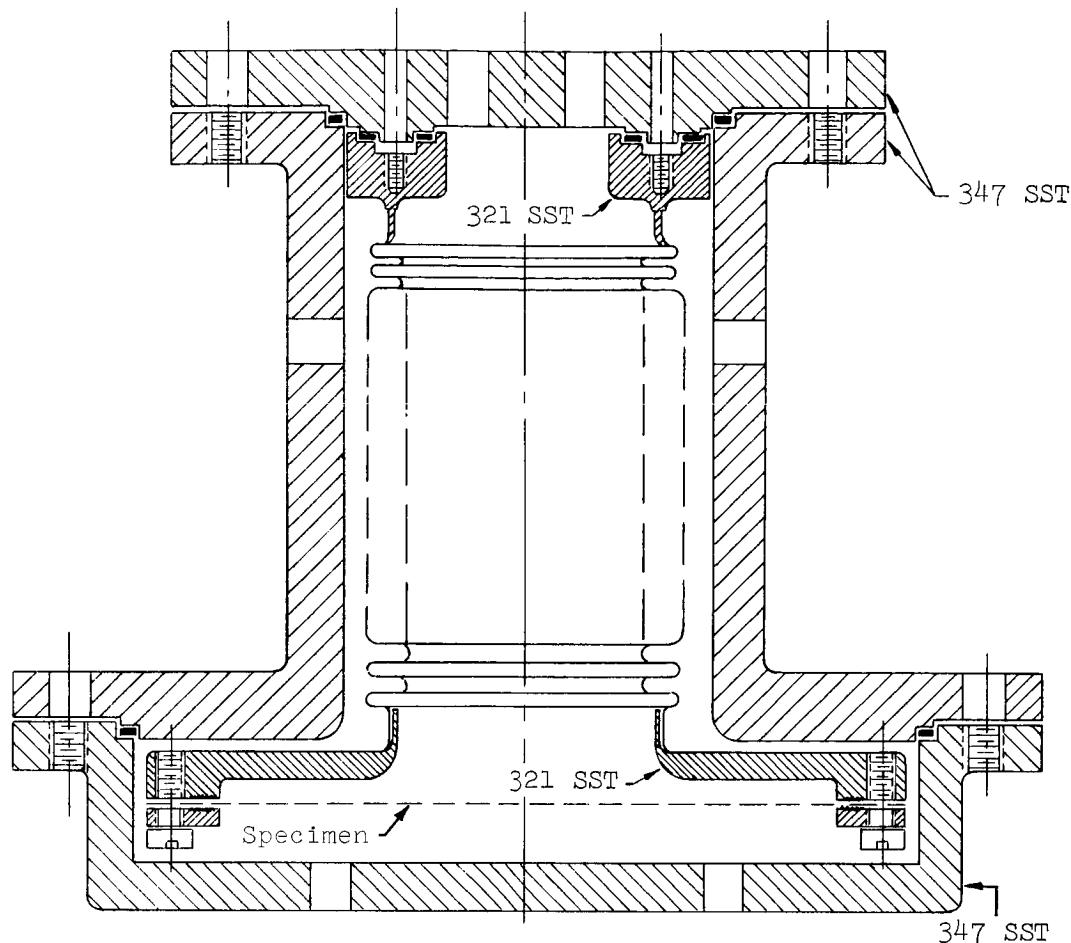
Notes: A. Approximately full-scale.
       B. All machined surfaces 63 RMS or better.

Figure 71. Permeability Apparatus Assembly

chamber. Further investigation of this design during this follow-on effort revealed four notable objections:

(1) Fabrication cost is high, $500 to $700 for a single unit. This cost may be reduced to $200 to $300 each for a dozen or more units.

(2) If permeation or leakage occurs laterally in the test specimen, and out the edge of the specimen into the gas space, the permeation rate through unit area of specimen would be in error. This error, however, would most likely be negligible.

(3) Because of the rather tortuous path between the gas volume immediately adjacent to the specimen and the gas space around the bellows, the composition of the entire gas volume may not be uniform. Therefore, a sample from the bottom of the unit may not be representative of the whole gas volume, and, in fact, might indicate a larger quantity of permeant present and a higher permeation rate than is actually present percentagewise at the given moment.

(4) The apparatus must be loaded and unloaded at a temperature below the boiling point of the test liquid (a temperature at which the vapor pressure is less than 14.7 psia), otherwise the vapor pressure on the liquid side will damage the unsupported test membrane.

Because of these problems a new design evolved as shown in Figures 72 through 75. (The basic concept for this design was suggested by Mr. Richard N. Porter of JPL.) A single unit of this design will cost about $200, or less than $100 for a number of units made at one time.
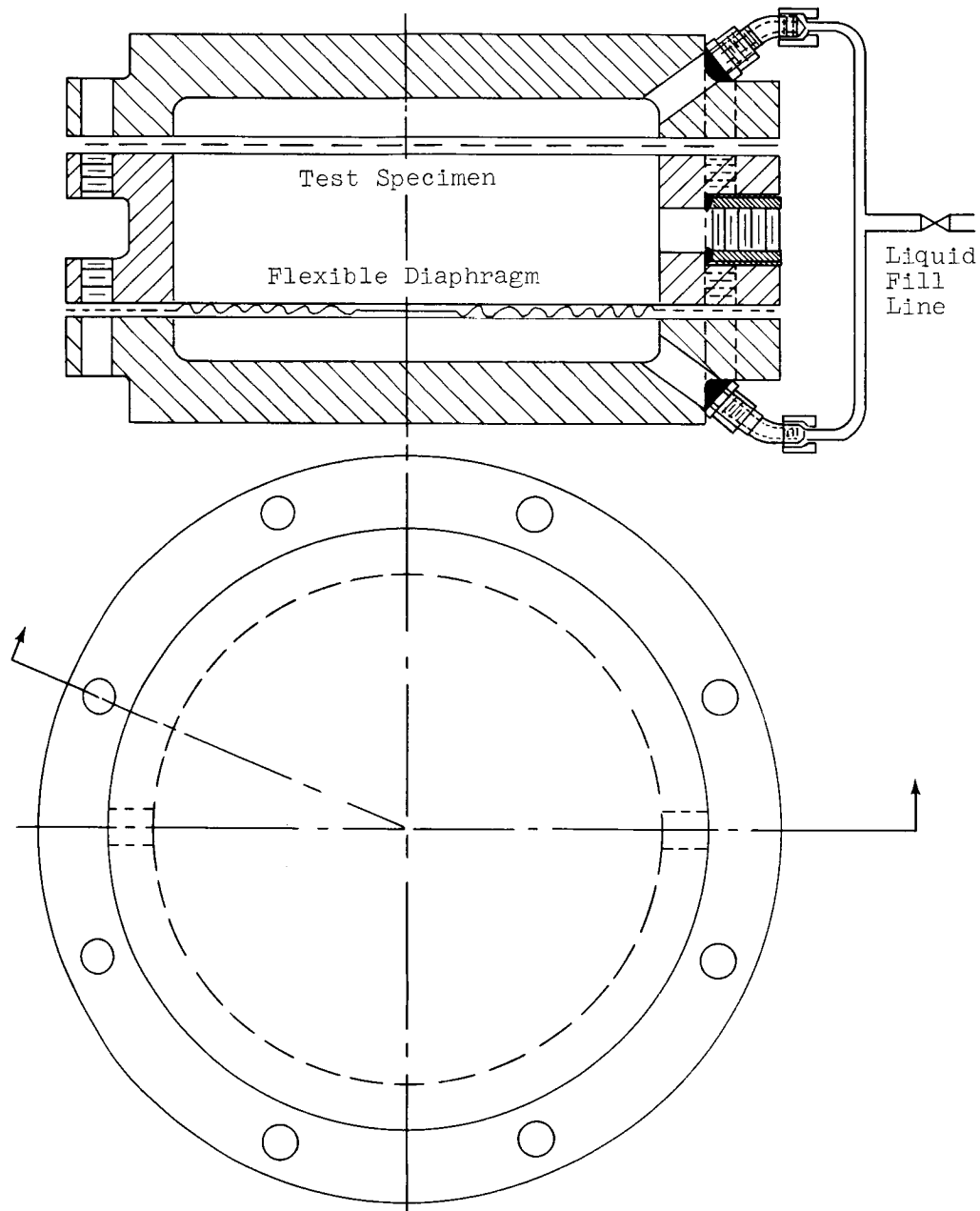
Figure 72. Permeation Chamber Assembly

Report No. 8230-933007
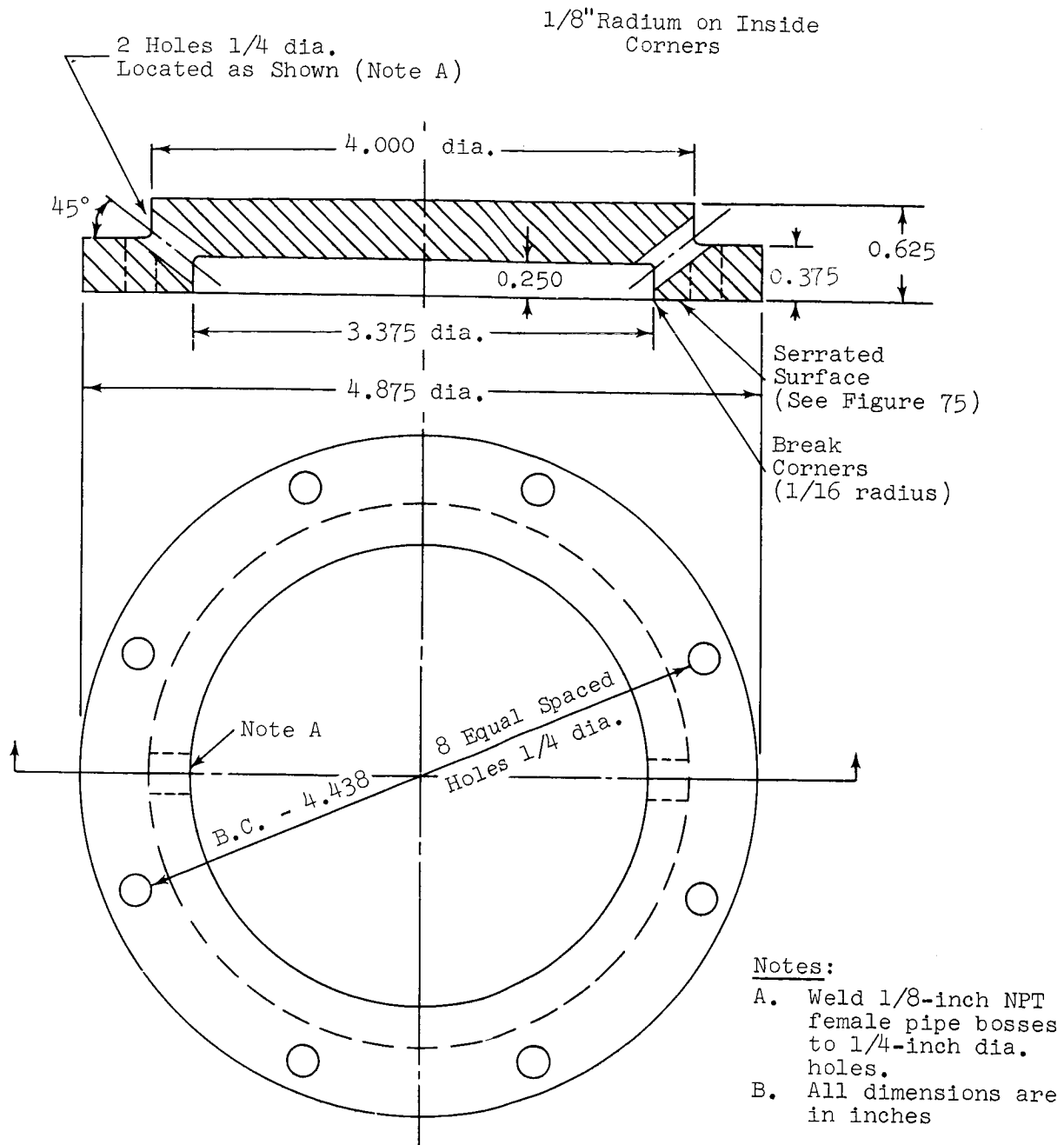
Figure 73. Permeation Chamber Cover

The second and third problems in the foregoing list are eliminated in this design. The fourth problem, concerning the loading and unloading temperature, would be inherent in any design in which the test specimen is not supported. Actually, this problem only becomes troublesome if the test liquid boils at or below room temperature (for example, N_2O_4 which boils at 70°F).
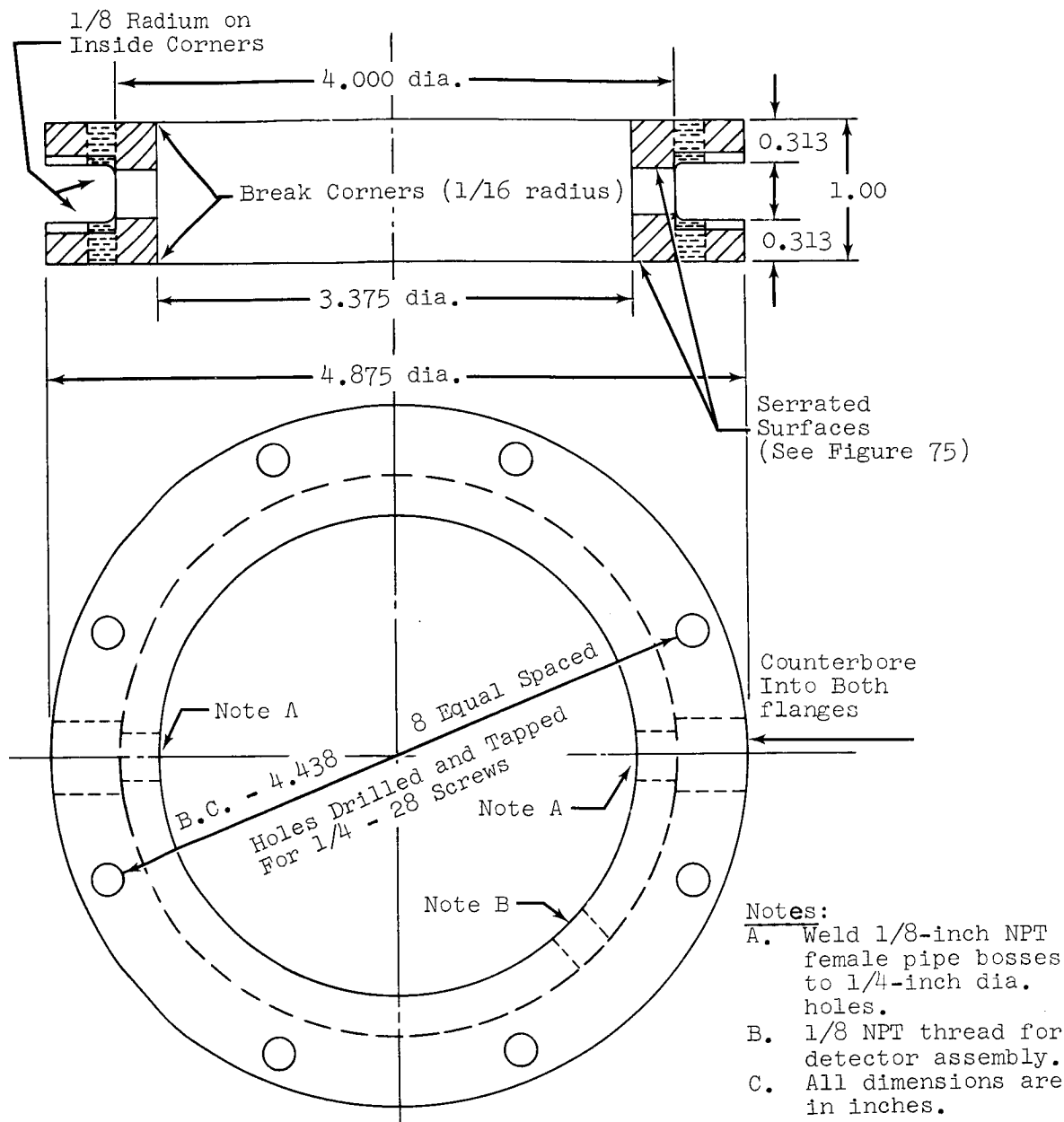
Figure 74. Permeation Chamber Middle Section

Notes:
A. Weld 1/8-inch NPT female pipe bosses to 1/4-inch dia. holes.
B. 1/8 NPT thread for detector assembly.
C. All dimensions are in inches.

The most critical component part of the current design (besides the thermistor detector) is the diaphragm. The function of the diaphragm is to allow for volumetric changes of the test liquid due to temperature changes. It should have a "spring constant" less than that of the test specimen so that the test specimen will undergo minimum deflection. Excessive strain or deformation of the test specimen can affect the permeation rate. The magnitude of the effect is not known.

The maximum allowable differential pressure across the specimen has been set at 0.7 psi. This was based on work with the bellows-type apparatus (Figure 71). This differential

Notes:

A. Mating serrated surfaces controlled to 0.005 inch maximum
B. Crest of serrations in plane which is flat within 0.001 inch T.I.R. for full diameter.
C. Depth of cut for first serration - 25% of full cut; 2nd serration - 50%; 3rd - 75%; all others, full cut.
D. All dimensions are in inches.
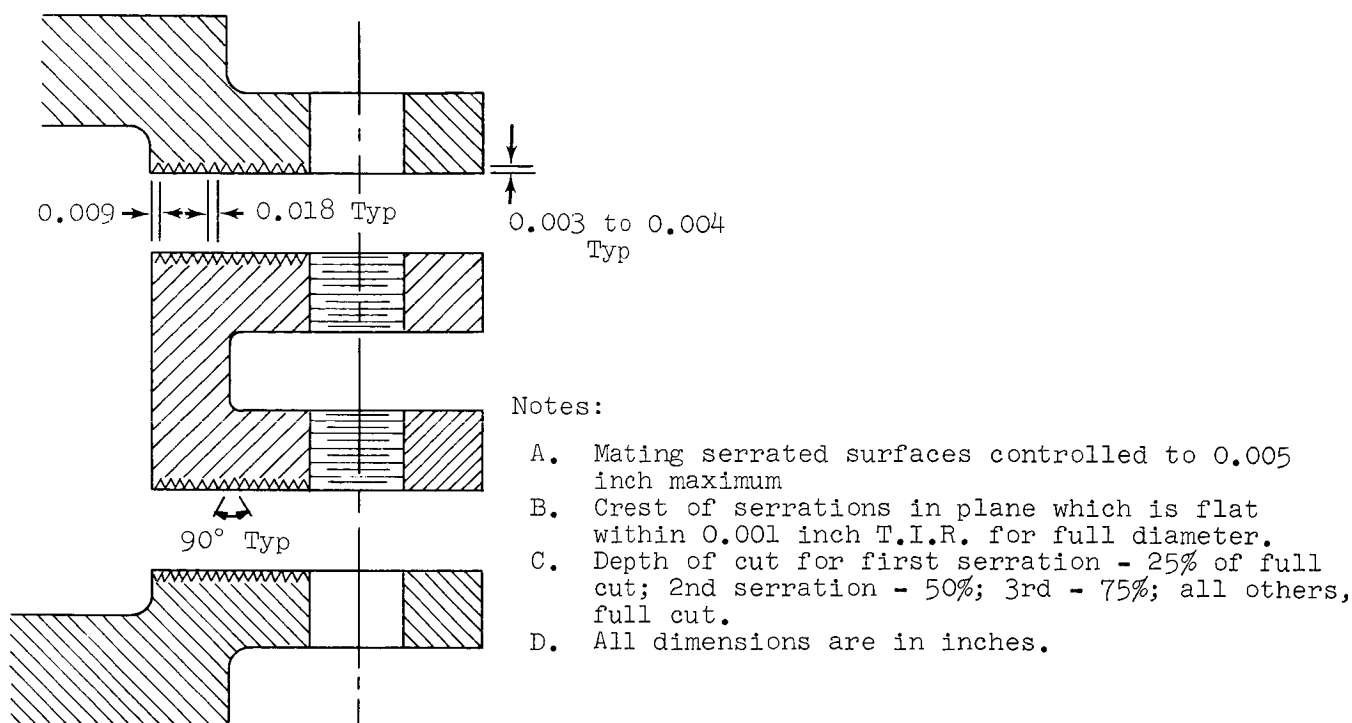
Figure 75. Detail of Serrations

pressure would cause the unsupported Teflon specimen to deflect 1/8 to 1/4 inch at the center. This deflection was not considered detrimental. If the metal diaphragm is weaker than the test specimen (the desirable situation), then most of the deflection due to volumetric changes would occur in the diaphragm.

Another reason for these operational requirements was to provide an apparatus that would not be limited to narrow operating temperature limits. Figure 76 shows the percentage volume change as a function of the chamber volume for various deflections of a 3.375-inch diameter diaphragm. Figures 77 and 78 show the percentage density change for temperatures above and below 70°F for N_2O_4 and UDMH, respectively. As an example of the use of these figures: if the diaphragm for the present apparatus will deflect 0.20 inch at a ΔP of 0.7 psi, the volume change for a 5-cubic-inch chamber (the liquid side of the apparatus is approximately 5 cubic inches) is plus or minus 4.1%. If the test liquid is UDMH, the usable temperature range is between 13° and 127°F; for N_2O_4, 20° to 121°F. These calculations assume that only the metal diaphragm moves, which would be the ideal situation. Since the test specimen moves also, the ΔP across the specimen and diaphragm will be less than 0.7 psi for a given percentage volume change.

Therefore, initial specifications were established for the diaphragm: 0.25-inch deflection with a differential pressure of 0.7 psi maximum, and a diameter of 2 to 4 inches. Letters were sent to the following companies inquiring as to the availability of such a diaphragm:

(1) Phoenix Products Co., Milwaukee, Wis.
(2) Hydroforming Company of America, Chicago, Ill.
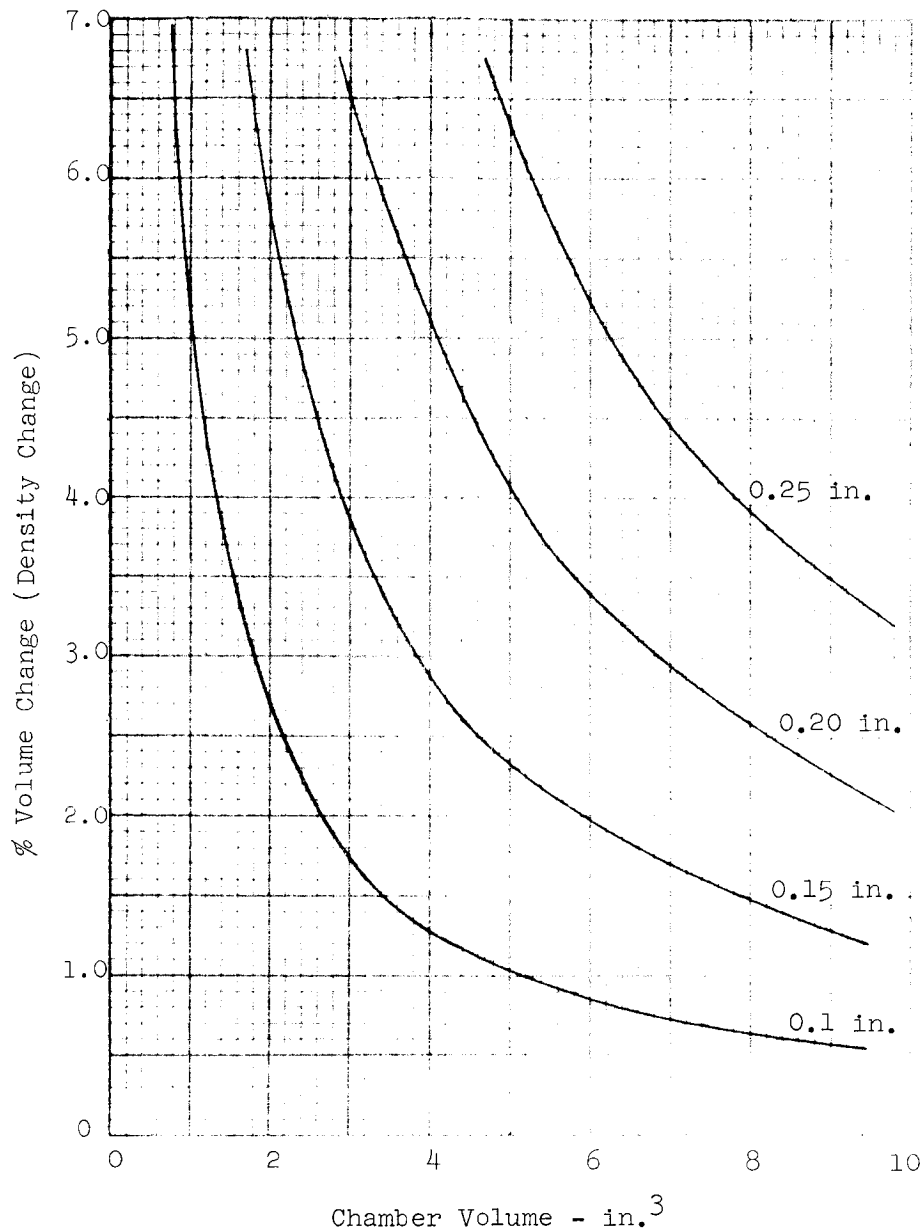
Figure 76. Chamber Volume vs Percentage of Volume Changes at
Various Deflections

(3) Cook Electric Company, Chicago, Ill.
(4) Metallurgical Processing Corp., Westbury, N. Y.
(5) Eastern Metals Industries, Inc., Glen Cove, N. Y.
(6) Giannini Controls Corp., Duarte, California
(7) Fulton Sylphon Division of Robertshaw Controls Co.

Results of the inquiry were negative. The first five companies had nothing to offer. Giannini
Controls did not reply. Robertshaw did not think a diaphragm could be made with these
specifications and suggested a bellows.

Report No. 8230-933007
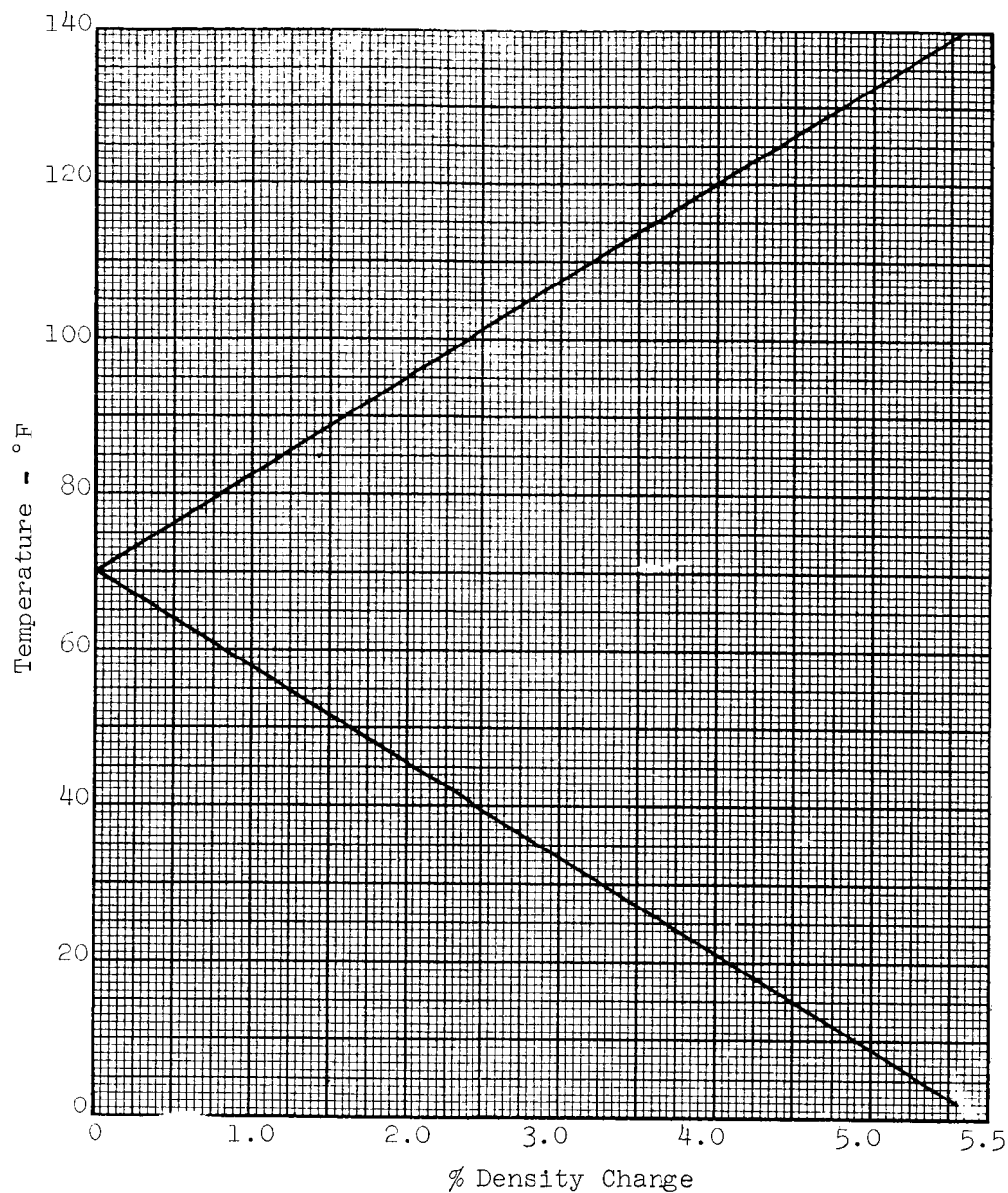
Figure 77. Percentage of Density Change vs Temperature for N_2O_4
(Load at 70°F)

An attempt was made to design a diaphragm. The necessary parameters (diameter, deflection, differential pressure, etc.) were fed into the 1753 Computer Program (described elsewhere in this report) for the design of a diaphragm having the following shape:
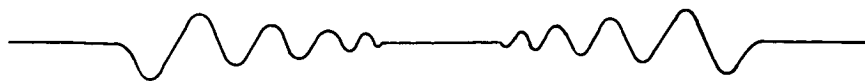
Tentative Diaphragm Design Configuration
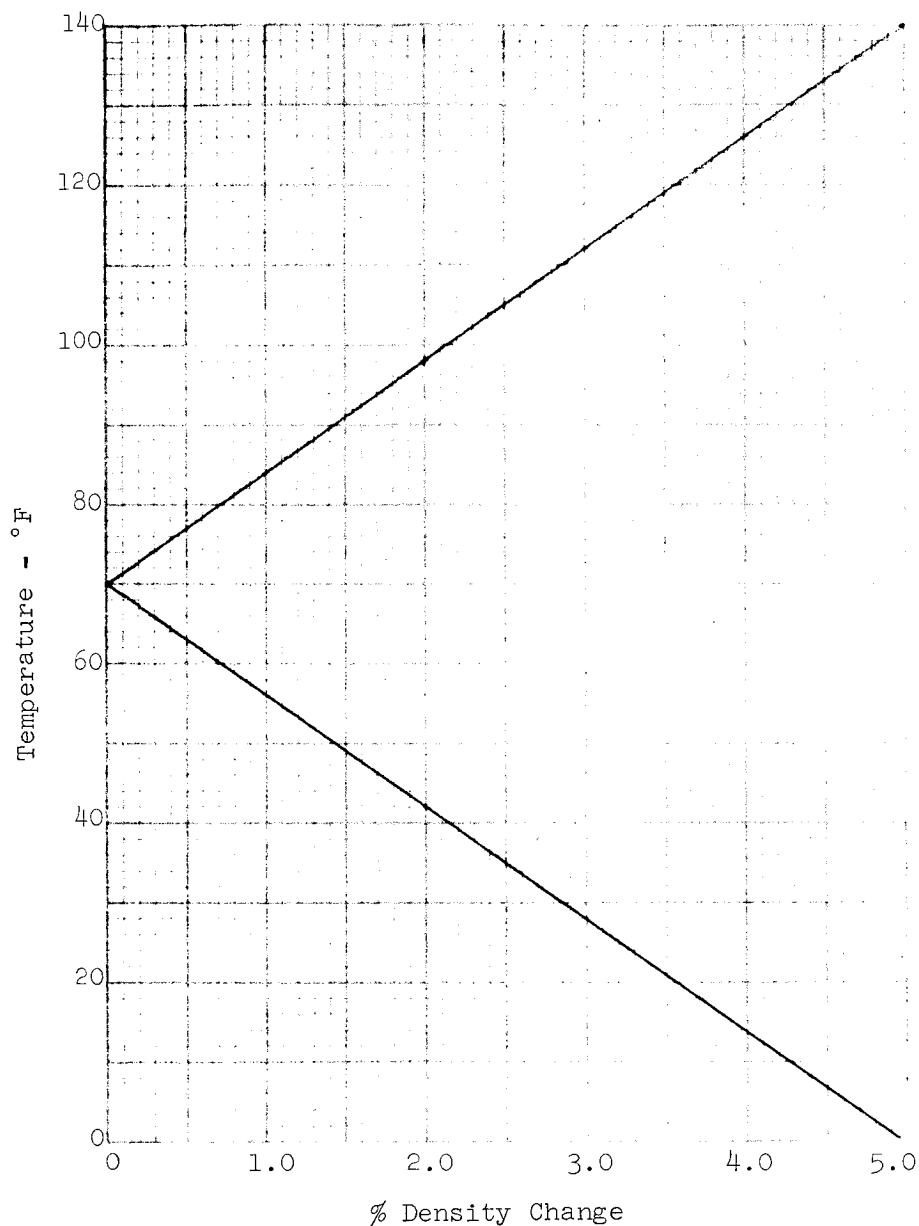
Figure 78. Percentage of Density Change vs Temperature for UDMH
(Load at 70°F)

Initial results indicated only small deflections were possible with an acceptable differential pressure; however, additional results indicated that, by use of the proper thickness and included angle between convolutions, it would be possible to obtain a design with a usable deflection at the 0.7 psi ΔP. The deflection, however, would be less than 0.25 inch.

Two companies were contacted to determine if a diaphragm with this configuration could be fabricated: the Hydroforming Co. of America, Chicago, Ill., and the Koch Metal Spinning Co., Buffalo, N. Y. These companies were concerned about the thinness of the material, 0.001 to 0.002 inch. Both were reluctant to estimate a cost, but a small number of diaphragms, 10 or less, would probably cost about $10 to $15 each.

Report No. 8230-933007

Carleton Controls Corp., of East Aurora, N. Y. was contacted regarding diaphragms. This company had several dies available, one with an over-all diameter of 4 inches with the convoluted area just under 3-3/8 inches in diameter. Carleton provided sample diaphragms made of 0.002 inch stainless steel and 0.002 inch aluminum alloy. These samples were tested at Bell Aerosystems for deflection. Twenty inches of water (approximately 0.7 psig) was found to deflect these diaphragms more than 0.25 inch at the center. This diaphragm configuration was chosen for subsequent permeation test work. The dimensions of the chamber shown in Figures 72 through 75 were chosen for this diaphragm. Dimensions and shape of this diaphragm (made to Carleton die number 1693-701-000-030-1) are shown in Figure 79. The cost of each diaphragm was $5.23.

As a final test of the integrity of the design, the permeation chamber was assembled with the diaphragm and Teflon specimen in accordance with Figure 72. The liquid side was loaded with methylene chloride and the unit pressurized with nitrogen to 200 psig. The unit was allowed to stand for several hours, after which it was depressurized and unloaded. There was no damage to the specimen or diaphragm. This test was repeated successfully three times.
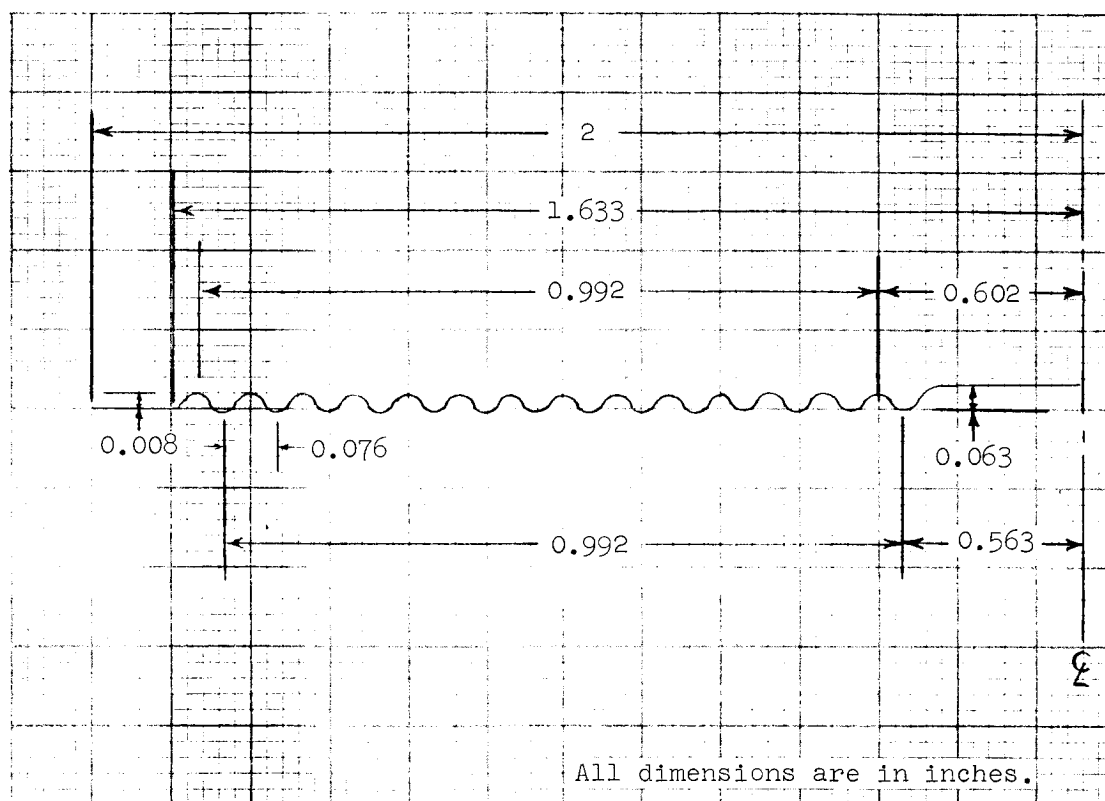
Figure 79. Convoluted Diaphragm From Carleton Controls Corp., E. Aurora, N.Y., Die No. 1693-701-000-030-1

As a back-up to the diaphragm-type permeation chamber, a chamber was designed retaining the bellows concept of the original design. Figure 80 compares the new bellows-type unit and the diaphragm-type unit. The bellows design has all the advantages of the diaphragm design (as compared to the original bellows apparatus shown in Figure 71) except possibly cost. The bellows design shown in Figure 80 is estimated to cost 10% to 20% more than the diaphragm unit.

diaphragm-type
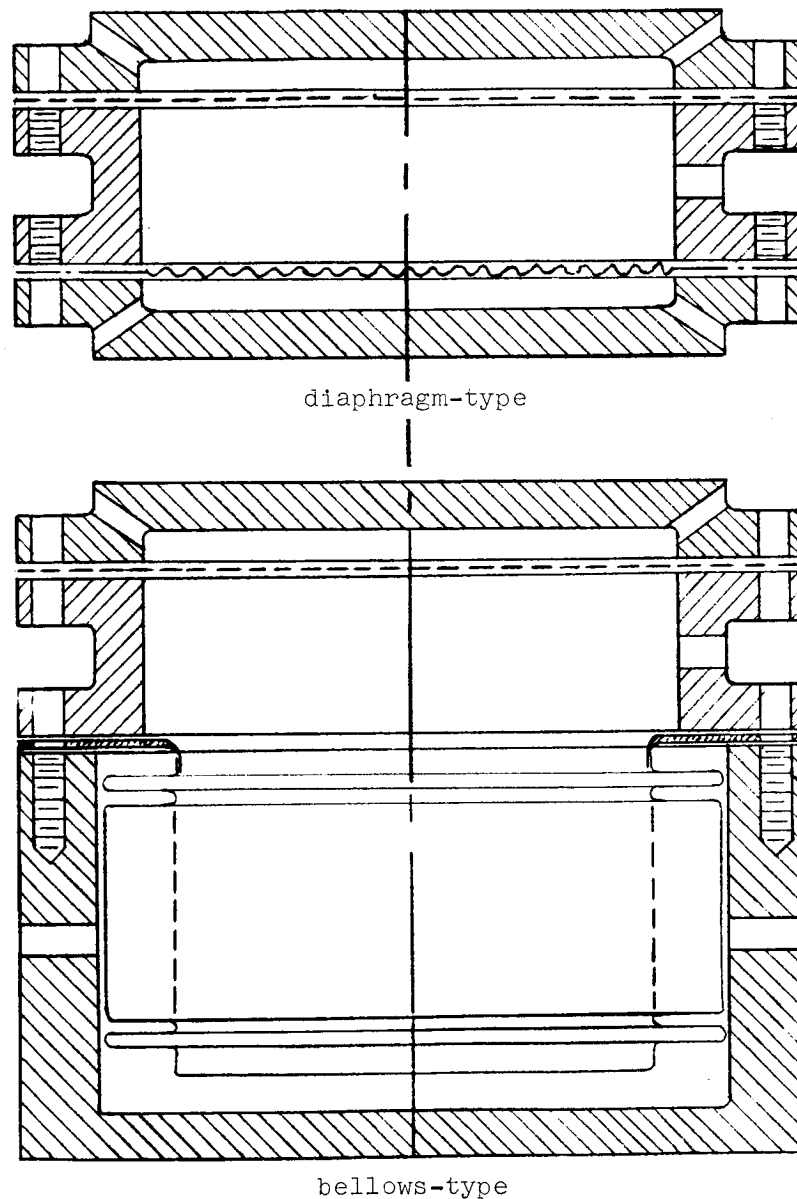
bellows-type

Figure 80. Diaphragm-Type and Bellows-Type Permeation Chambers

D.   DESIGN OF THERMISTOR DETECTOR

Thermistors are thermally-sensitive resistors whose primary function is to exhibit a change in electrical resistance with a change in temperature. They are hard, ceramic-like electronic semi-conductors which exhibit a relatively large negative temperature coefficient of resistance.

For thermal conductivity measurements, thermistors are usually wired into a Wheatstone bridge circuit (see Figure 81). In operation, a current flowing through the thermistor results in an increase in the thermistor temperature (and a decrease in resistance). If the volume around the thermistor is filled with a gas, the heat transferred from the thermistor to the walls of the container, at equilibrium conditions, is equal to the heat generated by the current in the thermistor.
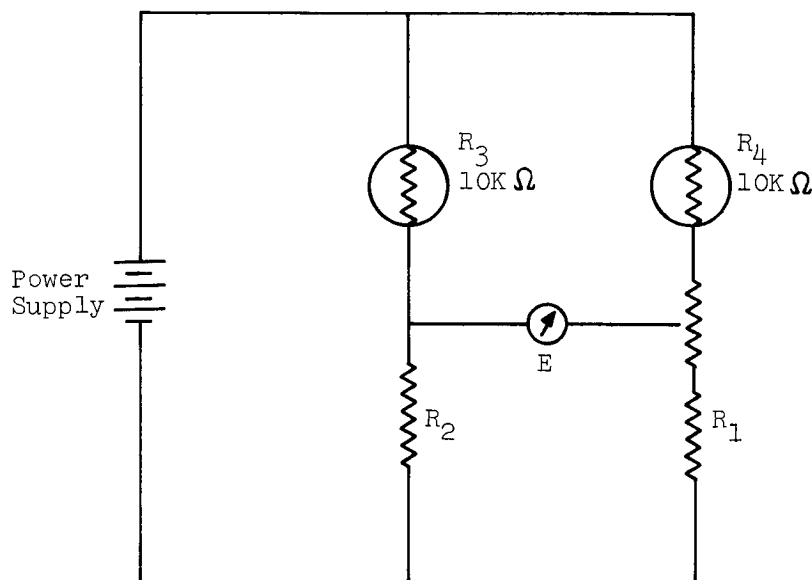
Notes:
A. R_1 and R_2 are matched, fixed resistors.
B. R_3 is a matched reference thermistor.
C. R_4 is a sensing thermistor.

Figure 81. Typical Thermistor Bridge Circuit

1.   Theoretical

If the thermistor temperature, t_b, the ambient wall temperature, t_a, and the current are maintained constant, the out-of-balance voltage, E, of the bridge is given by (Reference 23):

$$E = \frac{1}{4} \, I \, R_{t_b} \, \frac{\alpha (t_b - t_a)}{1 + \alpha t_b} \, \frac{\Delta k}{k} \, \frac{2\gamma}{1 + \gamma} \tag{64}$$

Where:

I = total bridge current

R_{t_b} = resistance of the thermistor at t_b

α = temperature coefficient of resistance of the thermistor

t_b = thermistor bead temperature

t_a = ambient temperature

k = thermal conductivity of the pure reference gas

Δk = change in thermal conductivity with an incremental addition of a contaminant gas or vapor

γ = a value such that $R_1 = R_2 = \gamma R_3 = \gamma R_4$ (Figure 81)

$\dfrac{2\gamma}{1 + \gamma}$ = constant for a given bridge circuit

Under these conditions, it is seen from Equation (64) that the bridge will remain in balance; i.e., $E = 0$, when $t_b = t_a$ and when $\Delta k = 0$; therefore, the bridge unbalance is directly proportional to $t_b - t_a$ and to Δk.

The degree of unbalance increases with the value of $t_b - t_a$. The voltage output can be increased by several orders of magnitude if the thermistor is operated at a sufficiently high temperature. However, in a static system, it is expected that the effects of convection will become appreciable when $t_b - t_a$ is large. Treatment of convection and radiation effects is complicated and beyond the scope of this report.

The sensitivity of detection, i.e., the change in voltage output with change in gas composition, is a direct function of $\Delta k / k$, the relative change in thermal conductivity.

For this program, calculations were made for systems using nitrogen as the pressurizing gas, and for systems using helium as the pressurizing gas. Typical calculations showing the effect of thermistor operating temperature and thermistor resistance are shown in Appendix I.

Complete evaluation of the detector requires a knowledge of the cell constant, a (to determine the value of $\sqrt{a}$ in Equation 82a of Appendix I), and of the value of $\Delta k / k$. The cell constant, a, is a function of the ratio of the surface area of the thermistor bead to the volume of the cell or chamber, and is a constant for a particular chamber.

There was insufficient experimental data obtained to make a complete evaluation of the detector; however, the experimental work indicates that there is a direct correlation between thermal conductivity data expressed in microwatts/cm °K and thermistor bridge response (see Table 5).

Theoretical thermal conductivity data were determined for He/H_2, He/O_2, He/N_2, He/F_2, and N_2/N_2O_4 mixtures. (The first gas in each case is the major component of the mixture, i.e., pressurizing gas; the second is the contaminant at propellant vapor.) Figures 82 and 83 show these data, in microwatts/cm °K, for various contaminant concentrations up to 0.10 mole fraction.
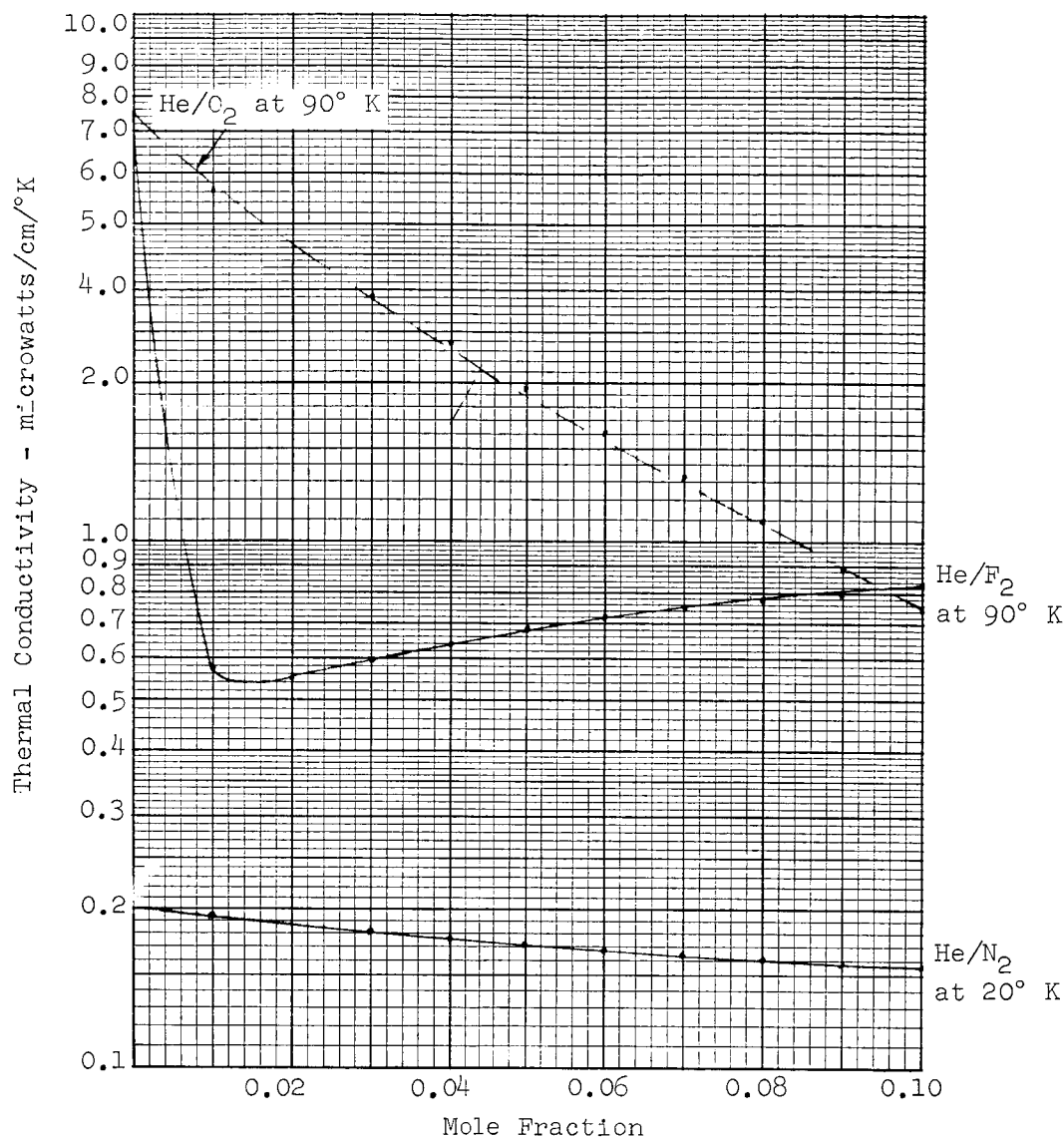
Figure 82. Thermal Conductivity of Mixture of Helium and Cryogenic
Propellant Vapors Near Their Boiling Points

2. Experimental Work

To determine the type of response and degree of bridge unbalance to be expected
with the propellants, several exploratory tests were made with a Veco (Victory Engineering
Co.) M-142, diffusion-type, thermal conductivity cell. Propellant vapor was injected by
means of a hypodermic syringe through a rubber septum.

Tests with UDMH vapor in nitrogen showed an appreciable increase in bridge out-
put (over pure N2) which was in nearly direct proportion to the increase in vapor added. The
response time was short.
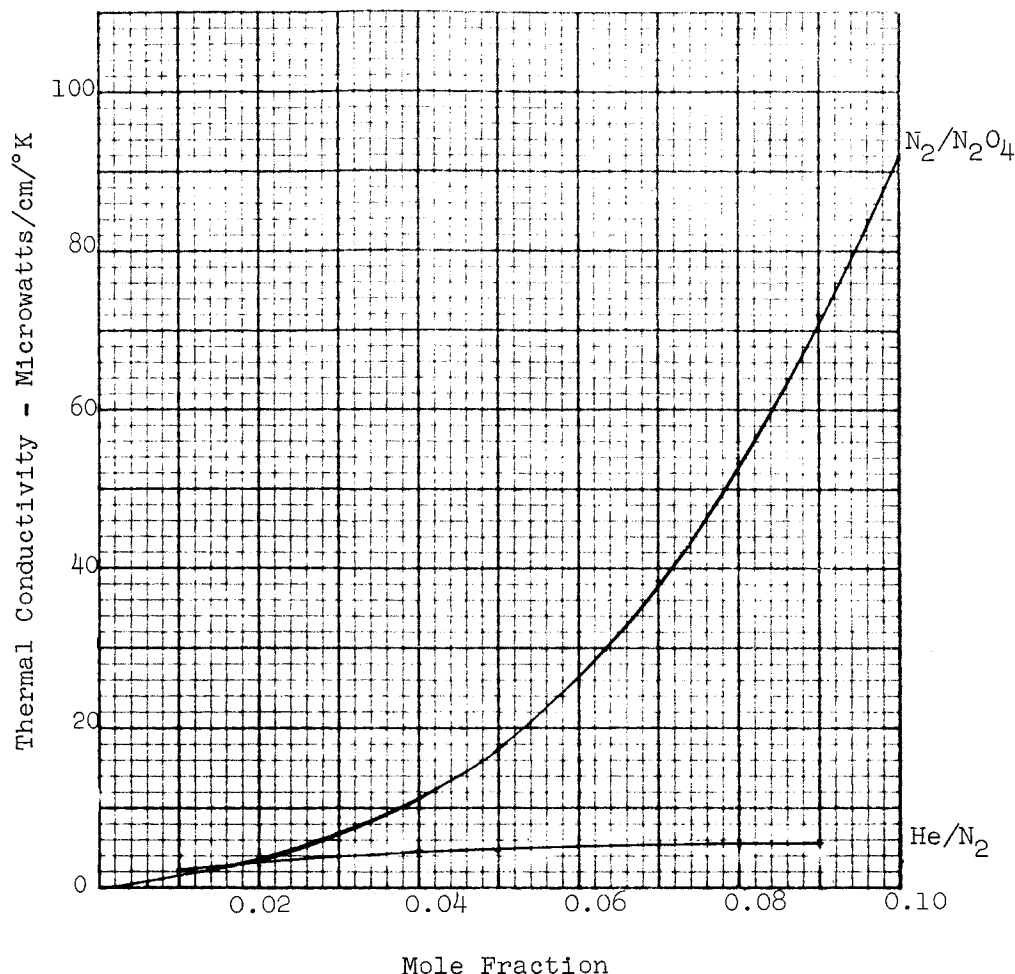
Figure 83. Thermal Conductivity of N_2/N_2O_4 and He/N_2 Mixtures Near the Propellant Boiling Points

Tests with N_2/N_2O_4 mixtures resulted in a rapid signal increase which reached a maximum and then slowly decreased until a steady state was reached. The maximum signal was found to be proportional to the increase in N_2O_4 concentration. However, in permeation tests, the increase in propellant vapor will be continuous and not incremental. Therefore, the steady-state signal is of interest. The observed response for N_2O_4 was believed to result from the fact that the vapor is an equilibrium mixture of N_2O_4 and NO_2, and a steady signal output is reached when chemical equilibrium is achieved under the temperature and pressure conditions in the cell. This same phenomenon was observed with the permeation chamber and thermistor.

These preliminary tests determined gross relative cell response (that is, without regard to time rate of change) for CO_2, N_2O_4, UDMH, N_2, and He referenced to air. The Veco unit was limited to a maximum pressure of 20 psig. This fact, along with the need to have the sampling volume similar to that of the actual permeation chamber, negated requirements for more than gross response measurements and for additional testing with this unit.

The bridge circuit used with the Veco cell is shown in Figure 84. This circuit also included a third thermistor exposed to the ambient wall temperature to provide temperature compensation when a meter (or other power-consuming read-out device) was used instead of a high impedance amplifier/recorder.

For extended-time permeation tests, the circuitry allowed either battery power supply or external power supply. In addition, provisions were made to include a variety of thermistor resistances to enhance the maximum response for a particular test.

Following these tests, a thermistor detector probe was constructed for the permeation chamber. To keep the construction relatively simple, a single plug contained both the reference and sensing thermistors side by side. The reference thermistor was sealed in a small glass bead containing an air atmosphere; a ceramic dental cement was used for the seal. The sensor thermistor was exposed to the test gas or vapor. The four leads were fed through a drilled-out stainless steel plug which was inserted in the port on the middle section of the apparatus (see Figure 74). Figure 85 shows a probe installed in the permeation chamber.

The two thermistors in the probe were connected to the bridge circuit previously described and shown in Figure 84. Figure 86 shows the complete permeation apparatus and Figure 87 shows the apparatus used for calibration work.

The thermistor resistances used for calibration and test work were 300 and 1000 ohms (at room temperature). The 300-ohm thermistors were selected for cryogenic use, and the 1000-ohm thermistors were selected for ambient temperature tests.

3. Discussion of Thermistor Detector Design Problems

The sensing thermistor in the design just described was exposed to the contaminant. The thermistors were coated with an epoxy. To prevent the propellant vapor from attacking the thermistor and, particularly, the epoxy coating, the sensing thermistor was coated with the ceramic dental cement. It was determined that this coating was not seriously affected by moderate concentrations of UDMH-N_2O_4 vapor. The thermistors can be purchased without the epoxy coating; however, the manufacturer, Yellow Springs Instrument Co., Yellow Springs, Ohio, will not guarantee their precision. The units are matched thermistors with room temperature resistances guaranteed within 1%. (The slightest chip of the hard, brittle bead through mishandling will markedly affect the resistance.)

Initial calibration tests using the probe design just discussed, and pure nitrogen at various pressures, gave a bridge output of 20 millivolts at 7.7 atmospheres. Calculations showed a change in thermal conductivity by a factor greater than two. Reference to the literature (References 29 and 30) indicated that any such change at this pressure should not exceed 3%. Investigation pointed to convection as the most probable cause of the large output because convective heat losses are a function of the gas density. The output was noted to change with pressure changes. Therefore, a pressure transducer was installed on the gas side and its output recorded with that of the bridge. Thus, the convection/pressure effects could be calculated from the data subsequently obtained during calibration and test.

To reduce the complexity of the test apparatus for field use and, in particular, to eliminate the pressure transducer, consideration was given to different detector designs to reduce the effects of convection.
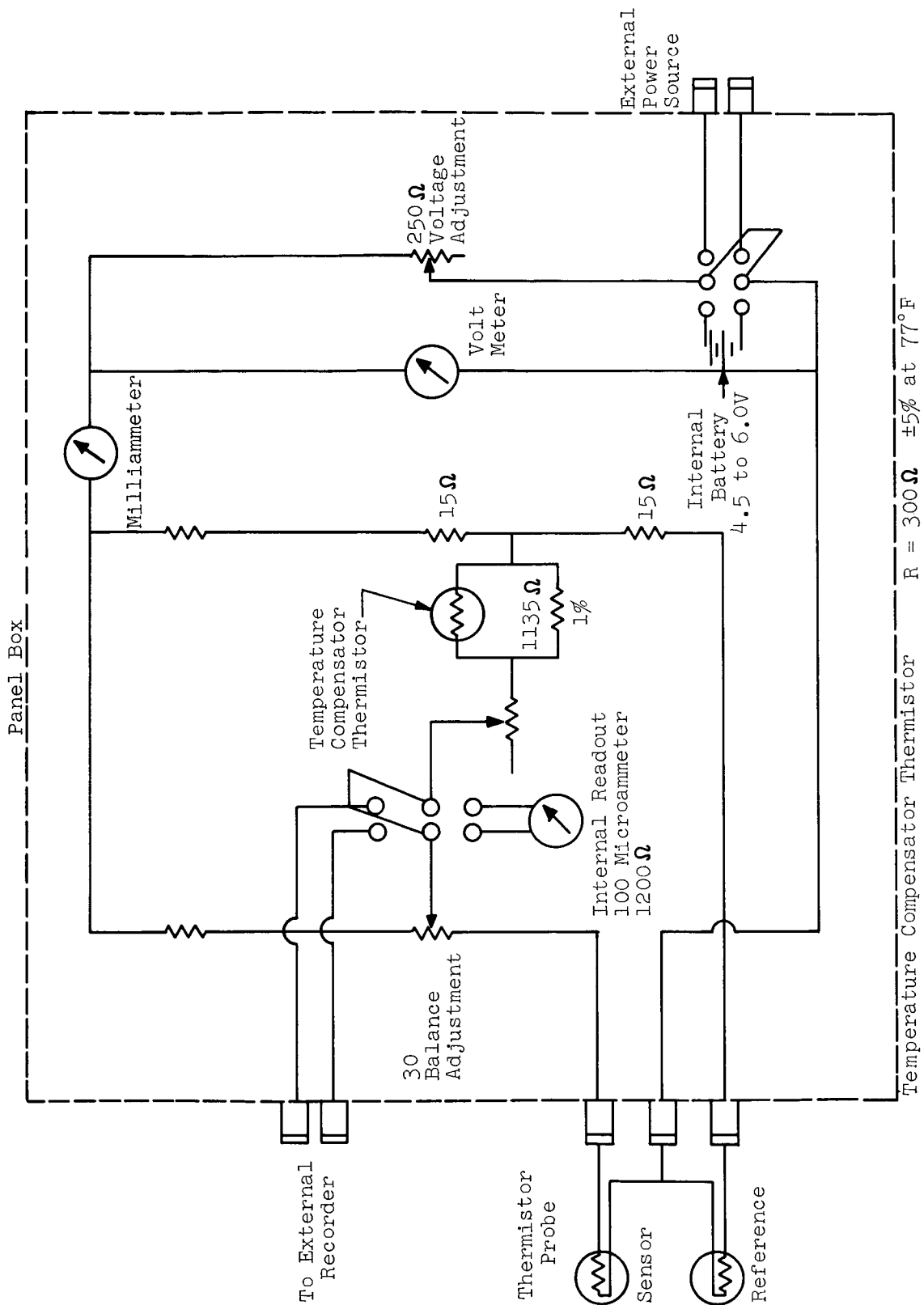
Figure 84. Thermistor Detector Bridge Circuit
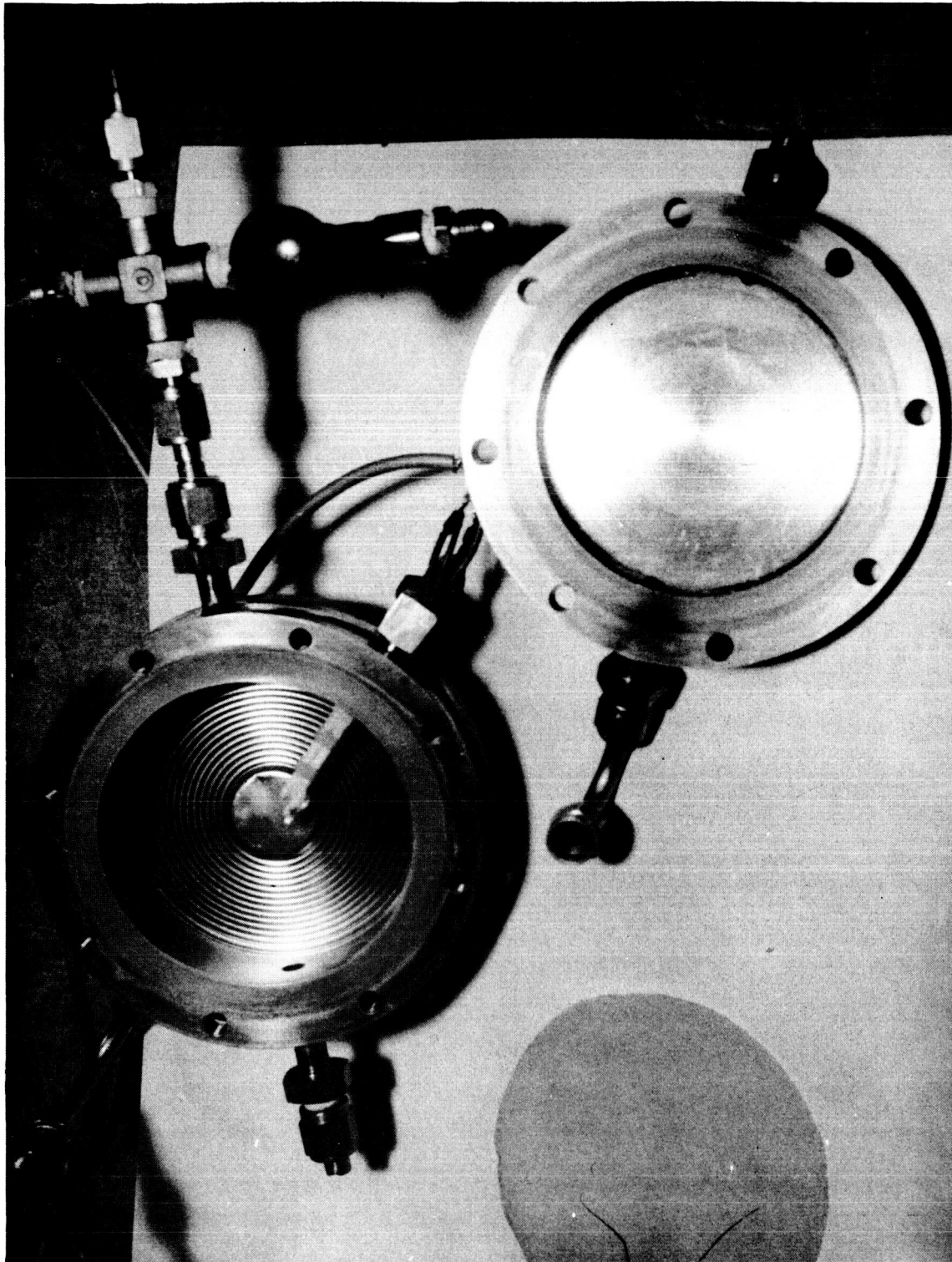
Figure 85. Interior View of Permeation Chamber Showing Diaphragm and Thermistor Detector Installed
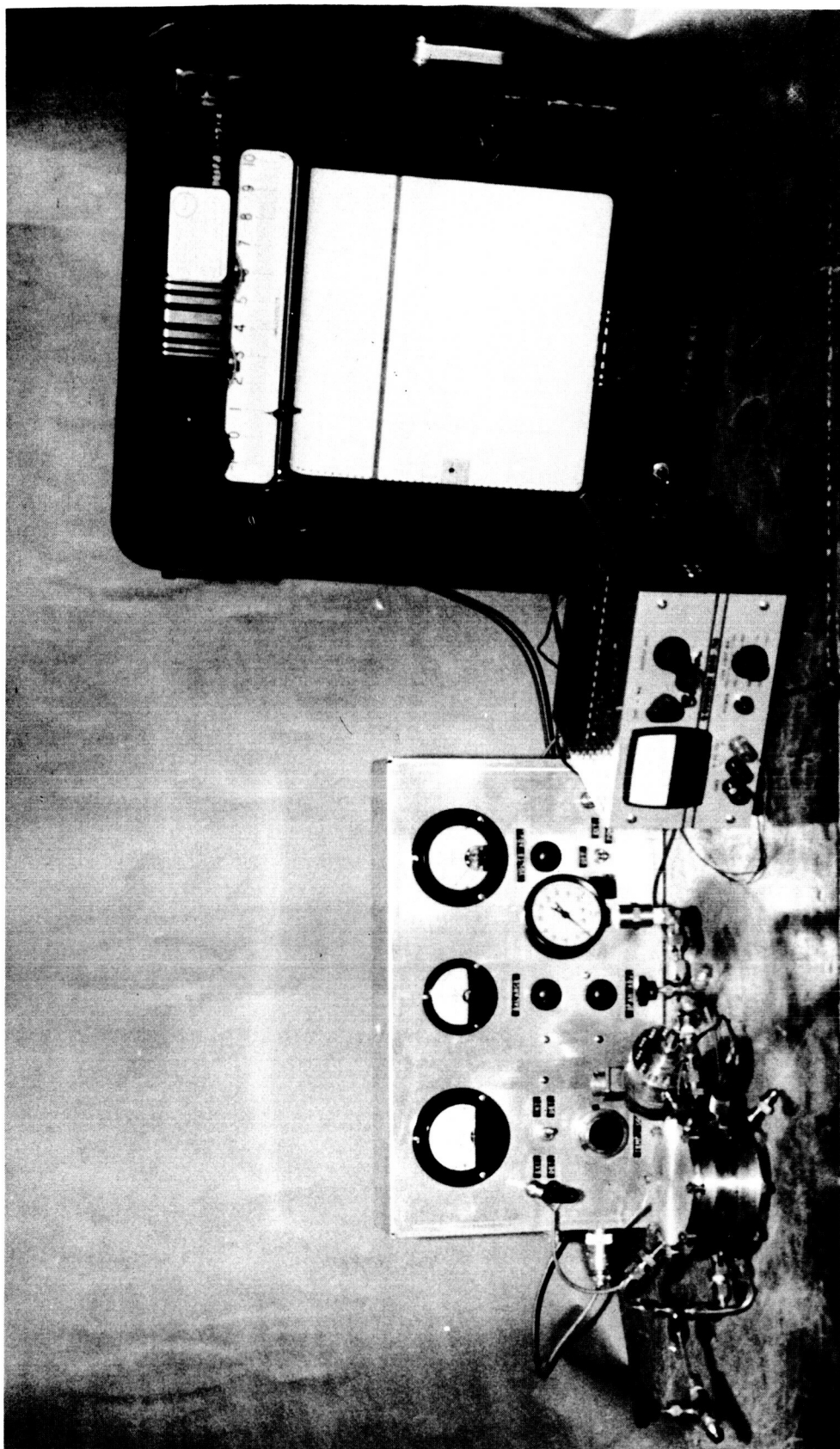
Figure 86. Complete Permeation Apparatus
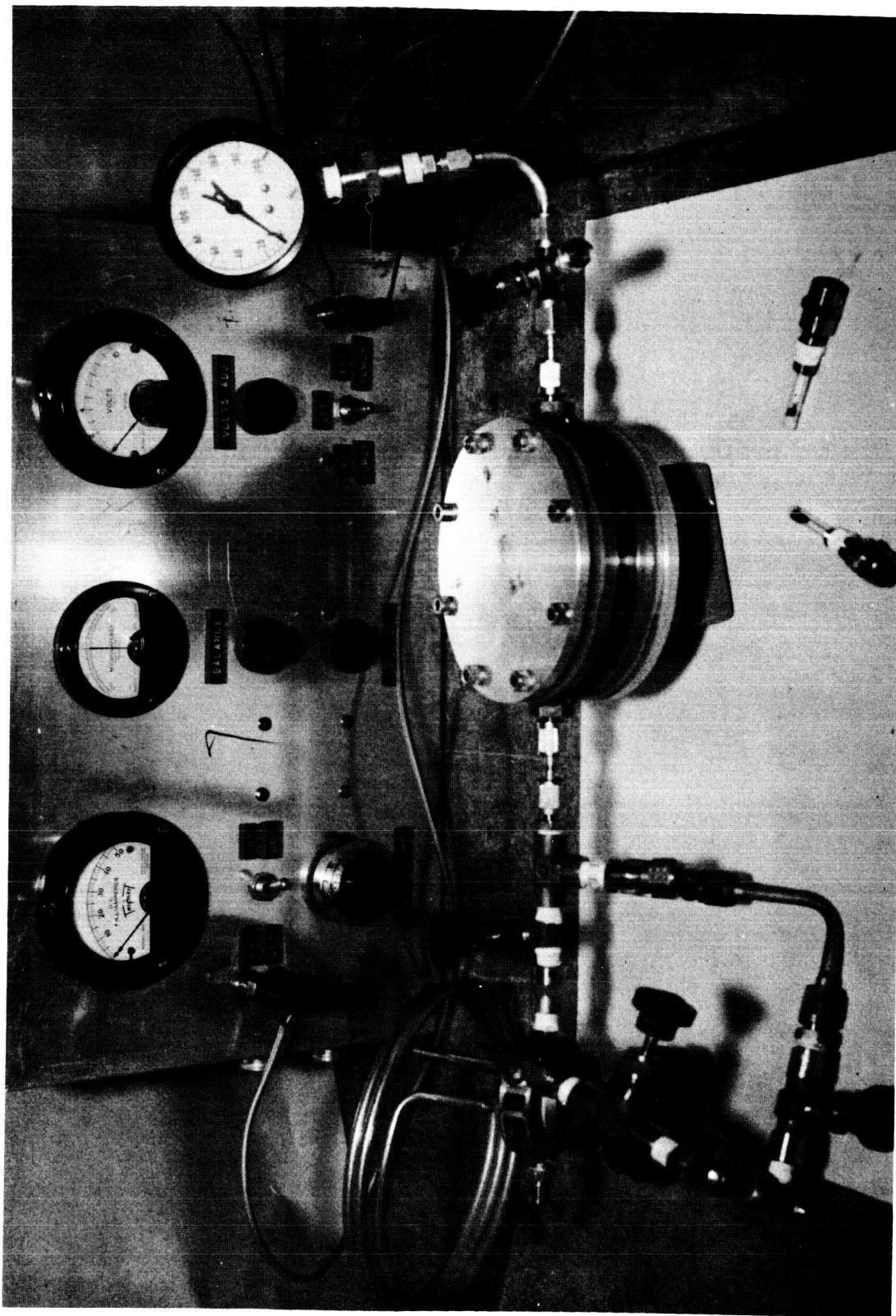
Figure 87. Apparatus Used for Calibration

The use of an insulation material such as micro-quartz in the gas volume to eliminate or at least minimize convection currents was decided against because of changes in the surface-to-volume ratio and the possibility of absorption problems.

An alternate detector design used a sealed glass tube for each thermistor (the sensing thermistor was thermally connected to the test gas via an aluminum alloy plug). This design was less susceptible to convection because of its larger area and lower surface temperature. Two such units completed the bridge circuit. A pair of thermistor assemblies of this design are shown in Figure 87. Construction details are shown in Figure 88. A third possible design for minimizing convection problems is shown in Figure 89. This design has not been fabricated.

The detector design problems encountered with cryogenic tests are discussed later in this section.

Aluminum Alloy Plug
(Cemented into Glass Tube)

Glass Tube

Reference Thermistor
(Suspended in Air)

Alumina Double
Bore Insulator

Stainless Steel
Fitting

Sensing Thermistor
(Cemented to Aluminum
Alloy Plug to provide
a good thermal path
to the test gas)
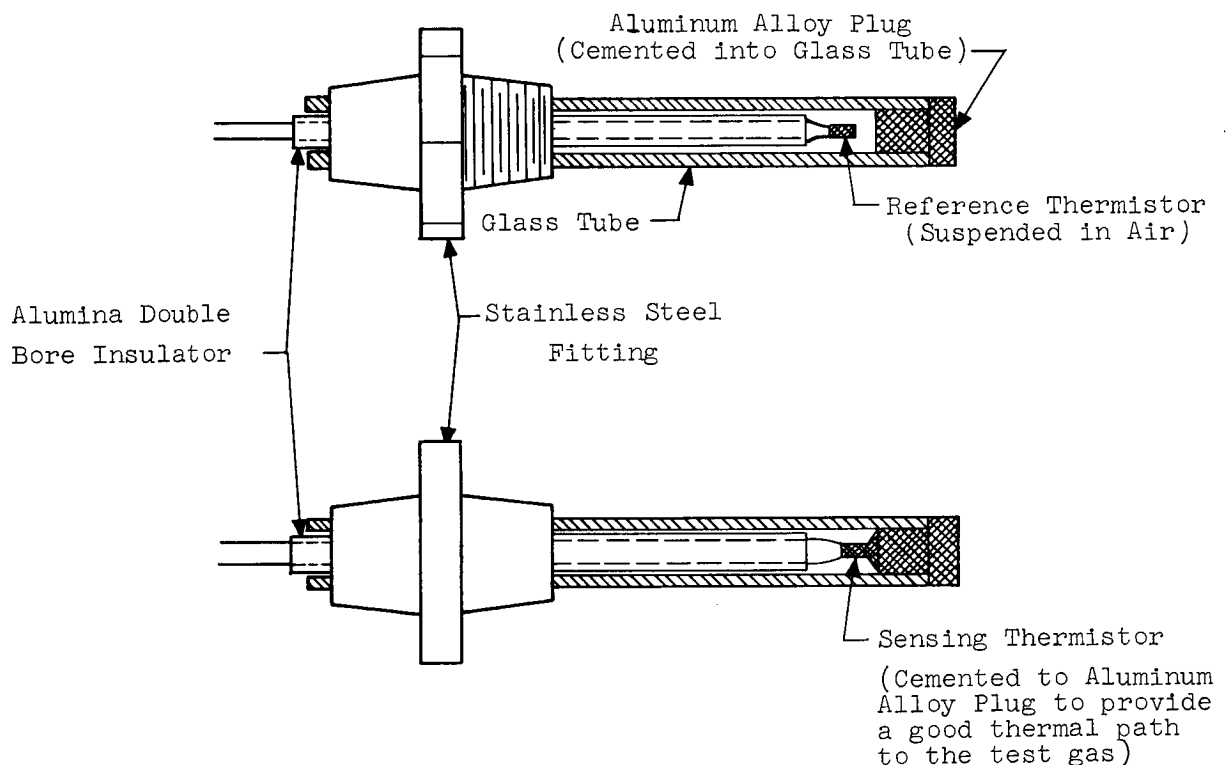
Figure 88. Modified Thermistor Detector Probes
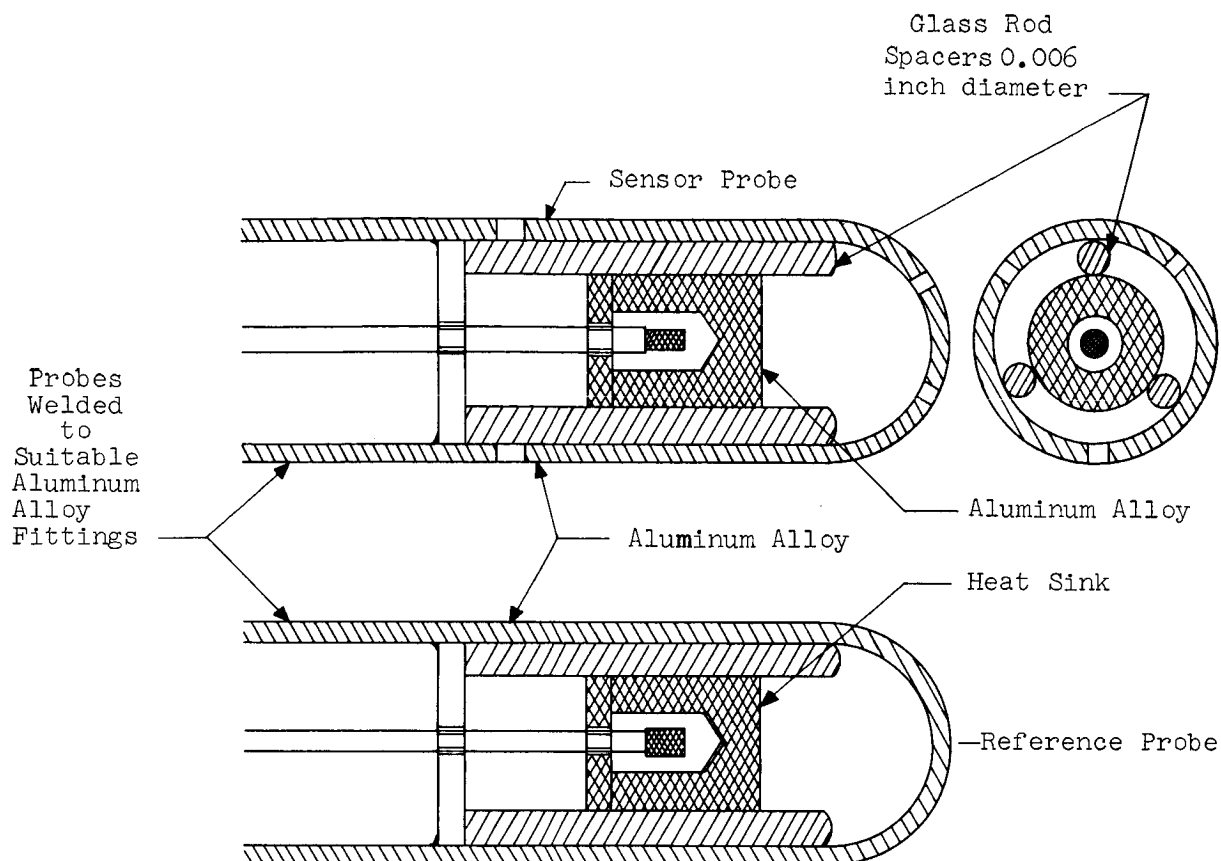
Figure 89. Proposed Design of Thermistor Detector Probes to Eliminate
Convection Difficulties

E. CALIBRATION TESTS

The calibration test setup is shown in Figure 87. Solid plates were bolted across the middle section of the permeation chamber for calibration; only the gas volume was of interest for these tests.

1. Calibration Procedure

In operation, the test chamber was purged with nitrogen and the thermistor bridge balanced at atmospheric pressure. The N_2O_4 vapor was then introduced into the test chamber by means of a Perkin-Elmer Precision Gas Sampling Valve, Catalog No. 154-0068. The N_2O_4 was allowed to flow through the valve to purge out any air or nitrogen and to allow the gas pressure in the sample volume to become equal to the vapor pressure of N_2O_4 at the test temperature. The N_2O_4 was then swept through the sampling valve into the test section.

Since the maximum operating pressure of the sampling valve was 50 psig, N_2 was passed through the valve until a 25-pound pressure was obtained, then the sampling valve was bypassed and the system pressurized to the desired total measure. Pressurization to 25 psig was equivalent to the passage of $\sim$ 15 volumes through the sampling valve (the volume of the chamber was approximately 200 cc) and was determined adequate for the complete transfer of the sample into the test section.

The thermistor bridge unbalance was observed on a dual range, 0-5/0-50 milli-volt Leeds & Northrup strip chart recorder. The time required to reach equilibrium at a given concentration and total pressure was from 10 to 30 minutes.

At the end of a test run, the system was vented to atmospheric pressure and purged with nitrogen until a constant recorder trace indicated that the system contained pure N_2 gas.

In practice, approximately 1.5 to 2 hours was required to obtain a single calibration point.

2. N_2O_4 Calibration Tests

Several problems with the detector probe, discussed under the section on detector design problems, were observed during the initial calibration tests. Two problems causing the most difficulty were: (1) variations in the output signal due to convection currents, and (2) attack on the thermistor coating by the higher concentrations of N_2O_4 vapor.

The calibration tests were stopped in favor of conducting permeation tests. These are described later under appropriate sections.

At a later date, a second apparatus was fabricated and put into service. With this apparatus, a few reproducible calibration points were obtained; however, there were too few to generate a satisfactory curve. As a result, an attempt was made to find a correlation between the power dissipation in the thermistor bridge, as a function of the bridge unbalance voltage, and the theoretical thermal conductivity of N_2/N_2O_4 mixture over the 0.0-0.10 mole fraction range.

Figure 90 is a plot of the power dissipated, in microwatts, corresponding to the thermistor bridge unbalance voltage over the full-scale range of the recorder. Compare these data with the theoretical conductivities of the N_2/N_2O_4 and He/N_2 mixtures shown in Figure 83.

It may be fortuitous that the two curves indicate that there exists the possibility of a direct correlation between the bridge voltage and concentration corresponding to the same power dissipation.

Table 5 shows the results computed from Figures 90 and 83 for the few experimental calibration points obtained at 150 psig total pressure. The requirement that total pressure be constant was dictated by the data in Figure 91 which shows the response of the bridge to change in nitrogen pressure for the two probe designs.

The results shown in Table 5 are surprisingly good except at the maximum concentration. The relatively large deviations at the higher concentration are probably due to chemical interaction between the N_2O_4 vapor and probe, a problem mentioned previously in the section on detector design problems. Although the ceramic coating prevented rapid attack on the epoxy, apparently there was an absorption problem because it was observed that an appreciable quantity of N_2O_4 was desorbed when a probe was placed in a nitrogen atmosphere and run under the same voltage/current conditions as used in testing.

It is also apparent from the data that the reliable minimum detection limit for N_2O_4 is about 0.10% by volume (0.001 mole fraction).
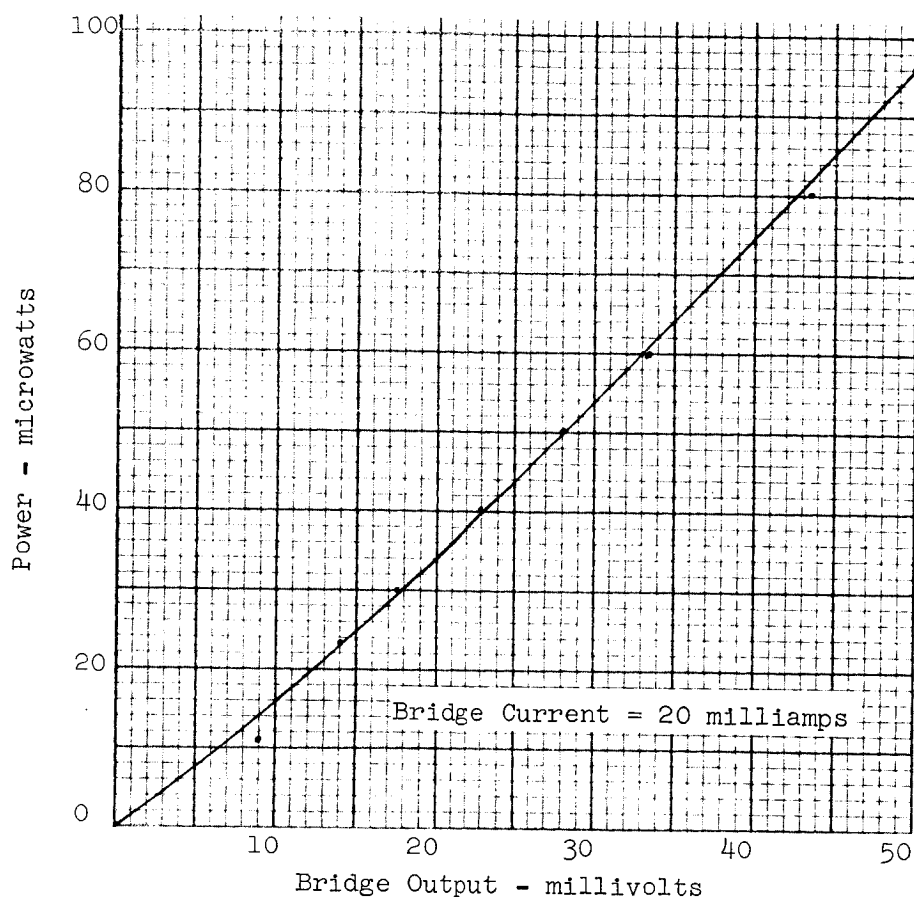
Figure 90. Power Dissipation in Thermistor Bridge vs Unbalance Voltage

TABLE 5

THERMAL CONDUCTIVITY OF NITROGEN/N_2O_4
MIXTURES OF KNOWN COMPOSITION

Mole Fraction (Measured)	Bridge Voltage (Millivolts) (Bridge Current = 20 ma)	Power Dissipated (Microwatts) (From Figure 90)	Mole Fraction (Calculated From Figure 83)
0.0118	1.6	3.0	0.010
0.0141	2.2	4.0	0.015
0.0177	2.7	5.0	0.018
0.0236	3.6	6.0	0.021
0.1157	23.7	41.7	0.073

(These data represent the increase in bridge voltage due to the introduction of N_2O_4 with reference to the bridge voltage for pure N_2 at the same total pressure.)
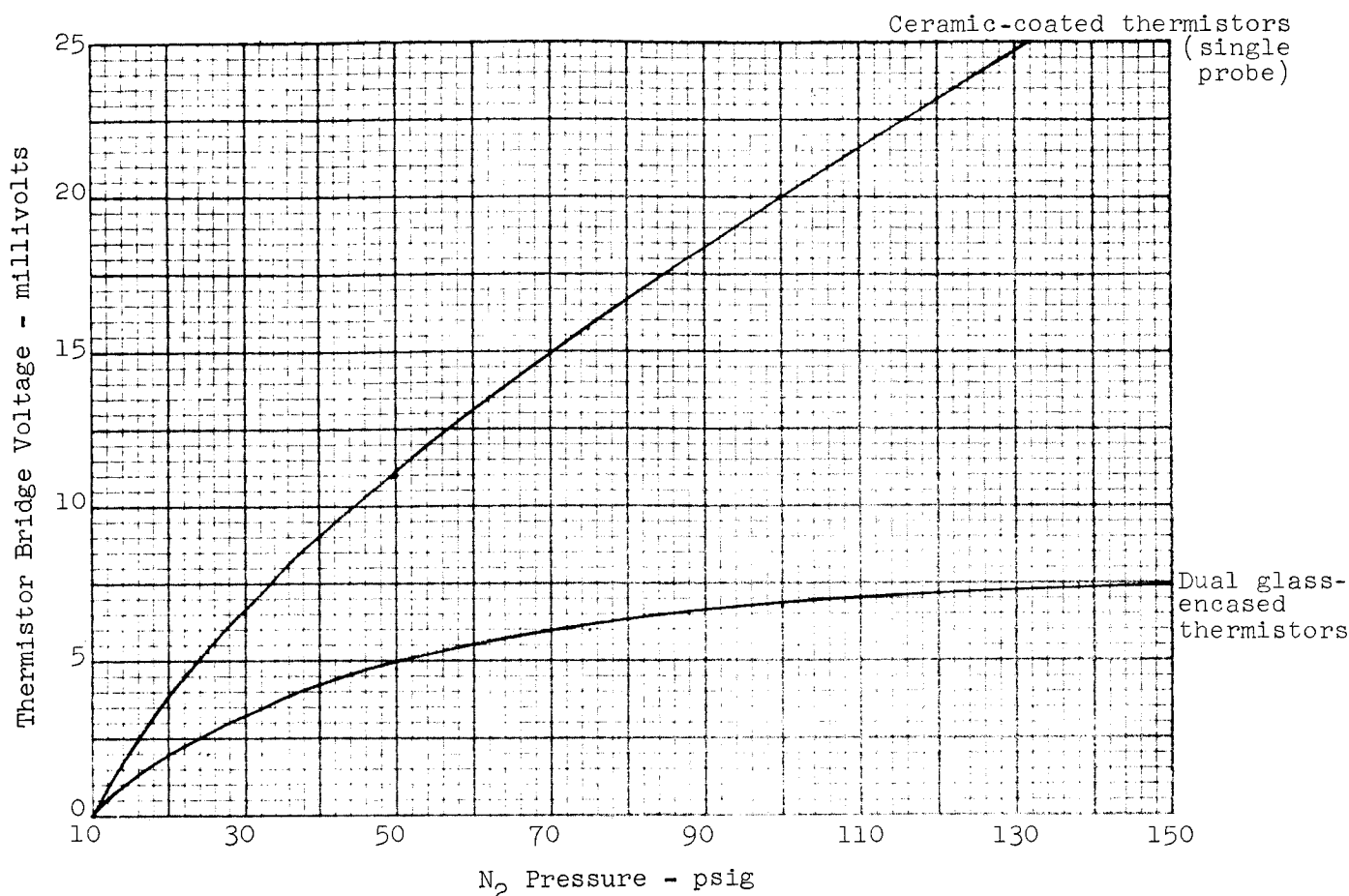
Figure 91. Thermistor Bridge Voltage vs N_2 Pressure

F.   PERMEATION TESTS

   1. N_2O_4 Permeation Tests

   Two N_2O_4 permeation tests were run with a 6-mil FE"/TFE laminated Teflon test specimen. The ceramic-coated thermistor probe was used for the tests. The operating procedures for the apparatus are presented in Appendix III.

   Figure 92 shows the test data taken from the recorder charts. The two plots indicate that the saturation level can be determined reproducibly. (The curves level out at approximately 23 millivolts which is equivalent to 46 microwatts. Figure 83 shows 46 microwatts equivalent to 0.076 mole fraction or approximately 76% saturation.)

   The importance of accurately knowing the pressure throughout the test became apparent during test No. 1. This value is important because both the bridge voltage and the mole fraction of propellant vapor are functions of the total pressure. It would be desirable if the pressure would remain constant (see Figure 91); however, the pressure will drop during a test. Pressurizing gas will permeate to the liquid side and dissolve in the liquid causing a pressure drop. (See Reference 1 for a more-detailed discussion of permeation.)
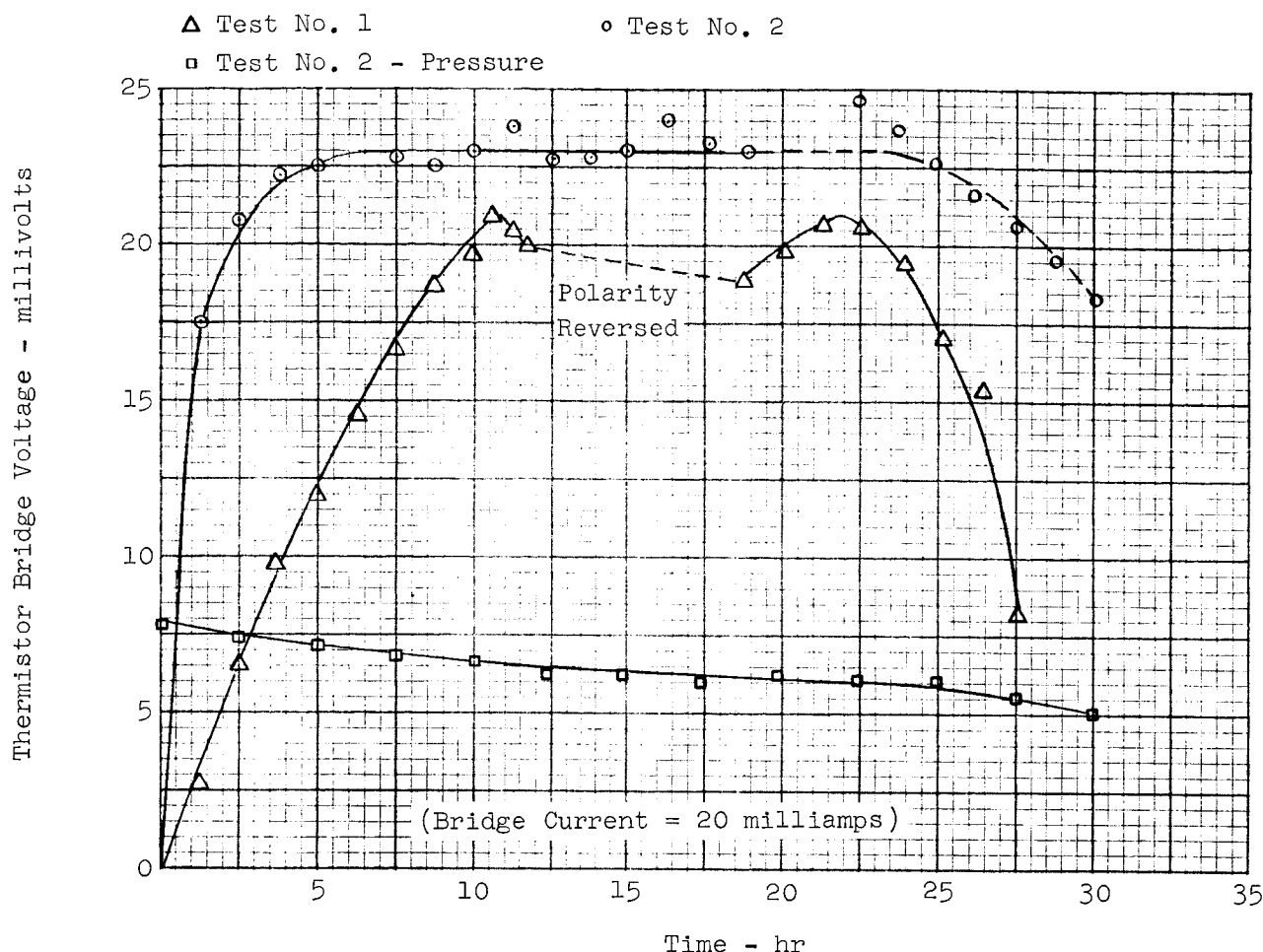
Figure 92. N_2O_4 Permeation Tests

In test No. 2, the pressure was continuously monitored by means of a pressure transducer output being recorded simultaneously with the thermistor bridge voltage. (In both tests, pressure decreased about 11 psi over a 24-hour period.) The rather abrupt decrease in bridge voltage after 24 hours of operation is probably due to failure of the seal on the reference thermistor (probable attack of the ceramic current by the higher concentration of N_2O_4 vapor in N_2).

The most serious point with respect to permeation measurements is the apparent discrepancy between the saturation times for the two tests. Zero time in the figure represents the time at which data recording was started after test pressure and temperature were reached. In the loading process, if the loading temperature and pressurization rate are not reasonably reproduced, discrepancies of this type would occur.

2.   UDMH Permeation Tests

Two tests were conducted with UDMH using 6-mil laminated Teflon specimens. Data for one of the tests, presented in Figure 93, is typical for the two tests. An initial pressure drop is experienced and the bridge voltage goes through a negative range. The

o - Pressure
x - Bridge Voltage
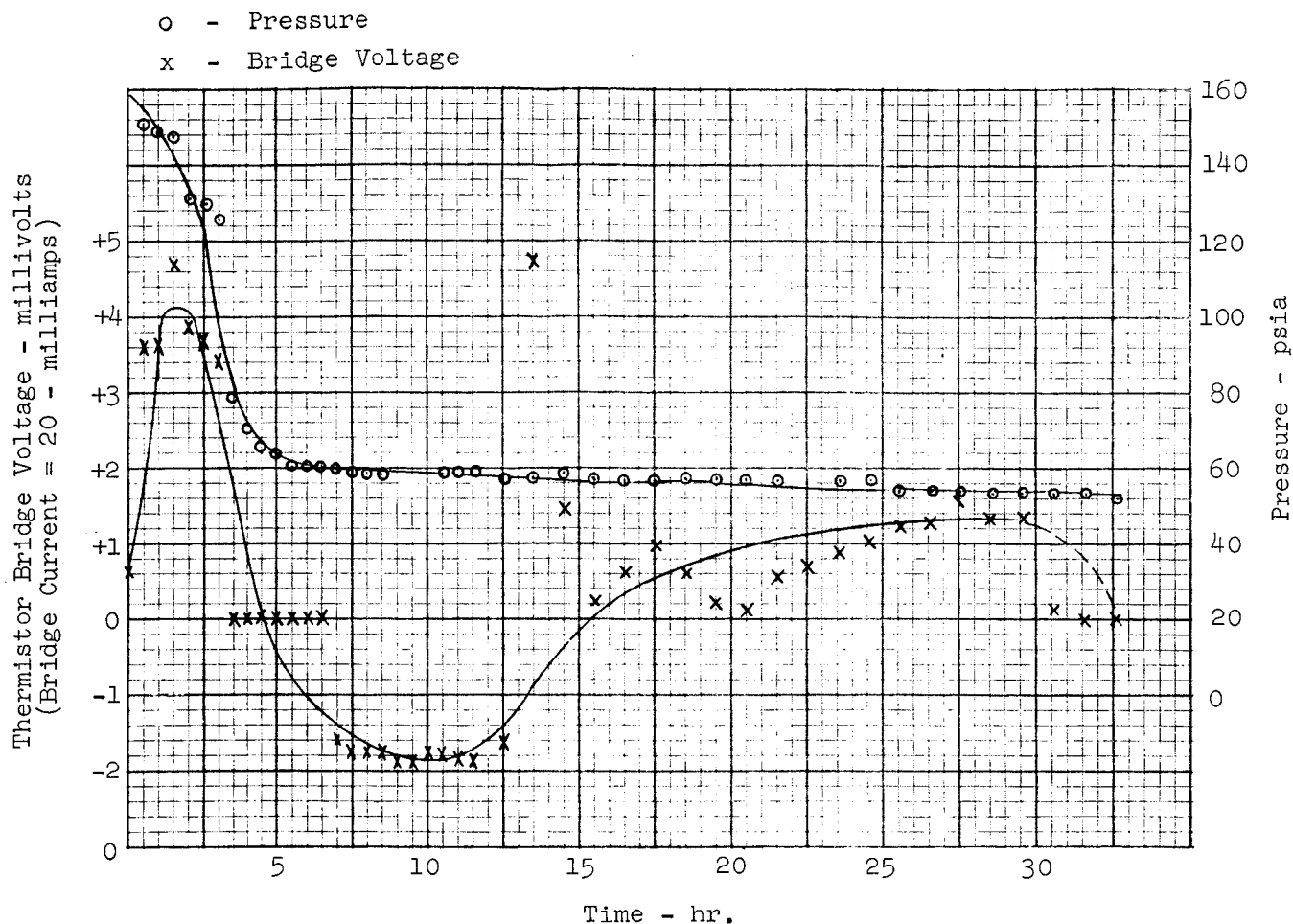
Figure 93. UDMH Permeation Tests

pressure drop is believed to be due to gas solubility in the liquid (N_2 was used for pressurizing the apparatus). A helium leak test indicated the apparatus to be leaktight. A high degree of saturation appears to have been reached after 25 to 30 hours. As with the N_2O_4 test, the drop in voltage may be due to attack on the thermistor probe by the high concentration of propellant.

The initial scatter or variation in bridge voltage is believed to be due to convection problems as a result of the pressure drop. Additional experimental work is needed to verify this.

There were no calibration tests conducted with UDMH vapor; therefore, the data cannot be converted to mole fraction of UDMH.

3. Cryogenic Permeation Tests

Cryogenic permeation tests, using the same power supply used for room temperature tests, were unsuccessful. The maximum voltage of 50 volts would not cause current to flow through the bridge. With the apparatus shown in Figure 94, still submerged in LN_2,

Report No. 8230-933007

Figure 94. Apparatus for Cryogenic Permeation Test

voltages (from a different power supply), up to 200 volts still would not cause current to flow. It was calculated that, at LN_2 temperatures, the thermistor resistance was of the order of 10^{14} ohms.

Efforts were directed toward finding other devices that might function at cryogenic temperatures and/or methods to make thermistors operable. Germanium diodes were

investigated, but their forward resistance changes, in going from ambient to liquid nitrogen temperature, were in the order of 50%, the same order of magnitude as for carbon resistors. The sensitivity in these cases would be several magnitudes less than with thermistors. Since sensitivity was considered to be of prime importance, efforts were continued with thermistors.

Independent methods of heating the thermistor to maintain its resistance in a usable range were considered. Two such methods were: (1) a carbon resistor with a drilled hole, in which a thermistor was cemented, and (2) a hollow Nobeloy resistor with a thermistor centered and cemented in its core.

A third method, and the most ideal, was to induce self-heating by maintaining a current in the thermistor during the transition from ambient to cryogenic temperature. This was accomplished with the use of a high-voltage supply wired with a large external series resistance to provide a constant current. With a current of 15 ma and 1.5 volts at room temperature, immersion in liquid nitrogen required an increase of about 60 volts across the thermistor. The calculated thermistor resistance value for these conditions indicated a thermistor temperature of 210°K. Operating conditions with continuous boiling of the nitrogen at the thermistor surface were stable. A second test using 30 ma constant current seemed to produce more vigorous boiling, although power dissipation was the same. The needle of the voltmeter wired across the thermistor oscillated during this test. It was assumed that this was caused by a change in the nature of the boiling at the thermistor surface, perhaps a nucleate-type boiling. The calculated resistance for this condition indicated a thermistor temperature of 241°K.

These tests indicate the variable range of a bridge supply voltage that must be provided for, and other factors that must be considered, in choosing a power supply to meet the needs of cryogenic testing.

The most significant factor is that power must be supplied to keep the thermistor above a certain temperature (indicated to be around 200°K for the 300-ohm Yellow Springs units); otherwise, the resistance increases sharply and it is virtually impossible to start current flowing again while the thermistor is at the low temperature. In other words, the thermistor acts as a thermal switch. The cutoff temperature is a characteristic of the particular make and resistance of the thermistor.

4.   Temperature-Cycling Tests

The purpose of this test was to try to determine if temperature cycling would have an effect on the amount of N_2O_4 that would permeate to the gas side of a Teflon membrane.

The apparatus consisted of two small stainless steel cups with flanges. The internal dimensions of each were 1.75 inch diameter by 0.75 inch deep, giving a volume of 30cc for each cup. The cups are bolted together with the Teflon specimen between the flanges. There was a valve on the liquid and gas sides, and a pressure gage on the gas side. For filling the liquid side, the liquid entered the valve and was allowed to overflow through a second port.

Two such units were prepared. The liquid side of each was loaded with N_2O_4 and sealed. (Valve closed and port capped off.) The gas sides were pressurized with nitrogen to 150 psig. One unit was kept in the hood in the laboratory and the second was placed in a

refrigerator at approximately 35°F for 24 hours, then in the hood for 24 hours and back in the refrigerator. The test ran for 5 weeks. The temperature in the hood varied between approximately 55° and 70°F.

At the conclusion of the test, the gas side of each unit was vented through a cold trap (dry ice and acetone) to collect the N_2O_4 that permeated to the gas side. The amount of N_2O_4 liquid collected in each U-tube was about the same, approximately 0.05 cc. The vapor space of both units was saturated with N_2O_4.

It was anticipated that the thermally cycled unit would have had a larger quantity of N_2O_4 on the gas side, a quantity in excess of the saturation level. The results of the test, therefore, are inconclusive. The test should be repeated with one unit being subjected to a broader temperature fluctuation and the other unit maintained at a temperature within 1° or 2°F of the reference temperature, e.g., 70°F ± 2°.

G.   CONCLUSIONS

The following conclusions pertain to the permeation work:

(1)   A permeation apparatus of relatively simple design has been tested and its integrity demonstrated.

(2)   The feasibility of using the change in thermal conductivity of a pressurizing gas, caused by contamination by propellant vapor, to monitor permeation tests, and under static conditions, has been demonstrated.

(3)   There are many different makes and types of thermistors. The scope of this program precluded the investigation of the many different thermistors to find the optimum design suitable for this unique application of thermistors. This area warrants further investigation.

(4)   The permeation chamber is designed for a pressure of 200 psig. If testing is to be done at substantially lower pressures, the construction can be made lighter (and cheaper). Serrated surfaces are used for sealing at the flanges. The use of propellants (and many other liquids) precludes the use of a more-simple O-ring seal, particularly for long-duration tests. For lower test pressures, a simpler seal would suffice.

(5)   With the permeation test apparatus as described, an apparent direct correlation was found between the power dissipated in the thermistor probe at a given bridge unbalance and the electrical equivalent of the theoretical thermal conductivity of the N_2/N_2O_4 mixture as calculated from Wassiljewa's equation and the semi-empirical equations of Lindsay and Bromley. (Experimental work is required to determine if this relation holds for other gas/vapor mixtures. Data are not available for theoretical calculations for many of the propellants of interest.)

(6)   The permeation tests conducted with N_2O_4 and UDMH demonstrated the feasibility of the design of the apparatus; however, further development is required to improve the thermistor probe design and to remove some of the electrical "noise" from the system.

(7)   Convection currents within the permeation chamber, resulting from pressure and temperature changes, cause the bridge output signal to vary and introduce "noise" into the system. The "noise" level will determine to a great extent what

minimum concentration of contaminant can be detected. The use of different types of thermistors, different probe designs, precise environmental temperature control, more sophisticated bridge circuits, and readout devices will minimize the "noise" and improve the minimum detection level. On the other hand, an appartus for general field use dictates as simple a design as possible. The tradeoffs involved warrant further study.

(8) Using a high-impedance millivolt readout device, the reproducible detection range for N_2O_4 is from a mole fraction of 0.001 (0.10% by volume) to the saturation level (vapor pressure at the test temperature).

(9) The use of thermistors at cryogenic temperatures requires more-sophisticated accessory equipment and test procedures. Power must be supplied before exposure to the low temperature, and must be capable of being varied during immersion into the cryogenic, and while being withdrawn from the cryogenic. Actually, the voltage is varied to maintain some safe current levels, to maintain a thermistor bead temperature, below which the resistance increases abruptly to a very high value. Upon withdrawal from the cryogenic, the voltage must be reduced to prevent damaging the thermistor.

SECTION 5

OPTIMUM ENVELOPE INVESTIGATION

A.   PURPOSE AND OBJECTIVES

The envelope investigation was conducted to determine if an optimum envelope exists for a given fuel requirement. The study was concerned with a basic geometric shape. The efficiency of this basic shape was related to and analyzed in terms of basic tank requirements. Emphasis was placed on presenting these parameters in an easy-to-analyze form, the end result being a method of quick evaluation of many basic shapes to provide a starting point for a conventional detailed design analysis. Also, provision was made to analyze various spans of plastic range deflection bellows.

The tank specification was assumed to have the following requirements:

(1)   Loadable propellant volume.

(2)   Required burst pressure of tank shell.

(3)   Tank shell material.

This analysis method is employed by assuming a series of radii and making a weight estimate for each. The resulting data are then presented on a radius-weight plot which defines the minimum weight configuration for a particular bellows span. This can be done for all three spans presented. Bellows spans can be further refined with a more-detailed design analysis.

B.   METHOD OF ANALYSIS

The initial step in the analysis is to assume a radius and bellows span. First to be determined is the thickness of the cylindrical shell section. The relationship for this is:

$$t = \frac{Pr}{S} \tag{65}$$

The nomenclature for this relationship and others is shown on Figure 95. Note that one of the heads is in a normal position while the other is inverted. For this analysis, the normal head thickness is assumed to be the same as the thickness of the cylindrical section, for both the elliptical and hemispherical heads. The elliptical head has an axis ratio of 2:1.

The increase in thickness of the inverted head is related to the basic shell thickness by a factor n. This factor for the 2:1 ellipse is:

$$n = \sqrt{\frac{4S^2}{0.366EP}} \tag{66}$$

a   = L/2r ratio
A_{sc} = Surface area of cylindrical section
A_{se} = Surface area of elliptical end
A_{sh} = Surface area of hemispherical end
b   = Bellows span
c   = Bellows expansion ratio extended length/nested length
E   = Modulus of elasticity
h   = Maximum bellows pitch
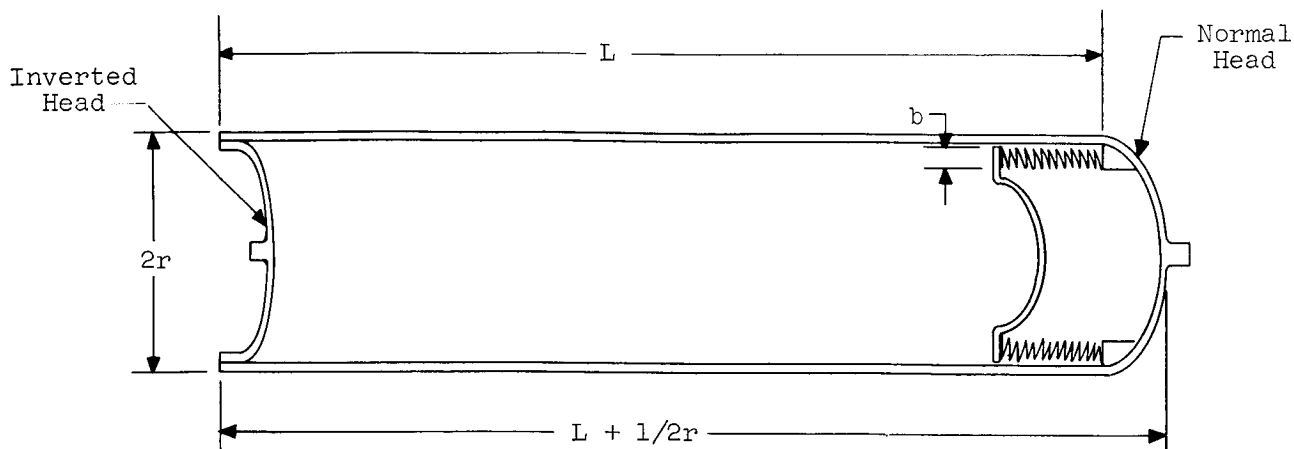
L   = Length of cylindrical section
P   = Design burst pressure
r   = Inside radius
S   = Ultimate tensile stress of material
t   = Cylindrical wall thickness
V_L = Loadable volume
V_T = Total internal volume of tank
η = Volumetric efficiency

Figure 95. Tank Nomenclature

where s is the ultimate tensile strength of the material. For the inverted hemispherical head:

$$n = \sqrt{\frac{S^2}{0.366EP}} \qquad (67)$$

Figures 96, 97, and 98 give the relationship between the loadable tank volume and the total tank volume. This represents the volumetric efficiency of the tank. Because of the symmetrical addition and reduction of the head volumes, the total tank volume is given by:

$$V_T = \pi r^2 L \qquad (68)$$

The internal volume of the bellows is:

$$V_L = \left(\frac{c-1}{c}\right) \pi (r - 1/2b)^2 L \qquad (69)$$

where the factor $\left(\dfrac{c-1}{c}\right)$ accounts for the volume lost in nesting the bellows and (r-1/2b) for the volume lost between the mean bellows diameter and the tank wall.
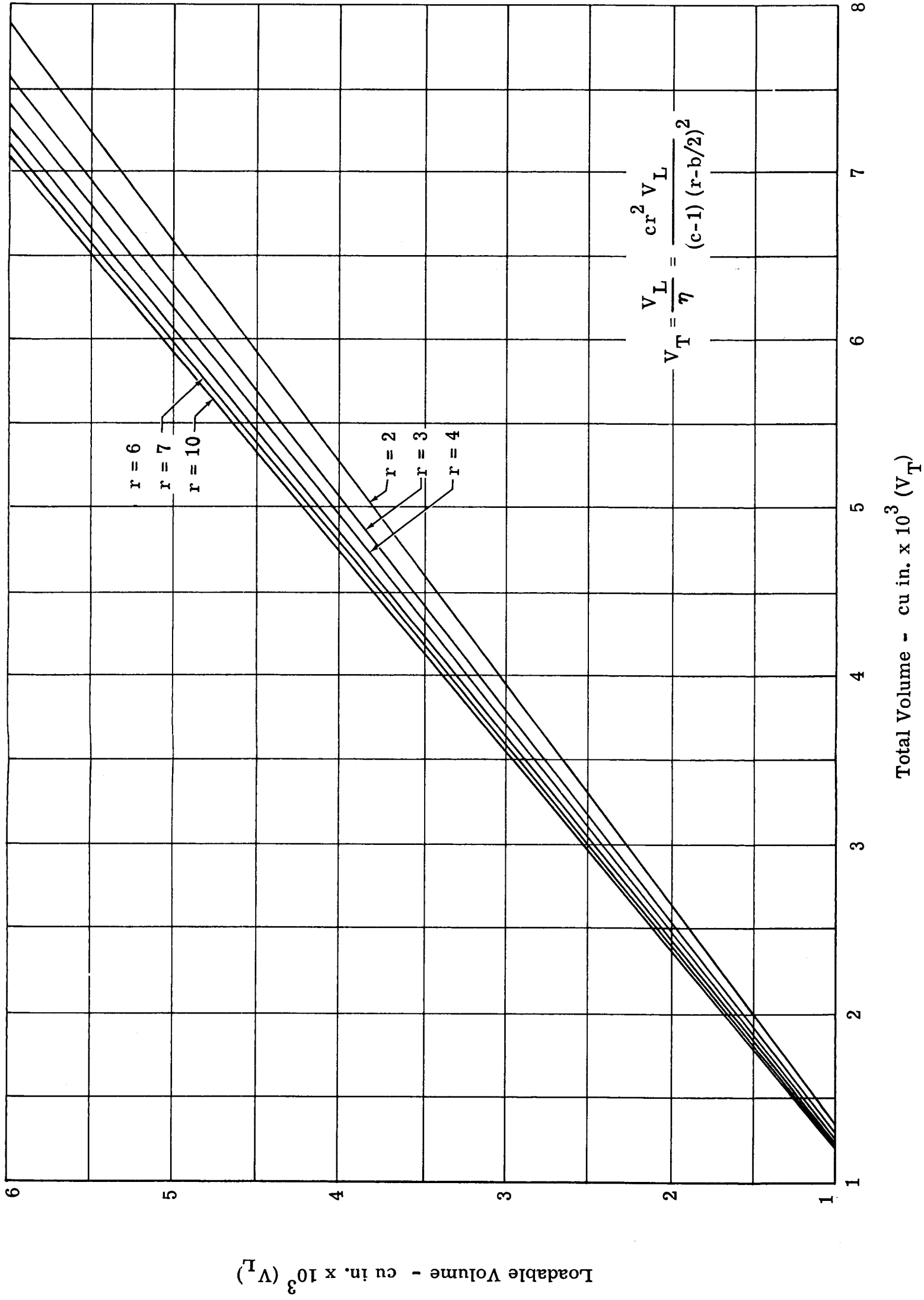
Figure 96a. Volumetric Efficiency Effect; 0.25 Span, 7.50 Expansion Ratio

$$V_T = \frac{V_L}{\eta} = \frac{cr^2\,V_L}{(c-1)\,(r-b/2)^2}$$

Total Volume – cu in. x 10^3 (V_T)

Loadable Volume – cu in. x 10^3 (V_L)

r = 6
r = 7
r = 10

r = 2
r = 3
r = 4
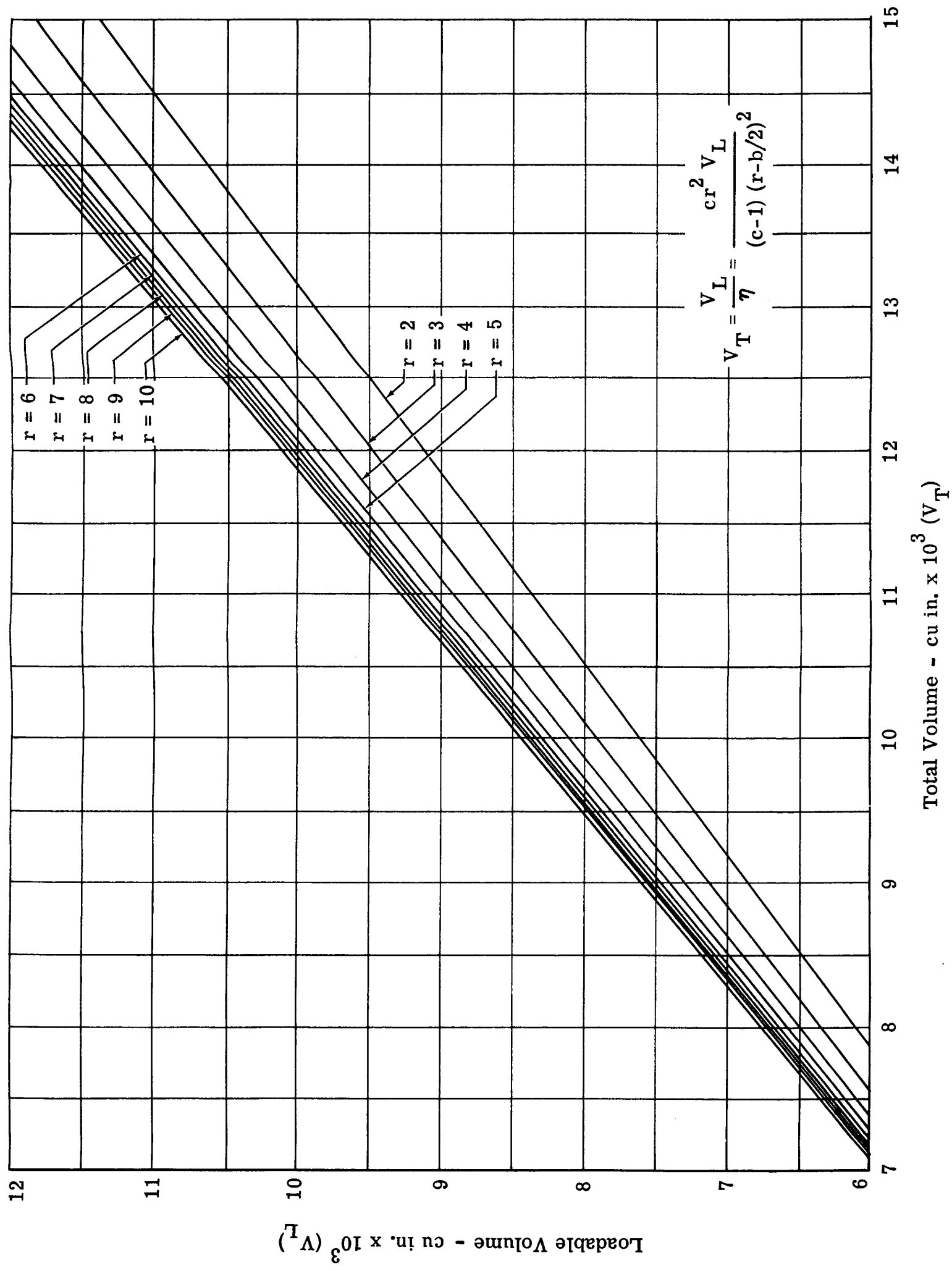
Figure 96b. Volumetric Efficiency Effect; 0.25 Span, 7.50 Expansion Ratio

$$\frac{V_L}{\eta} = \frac{cr^2 V_L}{(c-1)(r-b/2)^2}$$

$$V_T = $$

Total Volume – cu in. x 10^3 (V_T)

Loadable Volume – cu in. x 10^3 (V_L)

r = 6
r = 7
r = 8
r = 9
r = 10

r = 2
r = 3
r = 4
r = 5
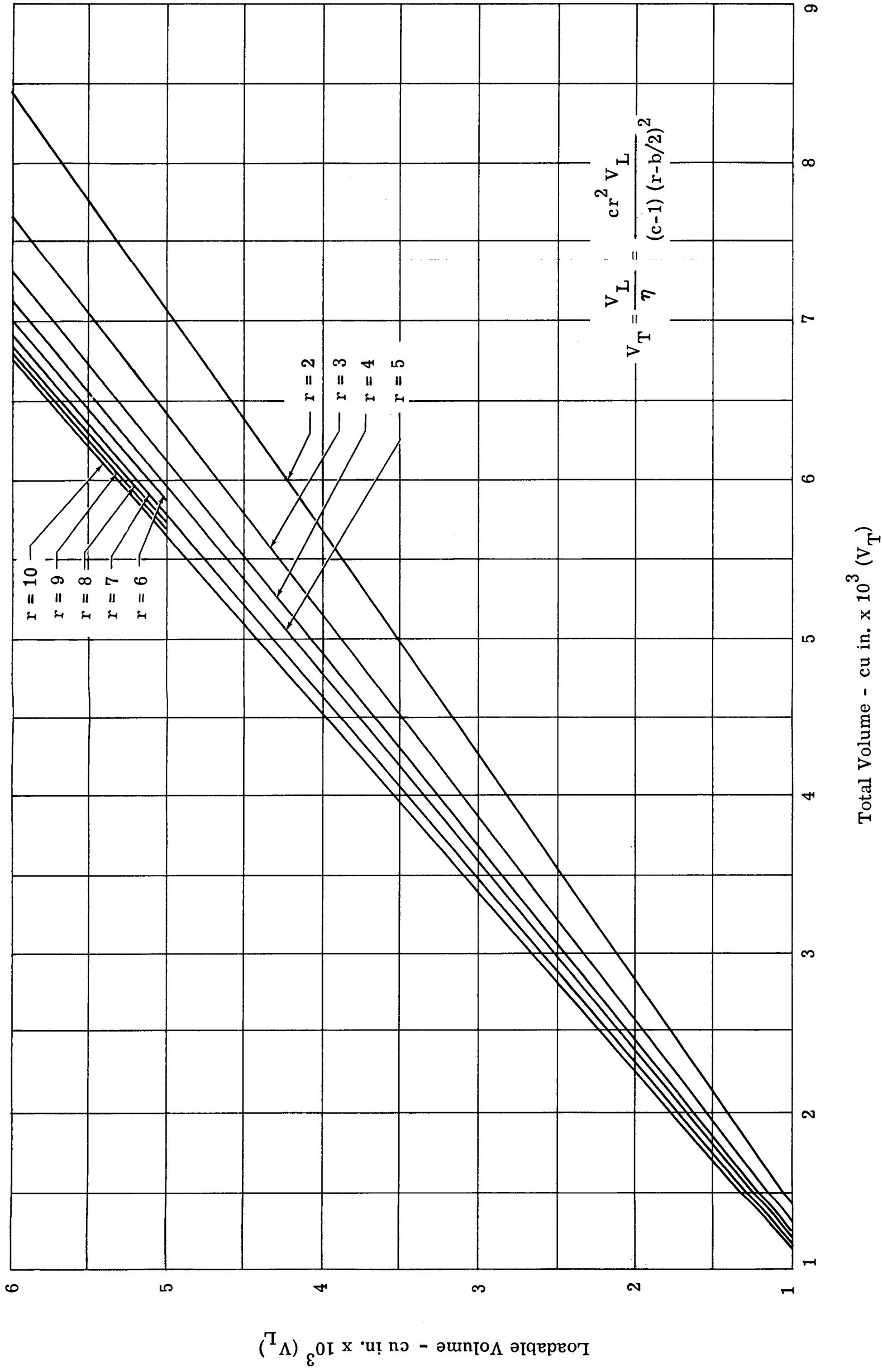
Figure 97a. Volumetric Efficiency Effect; 0.50 Span, 15.00 Expansion Ratio

$$V_T = \frac{V_L}{\eta} = \frac{cr^2 V_L}{(c-1)(r-b/2)^2}$$

Total Volume - cu in. x 10^3 (V_T)

Loadable Volume - cu in. x 10^3 (V_L)
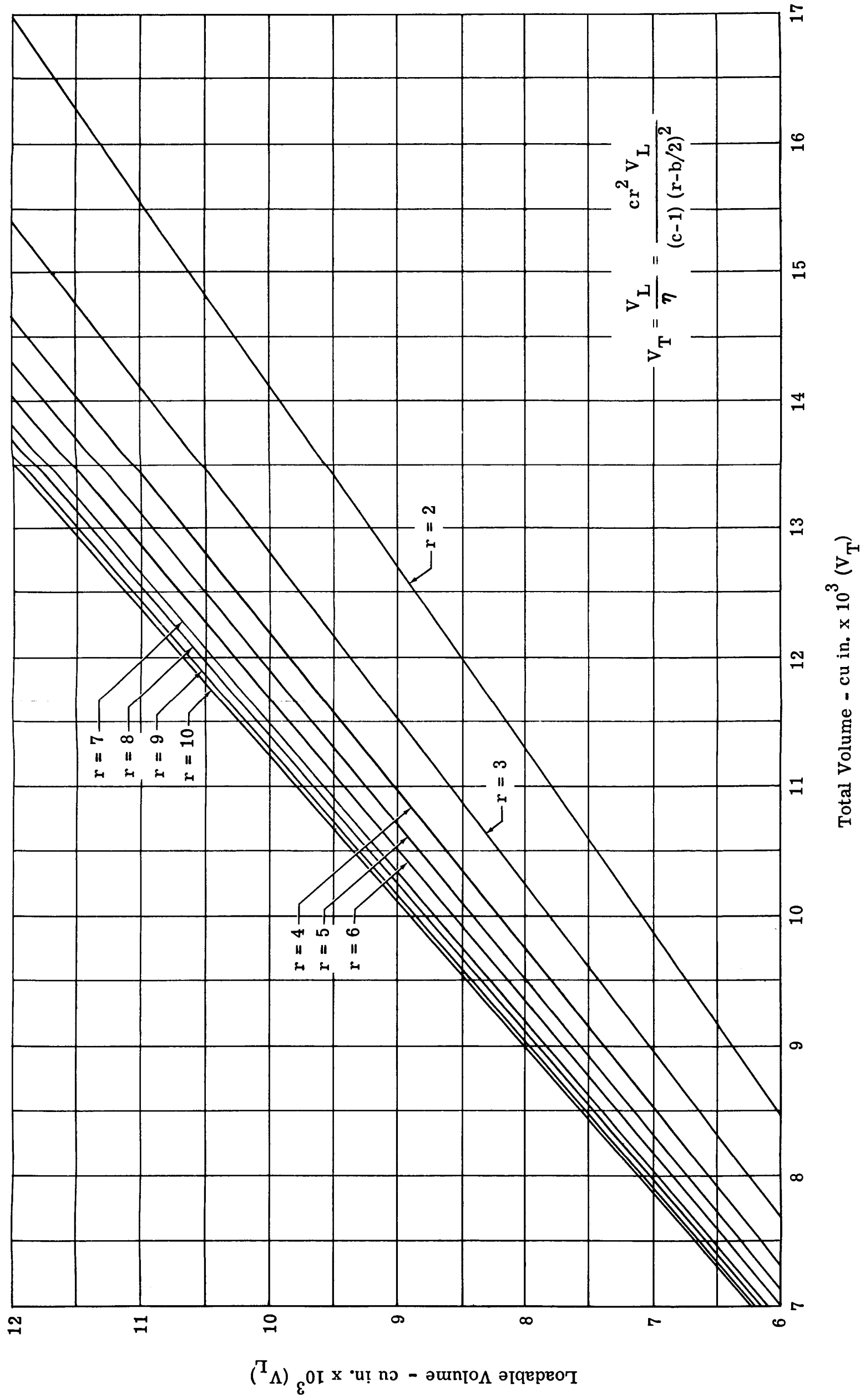
Figure 97b. Volumetric Efficiency Effect; 0.50 Span, 15.00 Expansion Ratio

$$V_T = \frac{V_L}{\eta} = \frac{cr^2 V_L}{(c-1)(r-b/2)^2}$$

Total Volume – cu in, x 10^3 (V_T)

Loadable Volume – cu in, x 10^3 (V_L)

136
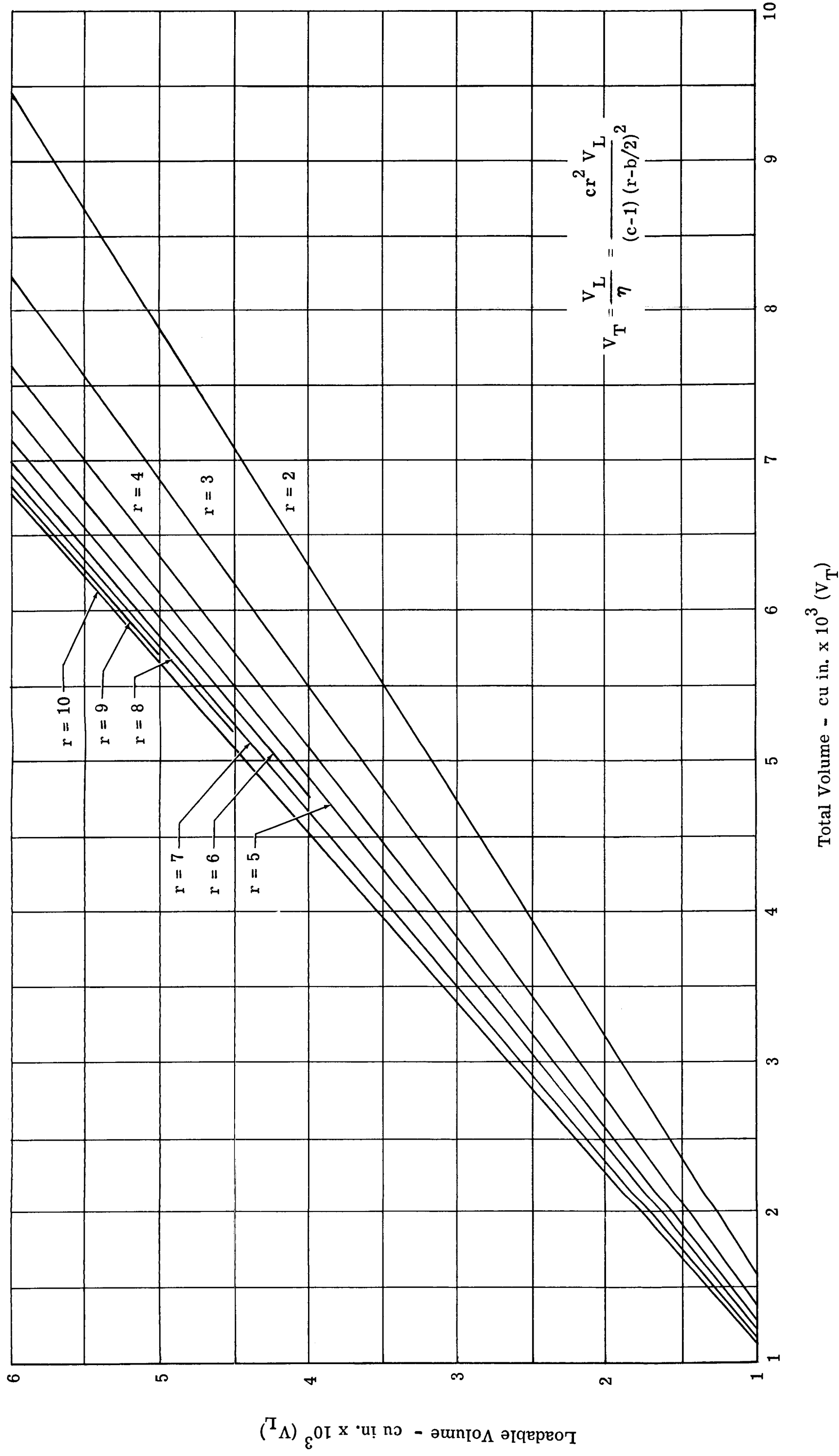
Figure 98a. Volumetric Efficiency Effect; 0.75 Span, 22.00 Expansion Ratio

$$V_T = \frac{V_L}{\eta} = \frac{cr^2 V_L}{(c-1)(r-b/2)^2}$$

Total Volume – cu in. x 10^3 (V_T)

Loadable Volume – cu in. x 10^3 (V_L)

$$V_T = \frac{V_L}{\eta} = \frac{cr^2 V_L}{(c-1)(r-b/2)^2}$$
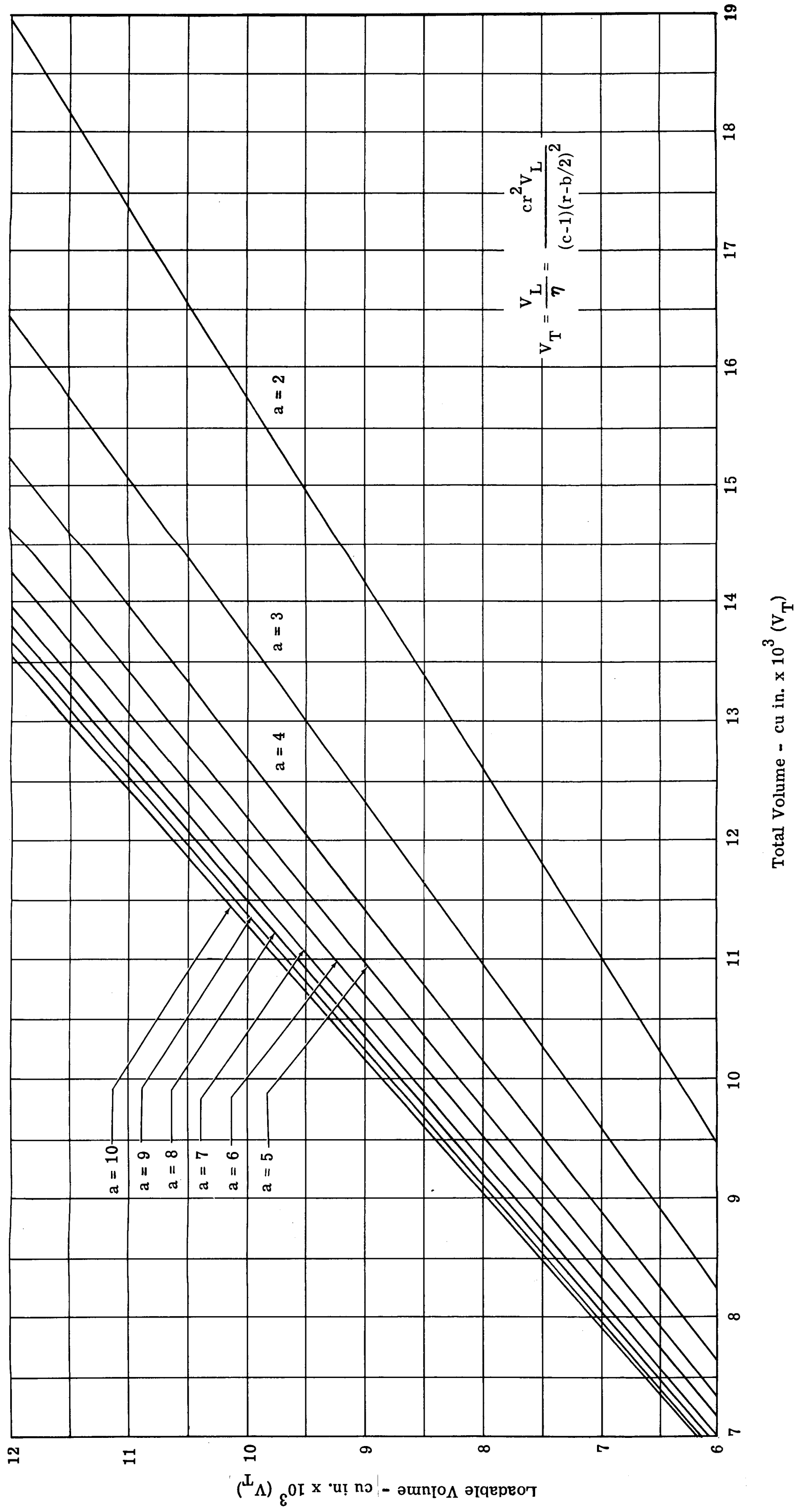
Figure 98b. Volumetric Efficiency Effect; 0.75 Span, 22.00 Expansion Ratio

138

The volumetric efficiency of the tank can now be written:

$$\eta = \frac{V_L}{V_T}$$

$$= \frac{\left(\frac{c-1}{c}\right) \pi \, (r-1/2b)^2 \, L}{\pi \, r^2 \, L}$$

$$= \left(\frac{c-1}{c}\right) \frac{(r-1/2b)^2}{r^2} \tag{70}$$

The illustrations give the total tank volume required in terms of bellows span, radius, and loadable volume:

$$V_T = \frac{V_L}{\eta}$$

$$= \frac{V_L}{\left(\frac{c-1}{c}\right) \frac{(r-1/2b)^2}{r^2}}$$

$$= \frac{cr^2 \, V_L}{(c-1) \, (r-1/2b)^2} \tag{71}$$

Figure 99 gives the required $L/2r$ ratio, or a, as a function of radius and loadable volume. From Equation 68:

$$V_T = \pi \, r^2 \, L$$

$$a = \frac{L}{2r}$$

$$V_T = 2 \pi \, a \, r^3 \tag{72}$$

At this point, the basic tank envelope is defined. The weight must now be calculated. The surface area of the cylindrical section is given by:

$$A_{sc} = 2 \pi \, r \, L$$
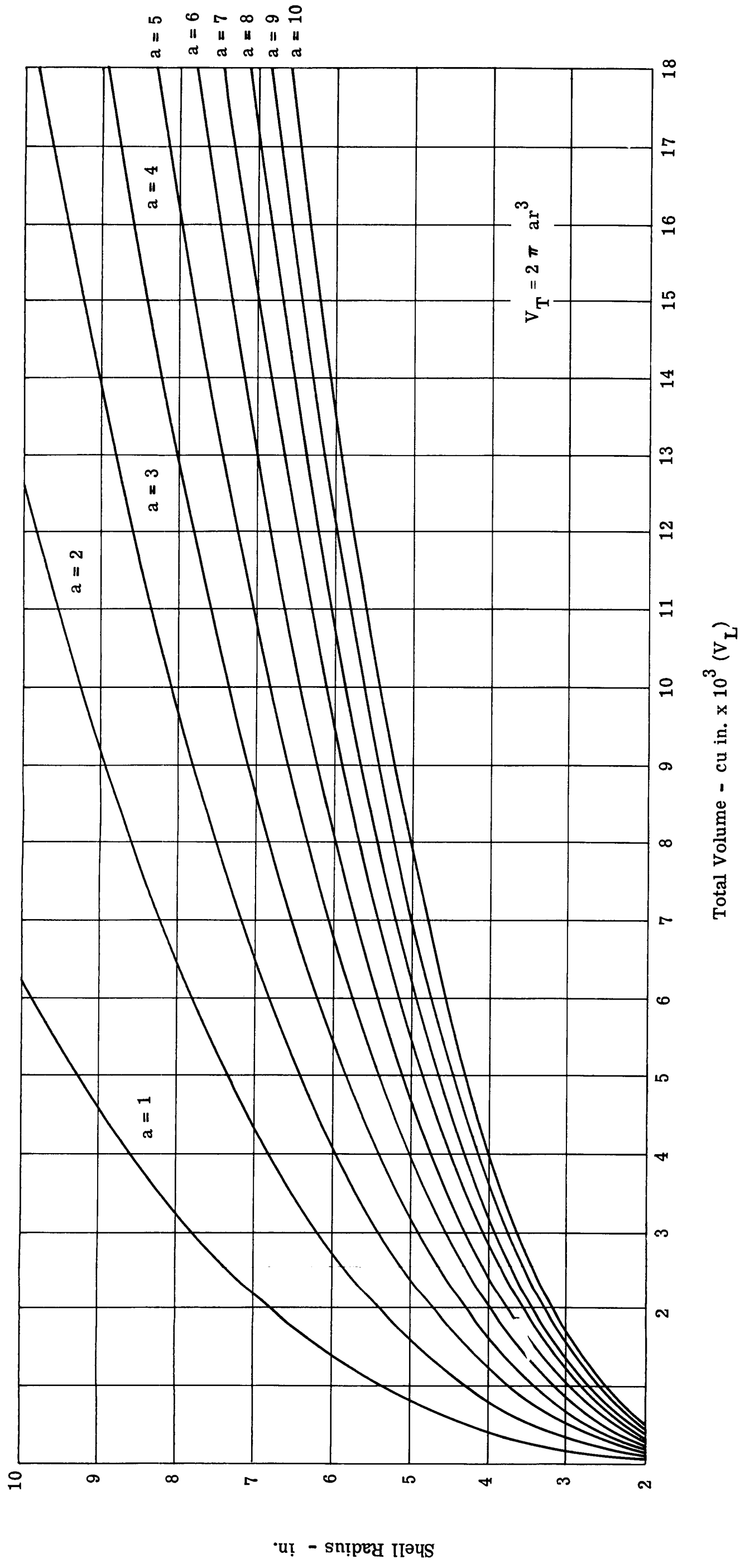
$$= 4 \pi \, r^2 \, a \tag{73}$$

Figure 99. Cylindrical Volume Relationships

and the weight of this section is:

$$\text{Weight} = \text{area x thickness x density}$$

$$\text{Wt} = A_{sc} \, td$$

substituting for A_{sc}:

$$\text{Wt} = 4 \, \pi \, r^2 \, atd$$

and, rearranging:

$$\frac{\text{Wt}}{td} = 4 \, \pi \, r^2 \, a \tag{74}$$

The term $\left(\dfrac{\text{Wt}}{td}\right)$ is the weight factor for this cylindrical section. This factor is plotted

in Figure 100 as a function of "a" and radius. Knowing both thickness and density, the weight is readily calculated.

The weight of the ends is obtained by a similar method. For the ellipse:

$$A_{se} = 1.379 \, \pi \, r^2 \tag{75}$$

$$\text{Wt} = A_{se} \, td$$

$$\frac{\text{Wt}}{td} = 1.379 \, \pi \, r^2 \tag{76}$$

For the hemisphere:

$$A_{sh} = 2 \, \pi \, r^2 \tag{77}$$

$$\text{Wt} = A_{sh} \, td$$

$$\frac{\text{Wt}}{td} = 2 \, \pi \, r^2 \tag{78}$$

It should be remembered that the thickness of the inverted head is n times the cylindrical section.

The weight of the bellows proper is obtained by adding the weight of the individual leaves. A factor is also introduced to account for the ripple in the leaves (1.07):

The weight is, therefore:

$$\text{Wt} = (\text{Leaf Area}) (\text{thickness}) (\text{number of leaves}) (\text{density})$$

$$= \text{Atnd}$$

The leaf area is:

$$A = \pi \left[r^2 - (r - 1.07 \, b)^2 \right]$$
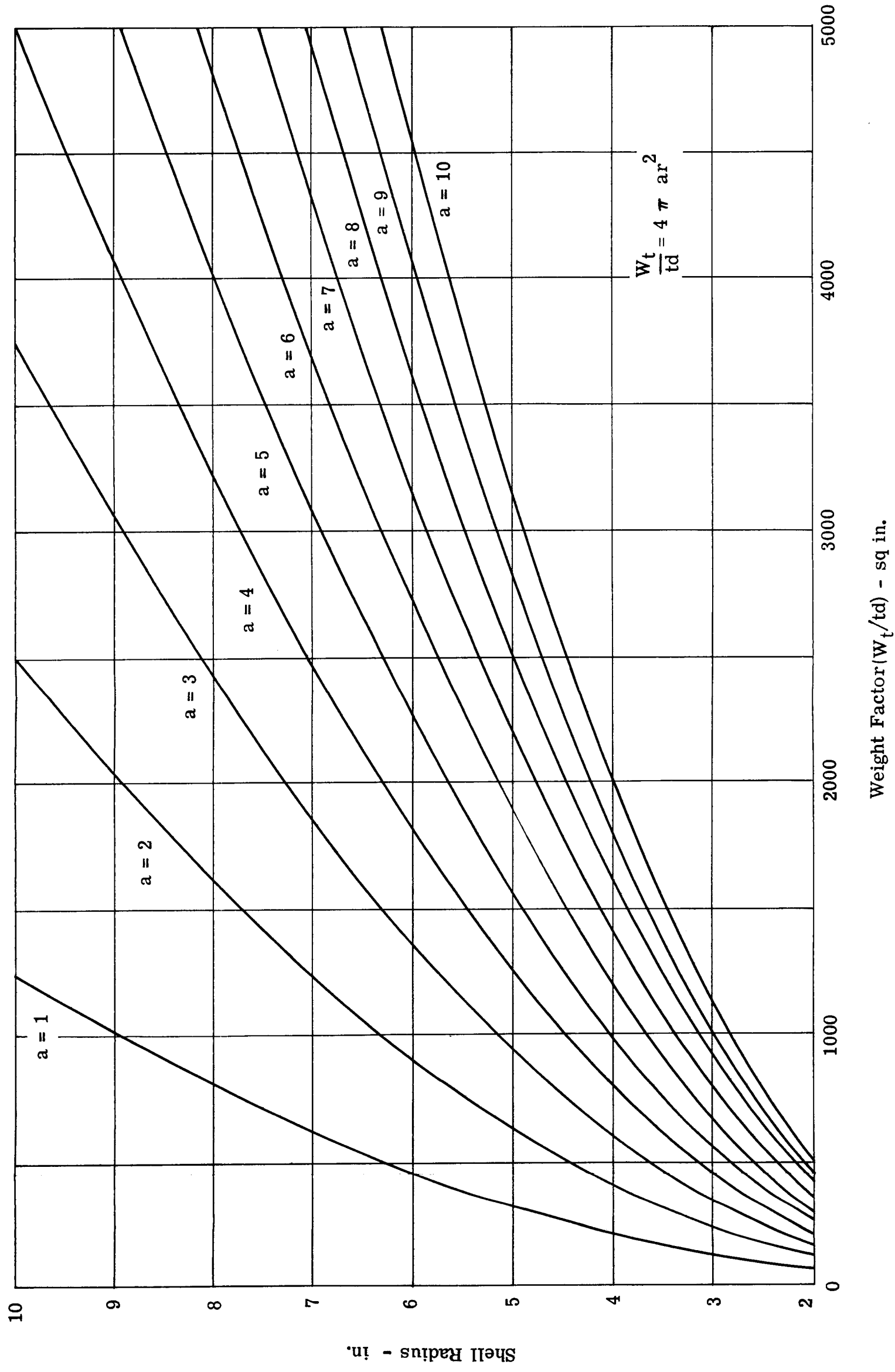
Figure 100. Weight Factor - Cylindrical Shells

$$\frac{W_t}{td} = 4 \pi \ ar^2$$

Shell Radius - in.

Weight Factor (W_t/td) - sq in.

a = 1
a = 2
a = 3
a = 4
a = 5
a = 6
a = 7
a = 8
a = 9
a = 10

The number of leaves is,

$$n = \frac{2L}{h} = \frac{4ar}{h}$$

For this analysis, d and t are held constant at 0.285 and 0.006 respectively, in accordance with current practice:

$$Wt = (4)\ (0.285)\ (0.006)\ \frac{\pi\ ar}{h} \left[r^2 - (r-1.07b)^2 \right]$$

$$= \frac{0.00684\ \pi\ ar}{h}\ (2.14\ rb - 1.14b^2)$$

$$= \frac{0.021\ ar}{h}\ (2.14rb - 1.14b^2) \tag{79}$$

The total weight is obtained by adding the incremental weights and allowing 20% for losses, weld, reinforcements, and other details not considered in this analysis.

C.   ILLUSTRATIVE EXAMPLE

To facilitate the use of the design illustrations in Figures 96 through 102, an example is provided in the following pages. The given requirements of this example are:

(1) Loadable volume - 5000 in.^{3}

(2) Burst pressure - 500 psig

(3) Material

   a.   Density - 0.285 lb/in.^{3}

   b.   Ultimate tensile strength - 180 ksi

   c.   Modulus of elasticity - 30 x 10^6 psi

(4) Use elliptical ends

With r in the range from 5 to 9 inches, the required thickness in the cylindrical section is:

$$t = \frac{Pr}{S}$$

$$= \frac{500\ r}{180000} = \frac{r}{360}$$

Therefore:

$t/r = 5\ \ = 0.014$ $\quad$ $t/r = 7 = 0.020$ $\quad$ $t/r = 9\ \ = 0.025$

$t/r = 6\ \ = 0.017$ $\quad$ $t/r = 8\ \ = 0.022$

Now, the n factor for the inverted head is to be determined:

$$n = \sqrt{\frac{4S^2}{0.366EP}}$$

$$= \sqrt{\frac{(4)\ (185{,}000)^2}{(0.366)\ (30 \times 10^6)\ (500)}}$$

$$= \sqrt{25}$$

$$= 5$$

To determine the weight of a 5-inch radius tank having a 1/4-span bellows, the following steps are taken:

(1) Knowing V_L and r, find V_T from Figure 96:

$$V_T = 6040\ \text{in.}^3$$

(2) Knowing V_T and r, find a from Figure 99:

$$a = 7.75$$

(3) Knowing a and r, find the weight factor for the cylindrical section from Figure 100 and calculate the weight:

$$\frac{Wt}{td} = 2440$$

$$Wt = (2440)\ (0.014)\ (0.285)$$

$$= 9.73\ \text{lb}$$

(4) Knowing r, find the weight factor for the ends from Figure 101 and calculate the weights:

$$\frac{Wt}{td} = 109$$

The normal end:

$$Wt = (109)\ (0.014)\ (0.285)$$

$$= 0.44\ \text{lb}$$

The inverted end:

$$Wt = (109)\ (0.014)\ (5)\ (0.285)$$

$$= 2.18\ \text{lb}$$
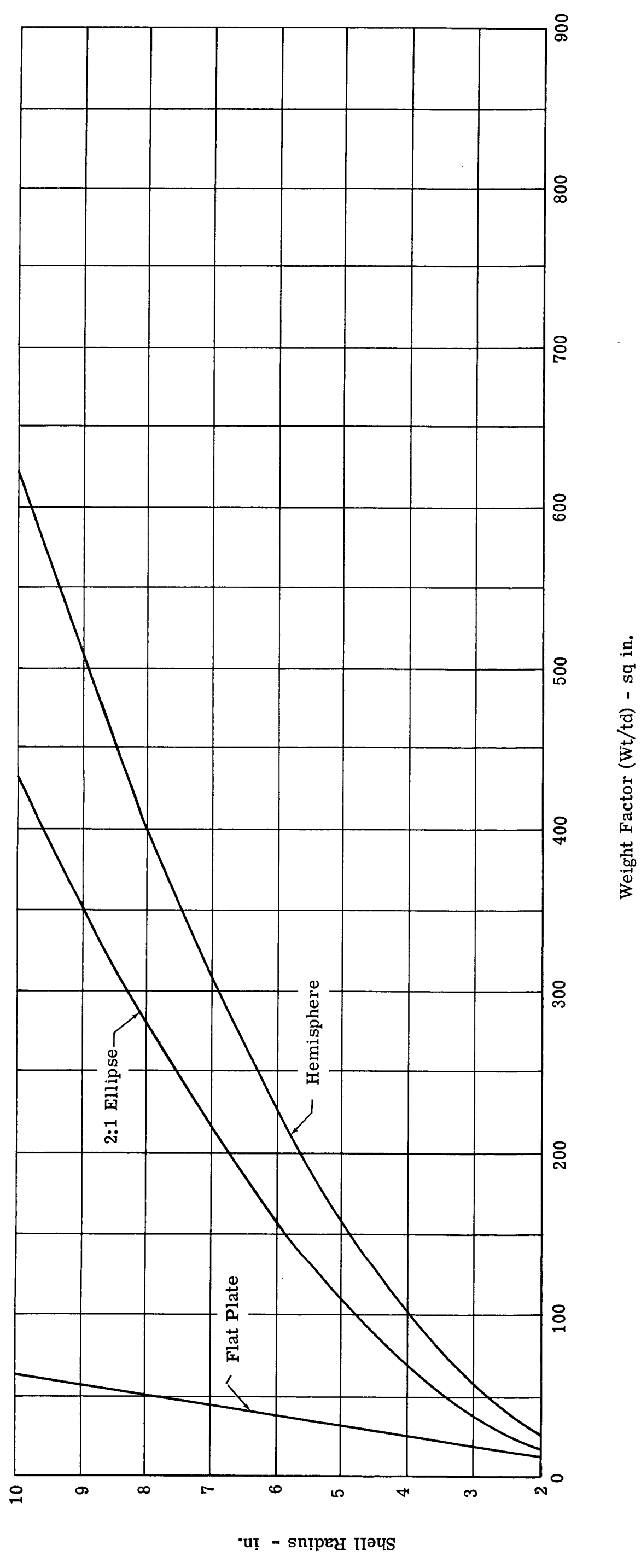
Figure 101. Weight Factor - End Closures

(5) Knowing r and a, the bellows weight from Figure 102a:

Wt = 14.53 lb

(6) Total weight:

Wt = 1.2 (9.73 + 0.44 + 2.18 + 14.53)

= 32.28 lb

This procedure is repeated over the full range of bellows spans and radii as shown in Table 6.

TABLE 6

WEIGHT-RADIUS RELATIONSHIP

Radius (in.)	Span (in.)	Weight (lb)
5	1/4	32.28
6	1/4	30.45
7	1/4	33.26
8	1/4	34.75
9	1/4	44.28
5	1/2	30.43
6	1/2	28.62
7	1/2	30.83
8	1/2	33.73
9	1/2	37.56
5	3/4	30.59
6	3/4	28.80
7	3/4	31.98
8	3/4	34.33
9	3/4	37.56

The data in Table 6 are shown graphically in Figure 103. The minimum weight appears at a radius of approximately 6 inches and a span equal to 1/2 inch. This, then, is the point from which detailed design analysis can begin.

Report No. 8230-933007
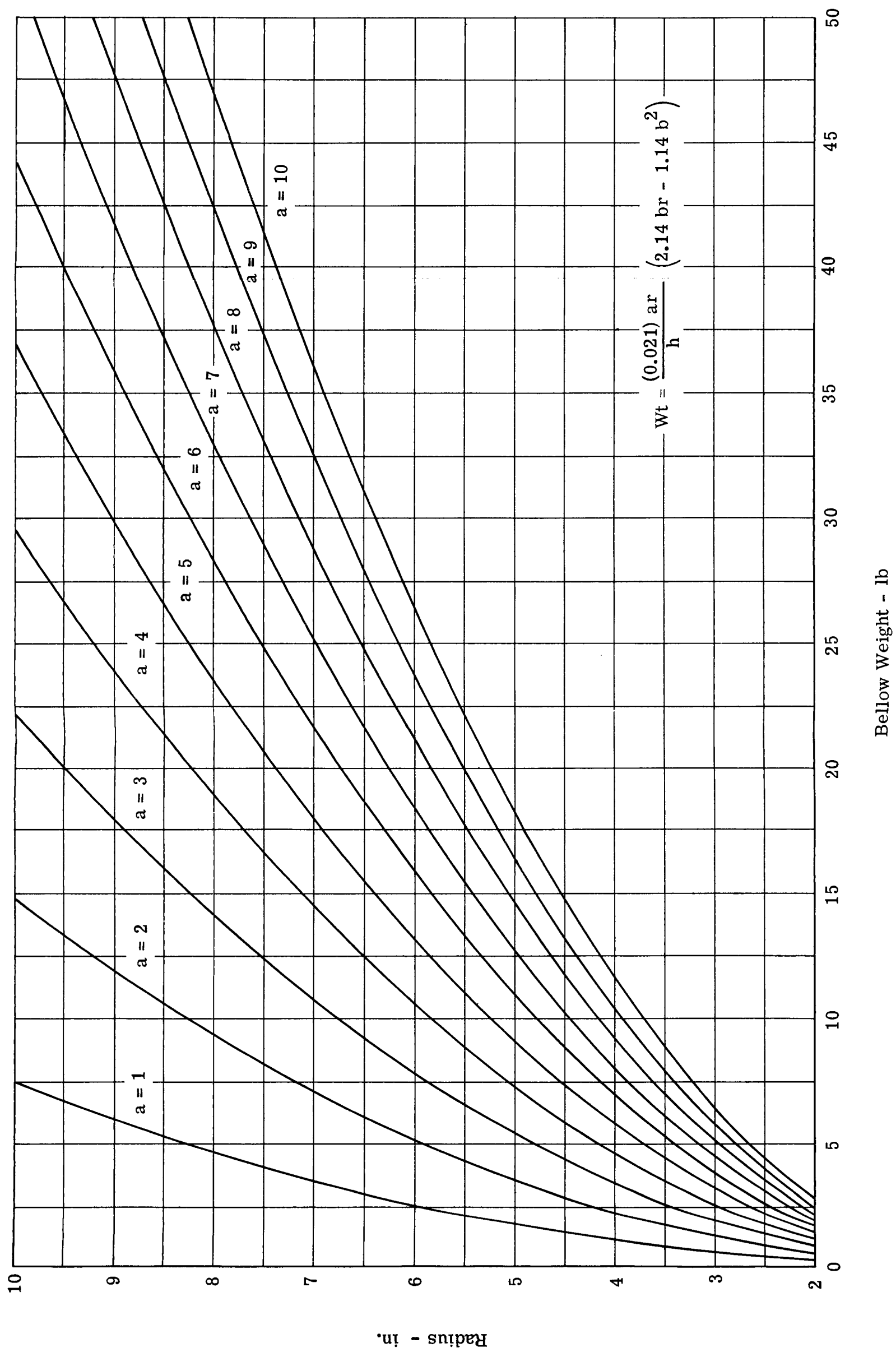
Figure 102a. Bellows Weight; Span = 0.25, Pitch = 0.15

$$Wt = \frac{(0.021) \ ar}{h} \left(2.14 \ br - 1.14 \ b^2\right)$$

Bellow Weight - lb
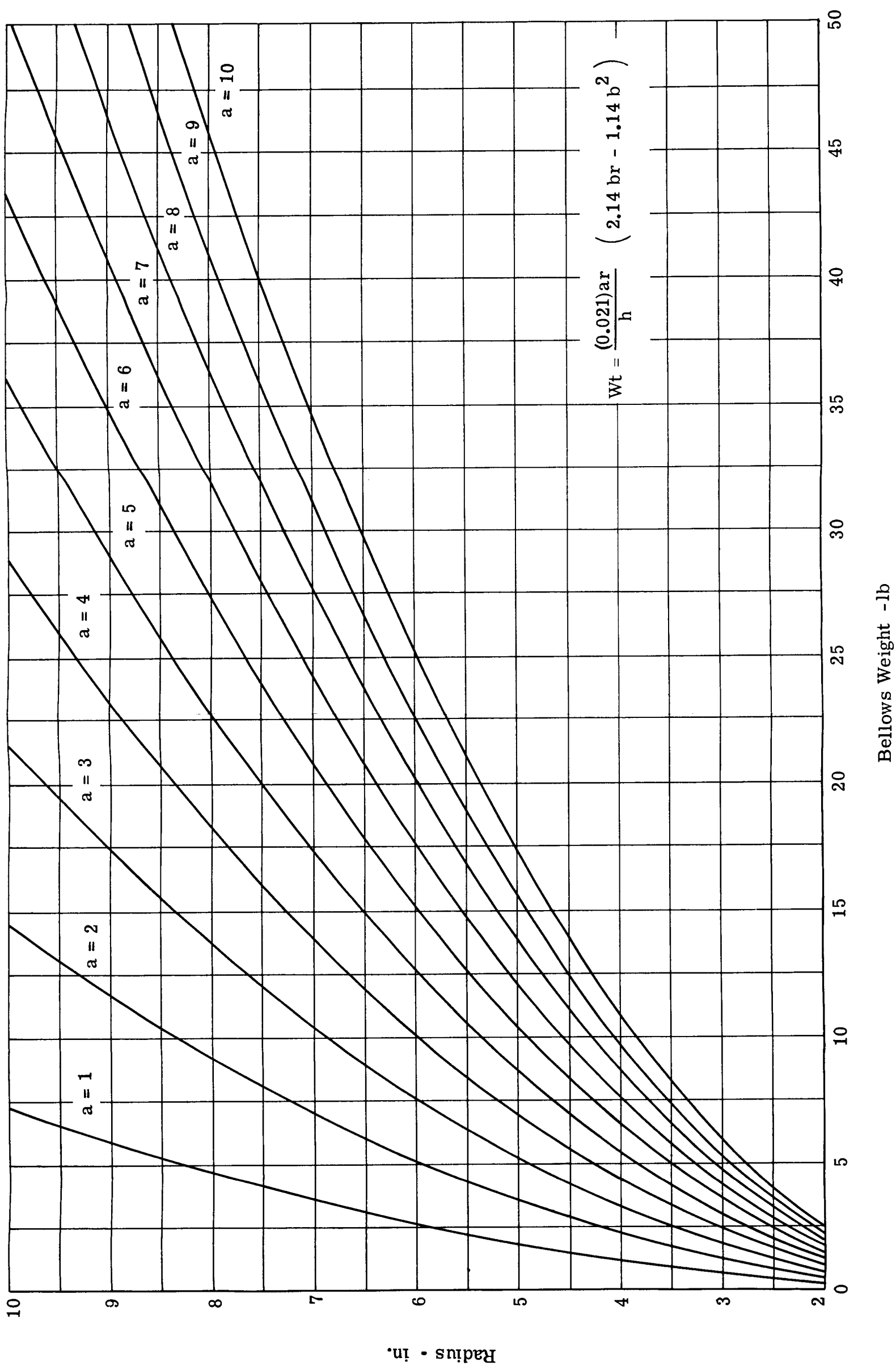
Radius - in.

Figure 102b. Bellows Weight; Span = 0.50, Pitch = 0.30

$$Wt = \frac{(0.021)ar}{h} \left(2.14\,br - 1.14\,b^2 \right)$$

Bellows Weight -lb

Radius - in.

148
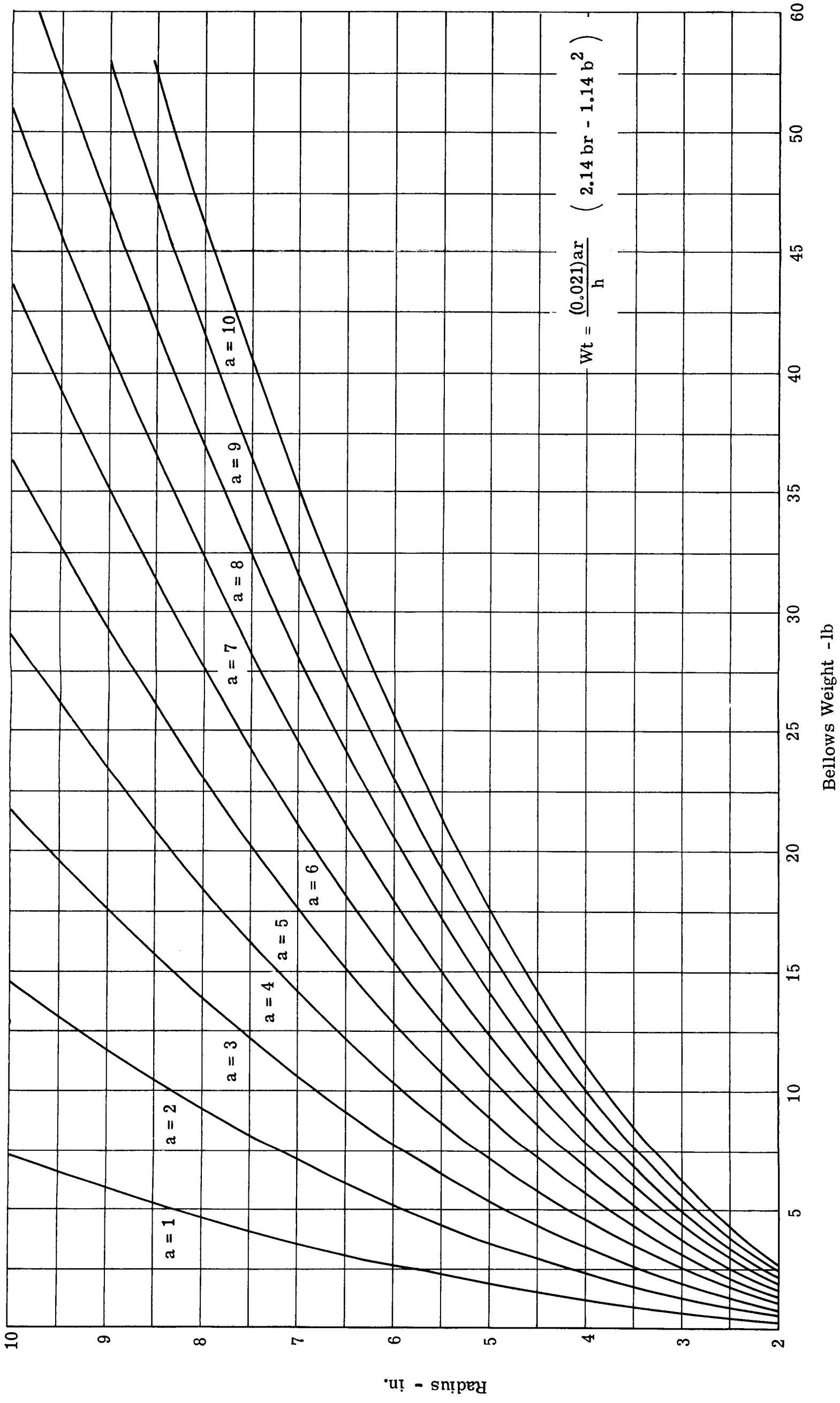
Figure 102c. Bellows Weight; Span = 0.75, Pitch = 0.45

$$Wt = \frac{(0.021)ar}{h} \left(2.14\, br - 1.14\, b^2 \right)$$

Figure 103. Weight-Radius Relationship

SECTION 6

REFERENCES

1. Bell Aerosystems Company; "Study of Zero-Gravity Positive Expulsion Techniques"; Report No. 8230-933004, June 1963; Unclassified.

2. Reissner, E.; "On Axisymmetric Deformation of Thin Shells of Revolution"; Proc. Symp. on Applied Math., 3, 1950; p. 32.

3. Archer, R.; "On the Numerical Solution of the Nonlinear Equations for Shells of Revolution"; Journal of Mathematics and Physics; Vol. XLI, No. 3; September 1962.

4. Hetenyi and Timms; "Analysis of Axially Loaded Annular Shells with Applications to Welded Bellows"; ASME Paper No. 59-A-175.

5. Weinitschke, H.; "Asymmetric Buckling of Clamped Shallows Spherical Shells"; NASA TN 0-1510; p- 481; 1962.

6. Huang, N. C., "Unsymmetrical Buckling of Thin Shallow Spherical Shells"; ONR Contract Nonr 1886 (02) Tech. Report No. 15, March 1963; Division of English and Applied Physics, Harvard University, Cambridge, Mass.

7. Berry, J. G. and Reissner, E.; "The Effect of an Internal Compressible Fluid Column on the Breathing Vibrations of a Thin, Pressurized, Cylindrical Shell"; Journal of the Aeronautical Sciences, pp. 288-294; May 1958.

8. Reissner, E.; "On Transverse Vibrations of Thin, Shallow, Elastic Shells"; Quarterly of Applied Math., Volume 13, pp. 169-176; 1955.

9. Uchida Shegeo; "The Pulsating Viscous Flow Superposed On the Steady Laminar Motion of Incompressible Fluid In a Circular Pipe"; Z AMP, Volume VII, pp. 403-422; 1956.

10. Yao, J. C.; "Stability of a Circular Cylinder Under Dynamic Radial Pressure"; ARS Journal, Volume 31, pp. 1705-1708; July-December 1961.
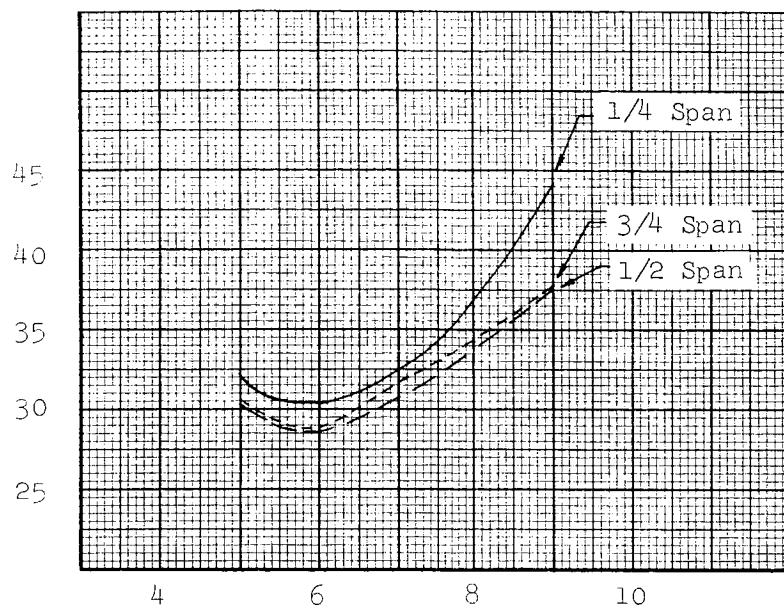
11. Donaldson, Coleman, and Sullivan; "Behavior of Solution of the Navier-Stokes Equations For a Complete Class of Three-Dimensional Viscous Flow; AFOSR No. TN-60-172; May 1960.

12. Minson, John S. and Herr, Robert W.; "An Investigation of the Vibration of Pressurized Thin-Walled Circular Cylinders Partly Filled With Liquid"; NASA Tech. Rept. R-145; 1962.

13. Rayleigh, Lord; "The Theory of Sound"; First Am. Ed., Vol. I and II, Dover Pub., pp. 395-432; 1945.

14. Timoshenko S. "Vibration Problems in Engineering"; Second Ed.; D. VanNostrand Co., Inc.; 1937.

15. Wylie, C. R. Jr.; "Advanced Engineering Math"; Second Ed.; McGraw-Hill Book Co., Inc.; 1960.

16. Watson G. N.; "A Treatise on the Theory of Bessel Functions"; Second Ed.; Cambridge Press; pp. 698-713; 1948.

17. Churchill R. V.; "Modern Operational Mathematics in Engineering"; First Ed.; McGraw-Hill Book Co.; 1944.

18. Sarbacher, Robert I. and Edson, William A.; "Hyper and Ultrahigh Frequency Engineering"; John Wiley and Sons; 1943.

19. Blackburn, J. F. et al; "Fluid Power Controls"; John Wiley and Sons; 1960.

20. Den Hartog, J. P.; "Mechanical Vibrations"; McGraw-Hill Book Co., Inc.; Fourth Edition; 1956.

21. Rouse, H., Editor; "Advanced Mechanics of Fluids"; John Wiley and Sons; 1959.

22. Harris, C. M., et al; "Shock and Vibration Handbook 1961"; Sections 36 and 37.

23. Keulemans, A. J. M.; "Gas Chromatography"; Second Ed.; 1960.

24. "Table of Thermal Properties of Gases"; National Bureau of Standards Circular 564; 1955.

25. Wassiljewa, A.; "Physikalische Zeitschrift"; Vol. 5, p. 737; 1904.

26. Lindsay, A. L. and Bromley, L. A.; "Industrial and Engineering Chemistry"; Vol. 42, p. 1508; 1950.

27. Gray, P. and Wright, P. G.; "Progress in Internal Research on Thermodynamics and Transport Properties"; ASME; p. 395; 1962.

28. "A Compendium of the Materials at Low Temperature (Phase I)"; National Bureau of Standards, Cryogenic Engineering Lab.; July 1960.

29. Nuttall, R. L., and Ginnings, D. C.; "Thermal Conductivity of Nitrogen from 50° to 500°C and 1 to 100 Atmospheres"; National Bureau of Standards; J. of Research, Paper No. 2760, Vol. 58, No. 5, p. 271ff; May 1957.

30. Johnson, V. J., Editor; "A Compendium of the Properties of Material at Low Temperature"; Part 1, Properties of Cryogenic Fluids; WADD Technical Report No. 60-56.

APPENDIX I

THERMISTOR CALCULATIONS

A. NITROGEN SYSTEM AT 25°C

Operating conditions (refer to Figure 81 of this report):

$$E = \frac{1}{4} \ I \ R_{t_b} \ \frac{(t_b - t_a)}{1 + \alpha \ t_b} \ \frac{\Delta k}{k} \ \frac{2 \ \gamma}{1 + \gamma} \tag{80}$$

Where: t_a = 25°C

t_b = 35°C

R_o = thermistor resistance at 25°C = 10K ohms

α = -4.4%/C° = -440 ohms/°C

R_1 = R_2 = 2K ohms = γR_o; $\therefore \gamma$ = 0.200

The thermistor resistance of t_b is given by:

$$\therefore R_{t_b} = R_o + \alpha \ t \tag{81}$$

Where: t = t_b - temperature at which R_o is measured

$$\therefore R_{t_b} = 10,000 + (\quad -440 \times 10)$$

$$= 5600 \text{ ohms}$$

The current required to maintain t_b is given by:

$$I^2 \ R_{t_b} = k_{t_m} \ (t_b - t_a) \ a \tag{82}$$

Where: k_{t_m} = thermal conductivity of nitrogen at the median

temperature: $\frac{1}{2} \ (t_b + t_a)$

$$= 0.624 \times 10^{-4} \text{ cal/cm/sec/°C}$$

a = constant depending upon cell geometry

or, $$I = \sqrt{\frac{k_{t_m} \ (t_b - t_a)}{R_{t_b}}} \ \sqrt{a} \tag{82a}$$

$$= \sqrt{\frac{0.624 \times 10^{-4} \times 10}{5600}} \sqrt{a} \quad = 3.34 \times 10^{-4} \sqrt{a} \quad \text{amperes}$$

From Equation 80, the bridge unbalance is:

$$\frac{E}{\sqrt{a}} = \frac{1}{4} (3.34 \times 10^{-4}) (5600) \frac{(-440)(10)}{1+(-440 \times 35)} \frac{\Delta k}{k} \frac{2 \times 0.200}{1 + 0.200}$$

$$= 0.0446 \frac{\Delta k}{k} \quad \text{volts}$$

B. HELIUM SYSTEMS

R_o = 500 ohms at 24°C (298°K)

x = -3.9%/°C = -19.5 ohms/°C

1. Liquid Hydrogen

At t_a = 20°K (-253°C)

t_b = 30°K (-243°C)

t_m = 25°K (-248°C)

$\therefore R_{t_b}$ = 5730 ohms $\hfill$ (81)

I = 3.18 x 10^{-4} $\sqrt{a}$ $\quad$ amperes

Where: k_{tm} = 0.58 x 10^{-4}, and, $\hfill$ (82a)

$$\frac{E}{\sqrt{a}} = -6.25 \times 10^{-4} \frac{\Delta k}{k} \quad \text{volts} \hfill (80)$$

2. Liquid Oxygen

At t_a = 90°K (-183°C)

t_b = 100°K (-173°C)

t_m = 95°K (-178°C)

$\therefore R_{t_b}$ = 4360 ohms $\hfill$ (81)

I = 6.10 x 10^{-4} $\sqrt{a}$ $\quad$ amperes

Where: k_{tm} = 1.628 x 10^{-4}, and, $\hfill$ (82a)

$$\frac{E}{\sqrt{a}} = -1.28 \times 10^{-3} \frac{\Delta k}{k} \quad \text{volts} \hfill (80)$$

3. Liquid Fluorine

At t_a = 85°K (-188°C)

t_b = 95°K (-178°C)

t_m = 90°K (-183°C)

∴ R_{t_b} = 4260 ohms $\qquad$ (81)

I = 6.07 x 10^{-4} $\sqrt{a}$ $\quad$ amperes

Where: k_{tm} = 1.565 x 10^{-4}, and, $\qquad$ (82a)

$$\frac{E}{\sqrt{a}} = -1.21 \times 10^{-3} \frac{\Delta k}{k} \quad \text{volts} \qquad (80)$$

4. Liquid Flourine*

At t_a = 85°K (-188°C)

t_b = 323°K (+50°C)

t_m = 204°K (-69°C)

∴ R_{t_b} = 12 ohms $\qquad$ (81)

I = 7.50 x 10^{-2} $\sqrt{a}$ $\quad$ amperes

Where: k_{tm} = 2.82 x 10^{-4}, and, $\qquad$ (82a)

$$\frac{E}{\sqrt{a}} = 0.358 \frac{\Delta k}{k} \quad \text{volts} \qquad (80)$$

*These data are included to show that, subject to the limitations mentioned previously, an increase in the thermistor bead temperature well within its temperature limits (500°C maximum) results in a 300-fold increase in bridge output.

APPENDIX II

THEORETICAL THERMAL CONDUCTIVITY CALCULATIONS

Thermal conductivity calculations for the gaseous systems under consideration are based upon the joint use of Wassiljewa's equation (Reference 25) and the semi-empirical equations of Lindsay and Bromley (Reference 26). These equations, based upon the kinetic theory of gases, require a knowledge of pure component conductivities, heat capacity or viscosity, boiling points, molecular weights, and polarity.

Wassiljewa's equation is represented by:

$$k = \frac{k_i}{1 + A_{ij} \, x_j/x_i} + \frac{k_j}{1 + A_{ji} \, x_i/x_j}$$

Where:

k = thermal conductivity of gas mixture

k_i = thermal conductivity of pure gas component, i

k_j = thermal conductivity of pure gas component, j

x_i = mole fraction of gas i

x_j = mole fraction of gas j

A_{ij} = ratio of the efficiency with which molecules j and molecules i impede the transfer of heat by molecules i. Values are derived from the equation of Lindsay and Bromley.

The Lindsay and Bromley equation is represented by:

$$A_{ij} = \frac{1}{4} \left\{ 1 + \left[\left(\frac{\eta_i}{\eta_j}\right)\left(\frac{M_j}{M_i}\right)^{3/4} \left(\frac{T + S_i}{T + S_j}\right)\right]^{1/2} \right\}^2 \left(\frac{T + S_{ij}}{T + S_i}\right)$$

Where:

η_i = viscosity of gas i at temperature T

η_j = viscosity of gas j at temperature T

M_i = molecular weight of gas i

M_j = molecular weight of gas j

S_i = Sutherland constant = 1.5 T_B (T_B = boiling point of gas i)

S_j = Sutherland constant = 1.5 T_B (T_B = boiling point of gas j)

$S_{ij} = \sqrt{S_i S_j}$ for non-polar gas mixture, or,

$0.733 \sqrt{S_i S_j}$ for polar components

T = absolute temperature, °K

The use of these equations for predicting thermal conductivities of binary gaseous systems was reported by Gray and Wright (Reference 27) to give data accurate within 2% to 5%. Based upon A_{ij} derived from binary mixtures, Gray and Wright also reported data accuracy to be within 2% to 5%.

During this contract, equations were programmed on an IBM 7090 computer to facilitate computations. Thermal conductivities of binary systems consisting of He/O_2, He/N_2, N_2/N_2O_4, He/F_2, He/H_2, He/CO_2, and N_2/CO_2 were calculated over a range of temperatures extending from cryogenic to 140°F. Conductivities and viscosity values of the pure gases were obtained from Reference 28.

A literature survey failed to provide the data required for calculations of the ternary mixture N_2/MON, or for UDMH, N_2H_4, H_2O_2, OF_2, CH_4, and CTF.

APPENDIX III

OPERATING PROCEDURES FOR

DIAPHRAGM-TYPE PERMEATING APPARATUS

A.   ASSEMBLY OF APPARATUS

See the sectional view of the permeation apparatus in Figure 71; a flow schematic is presented in Figure 104.

CAUTION

Before and during assembly, protect and/or handle with care parts with serrated sealing surfaces to avoid scratches or nicks on these surfaces.

1.   Thoroughly clean (degrease) and dry all components prior to assembly.

2.   Cut four ring-shaped gaskets (ID 3.375 inches) out of Teflon, polyethylene, or other compatible material.

3.   Position metal diaphragm on one side of middle section (Figure 73) sandwiched between two gaskets. Center corrugated area of diaphragm in apparatus.

4.   Carefully place cover (Figure 72) over diaphragm and secure with eight screws. Torque screws to 70 to 80 inch-pounds.

5.   Before completing the assembly, diaphragm should be tested for pinhole leaks. The most sensitive method is with the helium leak detector:

   (1)   Apply low-pressure helium to liquid side of diaphragm. Regulate pressure by deflection of diaphragm. Do not deflect beyond 1/8 inch at center of diaphragm.

   (2)   If no leaks, remove helium gas line and proceed with assembly.

6.   Install test specimen in manner similar to metal diaphragm; i.e., centered over opening and sandwiched between two ring-shaped gaskets. (Note: If specimen is 0.020 inch thick or more, separate gaskets can be eliminated.)

7.   Install cover and torque screws to 70 to 80 inch-pounds.

8.   Install lines and valves in accordance with flow schematic in Figure 104. The liquid line connecting the two liquid cavities should be as short as possible, and valve 1 must be in the middle of the line.

9.   Install thermistor detector in port on middle section. See Figure 73 Note B.

10.   After assembly is complete, apparatus must be leak-tested. The helium leak detector is recommended:

   (1)   Attach a manifold line between valves 1 and 2 (Figure 104) with a tee in the middle of the line. Attach a valve (No. 6) to the outlet on the tee. The lines

should be arranged so that the line pressure drop between valve 6 and the gas side of the apparatus will be approximately equal to the pressure drop between valve 6 and the liquid side of the apparatus.

(2) Open valves 1 and 2.

(3) Close valves 3, 4, and 5, or cap these ports.

(4) With helium line attached to valve 6, slowly pressurize apparatus to operating pressure; e.g., 150 psig. Pressure must be raised slowly (take 10 minutes or longer) so that no differential pressure is imparted across specimen or diaphragm due to unequal pressure drops in lines.

(5) Check for leaks. If none, depressurize slowly (take 10 minutes or longer) for the same reason as in (4).

11. Apparatus is now ready for loading and test.
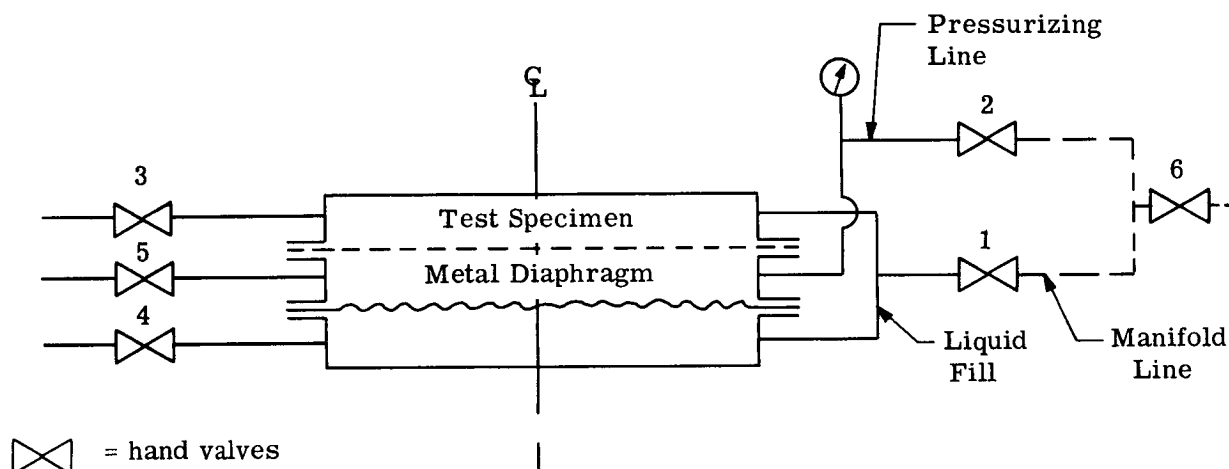
Figure 104. Flow Schematic of Diaphragm-Type Permeation Apparatus

B. LOADING PROCEDURE

1. Before loading, the apparatus must be cooled to a minimum of 5°F below the boiling point of the test propellant; e.g., 65°F for N_2O_4 and below 140°F for UDMH.

2. Connect reservoir of test liquid (100 cc or more) to valve 1 (Figure 104).

3. Open valves 3 and 4. These valves may be eliminated and caps used. In either case, an overflow line should be provided for each port.

4. Position apparatus with center line horizontal and valves 3 and 4 in uppermost position. Liquid level in reservoir must be above valves 3 and 4.

5. Open valve 1 and allow liquid to flow by gravity into liquid sides of specimen and diaphragm until a steady stream is noted at valves 3 and 4. Shake or move apparatus to eliminate gas bubbles.

6. Close or cap ports 3 and 4.

7. Close valve 1.

160   Report No. 8230-933007

8.   Close valve 5. This valve may be eliminated and a cap used to close the port. This port is only used for purging the gas side of the apparatus.

9.   Pressurize unit through valve 2 to test pressure; e.g., 150 psig.

C.   TEST

1.   Attach cable from thermistors in permeation chamber to Wheatstone bridge network.

2.   Hook up power supply to bridge network.

3.   Adjust power for required current to thermistors (see discussion of thermistors).

4.   For read-out device, use millivoltmeter or millivolt recorder. See Figure 86 for complete apparatus setup. The block diagram in Figure 105 shows the hook-up.

5.   Immediately following loading of permeation chamber, adjust bridge network for zero reading on recorder, or millivoltmeter.

6.   Record millivolt readings as the test progresses.

Figure 105. Block Diagram of Permeation Apparatus
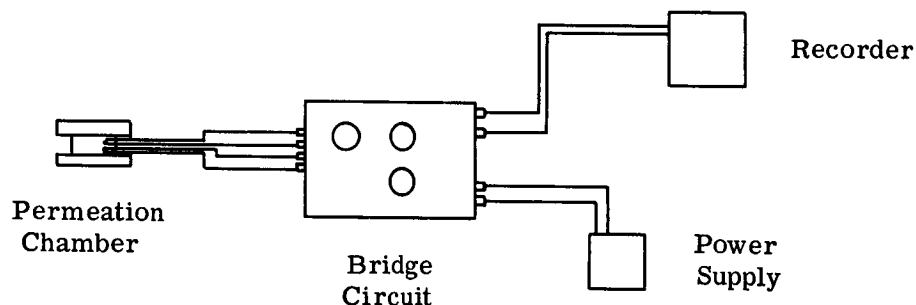
D.   UNLOADING PROCEDURE

1.   Before unloading, apparatus must be at a temperature 5°F below boiling point of test propellants.

2.   Slowly bleed off gas pressure through valve 2.

3.   Position apparatus with valve 1 in low position. Open valve 1. Carefully open valves 3 and 4, or remove caps.

4.   Drain liquid and purge chamber. Disassemble or cleaning.

DISTRIBUTION LIST FOR BELL AEROSYSTEMS COMPANY
REPORT NO. 8230-933007 - FINAL REPORT ON CONTRACT NAS7-149
STUDY OF ZERO-GRAVITY POSITIVE EXPULSION TECHNIQUES

Copies	Recipient	Copies	Recipient
	NASA Headquarters, Washington, D. C. 20546	2	Marshall Space Flight Center Huntsville, Alabama 35812
1	Contracting Officer, BCA		
1	Patent Office, AGP	2	Manned Spacecraft Center Houston, Texas 77001
	NASA Lewis Research Center 21000 Brookpark Road Cleveland, Ohio 44135	1	Advanced Research Projects Agency Washington 25, D. C.
1	Office of Technical Information		
1	Contracting Officer	1	Aeronautical Systems Division Air Force Systems Command Wright-Patterson Air Force Base Dayton, Ohio
1	Patent Office		
	NASA Marshall Space Flight Center Huntsville, Alabama 35812		
1	Office of Technical Information, M-MS-IPC	1	Air Force Missile Development Center Holloman Air Force Base, New Mexico
1	Contracting Officer, M-P&C-C		
1	Patent Office, M-PAT	1	Air Force Missile Test Center Patrick Air Force Base, Florida
	NASA Western Operations Office 150 Pico Boulevard Santa Monica, California 90406	1	Air Force Systems Command, Dyna-Soar Air Force Unit Post Office Los Angeles 45, California
1	Office of Technical Information		
1	Contracts Management Division		
1	General Counsel for Patent Matters	1	Arnold Engineering Development Center Arnold Air Force Station Tullahoma, Tennessee
	NASA Headquarters, Washington, D. C. 20546		
4	Mr. Henry Burlage, Jr. Chief, Liquid Propulsion Systems, RPL	1	Bureau of Naval Weapons Department of the Navy Washington 25, D. C.
1	Mr. Vernon E. Jaramillo Advanced Manned Mission, MTA	1	Central Intelligence Agency 2430 E Street, N. W. Washington 25, D. C. Attn: Miss Elizabeth F. Kernan
25	Scientific and Technical Information Facility NASA Representative, Code CRT P. O. Box 5700 Bethesda, Maryland 20014		
1	(Technical Manager) Mr. Richard N. Porter (122-23) Jet Propulsion Laboratory 4800 Oak Grove Drive Pasadena, California 91103	1	Defense Documentation Center Headquarters Cameron Station, Building 5 5010 Duke Street Alexandria, Virginia 22314 Attn: TISIA
2	Ames Research Center Moffett Field, California 94035	1	Headquarters, U. S. Air Force Washington 25, D. C.
2	Goddard Space Flight Center Greenbelt, Maryland 20771	1	Picatinny Arsenal Dover, New Jersey
2	Jet Propulsion Laboratory California Institute of Technology 4800 Oak Grove Drive Pasadena, California 91103	1	Rocket Research Laboratories Edwards Air Force Base Edwards, California
2	Langley Research Center Langley Station Hampton, Virginia 23365	1	U. S. Atomic Energy Commission Technical Information Services Box 62 Oak Ridge, Tennessee
2	Lewis Research Center 21000 Brookpark Road Cleveland, Ohio 44135	1	U. S. Army Missile Command Redstone Arsenal, Alabama 35809

Copies	Recipient	Copies	Recipient
1	U. S. Naval Ordnance Test Station China Lake, California 93557	1	Curtiss-Wright Corporation Wright Aeronautical Division Wood-Ridge, New Jersey
1	Chemical Propulsion Information Agency Johns Hopkins University Applied Physics Laboratory 8621 Georgia Avenue Silver Spring, Maryland	1	Douglas Aircraft Company, Inc. Missile and Space Systems Division 3000 Ocean Park Boulevard Santa Monica, California 90406
1	Aerojet-General Corporation P. O. Box 296 Azusa, California	1	Fairchild Stratos Corporation Aircraft Missiles Division Hagerstown, Maryland
1	Aerojet-General Corporation P. O. Box 1947 Technical Library, Bldg. 2015, Dept 2410 Sacramento 9, California	1	General Dynamics/Astronautics Library & Information Services (128-00) P. O. Box 1128 San Diego, California 92212
1	Aeronutronic A Division of Ford Motor Company Ford Road Newport Beach, California	1	General Electric Company Missile and Space Vehicle Department 3198 Chestnut Street, Box 8555 Philadelphia 1, Pennsylvania
1	Aerospace Corporation 2400 East El Segundo Boulevard P. O. Box 95085 Los Angeles, California 90045	1	General Electric Company Flight Propulsion Lab Department Cincinnati 15, Ohio
1	Arthur D. Little, Inc. Acorn Park Cambridge 40, Massachusetts	1	Grumman Aircraft Engineering Corp. Bethpage, Long Island, New York
1	Astropower, Inc., Subsidiary of Douglas Aircraft Company 2968 Randolph Avenue Costa Mesa, California	1	Kidde Aero-Space Division Walter Kidde and Company, Inc. 675 Main Street Belleville 9, New Jersey
1	Astrosystems, Inc. 1275 Bloomfield Avenue Caldwell Township, New Jersey	1	Lockheed California Company 10445 Glen Oaks Boulevard Pacoima, California
1	Atlantic Research Corporation Edsall Road and Shirley Highway Alexandria, Virginia	1	Lockheed Missiles and Space Company Attn: Technical Information Center P. O. Box 504 Sunnyvale, California
1	Beech Aircraft Corporation Boulder Facility Box 631 Boulder, Colorado	1	Lockheed Propulsion Company P. O. Box 111 Redlands, California
1	Bell Aerosystems Company P. O. Box 1 Buffalo 5, New York	1	The Marquardt Corporation 16555 Saticoy Street Box 2013 - South Annex Van Nuys, California
1	Bendix Systems Division Bendix Corporation Ann Arbor, Michigan	1	Martin Division Martin Marietta Corporation Baltimore 3, Maryland
1	Boeing Company P. O. Box 3707 Seattle 24, Washington	1	Martin Denver Division Martin Marietta Corporation Denver, Colorado
1	Chrysler Corporation Missile Division Warren, Michigan	1	McDonnell Aircraft Corporation P. O. Box 6101 Lambert Field, Missouri

Copies	Recipient	Copies	Recipient
1	North American Aviation, Inc. Space & Information Systems Division Downey, California	1	Space Technology Laboratories Subsidiary of Thompson-Ramo-Wooldridge P. O. Box 95001 Los Angeles 45, California
1	Northrop Corporation 1001 East Broadway Hawthorne, California	1	Stanford Research Institute 333 Ravenswood Avenue Menlo Park, California
1	Pratt & Whitney Aircraft Corp. Florida Research and Development Center P. O. Box 2691 West Palm Beach, Florida	1	TAPCO Division Thompson-Ramo-Wooldridge, Inc. 23555 Euclid Avenue Cleveland 17, Ohio
1	Radio Corporation of America Astro-Electronics Division Defense Electronic Products Princeton, New Jersey	1	Thiokol Chemical Corporation Redstone Division Huntsville, Alabama
1	Reaction Motors Division Thiokol Chemical Corporation Denville, New Jersey 07832	1	United Aircraft Corporation Research Laboratories 400 Main Street East Hartford 8, Connecticut
1	Republic Aviation Corporation Farmingdale Long Island, New York	1	United Technology Center 587 Methilda Avenue P. O. Box 358 Sunnyvale, California
1	Rocketdyne (Library Dept. 586-306) Division of North American Aviation 6633 Canoga Avenue Canoga Park, California 91304	1	Vought Astronautics Box 5907 Dallas 22, Texas
1	Space General Corporation 9200 Flair Avenue El Monte, California	1	The Garrett Corporation 9851 Sepulveda Blvd. Los Angeles, California 90009